

Attosecond pulse generation with tailored sub-cycle fields

**Dissertation
zur Erlangung des Doktorgrades
an der Fakultät für Mathematik, Informatik und Naturwissenschaften
Fachbereich Physik
der Universität Hamburg**

**vorgelegt von
Miguel Angel Silva Toledo**

**Hamburg
2024**

Gutachter der Dissertation:
Prof. Dr. Franz X. Kärtner
Prof. Dr. Markus Drescher

Zusammensetzung der Prüfungskommission:
Prof. Dr. Franz X. Kärtner
Prof. Dr. Markus Drescher
Prof. Dr. Markus Gühr
Prof. Dr. Francesca Calegari
Prof. Dr. Daniela Pfannkuche

Vorsitzende/r der Prüfungskommission:
Prof. Dr. Daniela Pfannkuche

Datum der Disputation:
12.12.2024

Vorsitzender Fach-Promotionsausschusses PHYSIK:
Prof. Dr. Markus Drescher

Leiter des Fachbereichs PHYSIK:
Prof. Dr. Wolfgang J. Parak

Dekan der Fakultät MIN:
Prof. Dr.-Ing. Norbert Ritter

*A mi madre y padre:
María Guadalupe Toledo Espinosa y Miguel Angel Silva Méndez.*

Abstract

Observing ultrafast molecular processes on the attosecond timescale of electrons is essential for understanding chemical and physical phenomena. Attosecond pulses offer the temporal resolution needed to capture electronic dynamics. Their tunability from the extreme ultraviolet (EUV) to soft X-ray regions enables probing both valence and deeper K- and L-shell electrons, with the latter providing site- and element-specificity. This thesis explores the generation of isolated attosecond pulses (IAPs) in the EUV and soft X-ray spectral regions, extending up to the water window (284–543 eV). Tailored optical fields, capable of reaching sub-cycle durations—i.e., shorter than their main oscillation period—are investigated as drivers of high-harmonic generation (HHG) to produce these IAPs.

The tailored optical fields are delivered by a parametric waveform synthesizer (PWS) pumped by a 1-kHz Ti:Sa laser system. In the PWS, two carrier-envelope-phase (CEP)-stable, few-cycle pulses—one in the near-infrared (NIR, 0.65–1 μm) and the other in the infrared (IR, 1.2–2.2 μm)—are coherently combined. Their synthesis produces fields centered at 1.4 μm , with full-width at half-maximum (FWHM) durations as short as 2.8 fs (0.6 optical cycles), and with 0.5 mJ of energy. By controlling the relative delay between the pulses and applying a common phase shift, waveforms can be tailored with sub-fs precision. These sub-cycle fields are then tightly focused into a thin gas-cell filled with argon, neon, or helium to drive HHG.

Attosecond streaking measurements directly characterize the sub-cycle fields, verifying their successful synthesis, and confirm the generation of EUV IAPs with FWHM durations ranging from 80 to 240 as, depending on the waveform. Additionally, waveform tailoring enables the generation of both narrowband and broadband IAPs, with spectra spanning from 30 to 110 eV in argon and up to 200 eV in neon, while maintaining pressures below 0.5 bar. Single-atom response simulations show that IAPs result from the confinement of HHG within a single cycle, while tunability is achieved via the precise control over the electron trajectories contributing to the high-harmonic emission.

Extension into the soft X-ray water window range is achieved using neon or helium at pressures up to 10 bar, producing photon energies up to 350 eV and 450 eV, respectively. A strong CEP dependence of the spectra suggests IAP emission, a finding supported by macroscopic, on-axis HHG simulations. At low plasma levels, IAPs arise from HHG confinement to a single cycle, while at higher levels, plasma defocusing likely contributes to their generation. Finally, absolute conversion efficiency measurements show that tailored waveforms increase HHG efficiency with respect to IR-driven HHG, though high plasma levels can reduce this gain. An eightfold efficiency increase is measured in helium in the water window range. Complete characterization of the driving field directly at the HHG target allows identifying the waveform responsible for the efficiency enhancement.

Zusammenfassung

Die Beobachtung ultraschneller molekularer Prozesse auf der Attosekunden-Zeitskala von Elektronen ist entscheidend für das Verständnis chemischer und physikalischer Phänomene. Attosekunden-Pulse bieten die notwendige zeitliche Auflösung, um elektronische Dynamiken zu erfassen. Ihre Einstellbarkeit vom extremen Ultraviolett (EUV) bis hin zu weichen Röntgenbereichen ermöglicht das Abtasten sowohl von Valenzelektronen als auch von tiefer liegenden K- und L-Schalen-Elektronen, wobei letztere orts- und elementspezifische Informationen liefern. Diese Arbeit untersucht die Erzeugung isolierter Attosekunden-Pulse (IAPs) im EUV- und weichen Röntgenspektralbereich, die bis zum Wasserfenster (284–543 eV) reichen. Maßgeschneiderte optische Felder, die Sub-Zyklus-Dauern erreichen können—d.h. kürzer als ihre Hauptoszillationsperiode—werden als Treiber für die Erzeugung hoher Harmonischer (HHG) zur Erzeugung dieser IAPs untersucht.

Die maßgeschneiderten optischen Felder werden von einem Parametric Waveform Synthesizer (PWS) geliefert, der von einem 1-kHz Ti:Sa-Lasersystem gepumpt wird. Im PWS werden zwei carrier-envelope-phase (CEP)-stabile, few-cycle-Pulse—einer im nahen Infrarot (NIR, 0.65–1 μm) und der andere im Infrarot (IR, 1.2–2.2 μm)—kohärent kombiniert. Ihre Synthese erzeugt Felder, die bei 1.4 μm zentriert sind, mit Vollbreiten bei halbem Maximum (FWHM) von nur 2.8 fs (0.6 optische Zyklen) und einer Energie von 0.5 mJ. Durch Steuerung der relativen Verzögerung zwischen den Pulsen und Anwendung einer gemeinsamen Phasenverschiebung können die Wellenformen mit Sub-Fs-Präzision angepasst werden. Diese Sub-Zyklus-Felder werden dann stark in eine dünne Gaszelle fokussiert, die mit Argon, Neon oder Helium gefüllt ist, um HHG anzutreiben.

Attosecond-Streaking-Messungen charakterisieren die Sub-Zyklus-Felder direkt, bestätigen ihre erfolgreiche Synthese und zeigen die Erzeugung von EUV-IAPs mit FWHM-Dauern von 80 bis 240 as, abhängig von der Wellenform. Darüber hinaus ermöglicht die Wellenformanpassung die Erzeugung sowohl von schmalbandigen als auch breitbandigen IAPs, mit Spektren, die von 30 bis 110 eV in Argon und bis zu 200 eV in Neon reichen, während die Drücke unter 0.5 bar gehalten werden. Einzelatomantwort-Simulationen zeigen, dass IAPs durch die Beschränkung der HHG auf einen einzigen Zyklus erzeugt werden, während die Einstellbarkeit durch die präzise Kontrolle der Elektrontrajektorien erreicht wird, die zur hochharmonischen Emission beitragen.

Die Erweiterung in den Wasserfensterbereich der weichen Röntgenstrahlung wird mit Neon oder Helium bei Drücken von bis zu 10 bar erreicht, wobei Photonenergien von bis zu 350 eV bzw. 450 eV erzeugt werden. Eine starke CEP-Abhängigkeit der Spektren deutet auf die Emission von IAPs hin, ein Befund, der durch makroskopische, on-axis HHG-Simulationen unterstützt wird. Bei niedrigen Plasmaniveaus entstehen IAPs durch die Beschränkung der HHG auf einen einzelnen Zyklus, während bei höheren Plasmaniveaus wahrscheinlich

die Plasmadefokussierung zu ihrer Erzeugung beiträgt. Schließlich zeigen absolute Konversionseffizienz-Messungen, dass maßgeschneiderte Wellenformen die HHG-Effizienz im Vergleich zu IR-getriebener HHG erhöhen, obwohl hohe Plasmaniveaus diesen Gewinn verringern können. Im Wasserfensterbereich wird eine achtfache Effizienzsteigerung in Helium gemessen. Eine vollständige Charakterisierung des Antriebsfeldes direkt am HHG-Ziel ermöglicht die Identifizierung der Wellenform, die für die Effizienzsteigerung verantwortlich ist.

Contents

Contents	xi
Abbreviations	2
1 Introduction	5
1.1 Thesis structure	8
2 Technology for attosecond science	9
2.1 Fundamentals of ultrafast laser physics	9
2.1.1 Linear response	12
2.1.2 Perturbative nonlinear response	13
2.1.3 Dispersion management	14
2.1.4 Focused Gaussian beams	15
2.2 The Ti:Sapphire femtosecond laser	16
2.2.1 Mode-locking	18
2.2.2 Chirped pulse amplification (CPA)	18
2.3 Optical parametric amplification (OPA)	19
2.3.1 Basic principles	19
2.3.2 OPCPA	21
2.4 Few- and single-cycle pulse generation	21
2.4.1 Ultrafast OPAs	22
2.4.2 Hollow Core Fiber (HCF) Compressor	24
2.5 Carrier-envelope phase (CEP) stabilization	24
2.5.1 Passive CEP stabilization	25
2.5.2 Single-shot f-2f spectral interferometry	26
2.6 Pulse and field characterization	27
2.6.1 Two-dimensional spectral shearing interferometry (2DSI)	28
2.6.2 Third-order reconstruction of electric fields via cross-correlation (TRES)	29

3	High-order harmonic and attosecond pulse generation	31
3.1	High-harmonic generation	31
3.1.1	Keldysh parameter	32
3.1.2	Photoionization rate and probability	34
3.1.3	The three-step model	36
3.1.4	Lewenstein's model	39
3.1.5	Trajectory emission probability	42
3.1.6	Dipole phase	45
3.2	On-axis phase-matching	46
3.2.1	Loose-focusing geometry	50
3.2.2	Tight-focusing geometry	54
3.3	Plasma blueshift and defocusing	57
3.4	Energy cutoff wavelength-scaling	59
3.5	Isolated attosecond pulse (IAP) generation	62
3.5.1	Half-cycle cutoffs	64
3.6	Attosecond streaking	66
3.6.1	Electron time-of-flight (eTOF) spectrometer	66
3.6.2	Direct measurement of optical waveforms	67
3.6.3	Attosecond pulse reconstruction	69
3.6.4	Volkov transform generalized projection algorithm	70
4	Sub-cycle optical field synthesis	73
4.1	Coherent waveform synthesis	73
4.1.1	Waveform synthesizers	75
4.2	Parametric waveform synthesizer	79
4.2.1	Laser system	82
4.2.2	CEP-stable seeder	83
4.2.3	Broadband parametric amplification	84
4.2.4	Pulse compression and characterization	86
4.2.5	Beam profiling	87
4.2.6	Waveform stabilization and control	88
4.2.7	Coherent spatiotemporal synthesis	89
4.3	Attosecond beamline	91
4.3.1	HHG driven by NIR and IR pulses	97
4.4	Direct measurement of synthesized waveforms	99
4.4.1	IAPs driven by synthesized waveforms	99
4.4.2	Attosecond streaking and waveform reproducibility	100
5	Tunable extreme ultraviolet isolated attosecond pulses	103
5.1	Sub-cycle control of attosecond pulses	103
5.2	Waveform-controlled EUV continua	106
5.2.1	HHG delay-cep scan	110
5.2.2	Attosecond pulse characterization	111
5.3	Single-atom HHG modeling with synthesized waveforms	114

6	Water-window, soft X-ray isolated attosecond pulses	121
6.1	Soft X-ray HHG beamline	121
6.2	Phase-matching water window HHG	125
6.2.1	HHG driven by IR pulses	125
6.2.2	HHG driven by synthesized waveforms	128
6.3	On-axis macroscopic modeling of HHG	132
6.3.1	Optical driving field propagation	133
6.3.2	Harmonic field propagation	135
6.3.3	Numerical solution	135
6.3.4	Simulations with Gaussian pulses	136
6.4	Tailored waveforms for high-flux IAPs	140
6.4.1	Methods	140
6.4.2	IR-only CEP scans	150
6.4.3	Relative delay scans	151
6.4.4	Water window yield efficiency	160
7	Conclusions and Outlook	167
A	Peak intensity estimation	175
B	Photon flux measurement	177
C	Derivation of propagation equations	181
D	Supplementary plots water window IAP generation	185
	Bibliography	193
	Publication list	223
	Acknowledgements	227

List of abbreviations

EUV	Extreme Ultraviolet
HHG	High-order Harmonic Generation
IAP	Isolated Attosecond Pulse
OPA	Optical Parametric Amplification
CEP	Carrier-Envelope Phase
FTL	Fourier Transform Limited
FWHM	Full-width at Half Maximum
GD	Group Delay
GDD	Group Delay Dispersion
TOD	Third-order Dispersion
AHG	Second Harmonic Generation
THG	Third Harmonic Generation
SFG	Sum-Frequency Generation
WLG	White Light Generation
DFG	Difference-Frequency Generation
FWM	Four-wave Mixing
SPM	Self-phase Modulation
XPM	Cross-phase Modulation
Ti:Sa	Ti:Sapphire
KLM	Kerr-lens Mode-locking
CPA	Chirped Pulse Amplification

UV Ultraviolet
IR Infrared
OPCPA Optical Parametric Chirped Pulse Amplification
HCF Hollow Core Fiber
CEO Carrier-Envelope Offset
FROG Frequency-resolved Optical Gating
2DSI Two-dimensional spectral Shearing Interferometry
TREX Third-order Reconstruction of Electric Fields via cross-correlation
APT Attosecond Pulse Train
SFI Strong Field Ionization
OBI Over-the-barrier Ionization
SFA Strong Field Approximation
ADK Ammosov-Delone-Krainov
PPT Perelomov-Popov-Terent'ev
MPI Multiphoton Ionization
ATI Above-threshold Ionization
TDSE Time-dependent Schrödinger Equation
SAE Single-active Electron
SPA Saddle-point Approximation
PWS Parametric Waveform Synthesizer
RP Relative Phase
eTOF electron Time-Of-Flight
MCP Microchannel Plate
COM Center-Of-Mass
SEWA Slowly-Evolving Wave Approximation

Chapter 1

Introduction

The characteristic timescales of molecular dynamics extend from protein folding in milliseconds, proton transfer in nanoseconds, rotations in picoseconds, and vibrations in femtoseconds, down to electronic dynamics within the attosecond regime [1, 2].

To investigate these ultrafast processes during or following light-matter interactions, pump-probe spectroscopy [3] employing ultrashort laser pulses is widely used. In this technique, a pump pulse induces a specific excitation within the system, and a subsequent probe pulse monitors the system's evolution with a controlled time delay. The interaction of the probe pulse with the sample allows for the measurement of various observables, such as transmission, reflection, or the detection of photoelectrons and photoions. By analyzing these observables as a function of the time delay between the pump and probe pulses, the dynamics triggered by the excitation can be elucidated [4, 5].

The study of molecular dynamics has advanced in parallel with laser technol-

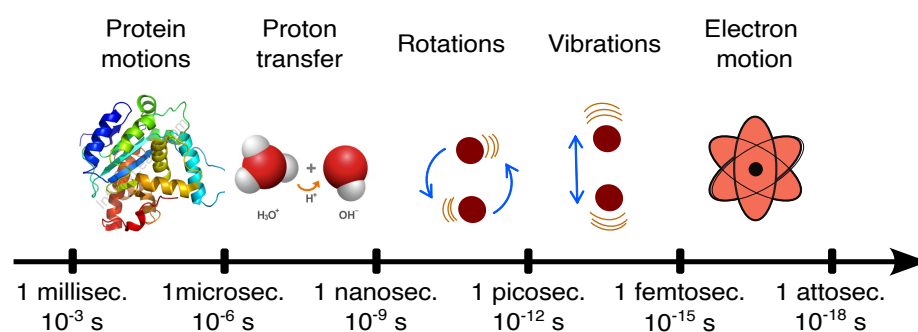


Figure 1.1: Natural timescales of molecular dynamics.

ogy developments, particularly through the progressive reduction of pulse durations [6, 7]. From the 1960s to the 1990s, laser pulse durations decreased from the picosecond to the femtosecond range, enabling the study of chemical bond formation and breaking within the field of femtochemistry [1, 8]. The development of high-power near-infrared lasers [6, 9] led to the discovery of high-harmonic generation (HHG) [10], enabling the production of extreme ultraviolet (EUV) laser pulse trains, with each burst being an attosecond pulse. The advent of few-femtosecond lasers, combined with so-called gating techniques [11], made it possible to extract isolated attosecond pulses (IAPs) from these trains. This breakthrough, achieved in 2001 [12], marked the transition from femtosecond to attosecond timescales, enabling unprecedented studies of valence electron dynamics in atoms [13], charge migration in molecules [14], photoemission delays [15], among other pioneering experiments [16, 17]. The discovery of HHG and the generation of IAPs laid the foundation for *attosecond physics* [2], a field recognized by the 2023 Nobel Prize in Physics awarded to Pierre Agostini, Ferenc Krausz, and Anne L’Huillier “for experimental methods that generate attosecond pulses of light for the study of electron dynamics in matter” [18].

Advancements in laser technology have enabled attosecond time resolution in pump-probe experiments. Equally important is the selection of photon energy for the pump and probe pulses, which determines the specific atomic or molecular components activated and the dynamics observed [5]. EUV photons primarily interact with valence electrons, which play a key role in chemical and optical properties due to their high reactivity. However, the delocalized nature of these electrons and their closely spaced energy levels result in a lack of specificity, often causing the simultaneous excitation of multiple states [19]. In contrast, soft X-rays target deeper K- and L-shell electrons, offering site- and element-specificity [20, 21]. Within this soft X-ray spectral range lies the ‘water window’—between the carbon K-edge (284 eV) and the oxygen K-edge (543 eV)— [22, 23] which is particularly valuable for studies in organic photochemistry and materials science. This window allows for the investigation of organic systems in their natural aqueous environment, as water remains transparent within this energy range [24–26]. Access to both EUV and soft X-ray energies enables selective probing of different electronic states, providing a complementary and more comprehensive understanding of the system. Incorporating IAPs within these photon energy ranges further enhances pump-probe studies by adding unprecedented time resolution [27, 28].

Extending the generation of IAPs into the water window spectral range has proven challenging, requiring nearly 13 years after the initial demonstration of EUV IAPs [29, 30]. The main obstacles included the development of intense, few-femtosecond driving pulses in the infrared/mid-infrared range [28], along with the need to meet stringent phase-matching requirements in

the soft X-ray spectral region with these pulses [31, 32]. Despite these challenges, pioneering time-resolved experiments [33–37] have been successfully conducted in the few laboratories capable of generating and utilizing these pulses, marking a significant progress in attosecond science beyond the EUV range.

Despite the success in generating IAPs in both the EUV and soft X-ray ranges, the energy of these pulses remains limited, typically ranging from nanojoules in the EUV range to picojoules in the soft X-ray range, with corresponding peak powers of megawatts and kilowatts, respectively [38–40]. This limitation, arising primarily from the inherently inefficient nature of HHG [41], restricts the scope of spectroscopic experiments and complicates the achievement of optimal signal-to-noise ratios. To date, most pump-probe experiments employing EUV or soft X-ray IAPs have relied on strong optical fields to compensate for the low yield of the IAPs. However, using a few-femtosecond optical field instead of an attosecond pulse for pumping or probing can complicate signal interpretation due to the triggered highly non-linear effects (such as multi-photon interactions) [42], while also reducing temporal resolution, thereby hindering true attosecond precision. Although pioneering EUV experiments using attosecond pump and probe pulses with megawatt to gigawatt peak powers have been conducted [38, 43], extending these capabilities to the soft X-ray range remains an unfulfilled goal. Addressing the HHG efficiency bottleneck would be beneficial across both the EUV and soft X-ray ranges, enhancing the capabilities of these relatively accessible tabletop setups [5]. This improvement would make them even more valuable complements to large-scale facilities like Free-Electron Lasers (FELs), which now deliver gigawatt-level soft X-ray attosecond pulses [39] and have only recently begun to demonstrate the potential for attosecond pump–attosecond probe experiments [44, 45].

To achieve tunability across the EUV to soft X-ray range, the driving field for HHG should ideally encompass spectral components from the visible to the infrared range [31, 46]. By tailoring the driving field’s waveform with sub-cycle precision, the field-dependent nature of HHG at the microscopic level can be exploited to optimize both photon yield and spectral range [47, 48]. Furthermore, if the tailored field is sufficiently short, it can enable the direct generation of an IAP, effectively bypassing the need for conventional gating techniques [11, 49–51].

This thesis investigates the optimization and generation of IAPs in the EUV and soft X-ray ranges using sub-cycle tailored fields from a parametric waveform synthesizer. By coherently superimposing near-infrared and infrared few-femtosecond pulses, the synthesizer achieves a 1.7-octave bandwidth, enabling the synthesis of mJ-level, sub-cycle pulses—pulses shorter than their main oscillation period. This approach allows for the generation of

IAPs that can be tuned from the EUV to the water window range. Additionally, the constructive interference inherent in waveform synthesis allows to enhance the efficiency of the HHG process. Consequently, this study demonstrates the potential of sub-cycle tailored optical waveforms as robust drivers for generating high-flux, tunable IAPs.

1.1 Thesis structure

This work is structured as follows:

- **Chapter 2:** Introduces fundamental laser physics concepts and the established technologies that enabled the generation of EUV and soft X-ray HHG, as well as the additional advancements that facilitated the production of IAPs.
- **Chapter 3:** Provides a comprehensive overview of HHG and its phase-matching, along with the physics underlying IAP generation and characterization. These foundational concepts are essential for understanding the discussions and interpreting the results in the subsequent chapters.
- **Chapter 4:** Details the parametric waveform synthesizer and provides solid evidence of sub-cycle waveform synthesis using the attosecond streaking technique. It also discusses the short- and long-term stability of these waveforms and confirms the successful generation of IAPs.
- **Chapter 5:** Demonstrates IAP spectral tunability in the EUV by tailoring the driving waveforms and elucidates the mechanisms behind this tunability.
- **Chapter 6:** Presents experimental evidence of IAP generation in the water window range, supported by a detailed theoretical analysis of the underlying generation mechanisms. Additionally, it includes a comprehensive study of measured absolute HHG yields and generation efficiency under various intensity conditions. The driving waveforms leading to the observed HHG yields are also presented.

The conclusion section (Ch.7) summarizes the observations and provides an outlook on the application of these tunable IAPs.

Technology for attosecond science

The advancement of critical laser technologies has been fundamental to the emergence and rapid growth of attosecond science. This section highlights the primary technologies and underlying physics that have facilitated this progress, with specific focus on the technologies integral to the work presented in this thesis. The chapter closely follows Refs. [52–55].

2.1 Fundamentals of ultrafast laser physics

A starting point for understanding ultrashort pulse behavior is the representation of the electric field $E(t)$ of a linearly polarized pulse as

$$E(t) = \varepsilon(t) \cos(\omega_0 t + \varphi), \quad (2.1)$$

This description includes a time-dependent field envelope function $\varepsilon(t)$, the carrier angular frequency ω_0 related to the conventional oscillation frequency as $\omega_0 = 2\pi\nu_0$, and the Carrier-Envelope Phase (CEP) φ – the phase offset between the carrier wave and the envelope’s maximum.

The envelope function is linked to the peak field amplitude E_0 as $\varepsilon(t) = E_0 \hat{\varepsilon}(t)$, where $\hat{\varepsilon}(t)$ is a normalized function accounting for the envelope’s shape. While real-world pulses may deviate from these forms, laser pulses are often modeled with idealized envelope shapes for analytical and numerical convenience. Common shapes include the Gaussian ($\hat{\varepsilon}(t) = e^{[-2\ln 2(t/\tau_p)^2]}$) and the hyperbolic secant ($\hat{\varepsilon}(t) = \text{sech}(1.76 \cdot t/\tau_p)$) functions. Here, τ_p is the pulse duration and corresponds to the Full-width at Half Maximum (FWHM) of the intensity envelope, $I_{\text{env}}(t) = I_0 \hat{\varepsilon}(t)^2$. The peak intensity, I_0 , is the maximum value of $I_{\text{env}}(t)$ and is given by

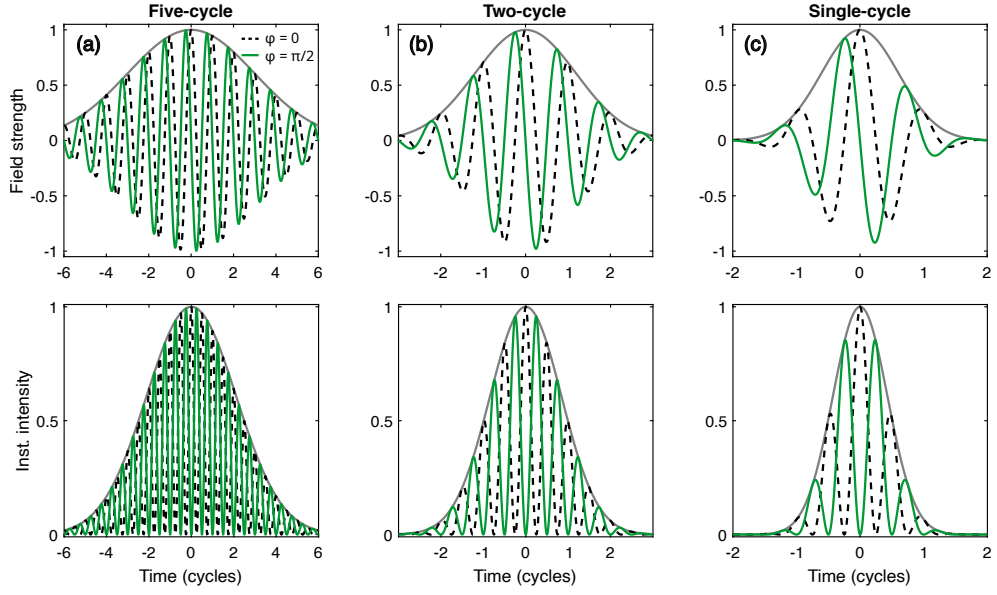


Figure 2.1: CEP sensitivity of ultrashort pulses. Gaussian pulses with decreasing durations: (a) 5 cycles, (b) 2 cycles, (c) 1 cycle. Fields are numerically adjusted for a zero net area (no DC component). CEP shifts of $\varphi = 0$ (dashed black) and $\varphi = +\pi/2$ (solid green) are shown. Top row: normalized electric field strength. Bottom row: normalized instantaneous intensity ($I(t) \sim E(t)^2$). Gray lines outline the field and intensity envelope functions (see Eq.2.1).

$$I_0 = \frac{1}{2}c\epsilon_0 E_0^2, \quad (2.2)$$

where c is the speed of light, and ϵ_0 is the vacuum permittivity.

The frequency representation of the electric field is obtained by Fourier-transforming $E(t)$, resulting in

$$\begin{aligned} \mathcal{F}\{E(t)\} = E(\omega) &= \frac{1}{2}[\varepsilon(\omega - \omega_0)e^{i\varphi} + \varepsilon(\omega + \omega_0)e^{-i\varphi}] \\ &\equiv E^+(\omega) + E^-(\omega) \end{aligned} \quad (2.3)$$

Here, $\varepsilon(\omega) = \mathcal{F}\{\varepsilon(t)\}$ is the Fourier transform of the envelope function, centered at the positive ($+\omega_0$) and negative ($-\omega_0$) frequencies. The terms E^+ and E^- represent such positive and negative frequency side of $E(\omega)$, respectively. For simplicity, subsequent discussions will focus only on the positive-sided component, treating $E(\omega)$ as $E^+(\omega)$.

An important characteristic of ultrashort pulses is their inherently broad spectrum. Due to the Fourier transform's fundamental properties, shorter

pulses possess wider spectral bandwidths ($\Delta\omega$). For idealized pulse envelopes such as Gaussian or hyperbolic secant, the relationship, $\tau_p\Delta\omega \geq \text{const.}$, dictates the shortest possible pulse duration supported by a given spectrum. A pulse achieving this limit is termed Fourier Transform Limited (FTL). For more general field waveforms with a given bandwidth, the FTL condition is satisfied when the pulse reaches its highest intensity.

In analogy to music, the inherent spectral bandwidth leads to a useful frequency-domain description used in the ultrafast optics and frequency comb communities: the concept of octaves. An octave-spanning pulse has a spectrum containing frequencies that span at least a factor of two (e.g., if it contains 800-nm light, it also extends to at least 1600 nm). Following this logic, a multi-octave spanning source would span two-octaves or more.

Along with their spectral bandwidth, categorizing ultrashort pulses based on the number of cycles within their intensity envelope helps to understand the physical interactions they induce. A pulse with a duration spanning N cycles (where $\tau_p = N \cdot T_0$, with $T_0 = 2\pi/\omega_0$ being the oscillation period corresponding to the *dominant* frequency component) is called an N -cycle pulse. Typically, pulses lasting longer than ≈ 10 cycles are termed *multi-cycle* pulses. As pulses shorten to durations spanning ≈ 2 to less than 10 cycles, they enter the *few-cycle* regime. A pulse whose duration approximately matches the central wave period is called a *single-cycle* pulse. Pulses even shorter than this are termed *sub-cycle* pulses.

The transition from multicycle to few-cycle, single-cycle, and ultimately sub-cycle pulses represents far more than just a decrease in duration. It marks a fundamental shift in how these pulses interact with matter. The interplay of $\varepsilon(t)$, ω_0 , and φ gives rise to linear and nonlinear phenomena that differ dramatically from those observed with quasi-monochromatic light. Main distinctions include:

- **Spectral bandwidth:** The broad spectrum of ultrashort pulses implies that matter will interact with multiple frequency components during the pulse duration.
- **Peak power:** Ultrashort pulses concentrate their energy (U) within a brief duration τ_p , enabling them to achieve high peak powers ($P_0 \sim U/\tau_p$).
- **CEP sensitivity:** As pulse durations decrease, variations in the CEP (φ) have an increasing impact on the electric field waveform $E(t)$ (see Fig.2.1). This effect is particularly important for field-dependent processes [56, 57], which will be explored in Sec.3. Conversely, CEP influence is often weak for multi-cycle pulses and negligible for quasi-monochromatic light.

2.1.1 Linear response

One direct consequence of the broad bandwidths found in ultrashort pulses is their interaction with first-order (linear) processes like dispersion and absorption. In a dispersive and absorptive isotropic medium, the electric field of a pulse acquires a complex spectral phase $\phi(\omega)$ over a distance z during propagation. This can be expressed as:

$$E(\omega, z) = E(\omega, 0) \exp[-i\phi(\omega, z)] \quad (2.4)$$

with

$$\phi(\omega, z) = \frac{\omega}{c} n_c(\omega) z = \frac{\omega}{c} \left[n(\omega) - i\beta(\omega) \right] z = \left[k_n(\omega) - i\frac{\alpha(\omega)}{2} \right] z, \quad (2.5)$$

Here, n_c and n are the complex and real refractive indexes, respectively, and β is the attenuation coefficient. The wavevector is defined as $k_n = n \cdot k$ (with $k = \omega/c$ being the free-space wavevector), and $\alpha = 2\beta \cdot k$ is the absorption coefficient. Note that when absorption acts alone, the Beer-Lambert law is recovered, demonstrating that different frequencies within the pulse experience varying degrees of damping. Contrariwise, when dispersion acts alone, each frequency acquires a phase shift determined by $k_n \cdot z$ and will travel at different velocity within the medium.

To further unveil the impact of these effects, the spectral phase $\phi(\omega, z)$ can be Taylor-expanded around the central frequency ω_0 (considering a transparent medium, i.e., $\alpha = 0$, and dropping the dependence on z , for convenience and clarity). This yields

$$\phi(\omega) \approx \phi(\omega_0) + \phi'(\omega_0)(\omega - \omega_0) + \frac{1}{2}\phi''(\omega_0)(\omega - \omega_0)^2 + \dots \quad (2.6)$$

The first term, $\phi(\omega_0)$, represents a constant phase shift induced by the medium to the carrier wave. The coefficient of the second term, $\tau_g \equiv \phi'(\omega_0)$, represents the Group Delay (GD), and imprints a delay in the pulse's temporal envelope relative to propagation in a vacuum. The coefficient of the third term, $\phi''(\omega_0)$, corresponds to the Group Delay Dispersion (GDD), and causes a symmetric temporal broadening of the pulse and a *chirp*.

In materials with positive dispersion ($\text{GDD} > 0$), lower frequencies travel faster, arriving before higher frequencies. This creates a positive chirp. On the contrary, in materials with negative dispersion ($\text{GDD} < 0$), higher frequencies arrive first, resulting in a negative chirp. GDD is also known as second-order dispersion. Higher-order terms in the expansion, such

as Third-order Dispersion (TOD), lead to an asymmetric distortion of the pulse's temporal envelope.

Beyond the spectral effects discussed along the propagation axis, ultrashort pulses are also susceptible to distortions in their transverse spatial profile due to space-time couplings during linear propagation [58, 59]. For example, spatial chirp can occur, where the frequency varies across the beam profile. This is often induced by elements like prisms or gratings. Additionally, pulse front tilt, which combines temporal and spatial chirp, can also arise.

2.1.2 Perturbative nonlinear response

The high peak intensities of ultrashort pulses open the door to nonlinear optical phenomena. Unlike the linear processes described in the previous section, where the induced electric polarization (P) scales linearly with the field strength (i.e., $P = \epsilon_0 \chi_e E$), nonlinear processes depend on higher powers of the electric field. Within the electric dipole approximation and perturbation theory, this nonlinear polarization can be expressed as a power series [60, 61]:

$$P = \epsilon_0 \left[\chi^{(1)} E + \chi^{(2)} E^2 + \chi^{(3)} E^3 + \dots \right] \quad (2.7)$$

Here, $\chi^{(n)}$ are the n -th order susceptibilities¹, describing n -photon interactions within the medium. The magnitude of $\chi^{(n)}$ generally decreases significantly with increasing order (at least by more than four orders of magnitude in condensed matter systems [55, 61]) and, as consequence, higher field strengths are needed to trigger the corresponding n -th order response. The power-law dependence on the electric field (E^n) implies that even small changes in field strength can drastically alter n -th order nonlinearity.

The $\chi^{(1)}$ -response corresponds to linear optical effects described in the previous section. In the frequency domain, the first-order susceptibility ($\chi^{(1)} = \chi_e$) it relates to the complex refractive index (n_c ; Eq.2.5) as [62]:

$$n_c(\omega) \approx 1 + \chi^{(1)}(\omega)/2. \quad (2.8)$$

The $\chi^{(2)}$ -response, present in centrosymmetric materials like BBO crystals, mediates processes such as Sum-Frequency Generation (SFG), Second Har-

¹In a more rigorous treatment, the electric polarization and fields would be represented as vectors to account for their polarization nature. Additionally, the time dependence of the fields and the delayed response of the $(n+1)$ -rank tensor $\chi^{(n)}$ susceptibilities would be included [55].

monic Generation (AHG), Difference-Frequency Generation (DFG), optical rectification and the electro optic effect.

The $\chi^{(3)}$ -response occurs in all media and gives rise to effects like Third Harmonic Generation (THG) and Four-wave Mixing (FWM). Of particular importance for high-intensity pulses is Self-phase Modulation (SPM), also known as the Kerr effect [63, 64]. SPM's phase-matching-free nature makes it particularly important among third-order processes, because it is effortlessly induced in a wide range of media. SPM creates an intensity-dependent change in the refractive index:

$$\Delta n = n_2 I, \quad (2.9)$$

where $n_2 \propto \chi^{(3)}$ is the nonlinear refractive index. A pulse experiencing SPM acquires a time-dependent phase shift modulated by its instantaneous intensity profile, broadening its spectrum and introducing a chirp. This spectral broadening is the foundation of White Light Generation (WLG) or supercontinuum generation [65], where a spectrally narrow input pulse can be transformed into a broadband, multi-octave output.

Spatial variation in the intensity profile can also lead to self-focusing (or Kerr lensing), where the beam's center experiences a higher refractive index, mimicking a focusing lens. At high enough intensities, self-focusing can create plasma, which counteracts the focusing with a process called plasma defocusing [66]. This dynamic interplay can lead to filaments, where the beam maintains a guided profile over long distances [67, 68].

It is worth mentioning that the power series expansion in Eq. (2.7) may not necessarily converge as the laser field approaches $\approx 10^{10} \text{ Vm}^{-1}$ (or an intensity of $\approx 10^{13} \text{ Wcm}^{-2}$) [69]. Beyond this point, the provided perturbative analysis is no longer valid. HHG is a prime example of a process falling outside this realm and will be discussed in Sec. 3.

2.1.3 Dispersion management

Managing dispersion introduced by linear effects becomes critical when working with ultrashort laser pulses, especially with those approaching already the few-cycle regime. The primary methods used are [54, 70]:

- **Material dispersion:** This method exploits the wavelength-dependent refractive index of materials. By selecting appropriate materials and thicknesses, precise chirp can be induced to compress or stretch pulses.
- **Geometrical dispersion:** These techniques adjust the optical path lengths of different spectral components. Grating [71] and prism compressors

[72] are common examples. Angular dispersion and strategic geometrical arrangement enable dispersion compensation, though prisms struggle with higher-order terms. Combining prisms with grating pairs can address these challenges [73].

- **Interference-based dispersion:** This method relies on interference effects to control dispersion. Gires-Tournois Interferometer (GTI) mirrors [74] employ a partially reflective front surface and a highly reflective back surface to introduce wavelength-dependent phase shifts, compensating for dispersion. Chirped mirrors [75–77] use multilayer structures with alternating refractive indices, causing different wavelengths to penetrate to varying depths and experience controlled group delay. These mirrors enable precise compensation of second- and higher-order dispersion terms while offering high damage thresholds and low energy loss, making them suitable for high-power pulse applications [78].
- **Active dispersion control:** These techniques offer real-time, dynamic dispersion adjustment with high flexibility. Acousto-Optic Programmable Dispersive Filters (AOPDFs) [79], Spatial Light Modulators (SLMs) [80], and Electro-Optic Modulators (EOMs) [81] achieve precise control through acoustic waves, liquid crystals, or electro-optic effects. However, they often introduce significant energy loss and may face limitations when handling the high power levels typical in ultrafast laser systems.

Chirped mirrors have been pivotal in generating few-cycle pulses [82, 83], even enabling compression to sub-cycle durations [78]. Their precise control over high-order dispersion, robustness under high-intensity pulses, and broadband phase manipulation with minimal loss make them ideal for optimizing ultrafast laser characteristics.

2.1.4 Focused Gaussian beams

The intensity of a focused laser beam varies spatially, both along the propagation axis and in the transverse direction. For a linearly polarized, monochromatic Gaussian beam, its free-space propagation along the z -axis is described by the Helmholtz equation in cylindrical coordinates. Under the paraxial approximation and in the reference frame moving at the speed of light, the solution for the electric field with an initial on-axis amplitude E_0 is given by (using the sign convention consistent with the definition of the complex electric field in Eq. 2.4) [52, 84]:

$$E(r, z) = E_0 \frac{w_0}{w(z)} \exp \left[-\frac{r^2}{w(z)^2} \right] \exp \left[-i \left(\frac{kr^2}{2R(z)} - \zeta(z) \right) \right], \quad (2.10)$$

where w_0 represents the beam waist, or the $1/e^2$ radius, at focus (located at $z = 0$), indicating that the beam intensity drops to 13.5% of its peak value at this radius. The other variables in the exponentials are defined as functions of the wavelength λ :

$$z_R = \frac{\pi w_0^2}{\lambda} \quad (\text{Rayleigh range}) \quad (2.11)$$

$$w(z) = w_0 \sqrt{1 + \left(\frac{z}{z_R}\right)^2} \quad (1/e^2 \text{ radius}) \quad (2.12)$$

$$R(z) = z \left[1 + \left(\frac{z_R}{z}\right)^2 \right] \quad (\text{Radius of curvature}) \quad (2.13)$$

$$\zeta(z) = \arctan \left(\frac{z}{z_R} \right) \quad (\text{Gouy phase shift}) \quad (2.14)$$

The Rayleigh range, z_R , determines the distance over which the beam's area doubles, providing a measure of its divergence. The beam radius, $w(z)$, describes the variation in beam width along the propagation direction (z), reaching its minimum at the waist before expanding due to diffraction. The Gouy phase shift, $\zeta(z)$, is an additional phase factor that varies smoothly from $-\pi/2$ to $+\pi/2$ across the focal region, representing a z -dependent change in the beam's CEP, which is crucial for attosecond pulse generation.

From Eq. 2.10, the peak intensity is expressed as:

$$I(r, z) = \frac{I_0}{1 + (z/z_R)^2} \exp \left[-\frac{2r^2}{w(z)^2} \right] \quad (2.15)$$

Figure 2.2 illustrates the characteristic features of a focused Gaussian beam, with negative z positions representing the pre-focus region and positive values the post-focus region. Fig. 2.2c showcases the the Gouy phase direction.

It is important to note that Eqs. Eqs. 2.10-2.14 remain reasonably accurate for multi-cycle pulses. However, as pulse durations approach the few-cycle regime, these equations become less valid due to the increased significance of frequency-time and spatial couplings [85], such as frequency- and radius-dependent Gouy phase effects [86–88].

2.2 The Ti:Sapphire femtosecond laser

The theoretical understanding of ultrashort pulses has advanced alongside the development of sophisticated laser sources. A key technology in this

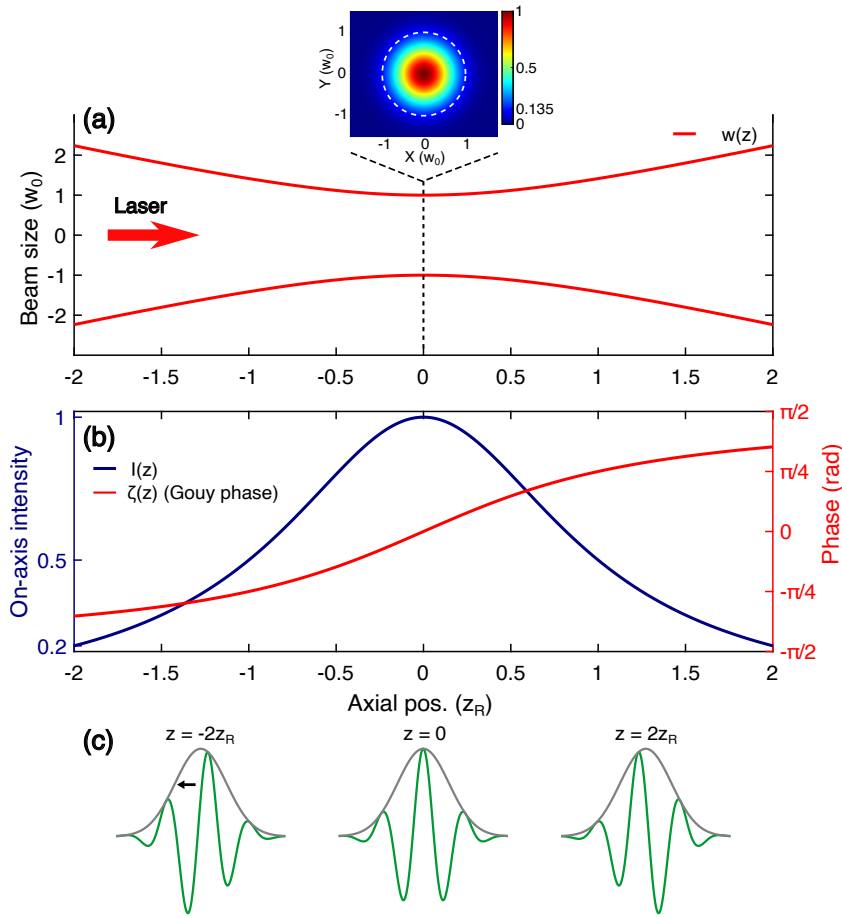


Figure 2.2: Focused Gaussian beam. (a) Beam waist evolution ($w(z)$) with transverse intensity distribution at $z_0 = 0$ (inset, $I(r, 0)$, see Eqs. 2.10 - 2.15). The white dashed circle (radius w_0) indicates the 13.5% maximum intensity contour. (b) On-axis, intensity (left axis, $I(0, z)$) and Gouy phase shift variation (right axis, $\zeta(z)$) along the propagation axis. (c) Gouy phase influence on a single-cycle pulse upon propagation. Black arrow points the direction of CEP variation.

field, dominating high-energy ultrashort pulse generation for nearly four decades, is the Ti:Sapphire (Ti:Sa) laser [89, 90].

Ti:Sapphire's (Ti:Al₂O₃) properties, including its broad gain bandwidth, have made it the most widely used laser material for generating tunable ultrashort pulses in solid-state systems. As a 4-level system, it efficiently absorbs photons around 500 nm, typically provided by frequency-doubled Nd-doped solid-state or diode lasers. The excited electrons rapidly relax to a metastable state, creating a population inversion that facilitates lasing emission near 800 nm. Notably, its broad gain bandwidth spans roughly 400 nm. Electrons then decay back to the ground state. Furthermore, Ti:Sapphire exhibits high thermal conductivity, allowing it to manage the heat generated during high-power operation. Its relatively large quantum defect (the dif-

ference between pump and emitted photon energies) creates challenges for scaling to both higher average and peak power levels [91], but its other properties make it already well-suited for generating the high-intensity fields needed for ultrafast science applications.

2.2.1 Mode-locking

Femtosecond solid-state lasers, especially those based on Ti:Sapphire, revolutionized ultrafast science following the discovery of Kerr-lens Mode-locking (KLM) in 1991 [92]. In a free-running laser, numerous cavity modes oscillate with random phases, resulting in chaotic light. Mode-locking forces these modes into a fixed phase relationship, producing a synchronized train of ultrashort pulses. Each round-trip within the cavity extracts energy through the output coupler, establishing a pulse train with a repetition rate typically ranging from 10 MHz to 1 GHz, depending on the cavity design.

KLM [54] is a passive technique that relies on the intensity-dependent Kerr effect within the Ti:Sa crystal to shape the pulse. This self-focusing effect acts as a fast saturable absorber, promoting the formation of high-intensity pulses with the shortest durations. To accommodate the broad bandwidth needed for such short pulses, precise dispersion compensation is required within the laser cavity. Elements such as prisms or, more commonly, chirped mirrors counteract material dispersion, ensuring the pulse components remain synchronized, which is critical for generating ultrashort pulses.

2.2.2 Chirped pulse amplification (CPA)

To reach high power levels, Ti:Sa lasers employ Chirped Pulse Amplification (CPA) [9, 93, 94], which involves the following [52]:

Ultrashort pulses from the oscillator are first temporally stretched, reducing their peak intensity and making them safe for high-energy amplification. A multi-stage amplifier then boosts the pulse energy. This typically starts with a regenerative amplifier, where a Pockels cell reduces the repetition rate from MHz to kHz by selecting individual pulses. Subsequent multipass stages further amplify the pulses to energies of several millijoules or more. Cryogenic cooling of the Ti:Sa crystal often improves thermal management, allowing for higher repetition rates and energy levels. Finally, a compressor reverses the initial stretching, restoring the ultrashort pulse duration.

CPA revolutionized ultrafast science, currently enabling cutting-edge systems delivering petawatt-level pulses at few Hz repetition rate and with sub-30 fs duration [95]. In contrast, commercial Ti:Sa systems routinely achieve sub-50 fs pulses reaching peak powers on the order of 10^2 GW at few kHz repetition rate. These multi-cycle pulses are still, however, not short enough for applications like Isolated Attosecond Pulse (IAP) generation [12], where

pulses approaching the sub-cycle regime would be ideal. To reach the first milestone of the few-cycle limit, extra-cavity pulse compression techniques [96] are required.

2.3 Optical parametric amplification (OPA)

The reliance on Ti:Sapphire technology within CPA inherently restricts the achievable wavelength range. For applications demanding broader spectral tunability, Optical Parametric Amplification (OPA) [97] offers a solution to overcome this constraint.

Unlike the fixed-frequency output of solid-state lasers, OPAs exploit nonlinear optical processes to enable frequency tunability across the Ultraviolet (UV) to Infrared (IR) spectrum [98, 99]. This tunability is crucial for applications such as ultrafast spectroscopy and strong-field physics, including HHG. Additionally, the parametric nature of OPAs, combined with their operation within the transparency range of the nonlinear crystal, offers superior thermal management and potential for power scaling. This section draws heavily from Ref. [99].

2.3.1 Basic principles

OPA is a nonlinear optical process rooted in second-order ($\chi^{(2)}$) nonlinear crystals, as described in Sec.2.1. It involves the dynamic transfer of energy between light beams of different frequencies. In essence, a high-energy pump photon (frequency ω_p) excites the crystal medium to a "virtual" [61] energy state. This excitation is followed by stimulated emission, where a seed photon (frequency ω_s) triggers the process. The result is the amplification of the seed beam and the simultaneous generation of a signal beam at the same frequency. To maintain energy conservation, a third beam, known as the idler (frequency ω_i), is also created. This relationship is expressed as follows:

$$\omega_p = \omega_i + \omega_s \quad (2.16)$$

The absence of fixed energy states in the OPA medium is what allows flexibility in choosing pump and seed frequencies. The primary constraint is simply ensuring energy conservation as outlined in Eq. 2.16.

Beyond energy conservation, momentum conservation (or phase-matching) is equally crucial for efficient amplification. This means the interacting waves must maintain a constant phase relationship within the nonlinear crystal, expressed as:

$$\Delta\vec{k} \equiv \vec{k}_p - \vec{k}_i + \vec{k}_s \stackrel{!}{=} 0 \quad (2.17)$$

which ensures that the interacting waves maintain a constant phase relationship within the nonlinear crystal.

To analyze the amplification process in an OPA, a simplified one-dimensional model can be employed. In this scenario, three monochromatic waves (pump, seed/signal, and idler) interact along the propagation axis, all sharing the same polarization. After applying certain approximations, including assuming an undepleted pump, a negligible initial idler intensity, and operation within the large gain limit (i.e., $gL_{\text{med}} \gg 1$), the OPA gain (the ratio of output signal intensity to input seed intensity) at the end of a medium of length L_{med} is expressed as

$$G(L_{\text{med}}) \simeq \left(\frac{\Gamma}{g}\right)^2 \frac{e^{2g \cdot L_{\text{med}}}}{4}, \quad (2.18)$$

where g (the *small gain*) and Γ are given by

$$g = \sqrt{\Gamma^2 - \frac{|\Delta k|^2}{4}}, \quad \Gamma^2 = \frac{2d_{\text{eff}}\omega_s\omega_i}{c\epsilon_0 n_p n_i n_s} I_p \quad (2.19)$$

where d_{eff} is effective nonlinear optical coefficient, I_p is the pump intensity and $n_{p,i,s}$ are the refractive indices at the pump, idler, and signal frequencies.

Equation 2.18 reveals several key aspects of OPA behavior. Firstly, the OPA gain G scales exponentially with both the medium length L_{med} and the pump intensity I_p . Secondly, the gain equation assumes no absorption of the three waves by the medium. This can be translated to the requirement that the chosen frequencies must fall within the nonlinear crystal's transparency range and emphasizes the importance of their energy exchange. Thirdly, the small gain is strongly dependent on the phase mismatch term ($|\Delta k|$), thus perfect phase-matching is ideal for maximizing amplification

Birefringent crystals [61] can allow phase-matching for beams with widely spaced frequencies. They exhibit different refractive indices depending on the beam's polarization and propagation direction, providing flexibility in fulfilling the phase-matching condition (Eq. 2.17). Uniaxial crystals, a specific type of birefringent crystal, offer two primary refractive indices: the ordinary refractive index (n_o) and the extraordinary refractive index (n_e). These indices are associated with specific axes referenced to the crystal's optical axis and the beam's propagation direction. A commonly used nonlinear

crystal (and used in this thesis), BBO, is classified as a negative uniaxial crystal since $n_e < n_o$. In negative uniaxial crystals, the pump frequency ω_p must always be polarized along the extraordinary axis to achieve phase-matching.

The use of birefringent crystals enables two common phase-matching types:

- **Type-I:** The lower-frequency beams (signal and idler) share the same polarization, orthogonal to the higher-frequency polarization of the pump beam.
- **Type-II:** The lower-frequency beams have orthogonal polarizations.

As discussed in Sec. 2.4, understanding OPA mechanisms is essential for generating and amplifying broadband pulses approaching the single-cycle limit. However, scaling OPA energy beyond a few millijoules remains challenging. To achieve significantly higher pulse energies, the technique of Optical Parametric Chirped Pulse Amplification (OPCPA) has been developed and further advanced.

2.3.2 OPCPA

Optical Parametric Chirped Pulse Amplification (OPCPA) [100, 101] addresses the energy scaling limitations of traditional OPAs. Inspired by the CPA technique discussed in Sec. 2.2, OPCPA utilizes high-energy picosecond pulses from well-established gain media like Nd- or Yb-doped crystals or fibers as the OPA pump source. A separate femtosecond laser system typically generates the seed pulse for amplification.

To maximize energy transfer from pump to seed while protecting the nonlinear medium, OPCPA first stretches the femtosecond seed pulse to match the picosecond pump pulse duration (see Sec. 2.4). Following amplification, the pulse is compressed as closely as possible to its FTL duration.

Although research continues to explore suitable materials for near- and mid-infrared OPCPAs [102] and to investigate IR-lasing materials as direct laser sources [103, 104], OPCPA has established itself as a versatile and scalable amplification method. Considered the third generation of femtosecond technology (following dye lasers and Ti:Sa lasers) [91], it enables the generation of frequency-tunable, mid-IR pulses with high peak powers (terawatt-scale), high average powers (kilowatt-scale), and durations of only a few cycles. For an in-depth exploration into recent OPCPA advancements, the reader is encouraged to consult Refs. [102, 105].

2.4 Few- and single-cycle pulse generation

To achieve few-cycle durations in the visible and infrared range, the pulse spectrum must first be broadened beyond the limits of the laser amplifier.

Here, techniques like OP(CP)As and hollow-core fiber (HCF) compressors play a crucial role. Emerging techniques such as multi-pass cells [106, 107] and hollow-core stretch fibers [108] show promise for compressing higher-power pulses. For a detailed discussion of these technologies and their energy-scaling benefits, the reader is referred to Ref. [96].

2.4.1 Ultrafast OPAs

In Sec. 2.3, the need for phase-matching and energy exchange in OPA with monochromatic beams was introduced. When working with pulses, these requirements translate into the necessity of temporal overlap and group velocity management for effective amplification. Due to the frequency differences inherent in OPA, achieving this overlap is crucial for both efficient amplification and generating broadband, ultrashort pulses [98, 99].

Group velocity mismatch causes the signal and/or idler pulses to gradually separate from the pump pulse during propagation. The pulse splitting length quantifies this walk-off:

$$L_{\text{split}}^{i,s} = \frac{\tau_p}{|1/v_{g_{i,s}} - 1/v_{g_p}|}, \quad (2.20)$$

where τ_p is the pulse duration of the pump beam and $v_{g_{p,i,s}}$ is the group velocity of the pump, idler or signal beam. This length helps determine the limits of crystal lengths for effective amplification. Understanding the pulse splitting length is important for crystal selection. When the signal and idler propagate in the same direction, $L_{\text{split}}^{i,s}$ approximates the maximum effective crystal length. If they propagate in opposite directions to the pump, a self-trapping effect can extend interaction distances, allowing for longer crystals.

In contrast to the temporal overlap considerations governed by pulse splitting length, the amplified frequency bandwidth is primarily determined by the group velocity differences between the signal and idler beams. This bandwidth, quantified by the FWHM of the parametric gain, $\Delta\omega_G$, under the large gain and undepleted pump approximations, is given by:

$$\Delta\omega_G \sim \sqrt{\frac{\Gamma}{L_{\text{med}}}} \cdot \frac{1}{|1/v_{g_i} - 1/v_{g_s}|} \quad (2.21)$$

Maximizing the amplification bandwidth requires closely matching the group velocities of the signal and idler beams. When these velocities are nearly identical, their combined group velocity dispersions should be considered. Equation 2.21 also reveals an inverse relationship between the bandwidth and the crystal length (L_{med}), indicating that thinner crystals generally support wider bandwidths.

While Eqs. 2.16 and 2.17 describe the fundamental requirements for OPA, maximizing the bandwidth in Eq. 2.21 within a collinear geometry can be challenging. Exploiting the vectorial nature of phase-matching allows for broader amplification bandwidths, leading to two main phase-matching geometries:

- **Collinear Degenerate OPA (DOPA):** Broadband phase-matching is inherently achieved when the signal and idler group velocities are equal ($v_{g_i} = v_{g_s}$), which occurs at degeneracy, where the pump frequency is twice the signal/idler frequency ($2\omega_i = 2\omega_s = \omega_p$). This condition is typically fulfilled by Type-I phase-matching. In the Parametric Waveform Synthesizer (PWS) [109, 110], discussed in Chapter 4, DOPA is used for the near-infrared ($\lambda_s \sim 800$ nm) and infrared ($\lambda_s \sim 1600$ nm) channels, pumped by 400-nm and 800-nm beams, respectively.
- **Non-Collinear OPA (NOPA):** For broadband amplification of a signal pulse away from degeneracy (i.e., $\omega_p/2$), a slight angle is introduced between the beams to improve group velocity matching, provided that the wavevectors $\vec{k}_{p,i,s}$ lie in the plane of the crystal's optical axis. Broadband amplification occurs when the signal's group velocity matches the projection of the idler's group velocity along the signal direction:

$$v_{g_s} = v_{g_i} \cos \Omega, \quad (2.22)$$

where Ω is the angle between the idler and signal beams. Although NOPA may slightly reduce spatial overlap, pulse tilting of the pump beam can mitigate this effect. The PWS [110] employs a Type-I NOPA for its visible ($\lambda_s \sim 600$ nm) channel, pumped by a 400-nm beam.

In practice, OPA systems often employ multiple amplification stages to minimize parametric superfluorescence (amplification of noise due to excess pump energy) and optimize walk-off, spatial overlap, and gain, thereby ensuring effective amplification across a broad bandwidth. The process for generating few-cycle pulses typically begins with a broadband seed, derived from the pump via WL generation. The pump wavelength and phase-matching conditions then dictate which portion of this multi-octave spectrum is amplified. Although amplification may slightly narrow the initial bandwidth, octave-spanning spectra remain achievable. Additional OPA stages sequentially amplify the signal to the desired energy level. Finally, an optional pulse compression stage, using a dispersive delay line, can be employed to reach the shortest possible pulse duration [99]. Numerous OPA architectures [111–113] have successfully implemented this approach, generating few-cycle—and even single-cycle [110]—visible and infrared drivers.

2.4.2 Hollow Core Fiber (HCF) Compressor

Among various pulse compression techniques, Hollow Core Fiber (HCF) compressors [82, 114] have become the most widely adopted tools for achieving the few-cycle regime in attosecond science. Their simplicity, unique geometry, and favorable characteristics provide significant advantages for guiding, spectrally broadening, and compressing intense pulses.

Spectral broadening in HCFs exploits the Kerr effect (introduced in Sec. 2.1). When filled with a noble gas, the enhanced nonlinearity produces multi-octave-spanning spectra capable of supporting sub-cycle pulses. This broadening is typically followed by dispersion compensation using standard techniques, often involving chirped mirrors [50, 83, 115].

Key benefits of HCFs include single-mode propagation, tunable nonlinearity (by varying the noble gas), and high damage thresholds. These features have enabled the compression of femtosecond pulses to sub-5 fs durations within the millijoule energy range [50, 83]. Furthermore, HCFs have generated spectra spanning over two octaves, facilitating waveform synthesis technology [70, 116], which has broken the femtosecond barrier, producing attosecond pulses in the optical range (at approximately 530 nm) with durations as short as 975 as [117]. Importantly, the CEP stability of the input pulse is preserved during spectral broadening [118, 119], ensuring that CEP control is maintained over the compressed output, provided the input is CEP-stabilized. These combined advantages of HCFs were critical in the generation of IAPs [57].

However, scaling power in HCFs poses challenges. To prevent gas ionization, which can introduce difficult-to-compensate higher-order dispersion, larger core radii are required for higher powers. This necessitates longer fibers to achieve sufficient Kerr-induced spectral broadening. Unfortunately, longer fibers are more prone to bending, increasing mode mixing and guiding losses. Stretched flexible HCFs [108] mitigate this issue by being held under tension at both ends to maintain straightness, though a detailed discussion of this technique is beyond the scope of this section.

2.5 Carrier-envelope phase (CEP) stabilization

The CEP of the pulse train from a laser system drifts from shot to shot due to subtle dispersive effects and pump fluctuations within the oscillator cavity [120]. This drift occurs with a periodicity related to the cavity's round-trip time, arising from the mismatch between the group and phase velocities of the light in the cavity. Over successive pulses, this mismatch causes a gradual phase slip between the carrier wave and the pulse envelope. For applications such as IAP generation, where precise control of the electric field waveform is crucial [57], this drift must be measured and stabilized.

f-2f Interferometry

The Carrier-Envelope Offset (CEO) frequency (f_{CEO}) [121, 122] quantifies the rate of CEP change. A widely used method to measure it is the f-2f technique, which expresses the frequencies of comb modes within the pulse train as:

$$f_1 = f_{\text{CEO}} + n f_{\text{rep}}, \quad (2.23)$$

where f_{rep} is the repetition rate of the laser. Frequency doubling a portion of the pulse spectrum generates a second harmonic at:

$$f_2 = 2f_{\text{CEO}} + 2n f_{\text{rep}}. \quad (2.24)$$

When the fundamental and second harmonic components overlap spectrally, they produce a beat signal at:

$$f_{\text{beat}} = f_2 - f_1 = f_{\text{CEO}}, \quad (2.25)$$

This beat frequency can be measured using a photodiode and a radio-frequency spectrum analyzer. Direct measurement of f_{CEO} usually requires spectral broadening of the pulses, as the pulse spectrum often does not span an octave. This broadening can be achieved using photonic crystal fibers [123] or bulk materials like sapphire.

Once measured, the f_{CEO} can be locked to a convenient fraction of the oscillator's repetition rate (e.g., $f_{\text{rep}}/4$) for optimal stability. This is typically achieved by controlling parameters such as the oscillator's pump power or cavity length. A feedback loop continuously monitors f_{CEO} and generates an error signal if a deviation from the desired value is detected, adjusting the system to maintain stable phase locking [52].

2.5.1 Passive CEP stabilization

Sections 2.3 and 2.4 explored the mechanisms of OPAs and their use in broadband amplification, focusing primarily on the pump and signal pulses. An advantageous feature of OPAs, particularly in terms of waveform reproducibility, is their ability to generate CEP-stable idler pulses [124, 125]. This feature underpins the initial passive CEP stabilization in the PWS system [110, 126].

The stability of the idler pulse results from inheriting the relative phase difference between the pump and seed pulses. In a typical OPA setup, the seed pulse originates from the spectral broadening of the pump pulse, so

both pulses share a common CEP. The CEPs of these pulses are expressed as follows:

$$\varphi_p = \varphi + c_p \quad (2.26)$$

$$\varphi_s = \varphi - \frac{\pi}{2} + c_s, \quad (2.27)$$

where c_p and c_s are additional phases introduced during propagation. The resulting idler beam, generated through DFG, exhibits a phase given by:

$$\varphi_{\text{DFG}} \equiv \varphi_i = \varphi_p - \varphi_s - \pi/2 = c_p - c_s \quad (2.28)$$

Thus, the original CEP cancels out during the DFG process, leaving the idler pulse with a passively-stabilized CEP. This inherent stability is another key benefit of using OP(CP)As for power-scalable infrared laser technology.

2.5.2 Single-shot f-2f spectral interferometry

In low repetition rate systems like CPA amplifiers, single-shot f-2f spectral interferometry [52, 127] actively stabilizes the CEP by compensating for pulse-to-pulse drifts. In the PWS setup, this technique adds an additional layer of stabilization to the passively stabilized CEP from the OPA, enabling precise stabilization and control of the waveform's CEP.

The f-2f spectral interferometry technique extracts CEP information by analyzing phase relationships in the spectral domain, enabling direct measurement and stabilization of the CEP, even in cases where the phase is not periodically varying. The method works by interfering a spectrally broadened fundamental beam and its second harmonic. A typical spectrally broadened pulse can be represented as $E_{WL}(\omega) = \varepsilon_{WL}(\omega)e^{i[\phi(\omega)+\varphi]}$, where $\phi(\omega)$ is the frequency-dependent phase acquired during propagation, and φ is the CEP. The second harmonic is expressed as $E_{SH}(\omega) = \varepsilon_{SH}(\omega)e^{i[\phi_{SH}(\omega)+2\varphi+\omega\tau_g]}$, where τ_g represents the group delay introduced between the fundamental and second harmonic pulses, resulting in a spectral beating signal.

When these two pulses interfere, the detected signal becomes:

$$\begin{aligned} S(\omega) &= |E_{WL}(\omega) + E_{SH}(\omega)|^2 \\ &= I_{WL}(\omega) + I_{SH}(\omega) \\ &\quad + 2\varepsilon_{WL}(\omega) \cdot \varepsilon_{SH}(\omega) \cos[\omega\tau_g + \delta\phi(\omega) + \varphi], \end{aligned} \quad (2.29)$$

where $I_{WL}(\omega)$ and $I_{SH}(\omega)$ are the respective spectral intensities, and $\delta\phi(\omega)$ represents the spectral phase difference. The key objective is to isolate the phase term $\Phi(\omega)$ from the interference signal [128, 129], defined as:

$$\Phi(\omega) = \omega\tau_g + \delta\phi(\omega) + \varphi \quad (2.30)$$

This phase is tracked shot-to-shot in a feedback loop, where the difference $\Delta\Phi_n = \Phi_n - \Phi_{\text{ref}} = \varphi_n - \varphi_{\text{ref}}$ serves as the error signal for the n -th shot, allowing for correction of CEP fluctuations between laser pulses. It is generally assumed that τ_g and $\delta\phi(\omega)$ remain constant across shots, which is a reasonable assumption in typical experimental setups.

To determine $\Phi(\omega)$, Eq. 2.29 is rewritten as $S(\omega) = b(\omega) + c(\omega)e^{i\omega\tau_g} + c^*(\omega)e^{-i\omega\tau_g}$, where $b(\omega) = I_{WL} + I_{SH}$ and $c(\omega) = \varepsilon_{WL}(\omega) \cdot \varepsilon_{SH}(\omega)e^{i[\delta\phi(\omega)+\varphi]}$.

Applying an inverse Fourier transform and using the shift theorem, the time-domain signal is obtained as:

$$S(t) = B(t) + C(t + \tau_g) + C(t - \tau_g) \quad (2.31)$$

Fourier-transforming the signal at the positive τ_g isolates $c^*(\omega)e^{-i\omega\tau_g}$. Finally, applying $\text{Im}[\log(c(\omega)e^{i\omega\tau_g})]$ reveals the phase $\Phi(\omega)$. If the CEP is the only source of phase variation between shots, this phase can serve as the error signal for shot-to-shot stabilization [130].

2.6 Pulse and field characterization

Accurate characterization of ultrashort laser pulses is essential for resolving and controlling light-matter interactions on relevant timescales [131].

Common methods for pulse characterization in the visible and infrared spectral ranges primarily focus on determining the complex electric field envelope. The spectral amplitude can be measured with a standard spectrometer, whereas techniques like Frequency-resolved Optical Gating Frequency-resolved Optical Gating (FROG) [132], spectral phase interferometry for direct-electric field reconstruction (SPIDER) [133], Two-dimensional spectral Shearing Interferometry (2DSI) [134], and dispersion scan (D-SCAN) [135, 136], among others [137, 138], are used to measure the spectral phase but do not provide information about the absolute CEP. These methods are sensitive to the field envelope rather than the full electric field waveform.

For field-dependent effects, complete characterization of the electric field waveform, including the CEP, is necessary. This requires a sub-cycle temporal gate, shorter than half of the field's oscillation period. Techniques like attosecond streaking [139–142] (see Sec. 3.6), which rely on HHG and use shorter-wavelength sampling pulses (in the Extreme Ultraviolet (EUV) and beyond [143]), meet this requirement. Similarly, other HHG-based methods, such as attosecond sampling of arbitrary optical waveforms (ARIES)

[144] and the PHz optical oscilloscope [145], provide direct access to the full electric field by exploiting sub-cycle electron trajectories. However, these techniques often require vacuum-based setups, high pulse energies, and specialized equipment such as time-of-flight detectors, EUV/soft X-ray CCDs, and optics, limiting their portability and flexibility.

Recent efforts have focused on developing more accessible field measurement techniques that reduce the need for high pulse energies [146], offer high detection bandwidths [131], and enable single-shot capability [147]. Approaches leveraging strong-field effects, such as tunnel ionization [146, 148–150] and multiphoton excitation [147, 151–155], alongside perturbative techniques like electro-optic sampling [156, 157], generalized heterodyne optical sampling (GHOST) [158], and the recently developed Third-order Reconstruction of Electric Fields via cross-correlation (TRES) [159], have enabled sub-cycle gating with greater experimental flexibility. These advancements reduce reliance on complex setups and specialized equipment, often allowing measurements in ambient conditions and expanding applicability in various experimental environments.

However, it is important to recognize that these techniques, including HHG-based methods, typically provide spatially averaged field measurements. This averaging can obscure spatio-temporal features, particularly in broadband waveforms. A more comprehensive characterization should consider both the temporal and spatial aspects of the field, as demonstrated in recent work [88].

In the experiments presented here, the 2DSI and TRES techniques were employed, and their details are briefly described in the following sections.

2.6.1 Two-dimensional spectral shearing interferometry (2DSI)

In Two-dimensional spectral Shearing Interferometry (2DSI) [134, 160], two narrowband, spectrally-sheared (ancillae) pulses centered at ω_{CW} and $\omega_{CW} + \Omega$ are frequency-mixed with the pulse under test (PUT) in a nonlinear crystal (typically a $\chi^{(2)}$ crystal, e.g., BBO). This process generates spectrally-sheared, frequency-mixed signals $E(\omega)$ and $E(\omega - \Omega)$. Here, $\omega = \omega_{PUT} \otimes \omega_{CW}$ represents the frequency-mixed output (e.g., SFG or DFG), where ω_{PUT} is the frequency of the test pulse. A variable delay stage introduces a delay (τ_{CW}) to one of the ancillae pulses. The interference pattern between the sheared signals is recorded as a function of this delay, yielding a spectrogram described as

$$\begin{aligned} S(\omega, \tau_{CW}) &= |E(\omega) + E(\omega - \Omega)e^{i\omega\tau}|^2 \\ &= I(\omega) + I(\omega - \Omega) \\ &\quad + 2\epsilon(\omega)\epsilon(\omega - \Omega)|\cos[\omega_{CW}\tau_{CW} + \phi(\omega) - \phi(\omega - \Omega)] \end{aligned} \tag{2.32}$$

The spectral phase of the pulse is encoded within the argument of the interference term. For sufficiently small shear frequencies Ω , the phase difference in this argument approximates the group delay:

$$\tau_g(\omega) \cdot \Omega \approx \phi(\omega) - \phi(\omega - \Omega). \quad (2.33)$$

Following a procedure similar to the one described in Section 2.5 for isolating the interference term, the spectral phase can be retrieved directly from $\tau_g(\omega)$ through integration along the angular frequency axis.

2.6.2 Third-order reconstruction of electric fields via cross-correlation (TREX)

In the TREX technique [159], two pulses, $E_1(t)$ and $E_2(t)$, centered at frequencies ω_1 and ω_2 , are focused into a noble gas target. The delay τ between the pulses is scanned while the resulting third-order nonlinear signal is recorded as a function of delay. The measured spectrogram is modeled as:

$$S(\omega, \tau) \propto |\omega \cdot \mathcal{F}\{P_{\text{NL}}(t, \tau)\}|^2 \cdot T(\omega), \quad (2.34)$$

where

$$P_{\text{NL}}(t, \tau) \propto [E_1(t - \tau) + E_2(t)]^3, \quad (2.35)$$

and $T(\omega)$ is a transfer function capturing the amplitude transmission properties of the optical setup. A genetic algorithm is used to reconstruct the electric fields $E_1(t)$ and $E_2(t)$, as well as the transfer function $T(\omega)$. With the reconstructed fields, the combined waveform $E_{\text{tot}}(t, \tau) = E_1(t - \tau) + E_2(t)$ is known at any delay τ .

The measured spectrogram reveals rich details about the nonlinear pulse interaction. It encodes mixing frequencies resulting from three-photon interactions between the two input fields, which include contributions from THG, SPM, Cross-phase Modulation (XPM), and other nonlinear mixing processes. Figure 2.3 illustrates this for few-cycle Gaussian pulses with central frequencies ω_1 and ω_2 , that are similar to the ones used in the PWS.

For narrowband pulses, the delay modulates the shape of the spectral bands associated with these mixing frequencies, primarily encoding information about their temporal envelopes. However, in cases where the central frequencies are properly matched, interference patterns can emerge even in narrowband pulses, encoding phase information. With broadband pulses, as shown in Fig. 2.3, the wide bandwidth generates clear beat patterns

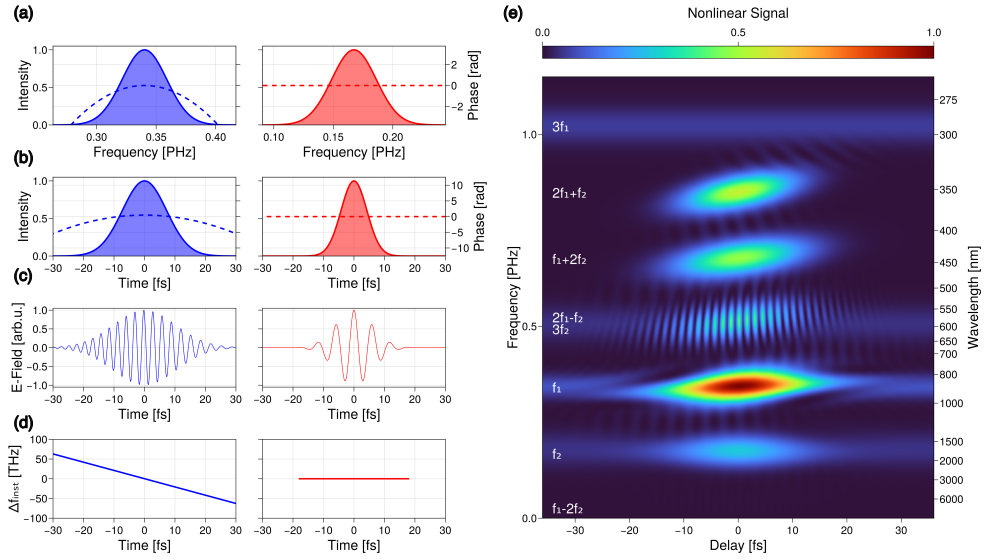


Figure 2.3: Simulated TREX trace. (a) Spectral intensity of input Gaussian pulses (800 nm, 10 fs, GDD < 0, blue; 1700 nm, 10 fs red). (b) Instantaneous intensity. (c) Field strength. (d) Instantaneous frequency shift. (e) TREX spectrogram. (Courtesy of M. Kubullek).

along the delay axis due to interference. These patterns are sensitive to the relative phase between the pulses and the CEP of the combined waveform E_{tot} .

High-order harmonic and attosecond pulse generation

This chapter presents the theoretical foundation for producing attosecond pulses in the Extreme Ultraviolet (EUV) and soft X-ray regions via High-order Harmonic Generation (HHG) using femtosecond optical pulses. It focuses on Isolated Attosecond Pulse (IAP) generation and their characterization.

3.1 High-harmonic generation

Pulse durations of optical laser pulses have been pushed to extremely short timescales, even entering the attosecond regime. Advanced pulse compression techniques [96] and waveform synthesis [70, 116] have led to the generation of 975-as pulses at 530 nm ($T = 1.77$ fs) [117]. Achieving even shorter pulses well within the attosecond regime requires a shift to higher frequencies. This became feasible with the observation of HHG in the extreme EUV range in the late 1980s [10, 161], coinciding with the development of the Ti:Sa laser [90], which laid the groundwork for attosecond pulse generation. Today, HHG extends into the soft and hard X-ray regimes [31], with the shortest reported pulse lasting only 43 as [162].

Early experiments [10, 163] drove HHG employing ps-pulses (at $\approx 1\mu\text{m}$) that were focused onto noble gas targets (Xe, Kr, Ar and Ne), reaching intensities of $\approx 10^{13} - 10^{15} \text{ Wcm}^{-2}$. Regardless of the target atom, the experiments revealed EUV emission in the form of a frequency comb, with harmonics being separated by twice the frequency of the 1- μm -pulses. The spectral profile of the emission exhibited an expected abrupt decay for the first harmonics, followed by a broad *plateau* where harmonics maintained roughly constant intensity. This plateau ended with a *cutoff* harmonic that scaled linearly with the atom's ionization potential (I_p), and beyond which the signal

decreased sharply. This universal behaviour, in analogy to a mode-locked laser, immediately hinted at the potential for generating an Attosecond Pulse Train (APT), with individual attosecond pulses emitted every half-cycle of the driving laser field [164, 165].

The unique characteristics of the observed HHG spectrum, particularly the plateau region, could not be understood in terms of the perturbative approach introduced in Sec. 2.1 [166], the prevailing framework for describing (non-resonant) nonlinear optical phenomena at the time [60]. This is because, in contrast to low-order harmonic generation, where intensities of $\lesssim 10^{13} \text{ Wcm}^{-2}$ result in weak atomic perturbations [69], the intensities involved in HHG ($\approx 10^{13} - 10^{15} \text{ Wcm}^{-2}$) necessitate a strong-field approach [167, 168], as the atomic potential can be significantly distorted.

Understanding the mechanisms behind HHG led to the establishment of *attosecond science* [2, 7, 169]. This section provides a theoretical overview of HHG, focusing on the concepts most relevant to this thesis. It begins by examining HHG at both microscopic and macroscopic scales. This is followed by an exploration of current techniques for isolating individual attosecond pulses from the generated pulse train, along with methods used to characterize them. For a more comprehensive treatment of the topic, the reader is referred to Refs. [52, 170].

3.1.1 Keldysh parameter

The observation of HHG [10, 161], along with early Time-dependent Schrödinger Equation (TDSE) simulations [166, 167], highlighted the limitations of traditional perturbative approaches and strongly suggested an underlying strong-field mechanism. This realization was built upon the seminal work of Keldysh back in 1964 [171], who provided an analytical framework for understanding tunneling ionization in strong, low-frequency fields.

Keldysh theory introduces a key parameter (γ), now known as the *Keldysh parameter* parameter, given by,

$$\gamma = \sqrt{\frac{I_p}{2U_p}}, \quad (3.1)$$

with U_p the ponderomotive energy (the average kinetic energy of a free electron of charge e and mass m_e oscillating in a laser field):

$$U_p = \frac{e^2 E_0^2}{4m_e \omega_0^2}, \quad (3.2)$$

Essentially, the Keldysh parameter compares the ionization (binding) energy (I_p) to the energy imparted by the laser field (which scales as $\propto I_0 \lambda^2$). This

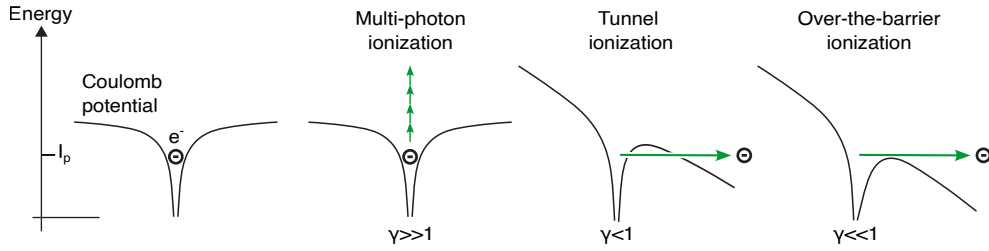


Figure 3.1: Photoionization regimes. For $\gamma \gg 1$, multi-photon ionization (including above threshold ionization) dominates. The electron absorbs n photons to escape from the ground state (at $-I_p$) into the continuum. When $\gamma < 1$, the light field distorts the atomic potential, allowing the electron to escape via tunneling ionization. As the field strength increases further into $\gamma \ll 1$, the potential barrier is suppressed, allowing the electron to escape freely. Adapted from "Laser light interacts with atoms in a gas," ©Johan Jarnestad/The Royal Swedish Academy of Sciences [172].

comparison dictates the light-matter interaction regime (see Fig. 3.1), categorized as follows [42]:

- Tunneling regime and over-the-barrier ionization** ($\gamma < 1$ and $\gamma \ll 1$): The laser field significantly distorts the atomic potential, leading to Strong Field Ionization (SFI) or tunneling ionization. In this regime, the electron tunnels through a suppressed Coulomb barrier within a fraction of the laser's oscillation period (T_0), emerging at a position $x_0 \approx |Ip|/eE_0$. As the field strength increases, the barrier becomes thinner, eventually leading to Over-the-barrier Ionization (OBI). Because tunneling occurs within a fraction of a half-cycle, it can be considered to follow the electric field's changes almost instantaneously - or *adiabatically*. Furthermore, in this limit, high field strengths quickly drive the freed electron away from its parent ion, minimizing the influence of the Coulomb force and leaving it negligible compared to the laser field [69]. These conditions define the Strong Field Approximation (SFA).
- Cross-over regime** ($\gamma \sim 1$): This regime marks a transition between tunneling ionization and multiphoton ionization. While tunneling remains the governing process, some multiphoton absorption happens [173, 174], leading to what is termed as *non-adiabatic* tunneling [175, 176].
- Multiphoton regime** ($\gamma \gg 1$): At higher laser frequencies, an electron can absorb a specific number of photons to reach the continuum and leave the atomic potential. This scenario defines Multiphoton Ionization (MPI). If the electron absorbs even more photons than strictly necessary for ionization, the process is termed Above-threshold Ionization (ATI) [177], and also falls within this regime.

3.1.2 Photoionization rate and probability

The previous discussion outlined different photoionization regimes, with SFI ($\gamma \ll 1$, $\gamma < 1$) being the common regime in HHG due to the low frequency and high field strength of femtosecond lasers. While this describes the early stages of HHG, calculating the degree of ionization requires specific models.

Common models for calculating static tunneling ionization rates, $w(E)$, include the Ammosov-Delone-Krainov (ADK) model [178] and the Tong-Lin ionization model [179]. These models are derived analytically under the assumption of a static laser field E and build upon the Perelomov-Popov-Terent'ev (PPT) theory [180]. However, both the ADK and Tong-Lin models overlook the frequency dependence inherent in the original PPT theory, which limits their accuracy in accounting for multiphoton ionization processes [52, 170]. The Tong-Lin model is better suited for higher intensities, including those approaching and leading to OBI [179]. In this thesis, it is the model used (unless otherwise stated), as the intensities employed generally fall within the range where this model is most effective.

The quasistatic approximation is particularly useful as it allows ionization rates in time-dependent fields to be computed using rates derived from static fields. For a time-dependent electric field $E(t)$, the approximation replaces $w(E)$ with $w(|E(t)|)$ [42, 69]. This holds as long as the barrier width remains relatively constant while the electron tunnels through it, ensuring an adiabatic response to the field. However, when $\gamma \gtrsim 0.5$ and the laser field varies too rapidly for the quasistatic approximation—such as with single-cycle and sub-cycle pulses—non-adiabatic models may be required [173, 175]. In the experiments presented here, the Keldysh parameter remains below this threshold, allowing quasistatic models to be used for calculating ionization rates.

The ionization probability -or fraction- (η_e) of an atom in an electric field $E(t)$ can be calculated using the ionization rate as [52, 170]:

$$\eta_e(t) = 1 - \exp \left[- \int_{-\infty}^t w(|E(t')|) dt' \right] \quad (3.3)$$

Figure 3.2a shows the exponential increase in ionization probability with peak intensity for various noble gases at the end of pulses ($\eta_e(t \rightarrow \infty)$). Atoms with higher ionization potentials (e.g., He; $I_p \approx 24.6$ eV) require higher intensities than those with lower ionization potentials (e.g., Ar; $I_p \approx 15.6$ eV). This arises from the thinner Coulomb-distorted potential barrier for lower binding energies, as the barrier width scales as $\approx |I_p|/eE_0$. In simpler terms, atoms with smaller ionization potentials are more weakly bound to their nuclei, requiring less force from the electric field to achieve ionization.

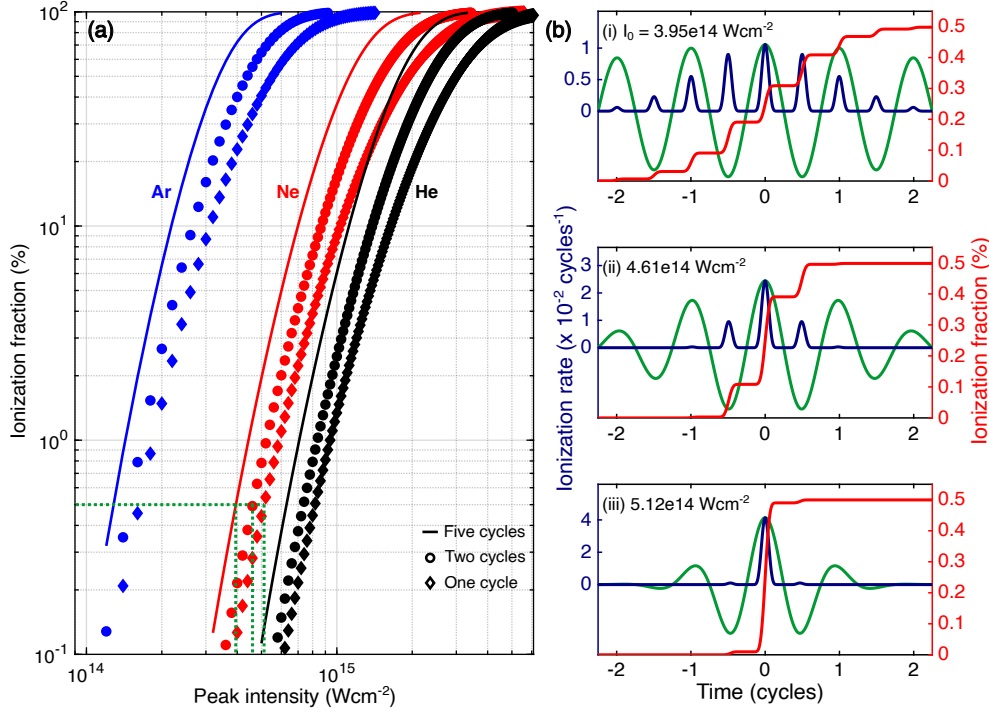


Figure 3.2: Tong-Lin ionization in noble gases. (a) Tong-Lin final ionization fraction ($\eta_e(t \rightarrow \infty)$) vs peak intensity for different gases (Ar, Ne, He) using 800-nm Gaussian pulses with varying durations (1, 2, and 5 cycles) at fixed CEP ($\varphi = 0$). (b) Instantaneous ionization rate ($w(t)$, left axis) and fraction ($\eta_e(t)$, right axis) in Ne for the same pulses. Intensities are adjusted to yield a final ionization probability of 0.5% for each case (i-iii, green dashed lines in (a)). The green solid line sketches the electric field waveform.

Figure 3.2a also highlights the impact of pulse duration on ionization probability. For a fixed intensity, longer pulses lead to greater ionization. This occurs because longer pulses contain more cycles that contribute to the ionization process, compared to shorter pulses with fewer cycles. Additionally, a longer pulse delivers more total energy to the atom, as energy scales with the product of intensity and duration.

Figure 3.2b illustrates the ionization rate and its build-up within pulses of varying durations. Peak intensities are adjusted to achieve a final ionization level of 0.5% for all cases. Two key aspects emerge from the figure: First, the exponential dependence of the ionization rate on field strength highlights how each half-cycle can liberate electrons within a fraction of its duration. With $\sim 1\text{-}\mu\text{m}$ laser pulses, this timescale easily falls in the sub-100-attosecond range, showcasing the intrinsic attosecond nature of HHG. Second, shorter pulses exhibit fewer ionization events, and these events become increasingly confined to the most prominent half-cycle, where most of the pulse energy is concentrated. This trend is reflected in the ionization level, which builds up at earlier cycles for longer pulses, but initiates near

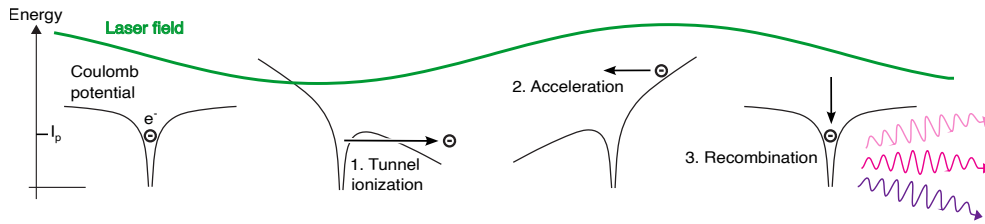


Figure 3.3: Three step model for high-harmonic generation. 1. The light field distorts the Coulomb potential, forming a barrier through which the electron can tunnel. 2. The laser field accelerates the electron, making it gain kinetic energy. 3. Upon field reversal, the electron may recombine with the parent ion, emitting a high-energy photon. Adapted from "Laser light interacts with atoms in a gas," ©Johan Jarnestad/The Royal Swedish Academy of Sciences [172].

the main half-cycle for shorter pulses.

3.1.3 The three-step model

Early efforts to understand HHG mechanisms heavily relied on TDSE simulations within the Single-active Electron (SAE) approximation [166]. These simulations successfully reproduced the key spectral features of the experimentally observed EUV frequency combs [10], and highlighted the dominant role of single-electron dynamics in HHG. Additionally, insights gained from studying ionization mechanisms under strong fields (discussed previously) confirmed that HHG operates within a regime where the SFA is valid and tunnel ionization is the primary ionization process.

This success led to the semiclassical three-step model [168, 181], which provides a simplified yet intuitive framework for understanding HHG. The model considers the following steps (see Fig. 3.3):

- **1. Tunnel Ionization:** The intense laser field distorts the atomic potential, allowing the most weakly bound electron to tunnel out into the continuum with zero initial velocity.
- **2. Acceleration:** The laser field accelerates and guides the freed electron away from the atom, where its interaction with the Coulomb potential becomes negligible.
- **3. Recombination:** As the laser field reverses direction, the electron is driven back towards the atom. Upon recollision, it may release its excess kinetic energy as a high-energy photon.

The semiclassical model can be formulated mathematically using Newton's equations of motion for an electron (mass m_e and charge e) under the influence of a linearly polarized laser field, by the following system of equations:

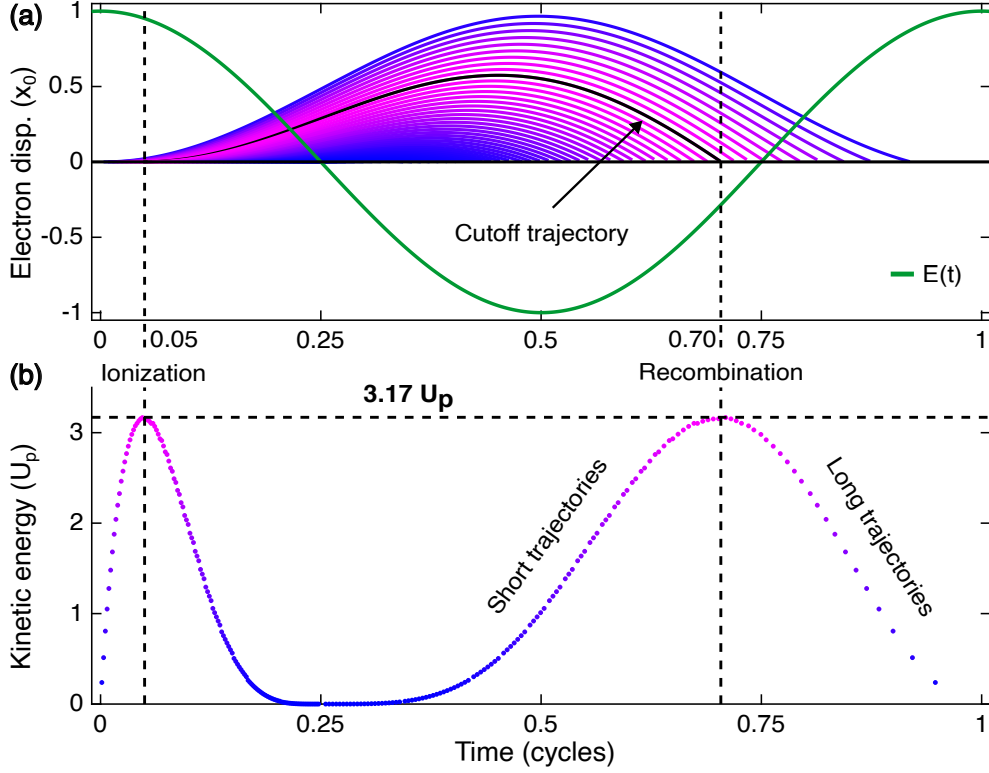


Figure 3.4: Classical returning electron trajectories. (a) Electron displacement ($|x(t)|$) normalized to the maximum excursion displacement (x_0 , Eq. 3.7) and normalized driving field (green solid line). The black solid line denotes the cutoff trajectory (maximum energy). (b) Kinetic energy of recombining trajectories as a function of ionization and recombination times. Trajectories are color-coded by their recombining energy.

$$\begin{cases} \dot{x}(t) = \frac{p}{m_e} \\ \dot{p}(t) = e\dot{A}(t) \end{cases} \quad (3.4)$$

where $E(t)$ is the electric field and $A(t)$ is the vector potential ($E(t) = -\dot{A}(t)$). Integrating these equations with the initial condition $\dot{x}(t_i) = 0$ yields the electron's position and momentum, x and p , respectively:

$$x(t) = x(t_i) + \frac{e}{m_e} \int_{t_i}^t [A(t') - A(t_i)] dt' \quad (3.5)$$

$$p(t) = e[A(t) - A(t_i)] \quad (3.6)$$

Here, $x(t_i) \approx |I_p|/eE_0$ is the initial electron position after having tunnel-ionized from the Coulomb barrier, with values typically around $\sim 10^{-10}$ m.

In the near-infrared regime, and assuming a sinusoidal driving field, the electron's maximum excursion is given by:

$$x_0 = \frac{2eE_0}{m_e\omega_0^2}, \quad (3.7)$$

and is usually at least ten times larger than $x(t_i)$, justifying the simplification of neglecting $x(t_i)$ in subsequent calculations [69].

For HHG to occur, the electron must recombine with its parent ion at time t_r . This condition can be expressed as:

$$x(t_r) = \int_{t_i}^{t_r} [A(t') - A(t_i)] dt' \stackrel{!}{=} 0, \quad (3.8)$$

from which ionization times (t_i) and recombination times (t_r) of returning electron trajectories can be computed. Defining the electron momentum upon recombination as $p(t_r) \equiv p_r$, the corresponding kinetic energy is given by:

$$E_r = \frac{|p_r|^2}{2m_e} \quad (3.9)$$

Figure 3.4a shows electron trajectories in a cosine field of constant amplitude E_0 . Two types of trajectories lead to the same kinetic energy: short trajectories with shorter excursion times and long trajectories with longer excursion times. These trajectories exhibit distinct properties, as seen in Fig. 3.4b, which plots kinetic energy versus ionization and recombination times. Firstly, short trajectories originate later than long ones and experience lower field strengths. Secondly, short trajectories exhibit a nearly-constant positive chirp ($\text{GDD} > 0$), with lower energies preceding higher energies, while long trajectories have a negative chirp ($\text{GDD} < 0$).

This chirp, termed *attochirp*, scales inversely with the slope of the kinetic energy versus recombination time curve. Since this slope is proportional to $U_p/T_0 \propto (I_0\lambda^2)/\lambda$, the attochirp is given by [52, 182]

$$\beta \propto \frac{1}{I_0\lambda} \quad (3.10)$$

Consequently, the attochirp can be minimized by increasing either the intensity or wavelength. This analysis shows that HHG timescales can extend

close to the full half-cycle duration, unlike the confinement predicted by SFI alone. Still, with near-infrared lasers, this falls in sub-fs time range.

A special case is the cutoff trajectory (black line in Fig. 3.4a). Here, trajectories coalesce (GDD = 0), the electron reaches its maximum energy of $3.17U_p$, and it marks the division between short and long trajectories. This trajectory originates at approximately 5% of the cycle duration and recombines at around 70%. Due to energy conservation, it defines the maximum emitted photon energy (the *cutoff energy*):

$$E_{\text{cutoff}} = I_p + 3.17U_p \quad (3.11)$$

The scaling of U_p with intensity and wavelength ($E_{\text{cutoff}} \propto I_0\lambda^2$) has been crucial for extending HHG from the EUV into the hard X-ray range [46], as discussed in Sec. 3.4.

3.1.4 Lewenstein's model

The classical three-step model [181] provides an intuitive picture of HHG and accurately predicts the cutoff law (Eq. 3.11) already deduced by Krause et al. (1992) [183] with TDSE simulations. However, its inability to quantify emission probabilities for individual trajectories or directly address the quantum nature of the liberated electron wavepacket limits its capacity to compute the spectral amplitude and phase of the induced dipole moment. While TDSE simulations can address these limitations, they are computationally demanding and do not readily reveal the underlying mechanism from a quantum mechanical perspective.

The semiquantum¹ mechanical approach by Lewenstein et al. (1994) [184] addresses this challenge by exploiting the SFA. Upon tunnel ionization, the electron wavefunction is modeled as a coherent superposition of two quantum states:

$$|\Psi(t)\rangle = e^{-\frac{I_p t}{\hbar}} \left[a(t)|0\rangle + \int b(v,t)|v\rangle dv \right], \quad (3.12)$$

where a portion remains bound in the ground state $|0\rangle$ with amplitude $a(t)$, related to the ionization fraction (see Eq. 3.3) by:

$$a(t) = \sqrt{1 - \eta_e(t)}, \quad (3.13)$$

¹Electric fields are treated classically

The remaining portion becomes an electron wavepacket directly released into the continuum of free-electron states $|v\rangle$ travelling with velocity v , and weighted by complex coefficients $b(v, t)$ (excited states are neglected²). The complex coefficients $b(v, t)$, found by solving the TDSE with the ansatz of Eq. 3.12, contain the information about the wavepacket's evolution in the laser field.

The total wavefunction, $|\Psi(t)\rangle$, is used to calculate the induced dipole moment, $d_h(t)$, via the expectation value of the classical dipole moment operator: $d_h(t) = \langle \Psi(t) | -e \cdot x | \Psi(t) \rangle$. This induced dipole moment serves then to obtain the complex single-atom harmonic field amplitude, $E_h(\omega)$, via the following relation [2, 170]:

$$E_h(\omega) = \mathcal{F}\{\ddot{d}_h(t)\} = -\omega^2 d_h(\omega) \quad (3.14)$$

The corresponding single-atom harmonic emission spectrum is thus, given by:

$$I_h(\omega) = |E_h(\omega)|^2 \quad (3.15)$$

Therefore, to compute the single-atom emission profile, the dipole moment must be calculated. This is given by the following expression (in atomic units)³ [52]:

$$d_h(t) = -i \int_0^\infty d\tau \left(\frac{\pi}{\varepsilon + i\tau/2} \right)^{3/2} \overbrace{\left[a(t-\tau)E(t-\tau)d(p_{\text{st}}(t,\tau) - A(t-\tau)) \right]}^{1. \text{ Ionization}} \\ \times \underbrace{e^{-iS_{\text{st}}(t,\tau)}}_{2. \text{ Excursion}} \cdot \underbrace{\left[a^*(t)d^*(p_{\text{st}}(t,\tau) - A(t)) \right]}_{3. \text{ Recombination}} + \text{c.c.} \quad (3.16)$$

In this calculation, the integral (known as the *Lewenstein integral*) is performed over the electron wavepacket excursion time $\tau = t - t_i$. The value ε is introduced to avoid integration singularities, and the term $d(v) = \langle v|x|0\rangle$ and its complex conjugate correspond to the hydrogenic transition dipole matrix elements. Finally, p_{st} and S_{st} denote the stationary canonical momentum and action, respectively, which are obtained via the Saddle-point Approximation (SPA) and defined as:

²Models incorporating excited states have been developed. For further details, see Refs. [185, 186].

³For a detailed derivation and conversion to SI units, please refer to [52].

$$p_{\text{st}}(t, \tau) = \frac{1}{\tau} \int_{t-\tau}^t A(t') dt' \quad (3.17)$$

$$S_{\text{st}}(t, \tau) = \int_{t-\tau}^t \left[\frac{|p_{\text{st}}(t-\tau) - A(t')|^2}{2} + I_p \right] dt', \quad (3.18)$$

The Lewenstein integral (Eq. 3.16) sums contributions from all possible electron trajectories with varying excursion times τ , where each trajectory leaves the atom and later recombines at time t . As indicated in Eq. 3.16, this semi-quantum framework reflects the classical three-step mechanism by means of three terms:

- **1. Ionization:** Accounts for the probability of the electron being promoted from its ground state with amplitude $a(t)$ to the continuum via the electric field $E(t)$.
- **2. Excursion:** Represents the phase acquired (including the kinetic energy gain) by the electron during its journey in the continuum. The stationary action S_{st} enforces the constraint that only trajectories that return to the parent ion contribute to the dipole, as imposed by the SPA.
- **3. Recombination:** Corresponds to the probability of the electron recombining with the ground state. The coupling, determined by the overlap in the dipole matrix element, leads to interference and an oscillating dipole, the source of HHG emission. Ground state depletion, caused by field ionization during either the electron's liberation or recombination, vanishes this dipole.

Finally, the $\tau^{-3/2}$ prefactor in Eq. 3.16 reflects wavepacket spreading due to dispersion during its continuum excursion. This dispersion, which scales with excursion time, affects longer trajectories more severely, resulting in greater wavepacket spreading. Regardless of the trajectory type, this spreading reduces the overlap between the free-field and ground states, leading to a τ^{-3} scaling of the dipole intensity. Given that $\tau \propto \lambda$, this dispersion leads to a λ^{-3} scaling, which significantly contributes to the well-known unfavorable scaling of HHG conversion efficiency, going as $\sim \lambda^{-(5-6)}$ [41, 187]. Mitigating this dispersion-induced scaling is a major focus of current research in HHG science and is central to this thesis. This work specifically addresses this issue at the single-atom level by tailoring the driving waveform to control the trajectory of the released wavepacket, reduce its spreading, and thereby enhance the efficiency of the HHG process [47, 48, 188–190]. Other approaches include exploiting phase-matching [191–193] and developing novel laser architectures [91, 194, 195].

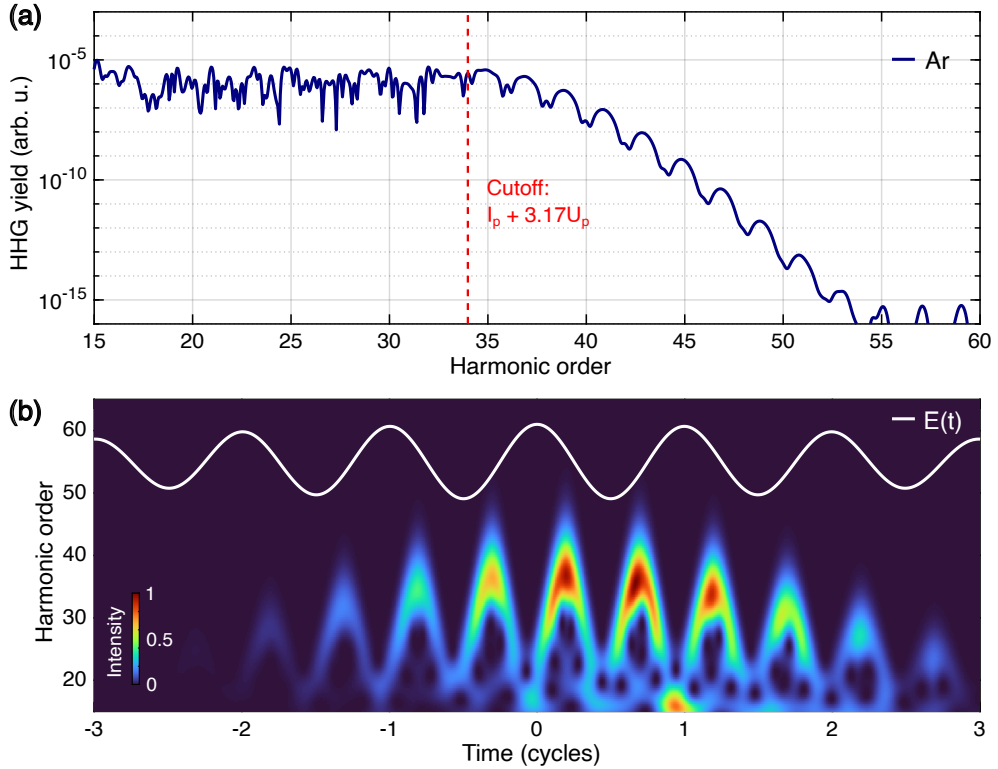


Figure 3.5: Single-atom harmonic emission. (a) High-harmonic spectrum and (b) time-frequency analysis for Ar driven by a 5-cycle, 800-nm Gaussian pulse at $2 \times 10^{14} \text{ Wcm}^{-2}$ peak intensity (CEP = 0). Red dashed line indicates the classical cutoff (Eq. 3.11). The final ionization fraction ($\eta_e(t \rightarrow \infty)$) is 6.56%.

To compute the single-atom dipole moment via the Lewenstein integral (Eq. 3.16), this thesis employs the open-source code *HHGmax* [196, 197]. *HHGmax* allows for the isolation of short trajectories within the Lewenstein integral by applying a \cos^2 window function [198] with adjustable width, thereby artificially accounting for phase-matching (see Sec. 3.2).

Figure 3.5 illustrates an example simulation in Ar with a cosine field. The harmonic spectrum (Fig. 3.5a) exhibits the characteristic HHG features: evenly spaced low-order harmonics, a plateau region, and a cutoff. The corresponding time-frequency analysis⁴ (Fig. 3.5b) reveals the presence of both short and long trajectories also in this semiquantum approach.

3.1.5 Trajectory emission probability

The Lewenstein integral reveals the dipole’s full spectral characteristics but obscures details of individual electron trajectories, such as ionization times

⁴Time-frequency analyses were performed using MATLAB’s *cwt* function.

and the exact trajectory shape. Conversely, classical trajectory calculations provide this information but cannot identify which trajectories contribute most to HHG emission. This requires factoring in ionization probabilities, quantum diffusion, and transition matrix elements. A model estimating the emission probability of a photon associated to specific trajectories would bridge this gap, offering insights into the interplay of ionization, excursion, and recombination dynamics within HHG.

Gordon and Kärtner (2005) [199] proposed a model that can bridge this gap. Their approach expresses the induced dipole acceleration at recombination time t_r as a coherent sum of contributions from individual electron wavepackets (born at t_i and recombining at t_r):

$$\ddot{d}_h(t_r) \propto \sum_i a_{\text{em}}(t_r, t_i) \psi_i(t_r) \quad (3.19)$$

The emission amplitude, $a_{\text{em}}(t_r, t_i)$, is the product of ionization, excursion, and recombination amplitudes:

$$a_{\text{em}}(t_r, t_i) = a_{\text{ion}}(t_r, t_i) \cdot a_{\text{ex}}(t_r, t_i) \cdot a_{\text{rec}}(t_r), \quad (3.20)$$

where

$$a_{\text{ion}}(t_r, t_i) = a(t_i) \cdot \sqrt{w(|E(t_i)|)/|E(t_i)|^2}, \quad (3.21)$$

$$a_{\text{ex}}(t_r, t_i) = (t_r - t_i)^{-3/2}, \quad (3.22)$$

$$a_{\text{rec}}(t_r) = a(t_r), \quad (3.23)$$

with $a(t)$ defined by Eq. 3.13. The set of wavefunctions $\psi_i(t_r) = \alpha_{\text{rec}}(t_r, t_i) e^{-iS(t_r, t_i)/\hbar}$ describes the evolution of electron wavepackets from the moment they are released at time t_i until they recombine at time t_r [199, 200]. While the amplitude of this term is crucial for precise calculations, neglecting it simplifies the analysis and allows to focus on the interplay between ionization and excursion dynamics. With this simplification, the probability that a trajectory contributes to photon emission is given by:

$$P_{\text{em}}(t_r, t_i) = |a_{\text{em}}(t_r, t_i)|^2 \quad (3.24)$$

The importance of considering emission probabilities when identifying the most dominant trajectories is illustrated in Fig. 3.6. Ionization probability

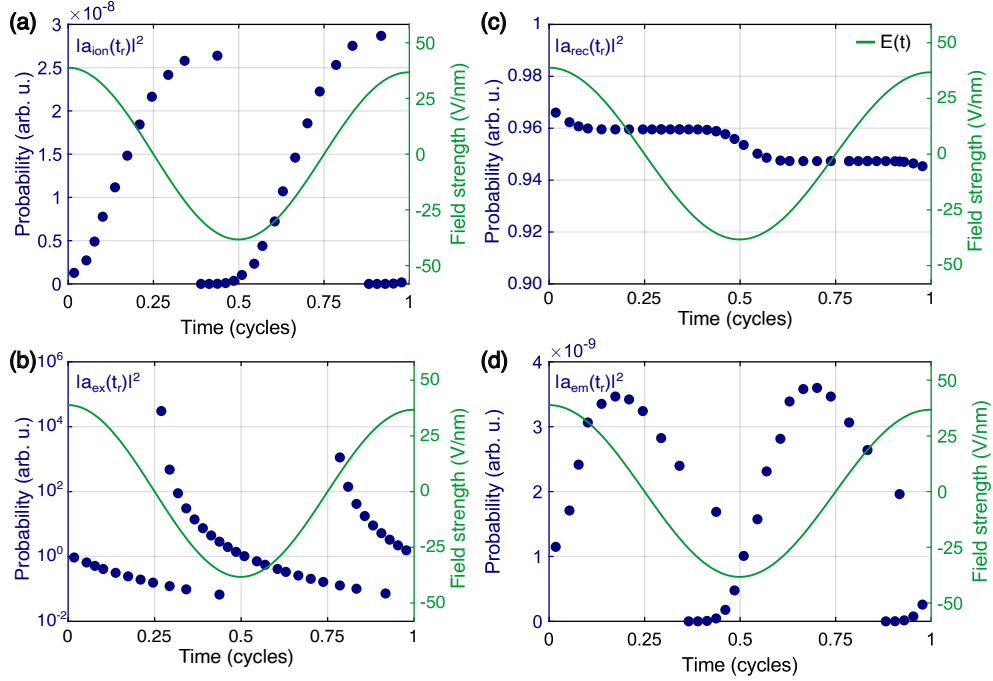


Figure 3.6: Trajectory emission probabilities over a cycle. (a) Ionization, (b) excursion, (c) recombination, and (d) full emission probabilities (Eqs. 3.20 - 3.23) vs. recombination times t_r (left axis) over a cycle. The driving electric field (right axis) is shown for reference (laser parameters as in Fig. 3.5).

(Fig. 3.6a) saturates near the field extrema. In contrast, the excursion probability (Fig. 3.6b) naturally is highest for the short trajectories (recombining between $\approx 0.25T_0$ and $0.7T_0$), and decreases exponentially toward the cutoff trajectory's recombination time. With low ionization (6.56%), the recombination probability (Fig. 3.6c) plays a minimal role ($|a_{\text{rec}}|^2 \approx 1$). Thus, in this example, ionization and excursion are the main determinants of HHG emission.

While long trajectories benefit from higher ionization probability (due to being released near the field peak), they also experience greater dispersion in the continuum, reducing their emission probability. Short trajectories, though less optimally ionized, experience less dispersion. This interplay results in similar emission contributions from both trajectory types, with emission probability (P_{em}) peaking around $0.2T_0$ and $0.7T_0$. This is shown in Fig. 3.6d and more explicitly in Fig. 3.7.

Figure 3.7 demonstrates how the trajectory analysis, when weighted by the emission probability (P_{em}), aligns with Lewenstein-based semiquantum simulations. In (a-b), unweighted electron trajectories and corresponding photon energies versus recombination times (t_r , calculated as $E = E_r + I_p$) are overlaid on the time-frequency analysis. In (c-d), trajectories are weighted by

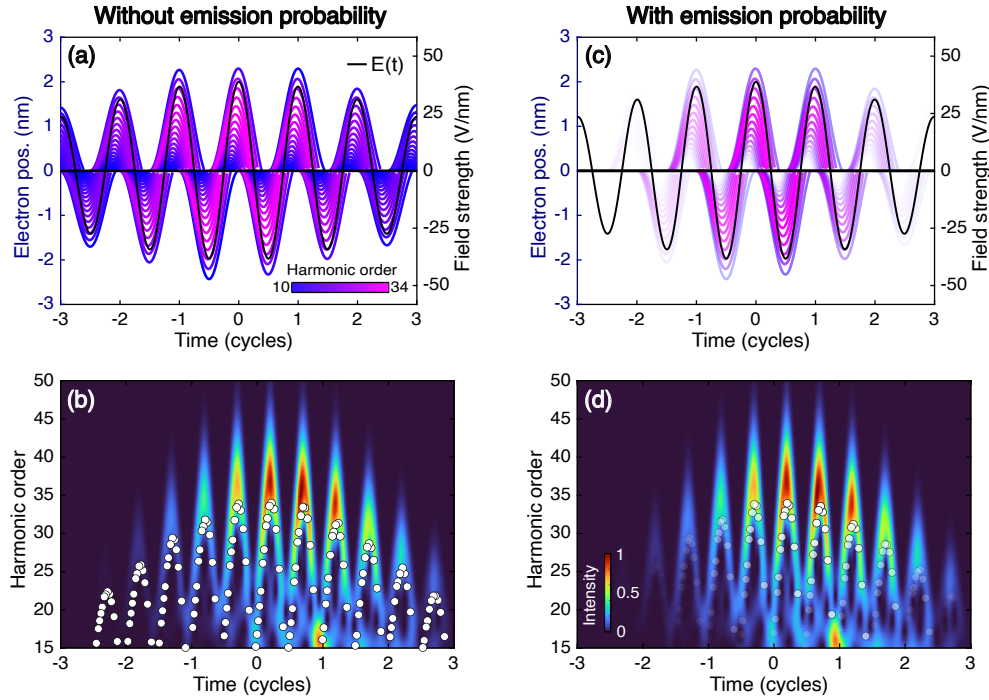


Figure 3.7: Dominant returning electron trajectories. (a) Unweighted electron trajectories (left axis) vs. driving field (right), color-coded by harmonic order (laser parameters as in Fig. 3.5). (b) Time-frequency analysis from the semiquantum simulation showing emitted harmonic order vs. time. Scattered dots indicate classical calculations. (c-d) Same as (a-b) but with trajectories weighted by their emission probability (Eq. 3.24). Transparency reflects emission probability.

P_{em} , revealing only those with the highest probability, which coincide with the intensity distribution in the time-frequency analysis.

Certain waveform shapes (see Ch. 5) can create scenarios where high ionization probability is counteracted by wavepacket diffusion or a reduced ground state population at the moment of recombination. This highlights the complex interplay of ionization, excursion, and recombination probabilities, illustrating the value of this analysis for visualizing the actual trajectories contributing to HHG emission.

3.1.6 Dipole phase

As mentioned previously, while the electron wavepacket travels through the continuum, it acquires a phase, ϕ_{dip} , proportional to the action along a trajectory born at t_i and recombining at t_r – meaning $\phi_{dip} \propto S(t_r, t_i)$. The distinct chirp behavior of short and long trajectory emissions suggests that their underlying dipole phases also differ. Indeed, the induced dipole has an intrinsic phase dependent on the trajectory type, primarily determined

by the ponderomotive energy and excursion time of the trajectory (short, denoted by s , or long, denoted by l) as $\phi_{\text{dip}} \simeq \tau_{s,l} U_p$ [201]. Since the ponderomotive energy is proportional to the intensity, the *dipole phase* associated to the harmonic q is expressed as [52]:

$$\phi_{\text{dip}}^q = \alpha_{s,l}^q I, \quad (3.25)$$

where the positive coefficients $\alpha_{s,l}^q$ account for the different trajectory excursion times. This scaling has important consequences for long trajectories: they experience stronger decoherence due to their longer excursion times and exhibit greater angular divergence than short trajectories (arising from the radial dependence of the intensity). These effects have been experimentally confirmed by Bellini et al. (1998) [202]. While more comprehensive expressions for the dipole phase exist [203], the form in Eq. 3.25 has proven successful in explaining these and other experimental observations [204, 205].

3.2 On-axis phase-matching

Building on the limitations of single-atom models for HHG highlighted by Antoine et al. (1996) [206], macroscopic propagation effects like phase-matching become crucial. This is not only for the coherent buildup of the HHG signal across the medium but, as envisioned shortly after the first HHG observations [10, 161, 167], for the generation of phase-locked APTs [164, 165].

The coherent nature of HHG implies constructive interference of light emitted by individual atoms within the medium, which requires a constant phase offset ($\Delta k = 0$) between neighboring emitters. This behavior can be analyzed within a simplified on-axis scenario assuming a dispersive, absorptive, and isotropic medium (length L_{med}). Here, a driving field induces a dipole moment d_h within each atom while remaining spatially and temporally undistorted during its propagation. In this case the emitted harmonic field E_h can be expressed as [207]:

$$E_h(\omega) \propto d_h(\omega) \cdot \mathcal{H}_h(\omega), \quad (3.26)$$

where \mathcal{H}_h is a transfer function that encapsulates the effects of the medium upon harmonic propagation. It has the form:

$$\mathcal{H}_h = 2\rho \frac{L_{\text{abs}}}{1 + i2\pi \left(\frac{L_{\text{abs}}}{L_{\text{coh}}} \right)} \cdot \left(e^{-\frac{L_{\text{med}}}{2L_{\text{abs}}}} - e^{i\frac{\pi L_{\text{med}}}{L_{\text{coh}}}} \right) \quad (3.27)$$

Here, the medium's density, ρ , is directly related to its pressure, P , and the pressure-normalized neutral atomic gas density, n_0^5 , through the relationship $\rho = P \cdot n_0$. The absorption (L_{abs}) and coherence length (L_{coh}), are defined via the attenuation coefficient β and phase-mismatch Δk as:

$$L_{\text{abs}} = \frac{c}{2\omega\beta} = \frac{c}{2\omega P\bar{\beta}}, \quad L_{\text{coh}} = \frac{\pi}{\Delta k}, \quad (3.28)$$

where β [208] can be expressed in terms of the medium's pressure and, similar to n_0 , to a pressure-normalized attenuation coefficient, $\bar{\beta}$.

The harmonic intensity is proportional to the *enhancement factor* [209], which is the modulus square of the complex transfer function, i.e., $I_h \propto \mathcal{S}_h \equiv |\mathcal{H}|^2$, given by:

$$\mathcal{S}_h \propto P^2 \frac{4L_{\text{abs}}^2}{1 + 4\pi^2 \left(\frac{L_{\text{abs}}}{L_{\text{coh}}}\right)^2} \cdot \left[1 + e^{-\frac{L_{\text{med}}}{L_{\text{abs}}}} - 2e^{-\frac{L_{\text{med}}}{2L_{\text{abs}}}} \cos\left(\frac{\pi L_{\text{med}}}{L_{\text{coh}}}\right) \right] \quad (3.29)$$

To determine the harmonic intensity, the phase-mismatch, Δk must be calculated. In a free-focusing geometry it comprises the following terms [52]:

$$\Delta k = qk - k_q = \underbrace{\Delta k_{\text{neu}}}_{\substack{\text{Neutral disp.} \\ > 0}} + \underbrace{\Delta k_{\text{p}}}_{\substack{\text{Plasma disp.} \\ < 0}} + \underbrace{\Delta k_{\text{G}}}_{\substack{\text{Gouy} \\ < 0}} + \underbrace{\Delta k_{\text{dip}}}_{\substack{\text{Dipole} \\ < 0, \text{ bef. focus} \\ > 0, \text{ aft. focus}}} \quad (3.30)$$

These terms arise from the following propagation effects:

- **Neutral atom dispersion:** Both the fundamental and harmonic beams propagate through a neutral noble gaseous medium. The difference in their refractive indices leads to a phase-mismatch given by:

$$\Delta k_{\text{neu}} = P \cdot \frac{2\pi}{\lambda_q} \delta \bar{n}_q, \quad (3.31)$$

where $\lambda_q = \lambda/q$ is the q -th harmonic wavelength, and $\delta \bar{n}_q = (\bar{n} - \bar{n}_q)$ is the difference between the pressure-normalized (real) refractive in-

⁵The pressure-normalized neutral atomic n_0 , is the ratio of the gas number density at standard pressure (1 atm) to the reference pressure \bar{P} (taken as 1 atm).

3. HIGH-ORDER HARMONIC AND ATTOSECOND PULSE GENERATION

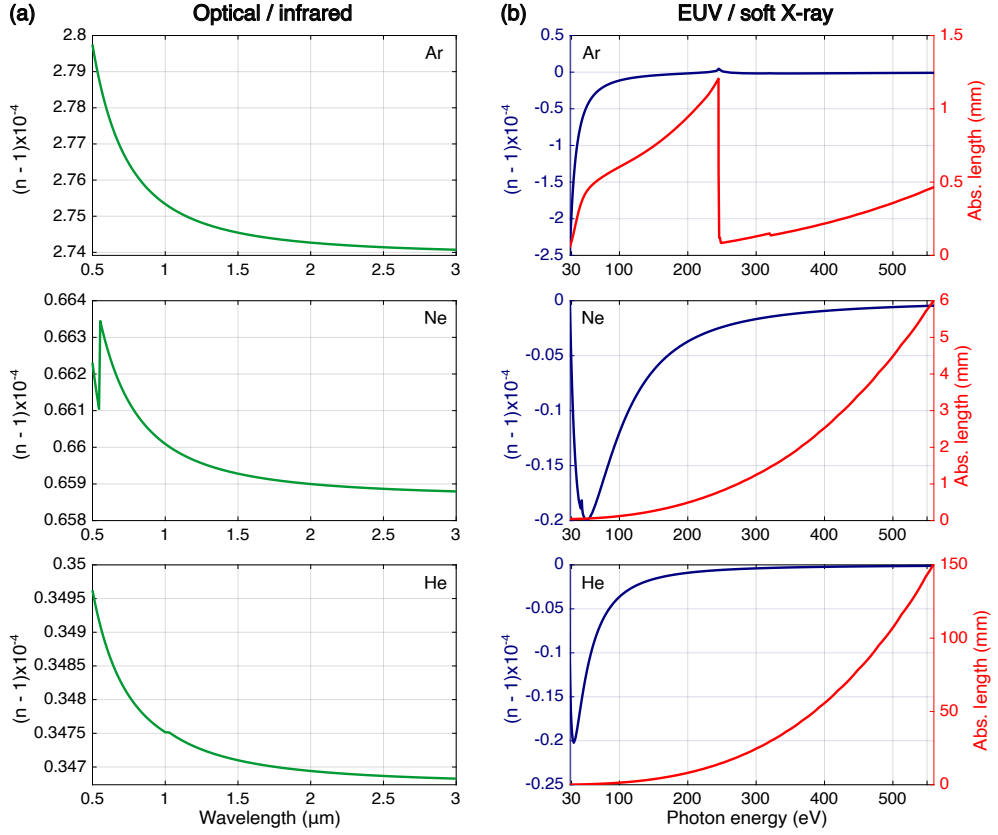


Figure 3.8: Refractive index and absorption length of noble gases. (a) Optical/infrared refractive indices and (b) EUV/X-ray refractive indices (left axis) with attenuation coefficients (right axis) for Ar, Ne, and He. Values are computed at 1 atm.

dices⁶ of the fundamental and harmonic beams. Figure 3.8 displays the refractive indices and attenuation coefficients of Ar, Ne and He. The term $\delta\bar{n}_q$ is positive because, the refractive index of the fundamental beam is greater than unity, while the refractive index of harmonics above the ionization potential is less than unity. Moreover, for most noble gases above ≈ 100 eV, $\delta\bar{n}_q$ exhibits a relatively flat spectral re-

⁶The pressure-dependent refractive index, denoted by n , is calculated using the following relationship:

$$n \approx 1 + \frac{P}{\bar{P}}(\bar{n} - 1),$$

where P is the pressure of the gas medium, \bar{P} is a reference pressure (1 atm), and \bar{n} is the refractive index at \bar{P} . Refractive indices in the optical/infrared range are obtained from Ref.[210]. For the EUV/X-ray range, refractive indices and attenuation coefficients are calculated using form factors (f_1 , and f_2) sourced from Ref.[208], by means of the expression:

$$n_c(\lambda) = 1 - \frac{P}{2\pi} n_0 r_e \lambda^2 (f_1 - i f_2).$$

sponse (with the exception of Ne, which happens after ≈ 200 eV). This results in a refractive index difference that is largely independent on the harmonic energy (or harmonic order q) beyond this value.

- **Plasma dispersion:** HHG generally involves a small degree of ionization within the medium. The resulting plasma affects the propagation velocity, primarily of the fundamental beam. This difference in velocities between the fundamental and HHG beams hinders phase-matching. The effect is described by the plasma phase-mismatch term. The plasma refractive index is given by:

$$n_p(\omega) = \sqrt{1 - \frac{\omega_p^2}{\omega^2}} \approx 1 - \frac{\omega_p^2}{2\omega^2}, \quad (3.32)$$

where ω_p , the plasma frequency, depends on the electron density n_e as:

$$\omega_p^2 = \frac{e^2 n_e}{\epsilon_0 m_e}, \quad (3.33)$$

The approximation in Eq. 3.32 is valid since plasma frequencies are typically much lower than optical frequencies (i.e., $\omega_p^2/2\pi \sim 10^{12}$ Hz). The electron density, n_e , can be expressed in terms of the gas pressure P , and ionization fraction η_e , as $n_e = P\eta_e n_0$. Consequently, the plasma phase-mismatch, Δk_p , is calculated as follows:

$$\begin{aligned} \Delta k_p &= \frac{q\omega_p^2}{2\omega c} \cdot \left[\frac{1}{q^2} - 1 \right] \approx -qP\eta_e n_0 \lambda \left[\frac{1}{4\pi\epsilon_0} \frac{e^2}{m_e c^2} \right] \\ &= -qP\eta_e n_0 r_e \lambda, \end{aligned} \quad (3.34)$$

where r_e is the classical electron radius. For HHG ($q \gg 1$), the first term in the approximation becomes negligible, making this term always negative.

- **Gouy phase shift:** As discussed in Sec. 2.1.4, a focused beam acquires a Gouy phase shift, $\zeta(z)$ (Eq. 2.14). Since $k_G(z) = -\zeta'(z)$, the Gouy phase-mismatch is:

$$\Delta k_G(z) = -\frac{q}{z_R} \cdot \frac{1}{1 + (z/z_R)^2} \quad (3.35)$$

Due to the wavelength dependence of the Rayleigh length ($z_R^q = q \cdot z_R$), the Gouy phase effect is significantly weaker for high-order harmonics, and has been neglected. This term is always negative and approaches zero for distances far from focus ($|z| \rightarrow \infty$).

- **Dipole phase shift:** Originates from the intrinsic dipole phase introduced earlier (Eq. 3.25). On-axis, and denoting $I(r = 0, z) \equiv I(z)$ (see Eq. 2.10), the dipole phase and corresponding phase-mismatch are given by:

$$\begin{aligned} \Delta k_{\text{dip}} &= -\alpha_{s,l}^q I'(z) = \alpha_{s,l}^q \frac{I(z)}{z_R^2} \cdot \frac{2z}{1 + (z/z_R)^2} \\ &= \pm \frac{\Phi_{\text{dip}}^q(z)}{z_R^2} \cdot \frac{2|z|}{1 + (z/z_R)^2} \end{aligned} \quad (3.36)$$

This contribution to the phase-mismatch is position-dependent, negative before the focus ($z < 0$), and positive after it ($z > 0$). It goes to zero at the focus ($z = 0$) and far away from it ($|z| \rightarrow \infty$).

The four contributing terms in the phase-mismatch expression unveil four parameters that can be manipulated to achieve phase-matching. These parameters are the pressure of the gas medium (P), the ionization fraction (η_e) determined by the driving laser intensity, the target position relative to the laser focus (z) and the Rayleigh length modifiable by the focusing optics (z_R). To understand how these parameters interact to achieve phase-matching ($\Delta k \stackrel{!}{=} 0$), and in some cases even estimate their values, one can analyze two main focusing scenarios:

3.2.1 Loose-focusing geometry

When the Rayleigh length significantly exceeds the medium length ($z_R \gg L_{\text{med}}$), the fundamental and harmonic beams can be approximated as plane waves within the medium. This allows to neglect Gouy and dipole mismatch contributions. In this scenario, phase-matching requires a balance between neutral atom dispersion and plasma dispersion, leading to the condition:

$$(1 - \eta_e) \frac{2\pi}{\lambda} \delta \bar{n}_q = \eta_e n_0 r_e \lambda \quad (3.37)$$

By solving for η_e , the specific plasma level required for phase-matching can be determined. This yields the critical ionization fraction, η_{cr} , given by:

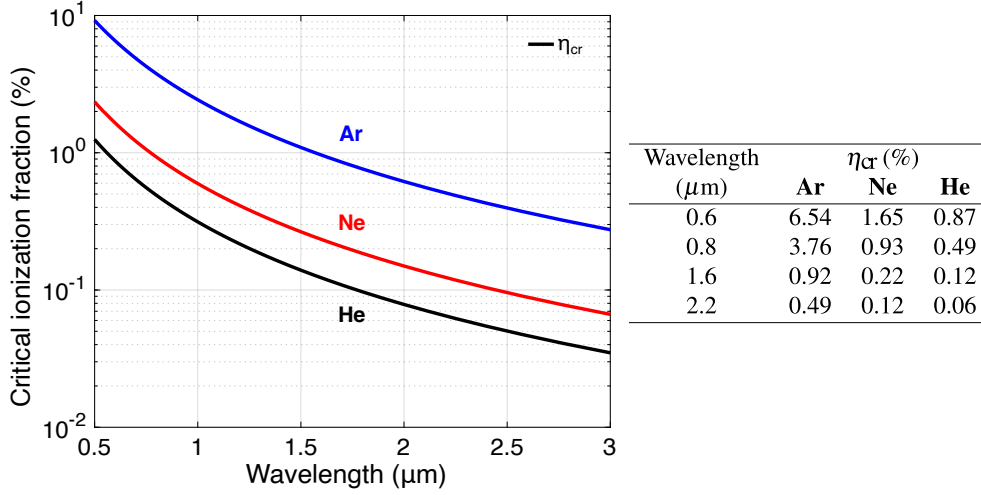


Figure 3.9: Critical ionization fraction. Wavelength dependence of critical ionization fraction (η_{cr} , Eq. 3.38) for Ar, Ne, and He. The q -th harmonic energy ($q\omega$) was fixed at 550 eV. Inset table: extracted values for the three gases at 0.6, 0.8, and 1.6 μm .

$$\eta_{\text{cr}} \equiv \left(1 + \frac{n_0 r_e \lambda^2}{2\pi \delta \bar{n}_q}\right)^{-1} \quad (3.38)$$

The main scaling of $\eta_{\text{cr}} \propto \lambda^{-2}$ features that phase-matching with longer wavelength requires lower plasma generation levels. Figure 3.9 illustrates this trend with Ar, Ne and He, along with a table presenting specific values at different wavelengths. For instance, achieving phase-matching in Ar demands an ionization level of 3.76% at 0.8 μm , but only 0.92% at 1.6 μm . The gas type also influences the critical ionization through its refractive index difference ($\delta \bar{n}_q$); lighter gases, with smaller $\delta \bar{n}_q$, exhibit a lower η_{cr} . At 1.6 μm wavelength, η_{cr} for Ne is around 0.22%, while He requires nearly half that.

This critical ionization level corresponds to a *critical intensity*, I_{cr} , the intensity needed to reach η_{cr} at the peak of the pulse ($t = 0$) for a given pulse duration. Figure 3.10a shows how I_{cr} varies with pulse duration and gas type for different wavelengths, with shorter pulses supporting higher critical intensities.

Since phase-matching depends on the critical intensity, and given the linear relationship between the HHG energy cutoff and intensity, there is a maximum phase-matched energy, referred to as the *phase-matching cutoff*. This cutoff, $E_{\text{cutoff}}^{\text{PM}}$ is given by:

$$E_{\text{cutoff}}^{\text{PM}} = I_p + 3.17U_p^{\text{cr}}, \quad (3.39)$$

3. HIGH-ORDER HARMONIC AND ATTOSECOND PULSE GENERATION

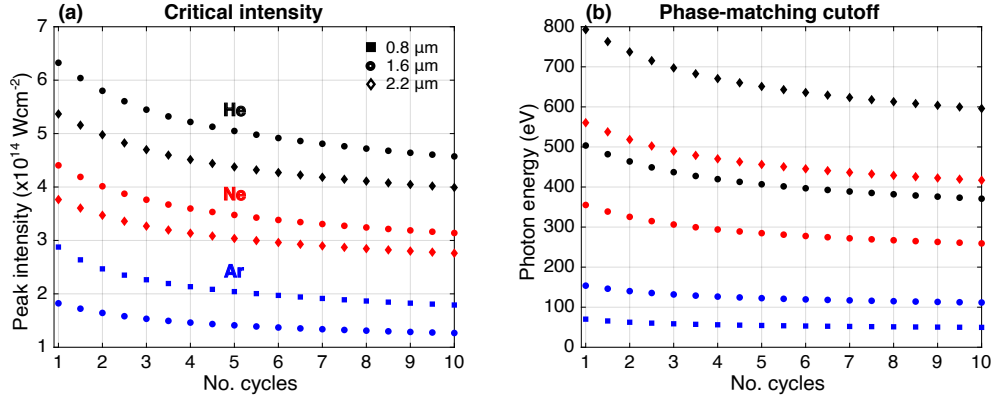


Figure 3.10: Critical intensity and phase-matching cutoff vs. pulse duration (a) Critical intensity required to reach critical ionization fractions (from Fig. 3.9) at the peak of the pulse ($\eta_e(t=0) = \eta_{cr}$) and (b) corresponding phase-matching cutoff (E_{cutoff}^{PM}) vs. pulse duration (in cycles) for Ar, Ne, and He.

where $U_p^{cr} \propto I_{cr}\lambda^2$ [31].

Figure 3.10 shows the relationship between pulse duration, critical intensity, and the resulting phase-matching cutoff. Panel (a) displays the critical intensities required for Ar, Ne, and He at wavelengths of 0.8 μm, 1.6 μm, and 2.2 μm, across varying pulse durations (in number of cycles). As the pulse duration shortens, the critical intensity increases, and, as shown in panel (b), these higher intensities lead to higher phase-matching cutoffs.

For example, in argon at 0.8 μm, the critical intensity increases from approximately $1.8 \times 10^{14} \text{ Wcm}^{-2}$ with a 10-cycle pulse to $2.9 \times 10^{14} \text{ Wcm}^{-2}$ with a single-cycle pulse, raising the phase-matching cutoff from 50 eV to 70 eV. In neon at 1.6 μm, the intensity grows from approximately $3.1 \times 10^{14} \text{ Wcm}^{-2}$ to $4.4 \times 10^{14} \text{ Wcm}^{-2}$, increasing the cutoff from 260 eV to 355 eV. Similarly, for helium at 2.2 μm, a single-cycle pulse raises the cutoff to 800 eV, compared to 600 eV with a 10-cycle pulse.

However, longer pulse durations can limit the achievable energy cutoff. As highlighted by Wissenbilder et al. (2022) [203], beyond a certain pulse duration, the maximum photon energy that can be phase-matched falls below the value predicted by the single-atom cutoff law (see Eq. 3.11). This indicates that while higher cutoffs may be theoretically achievable at the single-atom level, excessive plasma generation prevents their realization.

Another important point to consider, particularly with the time scales introduced by shorter pulses, is the time-dependent nature of the ionization fraction, i.e., $\eta_e \rightarrow \eta_e(t)$. In shorter pulses, plasma buildup occurs more abruptly and is highly localized in time, as shown in Fig. 3.2. This has significant implications for phase-matching, as intensity and CEP stability

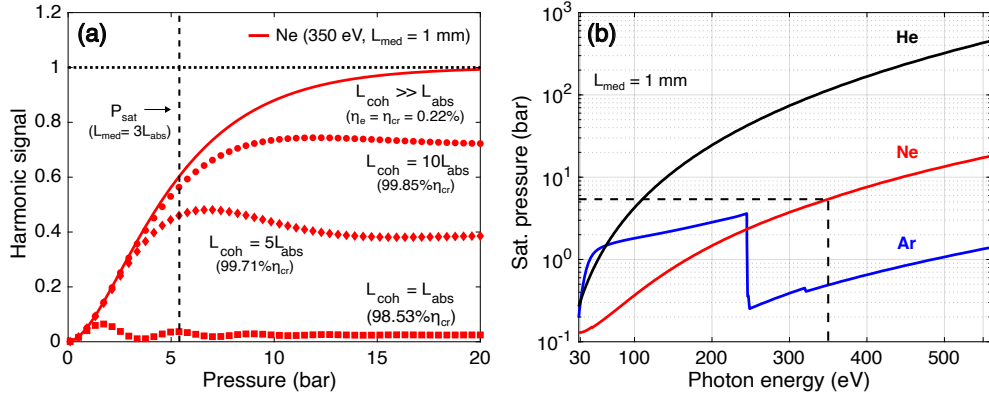


Figure 3.11: Harmonic signal buildup and saturation pressure (a) Enhancement factor (S_q , Eq. 3.29) vs. pressure for Ne under different phase-matching conditions ($L_{\text{coh}} = x \cdot L_{\text{abs}}$ with $x = 1, 10, \infty$). The harmonic energy is 350 eV and the medium length (L_{med}) is 1 mm. The percentage offset with respect to the critical ionization at $1.6 \mu\text{m}$ is shown. Vertical dashed line: saturation pressure ($L_{\text{med}} = 3L_{\text{abs}}$). (b) Saturation pressure vs. photon energy for Ar, Ne, and He. Dashed lines correspond to saturation pressure marked in (a).

become increasingly important, as even small fluctuations can dramatically affect ionization dynamics, leading to phase mismatch.

To quantify how deviations from the ideal ionization fraction affect phase-matching, it is helpful to examine the equation governing the total phase mismatch. From the expression for the critical ionization fraction η_{cr} , the total phase mismatch is given by [31, 191]:

$$\Delta k = P \frac{2\pi}{\lambda_q} \delta \bar{n}_q \left(1 - \frac{\eta_e}{\eta_{\text{cr}}} \right) \quad (3.40)$$

Figure 3.11a illustrates how deviations from critical ionization affect phase-matching as a function of pressure in neon, based on Eq. 3.29. The calculations assume a fixed medium length of 1 mm, a photon energy of 350 eV, and varying coherence-to-absorption length ratios ($L_{\text{coh}}/L_{\text{abs}}$), simulating different ionization fractions. Under perfect phase-matching conditions ($L_{\text{coh}} \gg L_{\text{abs}}, \eta_e = \eta_{\text{cr}}$), the HHG signal increases with pressure until saturation occurs at P_{sat} due to reabsorption. However, even a small deviation of 0.2% in laser intensity can disrupt this balance, resulting in $L_{\text{coh}} = L_{\text{abs}}$ or $\eta_e = 0.985 \cdot \eta_{\text{cr}} = 0.217\%$. As L_{coh} decreases, the HHG signal weakens, and the peak emission shifts to lower pressures. Additionally, this shift introduces pressure-dependent oscillations in the signal, with the oscillation frequency determined by the coherence length.

Building on these insights, Fig. 3.11b highlights the role of *saturation pressure* once phase-matching conditions ($\Delta k = 0$) have been achieved. The saturation pressure (P_{sat}), indicated in Fig. 3.11a, occurs when $L_{\text{med}} = 3L_{\text{abs}}$. This

pressure represents the minimum level required for optimal signal generation [207]. Achieving this balance is crucial: while sufficient atomic density is required to maximize the number of emitters, excessive density leads to reabsorption of the generated harmonics by the medium.

Figure 3.11b shows significant differences in optimal pressure ranges for Ar, Ne, and He across the EUV and soft X-ray regions (assuming a 1-mm medium). For instance, HHG in the EUV region for Ar requires pressures up to 3 bar, while soft X-ray HHG in Ne can require up to 20 bar. HHG in He can demand even higher pressures, reaching as much as 300 bar. Importantly, exceeding P_{sat} only leads to a further increase in the HHG signal when perfect phase-matching is maintained. As pressure increases, the relationship between coherence length and absorption length becomes even more crucial. As discussed earlier (see Fig. 3.11a), reductions in L_{coh} can induce pressure-dependent oscillations in the signal. Therefore, optimizing the pressure beyond P_{sat} requires careful balancing of emitter density and coherence length to achieve maximum output.

3.2.2 Tight-focusing geometry

When the Rayleigh length is comparable to the medium length ($z_R \approx L_{\text{med}}$), all four terms in the phase-matching expression become significant. In this scenario, phase-matching, after rearranging Eq. 3.30, imposes that:

$$P \left[\frac{2\pi \cdot z_R}{\lambda_q} \delta \bar{n}_q \cdot \left(1 - \frac{\eta_e}{\eta_{\text{cr}}} \right) \right] \pm \left(\frac{\Phi_{\text{dip}}^q(z)}{z_R} \cdot \frac{2|z|}{1 + (z/z_R)^2} \right) = q \quad (3.41)$$

The analysis becomes more straightforward in two specific cases: at low pressures ($P \approx 0$) or when the ionization fraction approaches its critical value ($\eta_e \approx \eta_{\text{cr}}$). In these situations, the Gouy phase and dipole phase dominate, leading to the condition where $\Delta k_{\text{dip}} = -\Delta k_G$, which simplifies to:

$$\pm \frac{2|z|}{z_R} \cdot \Phi_{\text{dip}}^q(z) = q \quad (3.42)$$

Since the right-hand side is always positive, this equation shows that phase-matching occurs only when the gas target is placed after the focus ($z > 0$). The precise phase-matching position, z_{PM} , can be found by solving the equation for z . Additionally, as the harmonic order increases, the required distance from the focus also increases to maintain phase-matching.

In terms of trajectories, short trajectories are more likely to be phase-matched due to their smaller dipole phase coefficients compared to long trajectories ($\alpha_l^q > \alpha_s^q$) [52]. This preferential phase-matching of short trajectories is consistent with the findings of Antoine et al. (1996) [206], where macroscopic simulations demonstrated that placing the gas target after the focus selects short trajectories, resulting in a well-defined attosecond pulse train. This theoretical prediction was experimentally confirmed by Paul et al. (2001) [211], who reported the first measurement of APTs, with individual pulses lasting just 250 attoseconds.

For ionization fractions below the critical value ($\eta_{cr} > \eta_e \geq 0$), Eq. 3.41 reveals that phase-matching favors different positions depending on the gas pressure. Higher pressures promote phase-matching before the focus ($z < 0$) where the neutral and plasma dispersion terms can outweigh the negative dipole contribution. Positioning the gas target further upstream from the focus makes possible phase-matching of progressively lower harmonic orders. Alternatively, with lower pressures, phase-matching is possible after the focus ($z > 0$) as long as the pressure remains low enough to maintain the balance in Eq. 3.41. In this regime, placing the gas target further downstream enables phase-matching of increasingly higher harmonic orders.

As pressure increases, the phase-matching position, z_{PM} , shifts from post-focus to pre-focus. At the focus position itself ($z = 0$), the dipole term vanishes, simplifying Eq. 3.41, and allowing to calculate the pressure threshold defining the boundary between pre- and post-focus regimes:

$$P_{PM}|_{z=0} = \frac{\lambda}{z_R 2\pi \delta \bar{n}} \left(1 - \frac{\eta_e}{\eta_{cr}} \right) \quad (3.43)$$

Figure 3.12a illustrates how the phase-matching pressure threshold in Ar, Ne, and He varies with ionization fraction for different wavelengths, assuming a Rayleigh length of $z_R = 2$ mm. In weak ionization conditions ($\eta_e \approx 0$), Eq. 3.43 indicates that the refractive index difference ($\delta \bar{n}_q$) is the primary factor governing phase-matching for the q -th harmonic. For harmonics above 100 eV, as discussed earlier, this refractive index difference flattens, resulting in broadband phase-matching.

Table 3.1 shows the phase-matching pressures for Ar, Ne, and He under low ionization conditions ($\eta_e \approx 0$). For Ar, pressures remain below 1 bar, while Ne and He require a few bars. It's important to note that the experimentally measured backing pressures may differ by up to 50% from the actual pressure at the interaction point. This difference arises from factors such as the medium geometry, wall thickness, the size of holes (e.g., in gas cells), and the external vacuum environment. These variations are well-expected

3. HIGH-ORDER HARMONIC AND ATTOSECOND PULSE GENERATION

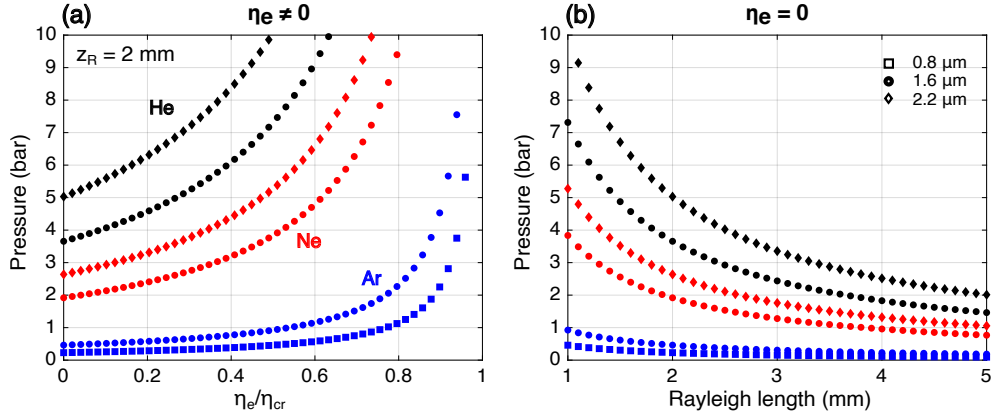


Figure 3.12: Phase-matching pressure dependence on ionization fraction. At-focus phase-matching pressure dependence on ionization fraction at 0.8 μm , 1.6 μm , and 2.2 μm for (a) different gas types and with $z_R = 2$ mm, and (b) with varying Rayleigh length for no ionization ($\eta_e = 0$). The q -th harmonic photon energy was fixed at 550 eV.

and align with the measurements presented in this thesis and other studies [32, 212] for Ne and He.

As evident from Fig. 3.12a, slight deviations from $\eta_e = 0$ (up to $\lesssim 0.4 \cdot \eta_{cr}$) have minimal impact on the phase-matching pressure. However, as the ionization fraction approaches η_{cr} , higher pressures are required to sustain phase-matching, both *at* and *away* from the focus (see Eq. 3.41).

Further inspection of Eq. 3.43 reveals two scaling relationships: First, from the wavelength dependence of the Rayleigh length ($z_R \propto \lambda^{-1}$), the familiar quadratic scaling of pressure with wavelength is recovered ($P \propto \lambda^2$) [52]. Second, the hyperbolic dependence of phase-matching pressure on the Rayleigh length ($P \propto z_R^{-1}$) suggests that tighter focusing geometries (shorter Rayleigh lengths) require higher pressures (see Fig. 3.12b). Longer Rayleigh lengths, by contrast, exhibit a slower Gouy phase gradient, reducing the pressure needed for phase-matching. This lower pressure requirement can be advantageous, as it reduces the load on vacuum pumps. For example, a Rayleigh length of 5 mm enables phase-matching for all gases with less than 3 bar of pressure.

Finally, even with ionization exceeding the critical fraction ($\eta_e > \eta_{cr}$), phase-matching is possible but only after the focus, as the dispersive term becomes negative (see Eq. 3.41). However, the pressure must be moderate enough to ensure that its contribution, when combined with the dipole term, still yields a net positive value.

Table 3.1: Phase-matching pressure with $\eta_e = 0$ and $z_R = 2$ mm. Pressure thresholds calculated using Eq. 3.43 for Ar, Ne and He and at different wavelengths. The q -th harmonic photon energy was fixed at 550 eV.

Wavelength (μm)	P_{PM} (bar)		
	Ar	Ne	He
0.8	0.2	-	-
1.6	0.5	1.9	3.7
2.2	-	2.6	5.0

3.3 Plasma blueshift and defocusing

It is important to note that the previous analysis assumed on-axis phase-matching and an undistorted driving field. While useful as a starting point, these assumptions become less accurate for intense few-cycle pulses, where plasma-induced effects play a significant role [209, 213]

In addition to energy loss due to ionization [214], which attenuates the field more on-axis than off-axis, the refractive index change caused by newly generated electrons distorts the driving waveform. This effect is captured by the plasma refractive index (Eq. 3.32) [96]:

$$\Delta n_p(r, z, t) \approx -\frac{\omega_p^2(r, z, t)}{2\omega^2} \propto -\eta_e(r, z, t), \quad (3.44)$$

where the definitions of plasma frequency (Eq. 3.33) and ionization fraction (Eq. 3.3) have been used. This equation describes *plasma defocusing*, as the stronger negative refractive index in the beam center acts as a negative lens. Additionally, the instantaneous phase-shift due to plasma, $\Delta\phi_p \propto -\eta_e \cdot z$, leads to an instantaneous frequency shift proportional to the ionization rate:

$$\Delta\omega_p(r, z, t) \propto w(|E(r, z, t)|) \cdot z. \quad (3.45)$$

This positive frequency shift results in spectral components shifting towards higher frequencies than the field's central frequency—a phenomenon known as *plasma blueshift*.

Figure 3.13 illustrates the effects of plasma generation on a nearly-single-cycle Gaussian pulse with a Gaussian beam profile as it propagates through a Ne target (see Figs. 3.13a-b)⁷. The on-axis peak intensity at the start of the medium is set to $4.57 \times 10^{14} \text{ Wcm}^{-2}$. As the pulse propagates, interaction with the generated plasma reduces the beam intensity, which in turn affects the ionization fraction along the propagation distance, as shown in Fig. 3.13c.

⁷The propagation code, developed by I. Tyulnev [215], extends the model of Geissler et al. (1999) [216] to include third-order effects like SPM and self-steepening.

3. HIGH-ORDER HARMONIC AND ATTOSECOND PULSE GENERATION

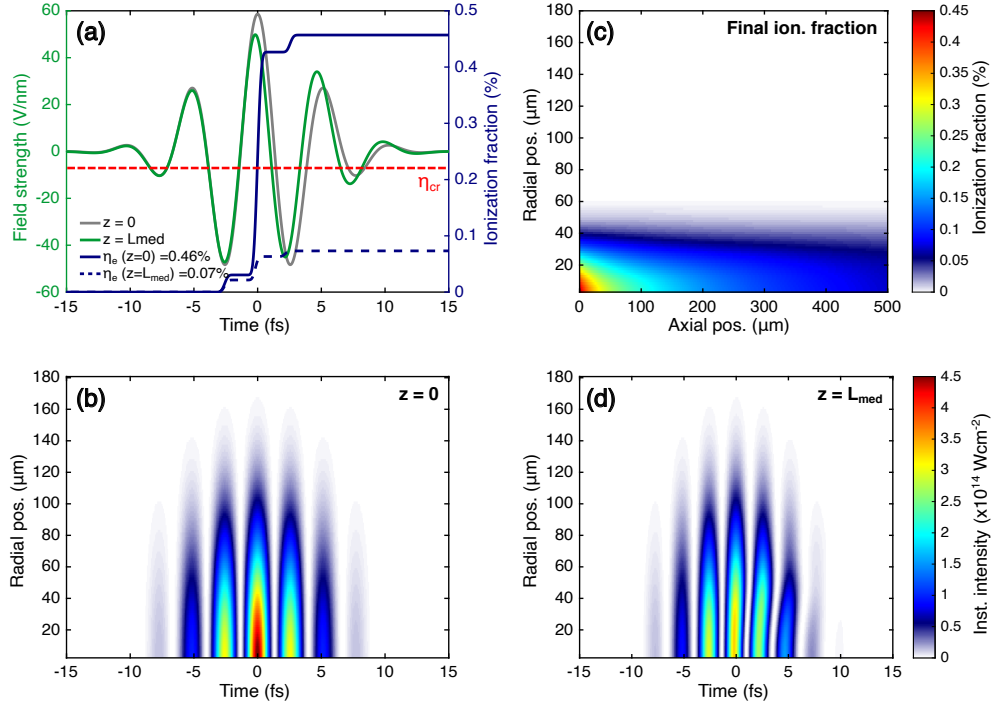


Figure 3.13: Nonlinear propagation in ionizing media. (a) Electric field (left axis) at the input ($z = 0$; $I_0 = 4.57 \times 10^{14} \text{ Wcm}^{-2}$) and output ($z = L_{\text{med}} = 0.5 \text{ mm}$) of a Ne target (6 bar), and ionization fraction evolution (right axis). The critical ionization fraction ($\eta_{\text{cr}} = 0.22\%$) is shown as a red dotted line. The simulation uses a Gaussian pulse (7 fs, 1600 nm) with a Gaussian beam profile ($w_0 = 100 \mu\text{m}$). (b-d) Spatiotemporal intensity distribution at (b) $z = 0$ and (d) $z = L_{\text{med}}$. (c) Final ionization fraction distribution, $\eta_e(r, z, t \rightarrow \infty)$. The ADK model (cycle-averaged) was used to compute ionization rates. The Tong-Lin model predicts an ionization fraction of 0.63%.

Plasma-induced distortions are more prominent at the center of the beam, where the ionization is highest, while off-axis regions maintain a more stable ionization fraction. This distinction is clearly illustrated by comparing the pulse profiles at the input ($z = 0$) and output ($z = L_{\text{med}}$) of the medium, as shown in Figs. 3.13b and 3.13d.

Beyond the reduction in intensity, as mentioned earlier, the interaction with the plasma results in a time-dependent blueshift and a progressively curved wavefront toward the trailing edge of the pulse, which coincides with the rapid increase in ionization (Fig. 3.13d). In this simulation, plasma defocusing is less pronounced due to the relatively low ionization fraction; however, higher ionization fractions would significantly accentuate this effect [209, 217].

From these observations, one can infer the impact of pulse deformation on the phase-matching of HHG and the generation of IAPs. For HHG phase-matching, as seen in the on-axis profile in Fig. 3.13a, near the input ($z = 0$) of the medium, η_{cr} is reached close to the peak of the pulse. Harmonics gen-

erated at this point, with the highest photon energies, can be preferentially phase-matched near the beginning of the medium. As the pulse propagates, the ionization fraction decreases, and, as shown in Fig. 3.13c, around $100\ \mu\text{m}$ into the medium, the ionization fraction at the end of the pulse ($\eta_e(t \rightarrow \infty)$) approaches η_{cr} . This suggests that harmonics generated during the weaker, later cycles of the pulse, with lower photon energies, can be preferentially phase-matched further along the propagation path.

Plasma defocusing also plays a crucial role in IAP generation. By further attenuating the weaker cycles that follow the stronger cycle near the pulse peak, this defocusing effect helps to generate even lower-energy harmonics. These lower-energy harmonics can then be used in combination with amplitude gating (see Sec. 3.5) to produce a broadband IAP.

The plasma-induced phase-matching mechanisms described above are closely connected to transient phase-matching techniques, such as non-adiabatic self-phase-matching (NSPM) and phase-matching in the overdriven regime [212, 213, 217–222]. These techniques exploit rapid changes in the driving waveform to achieve phase-matching over specific regions of the medium.

3.4 Energy cutoff wavelength-scaling

The quest to extend HHG towards higher energies, particularly within the water window (284 - 543 eV), while simultaneously achieving high photon flux has been a central focus for nearly three decades. Two main strategies have been explored: increasing the laser intensity or the driving wavelength.

- **Increasing intensity:** While this approach successfully extends the HHG cutoff, it also has significant drawbacks. It depletes the atomic ground state (reducing the likelihood of electron recombination) and generates excessive plasma (causing phase-mismatch and distorting the driving field). Ultimately, these effects generally limit both the HHG photon flux and beam quality, hindering any practical application.
- **Increasing wavelength:** Allows for significantly higher photon energies with minimal changes in wavelength due to the quadratic scaling and relaxes the intensity requirements. However, a major drawback of this approach is the substantially decreased conversion efficiency, unfavorably scaling as $\sim \lambda^{-(5-6)}$ [41], which arises primarily from the increased quantum diffusion. OP(CP)A platforms (described in Sec. 2.3) and novel mid-infrared laser architectures, with their energy/power scalability, offer the most suitable means for overcoming this issue and have become the mainstream for future soft X-ray HHG sources.

Intensity-scaling

Early demonstrations [223–231] of cutoff extension into the water window range, due to the widespread availability of the already-existing Ti:Sa technology, focused on increasing the intensity of 800 nm pulses, targeting intensities of $\sim 10^{15} - 10^{16}$ W/cm² with helium as the preferred gas due to its high ionization threshold. Strategies included increasing laser energy, tighter focusing, and utilizing shorter pulses (down to a few-cycle duration), with the latter approach offering a substantial advantage. As discussed in Sec. 3.1.2, since plasma density builds up during each half-cycle of the laser field, fewer cycles effectively reduce plasma levels and ground-state depletion at the end of the pulse.

As laser intensities approach and exceed $\approx 10^{16}$ W/cm², neutral atoms become fully depleted, shifting HHG toward generated ions. This allows for significantly higher photon energies, as ions can withstand greater intensities without further ionization. However, freed electrons can travel larger distances at these high intensities before recombination, increasing the likelihood of interactions with neighboring atoms. This challenges the Single Collision Condition (SCC – the assumption of no such interactions), reducing HHG efficiency and producing spatially and temporally incoherent radiation [232]. Even within the intensity range where the SCC remains mostly valid, excess plasma hinders conventional phase-matching, and specialized techniques such as quasi-phase-matching (QPM) [226, 230, 231] or NSPM [218, 233] are needed to optimize the HHG yield.

NSPM arises from the rapid ionization dynamics within a single cycle of the intense laser pulse, in contrast to the adiabatic case where the system responds smoothly to slow electric field changes. As the medium experiences the peak of the pulse, rapid plasma buildup leads to both an intensity decrease and a steep change in the refractive index. The latter results in a time-dependent blue-shift that increases towards the end of the pulse. Such dynamic blue-shift, along with the intensity reduction, directly modifies the electron trajectories and consequently influences the phase of the emitted harmonics [234–236]. This, even under high plasma levels, can allow transient (e.g., within a half-cycle) phase-matching at specific locations and over short distances within the medium [213, 218, 233], at a scale well below the Rayleigh length.

An alternative approach to address the plasma-induced phase mismatch is QPM. In QPM, periodic modifications to the harmonic generation medium are used to counteract the phase mismatch that limits the high-energy harmonic buildup. Experiments have demonstrated QPM in the water window spectral range, primarily by modulating the intensity and phase of the driving field along the propagation axis. This can be achieved through waveguide diameter changes [226], with successive gas targets exploiting

the diffraction of the focused driving field [231], or by exciting multiple waveguide modes [230] whose interference creates an on-axis modulation. Unlike traditional QPM in perturbative nonlinear optics, where the material's crystalline structure is altered, HHG schemes focus on manipulating the driving field itself, thereby exploiting the dependence of HHG on the field's waveform.

While NSPM and QPM both offer strategies to overcome phase-matching limitations, their implementation for high-energy, high-flux IAP sources presents challenges. NSPM relies on strong plasma-induced reshaping of the driving field, reducing controllability and affecting HHG efficiency. QPM, particularly waveguide-based schemes, faces material damage thresholds, and fixed modulation periods limit flexibility for phase-matching broadband IAPs driven by infrared sources. These limitations have led to a shift in research towards using longer wavelengths and neutral media to achieve phase-matching.

Wavelength-scaling

The dramatic increase in HHG energy cutoff (from 64 to 160 eV) observed when shifting the driving-field wavelength in neutral argon atoms from 800 nm to 1.5 μm [237] inspired investigations into extending this principle to neon and helium for generating harmonics within and beyond the water window spectral range [191]. Experiments utilizing near- and mid-IR drivers (centered between 1-4 μm wavelengths) in both free-focusing [24, 40, 194, 238–245] and waveguide [31, 46, 195, 246–248] geometries successfully implemented this scheme, after optimization of the macroscopic conditions (i.e., medium dimensions, geometry, and density). This wavelength-scaling holds promise, as evidenced by the observation of harmonics up to 1.6 keV [46] and the development of nJ-class water window HHG systems [40]. Importantly, it demonstrates adaptability across a range of laser sources (high-energy [40], high-repetition-rate [194, 240], with few-cycle [29, 30, 249] down to sub-cycle pulse durations [250]).

The success and adaptability of this wavelength-scaling approach, stems from key advantages: Firstly, it exploits the quadratic scaling nature of HHG energy cutoff, enabling the use of lower intensities ($\approx 10^{14}$ W/cm²), thus reducing the degree of ionization in the medium and facilitating phase-matching. Secondly, this approach is energy/power scalable, meaning optimal focusing conditions (or waveguide dimensions) can be adapted for higher energy/power lasers while maintaining low plasma levels.

Despite its advantages, this approach also naturally faces certain limitations and challenges. The low efficiency of the single-atom response necessitates higher pressures to both maximize the number of emitters and achieve optimal phase-matching. This presents challenges in developing complex

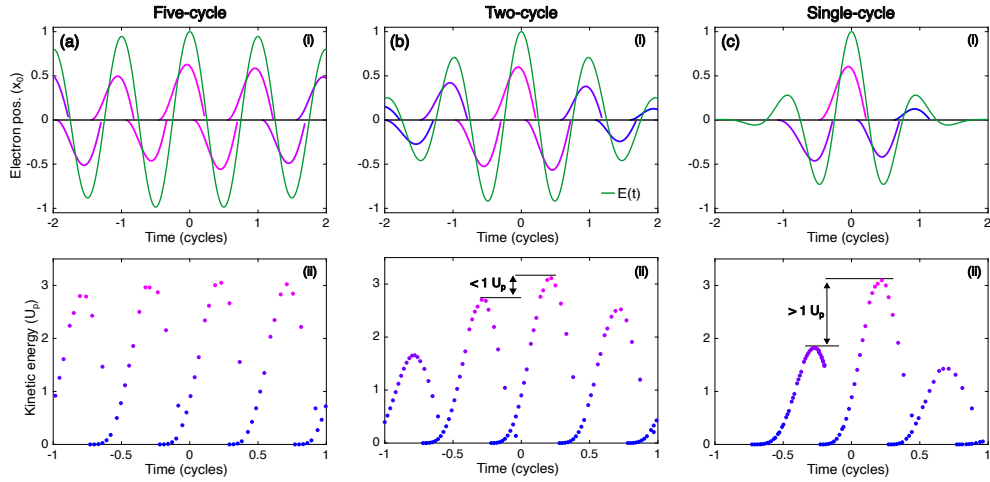


Figure 3.14: Principle of amplitude gating. Recombining electron cutoff trajectories (i) and (ii) their kinetic energy vs. recombination time for (a) a 5-cycle, (b) a 2-cycle, and (c) a single-cycle 800-nm laser pulse. Cutoff trajectories are normalized to the maximum excursion displacement (x_0 , Eq. 3.7), with the driving electric field shown for reference (green line). Trajectories are color-coded by their recombining energy.

medium architectures capable of handling multi-atmospheric pressures, as well as the need for powerful pumping systems to mitigate reabsorption of harmonics. Moreover, developing high-energy/average power mid-IR sources, essential for high-flux water window HHG, remains a complex research and engineering task. The added requirements of near-single-cycle durations and CEP stability for IAP generation increase the complexity of this development further.

3.5 Isolated attosecond pulse (IAP) generation

Pump-probe, time-resolved spectroscopies investigating electronic dynamics require isolated attosecond pulses (IAPs). However, HHG naturally produces APTs, with bursts emitted every half-cycle of the driving laser. To address this, techniques have been developed to isolate single attosecond pulses. These techniques either restrict the HHG process to a single recollision or extract a single pulse from the train. For a comprehensive analysis of these methods, the reader is referred to Refs. [2, 11, 251–254]. Techniques that have been applied both in the EUV and water window ranges are:

- **Amplitude gating:** Initially utilized with few-cycle pulses [12], the amplitude gating (AG) technique progressively improves as pulses approach the sub-cycle regime [50, 255, 256] (ideally a half-cycle duration [117]). Figure 3.14 shows the principle of amplitude gating. As pulse duration decreases, amplitude differences between neighboring electric field half-cycles become more pronounced, and are directly

mapped onto distinct cutoff energies for each attosecond burst. The most intense half-cycle generates the highest cutoff. Strategic spectral filtering between the highest cutoff and its nearest neighbor isolates the corresponding attosecond burst (shown in Fig. 3.14 as the most energetic cutoff trajectory). Lower-energy components, resulting from interference between multiple bursts, are blocked, ensuring an IAP.

As shown by Fig. 3.14, for a five-cycle pulse, the minimal half-cycle cutoff differences make filtering impractical. With a two-cycle pulse, filtering becomes viable near the cutoff of the most intense burst, as experimentally demonstrated by Hentschel M., et al. (2001) [12]. A single-cycle pulse provides an even wider filtering window, extending into the plateau of the brightest burst (as shown by Goulielmakis E., et al., 2008 [50]). As later chapters will reveal, sub-cycle pulses enable filtering a significant portion of the HHG plateau up to the cutoff, facilitating the generation of broadband isolated attosecond pulses [256]. Importantly, sufficiently short pulses naturally confine ionization to the most prominent half-cycle, suppressing it in the neighboring cycles. This means the pulse itself effectively acts as a temporal gate, with its width directly proportional to the laser period. Moreover, as shorter pulses concentrate more energy into the central half-cycle, the IAP generation can become more efficient, as less energy is spent onto the weaker neighboring pulses.

The AG technique has been successfully applied not only in the EUV range, but also to generate broadband isolated attosecond pulses in the early soft X-ray [162] and even the water window range [29, 30, 32, 143, 212], with transient phase-matching dynamics also contributing to the isolation process.

- **Polarization gating:** This technique functions as a temporal gate, exploiting electron trajectories trajectory under varying polarization to isolate a single attosecond burst [257]. A driving field combining linear and elliptical polarization suppresses HHG during the elliptically polarized half-cycles. During linear polarization, the electron can recombine with its parent ion, enabling HHG. In contrast, elliptical polarization displaces trajectories, preventing them from recombining. By positioning the linearly polarized gate within the most intense, central cycle, while placing the elliptical polarization section on the leading and trailing edges, ensures the generation of a single burst. Polarization gating (PG) has been applied in the EUV spectral range [258, 259] and even in the water window range [249, 260]. Techniques that extend the principles of (PG) have been developed and applied mostly in the EUV regime. Some of these are Double Optical Gating (DOG) [261–264] generalized DOG [265, 266] (both which were applied also in the

soft X-ray regime [267, 268]), interferometric PG [269] and Polarization-Assisted Amplitude Gating (PASSAGE) [270].

The main advantage of PG (and most of its variations) is the flexibility in driving pulse duration requirements [266] and its ability to generate ultrabroadband - spanning a large portion of the plateau up to the cutoff energy- isolated attosecond pulses. Amplitude gating, in contrast, requires sub-cycle durations to achieve similar spectral bandwidths. However, PG potentially faces challenges in both conversion efficiency and scalability to higher intensities. While further experimentation is needed for a definitive assessment, longer pulses can lead to higher ionization fractions at high intensities. Techniques like DOG partially mitigate this, but excessive plasma generation (affecting phase-matching) and/or ground state depletion could still limit efficiency. Additionally, the energy distribution across the elliptically polarized portions reduces the energy dedicated to the isolated pulse, potentially lowering conversion efficiency compared to a sub-cycle pulse where most of the energy is concentrated within the main cycle.

- **Spatiotemporal gating:** By imposing a wavefront rotation on the driving field, this technique angularly separates attosecond pulses generated during different half-cycles [145, 220]. The rotation causes each burst to be emitted perpendicular to the instantaneous wavefront of the driving laser at its generation, resulting in distinct propagation directions. An IAP is obtained after spatial filtering in the far field. Unlike previous techniques focusing on temporal manipulation of the driving waveform, this gating approach exploits spatiotemporal couplings.

Similar to polarization gating, this technique offers flexibility in driving field pulse duration and can generate broadband isolated attosecond pulses without requiring sub-cycle durations. However, sensitivity to fluctuations in the driving laser's CEP is a disadvantage. CEP shifts alter the birth location of the attosecond pulse within the rotating wavefront, directly changing its propagation direction. This leads to CEP-driven pointing fluctuations, potentially limiting the experimental applicability of this technique.

3.5.1 Half-cycle cutoffs

IAP generation is highly sensitive to the CEP, which directly affects the emission timing, cutoff energy, and amplitude of attosecond bursts [271]. This sensitivity results in a π -periodic modulation of the cutoff energy and yield of each attosecond burst emitted within each half-cycle of the laser field as the CEP varies. A CEP scan, where a series of HHG spectra is recorded as a function of CEP, reveals these modulations, commonly referred to as *half-*

3.5. Isolated attosecond pulse (IAP) generation

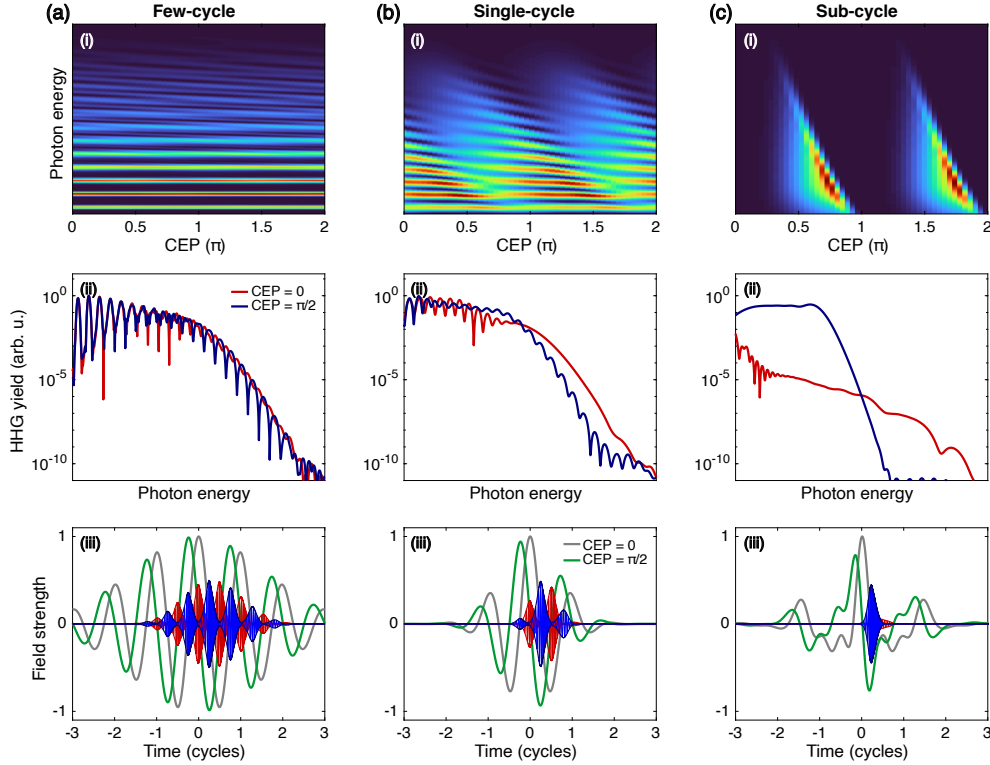


Figure 3.15: Illustration of half-cycle cutoffs. (i) CEP-dependent HHG spectra driven by different by a (a) few-cycle, (b) single-cycle, and (c) sub-cycle pulse. For each pulse duration: (ii) HHG spectrum for $\text{CEP} = 0$ and $\pi/2$. (iii) Corresponding instantaneous emission (blue and red lines), and driving electric fields (green and red lines). Short trajectories have been selected only.

cycle cutoffs. These cutoffs can serve as a signature of IAP generation (see Fig. 3.15).

With few-cycle pulses (Fig. 3.15a), the absence of significant CEP influence on half-cycle amplitudes results in spectral fringes across the entire HHG spectrum, irrespective of the CEP value. This leads to a relatively constant amplitude of attosecond bursts in the time domain as the CEP varies. The spectral fringes spanning the entire spectrum arise because, as illustrated in Figure 3.14a, the attosecond bursts emitted within each half-cycle share a similar cutoff (or bandwidth), thus generating spectral interference.

For single-cycle pulses (Fig. 3.15b), specific CEP values can cause one half-cycle cutoff to dominate, producing a fringe-less continuum at the highest energies, which can be filtered to extract an IAP. In the low-energy region of the spectrum, as shown in Figure 3.14c, spectral fringes arise due to the presence of satellite pulses that spectrally overlap in that regime. Other CEP values can enhance the intensity of these satellite pulses, causing them to cover the same spectral bandwidth as the main emitted burst, resulting in

fringes across the entire spectrum.

Finally, in the sub-cycle regime (Fig. 3.15c), a broad, continuous, fringeless spectrum emerges due to spectral fringes shifting to lower energies and being potentially blocked by a metallic filter. The time domain reveals the emission of a high-contrast IAP. In comparison to longer pulses, at other CEP values, emission in the sub-cycle regime can be almost entirely suppressed. Thus, in this example, such a strong CEP-dependent modulation is related to a high-contrast IAP.

The observation of such a well-defined pattern generally suggests IAP generation, however, techniques like attosecond streaking are required to provide a more direct confirmation. Such strong π -periodic modulation of half-cycle cutoffs have been extensively observed in the EUV [140, 256, 270], and soft X-ray ranges [29, 32, 162, 250, 267], and attosecond streaking experiments have repeatedly demonstrated the involvement of IAP generation.

3.6 Attosecond streaking

Since its early experimental implementations [12, 272], attosecond streaking [139] has been the standard technique for characterizing IAPs. In contrast, the Reconstruction of Attosecond Harmonic Beating by Interference of Two-photon Transitions (RABBIT) [273] is the established method for characterizing APTs. As this thesis focuses on IAPs, RABBIT-related measurements are not discussed further.

Attosecond streaking functions as a cross-correlation measurement in a noble gas, between the IAP and a synchronized streaking field (the same generating the IAP), both featuring parallel polarization. The IAP liberates photoelectrons, and the streaking field modulates their kinetic energy. The streaking field must be strong enough to modulate the photoelectron's kinetic energy (ideally shifting it by at least its own spectral bandwidth) but weak enough to avoid further ionization. By aligning the fields' polarization with the detector and analyzing the photoelectron kinetic energy as a function of the IAP-streaking field delay, both the IAP and the streaking field itself can be characterized.

3.6.1 Electron time-of-flight (eTOF) spectrometer

Attosecond streaking relies on the measurement of photoelectron spectra. This is often achieved with an electron Time-Of-Flight (eTOF) spectrometer. The eTOF operates on the principle that the time (τ_{TOF}) it takes for a photoelectron, from its generation point to reach a detector positioned at a known distance (L_d) within the spectrometer, is inversely proportional to

the electron's initial velocity. This relationship enables the determination of the photoelectron's kinetic energy as:

$$E_k = \frac{1}{2}m_e \left(\frac{L_d}{\tau_{\text{TOF}}} \right)^2 \quad (3.46)$$

One of the common types of eTOF spectrometers, as the one used in this thesis, consists of an electrostatic lens, a drift tube, a post-acceleration stage, and the detector [274]. The entire assembly is typically enclosed within a μ -metal shield to minimize the influence of Earth's magnetic field. The electrostatic lens serves to increase the collection angle of photoelectrons or to decelerate them, thereby enhancing the energy resolution [52]. In the drift tube, electrons propagate in either a field-free region or under a controlled electric field to mitigate the effects of any residual magnetic fields. The post-acceleration stage accelerates the electrons to ensure they meet the detection threshold of the detector, typically a Microchannel Plate (MCP) stack in Chevron configuration coupled to an anode. When electrons strike the MCPs, they trigger an avalanche of secondary electrons, resulting in signal amplification. This amplified electron signal induces a current in the anode, which is subsequently detected and processed by the electronics. This detected signal serves as the stop signal, while the start signal can be derived from a synchronized electrical signal generated by the optical laser. The time difference between these two signals corresponds to the time-of-flight τ_{TOF} in Eq. 3.46.

3.6.2 Direct measurement of optical waveforms

The mechanism by which attosecond streaking measures the optical streaking field can be understood through a classical approach. An IAP with energy $h\nu$ liberates a photoelectron at a delay τ with respect to the streaking field (characterized by its vector potential $A(t)$). The photoelectron has initial momentum $p_0 = \sqrt{2m_e E_k^0}$ and kinetic energy $E_k^0 = h\nu - I_p$. Since, $h\nu \gg I_p$, the photoelectron rapidly escapes into the continuum and its subsequent motion is dictated by the streaking field (i.e., the SFA remains valid). Integrating Newton's equations (Eq. 3.4) from the release time ($t = \tau$) until the field ends ($t \rightarrow \infty$), and noting that $A(t \rightarrow \infty) = 0$ (due to the absence of DC components), yields the final (streaked) momentum p_k :

$$p_k(\tau) \equiv p(t \rightarrow \infty) = p_0 - eA(\tau) \quad (3.47)$$

Consequently, the final kinetic energy $E_k = p_k^2/2m_e$ can be expressed as:

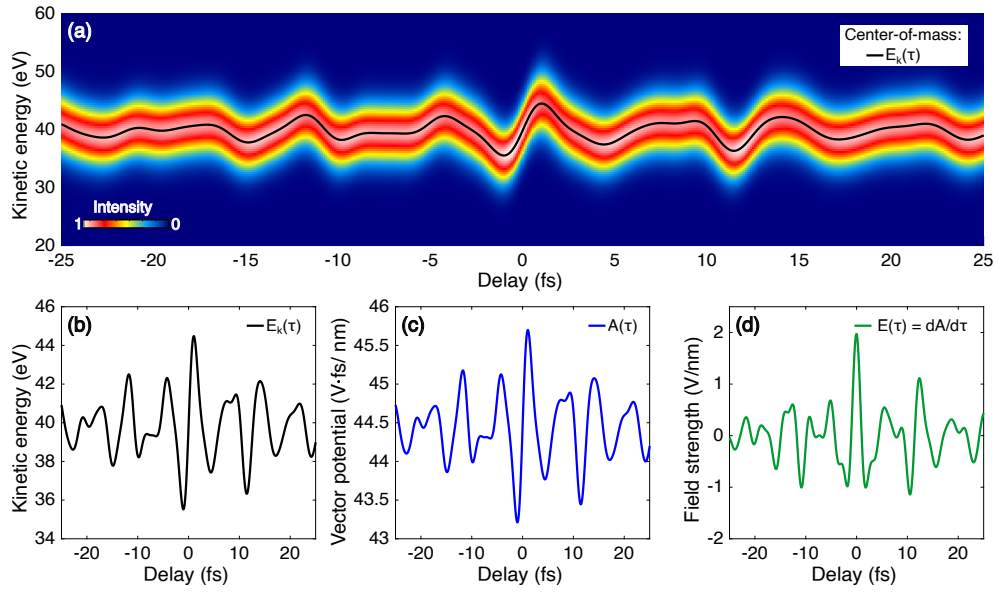


Figure 3.16: Direct electric field measurement. (a) Simulated photoelectron spectrogram in Ne ($I_p = 21.7$ eV). The simulation employs an experimentally measured streaking field. (b) Central kinetic energy (corresponding to center-of-mass trace indicated in (a) as a black line). (c) Vector potential computed via Eq. 3.48, and (d) corresponding electric field.

$$E_k(\tau) = E_k^0 - ev_0 \cdot A(\tau) + \frac{e^2}{2m_e} A^2(\tau), \quad (3.48)$$

where $v_0 = p_0/m_e$ is initial velocity. Equations 3.47-3.48 demonstrate how the streaking field accelerates and decelerates the photoelectron, influencing its momentum and kinetic energy. Importantly, the quadratic dependence of Eq. 3.48 on the vector potential $A(\tau)$ allows its determination by measuring E_k at each delay τ (in practice, extracted from the photoelectron spectrum's Center-Of-Mass (COM)). A simple derivative with respect to the delay axis then yields the corresponding streaking electric field, i.e.,

$$E(\tau) = -\frac{dA}{d\tau}(\tau). \quad (3.49)$$

Note that this technique provides full characterization of the light wave as it retrieves the electric field with its absolute magnitude. This establishes it as one of the most accurate electric field measurement techniques to date. Figure 3.16 illustrates the procedure to retrieve the electric field according to Eqs. 3.48-3.49.

Naturally, this direct retrieval approach has limitations. It assumes a monochromatic and instantaneous ionization process, neglecting the temporal extent

and spectral bandwidth of the IAP. These assumptions stem from the classical treatment, which ignores the wavepacket nature of the released photoelectron. If the IAP has a complex temporal structure or significant bandwidth, the initial velocity distribution becomes important, and this treatment loses validity. To account for these effects, a semiquantum mechanical approach is needed [139, 275].

3.6.3 Attosecond pulse reconstruction

As discussed in Sec. 3.5.1, the observation of π -periodic half-cycle cutoffs in the HHG spectrum (see Sec. 3.5.1) suggests the presence of IAPs. However, definitive confirmation and characterization of these pulses require a well-defined attosecond streaking trace, characterized by smooth and continuous photoelectron spectra at each delay. The presence of spectrally overlapping satellite pulses alongside the primary attosecond burst would result in the appearance of fringes in the photoelectron spectra, progressively transitioning the measurement into a RABBIT-like trace with increasing number of pulses [2].

To accurately reconstruct the streaking trace and reveal the temporal profile of the emitted HHG burst, a semiquantum model of the cross-correlation measurement is employed. This model involves determining the photoelectron wavepacket's evolution under the combined electric field $E_{\text{tot}}(t, \tau) = E(t) + E_h(t - \tau)$ of the delayed HHG burst, $E_h(t - \tau)$, and streaking field, $E(t)$. Under the SFA, the total wavefunction can be expressed as in the Lewenstein model (see Sec. 3.1.4), where the continuum states of the photoelectron wavepacket are weighted by complex coefficients $b(v, t, \tau)$. These coefficients now capture the wavepacket's time evolution under the combined field at a specific delay τ .

Unlike in HHG, the attosecond burst is the one promoting the electron from its highest-occupied electronic orbital to the continuum via a single-photon transition. Once released, the electron is only accelerated by the streaking field. With these considerations, the photoelectron wavepacket's complex amplitude after both pulses have ended ($t \rightarrow \infty$) is (in atomic units) [52]:

$$b(v, \tau) = i \int_{-\infty}^{\infty} dt E_h(t - \tau) \cdot d(v + A(t)) \times \exp \left\{ -i \left[\left(I_p + \frac{v^2}{2} \right) t + \int_t^{\infty} dt' \left(v A(t') + \frac{A^2(t')}{2} \right) \right] \right\} \quad (3.50)$$

Thus, the probability of measuring the photoelectron with velocity v and delay τ is given by:

$$S(v, \tau) \equiv |b(v, \tau)|^2 \quad (3.51)$$

Equation 3.50 incorporates the full temporal structure of both the attosecond burst and streaking fields, as no assumptions have been made regarding their specific waveforms. Moreover, it shows that the photoelectron wavepacket inherits the HHG field's temporal structure (E_h), reshaped by the ground-to-continuum, complex-valued transition matrix element $d(v)$, which accounts for the atom's spectral response. The exponential phase term closely resembles Eq. 3.48 derived from the classical approach, however, the vector potential acts now on all the velocities (v) within the wavepacket. This explicitly reveals the streaking field's role as a phase modulator.

For narrowband IAPs, where the ejected photoelectron satisfies $v_0 \gg \Delta v$, the central momentum approximation (CMA) applies. This simplifies Eq. 3.51 to a FROG-like form [276]. Using an iterative algorithm [277, 278] both the IAP and streaking field pulses can be reconstructed.

The broadband IAPs generated in the experiments presented in this thesis violate the CMA. Furthermore, the employed sub-cycle streaking fields possess arbitrarily complex waveforms, precluding any simplifications [279, 280] that could compromise reconstruction accuracy. Therefore, these experimental conditions require a reconstruction algorithm that makes use of the full photoelectron wavepacket expression given by Eq. 3.50.

3.6.4 Volkov transform generalized projection algorithm

This thesis employs the Volkov transform generalized projection algorithm (VTGPA) developed by Keathley, P.D. et al. (2016) [281]. VTGPA's flexibility allows the reconstruction of both broadband IAPs (without relying on the CMA) and streaking fields with arbitrary shapes.

Briefly, VTGPA initializes guesses for the attosecond burst and streaking field, then numerically integrates to compute the spectrogram $S(v, \tau)$ (Eq. 3.51). The reconstruction employs complex-valued dipole transition matrix elements for Kr, Ar, and Ne, calculated using the method described in [282]. Similar to other FROG techniques, VTGPA includes a projection step. However, it minimizes the difference between the computed and (projected) experimental spectrograms directly in the time-velocity domain, eliminating the need for Fourier transforms. The attosecond pulse is modeled as:

$$E_h(t) = \varepsilon_h(t)e^{i\phi_h(t)}, \quad (3.52)$$

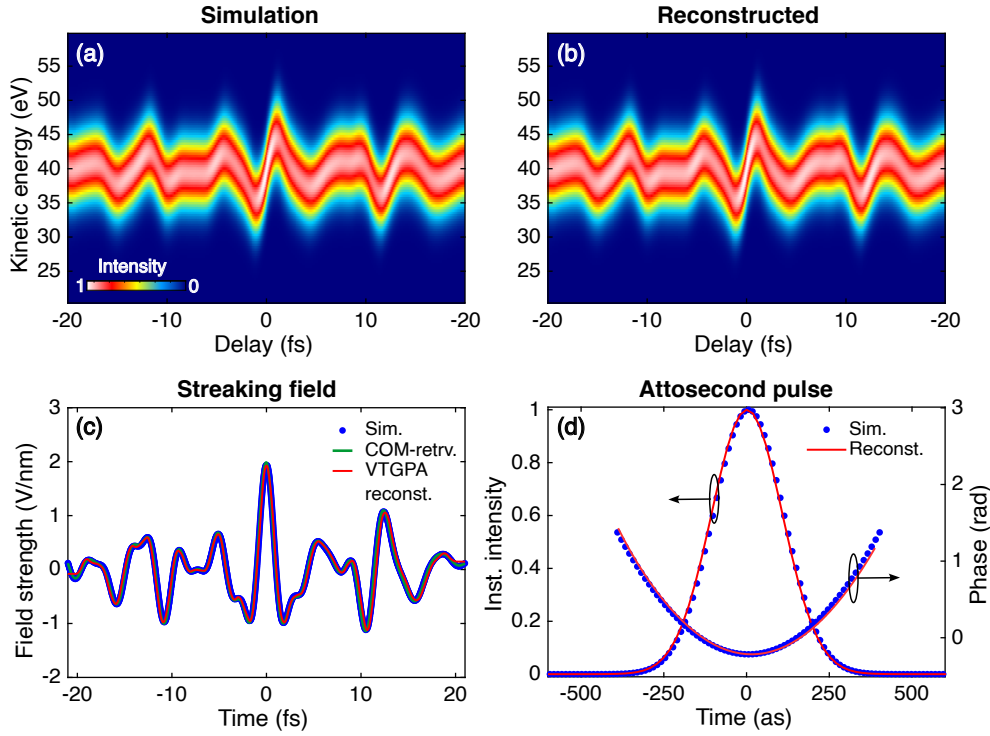


Figure 3.17: Attosecond streaking reconstruction with VTGPA. (a) Simulated photoelectron spectrogram (as in Fig. 3.16). The IAP is modeled as a chirped Gaussian pulse centered at 60 eV. (b) Reconstructed spectrogram after 300 iterations ($N=60$ cubic-spline interpolation points). (c) Comparison of simulated (blue dots), center-of-mass (COM)-retrieved (green, with Eq. 3.48), and reconstructed (red) electric fields. (d) Simulated (blue dots) and reconstructed (red) IAP envelope intensity profile (left axis) and phase (right axis). Adapted from [256].

where ε_h is an envelope function and ϕ_h an instantaneous phase. The streaking field's vector potential is expressed as the product of a cubic-spline interpolated envelope function \tilde{A}_N (with N anchor points) and a carrier wave defined by a polynomial expansion:

$$A(t) = \tilde{A}_N(t) \cos(\alpha_0 + \alpha_1 t + \alpha_2 t^2 + \dots + \alpha_k t^k), \quad (3.53)$$

The attosecond burst's initial guess is an IAP with a Gaussian envelope (central energy inferred from the spectrogram), while the streaking field's initial guess is user-defined based on pulse duration and central wavelength. For the complex waveforms used in this thesis, up to $N = 60$ points were necessary for the envelope function and $k = 3$ coefficients for the carrier wave (see Fig. 3.17).

VTGPA's efficacy in reconstructing broadband IAPs has been demonstrated in recent studies [162, 256, 283]. Furthermore, its versatility has been ex-

3. HIGH-ORDER HARMONIC AND ATTOSECOND PULSE GENERATION

tended to consider multiple atomic energy levels [162], spatial averaging upon detection [284], and computational efficiency [285].

Sub-cycle optical field synthesis

This chapter details the technology used in this thesis to generate custom-tailored sub-cycle waveforms with the Parametric Waveform Synthesizer (PWS). Attosecond streaking measurements confirm successful waveform synthesis and demonstrate the synthesizer's short- and long-term stability – necessary for attosecond science applications. The content presented herein draws heavily on Refs. [110, 126].

4.1 Coherent waveform synthesis

The primary approach for generating custom-tailored sub-cycle optical pulses relies on coherent waveform synthesis [70]. This technique involves the controlled interference of multiple constituent pulses. The synthesized waveform results from the coherent superposition of N individual electric fields, $E_i(t)$, expressed as:

$$E(t) = E_1(t) + E_2(t) + \dots + E_N(t), \quad (4.1)$$

and each constituent field $E_i(t)$ can be written as

$$E_i(t) = \varepsilon_i(t - \tau_{1i}) \cos(\omega_i(t - \tau_{1i}) + \varphi_i) \quad (4.2)$$

Following a similar definition to that introduced in Sec. 2.1, the field envelope function is represented as $\varepsilon_i(t) = E_0^i \hat{\varepsilon}_i(t)$, where E_0^i is the field amplitude and $\hat{\varepsilon}_i(t)$ is the normalized envelope shape. The constituent field is further defined by its central angular frequency (ω_i), a phase offset (φ_i), and a time offset relative to the reference field $E_1(t)$ (whose envelope centers at $t = 0$, implying $\tau_{11} = 0$). Note that φ_i denotes the CEP of the i -th field.

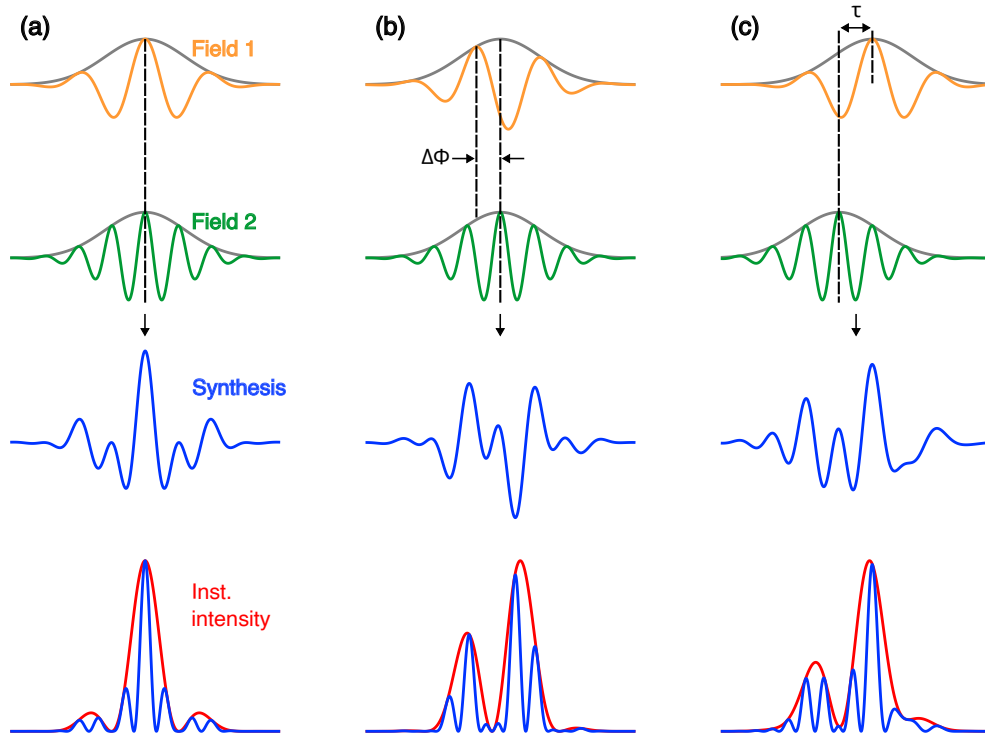


Figure 4.1: Coherent waveform synthesis. (a) Two constituent fields (orange: Field 1, green: Field 2) with coincident envelopes and carrier waves. (b) The same fields with a phase offset ($\Delta\phi$) by introducing a CEP shift in Field 1 (φ_1 in Eq. 4.2). (c) The same fields with a relative delay (τ) but no phase offset. The fourth row depicts the resulting instantaneous intensity (blue) and corresponding intensity envelope (red) for each scenario.

For fixed constituent waveform shapes and carrier frequencies ω_i , arbitrary synthesized waveforms can be tailored through adjustments to the amplitude of each constituent pulse, their relative delays, and their CEPs. The duration of the constituent fields determines the temporal window within which the synthesized waveform's properties can be manipulated. Thus, in order to achieve control on a few-femtosecond timescale with constituent pulses in the optical range, these pulses must themselves span only a few oscillation cycles.

Figure 4.1 illustrates the principle of waveform synthesis using two single-cycle pulses of equal amplitude, one oscillating at twice the frequency of the other. When these pulses perfectly overlap in time (Fig. 4.1a), the synthesized waveform exhibits its shortest possible duration. Small changes in either the phase offset ($\Delta\phi$) or relative delay (τ) between these pulses (Fig. 4.1b-c) significantly alter the waveform's shape. Furthermore, upon defining the constituent pulse intensity as $I_i(t) = |E_i(t)|^2$, the instantaneous intensity of the resulting synthesized waveform follows:

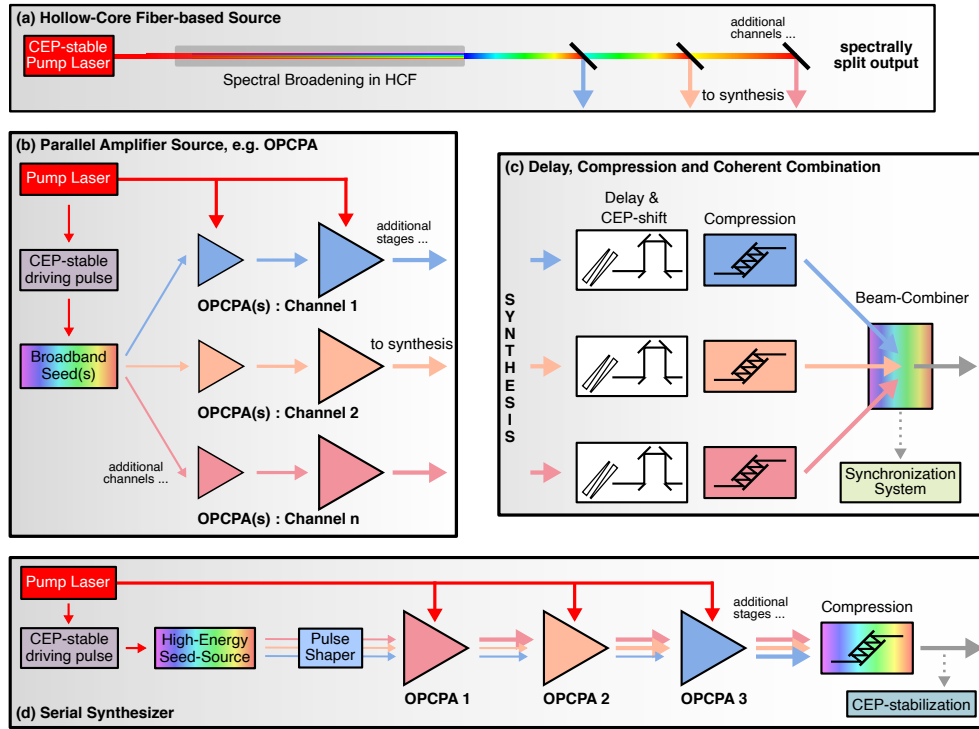


Figure 4.2: Waveform synthesizer schemes. (a) HCF-based: Broadband HCF output split into channels, each adjustable in CEP, delay, and phase before recombination. (b) Parallel PWS: Broadband seed split, amplified in parallel channels with dedicated amplifiers. (c) Both HCF and parallel PWS allow per-channel manipulation (delay, CEP) and chirped mirror compression. Dichroic recombination yields the final pulse, requiring precise synchronization. (d) Serial PWS: Shaped broadband seed sequentially amplified in spectral regions along a common path, necessitating full-bandwidth compression optics. Adapted from [116].

$$I(t) = I_1(t) + I_2(t) + 2|E_1(t)||E_2(t)|, \quad (4.3)$$

This equality demonstrates the potential for strong modulation of the resulting instantaneous intensity through control of relative phase and relative delay between the constituent fields (see last row in Fig. 4.1). Moreover, the intensity can exceed the simple sum of individual field intensities, creating temporary, abrupt enhancements. This phenomena have a strong impact on HHG, as detailed in Ch. 5.

4.1.1 Waveform synthesizers

Three main approaches have been developed for coherent waveform synthesis, as illustrated in Fig. 4.2. Table 4.1 summarizes recent synthesizer setups (reported after 2016) that employ these schemes. The table details the

Table 4.1: Overview of waveform synthesizer setups (from 2016 onwards). Adapted from [116].

Ref.	Laser system	Synth. scheme	Average energy (μJ)	Central wavelength (μm)	Pulse duration (fs)	No. of cycles
[117]	Ti:Sa, 10 kHz	HWS	320 [4 \oplus 15 \oplus 45 \oplus 255]	0.5 [0.3 \oplus 0.4 \oplus 0.6 \oplus 0.8]	0.98 [6.5 \oplus 6.5 \oplus 7 \oplus 8.5]	0.5
[286]	Yb:YAG, 1 kHz	Parallel	40 [24 \oplus 16]	\sim 1.0 [0.8 \oplus 2.0]	\sim 10.5 [12 \oplus 31]	\sim 3.2
[287]	Yb:YAG, 1 kHz	Parallel [S \oplus I]	33 [21 \oplus 12]	4.2 [3.5 \oplus 6.7]	12.4 [20 \oplus 31]	0.88
[288]	Nd:YAG, 10 Hz	Serial	101×10^3	0.8 [0.5 - 1.0]	4.4	< 2
[289]	Ti:Sa, 0.2 kHz	Parallel + Serial	32	1.8 [1.0 - 2.4]	4.3	0.73
[290]	Yb:YAG, 5 kHz	Parallel	25 [20 \oplus 5]	\sim 1.2* [1.1 \oplus 2.1]	\sim 4* [6 \oplus 18]	\sim 1*
[110]	Ti:Sa, 1 kHz	Parallel	500 [600 \oplus 150]	1.4 [0.8 \oplus 1.6]	2.8 [6 \oplus 8]	0.6
[291, 292]	Ti:Sa, 10 Hz	Parallel [P \oplus S \oplus I]	50×10^3 [44 $\times 10^3 \oplus 6 \times 10^3 \oplus 3 \times 10^3$]	\sim 0.9* [0.8 \oplus 1.4 \oplus 2.1]	\sim 28* [30 \oplus 44 \oplus 88]	\sim 9*
[157]	Yb:YAG, 3 kHz	HWS	5	1.7 [1.0 \oplus 2.0]	3.8 [4.8 \oplus 10.8]	0.66

HWS: HCF-based waveform synthesizer, S \oplus I = signal \oplus idler, P \oplus S \oplus I = pump \oplus signal \oplus idler.
Values in '[...]' represent constituent pulse parameters. * Estimation based on reported values.

laser systems used, constituent pulse characteristics (energy, central wavelength, duration), and the duration of the final synthesized waveform. These schemes can be classified as follows:

- **HCF-based scheme:** This design utilizes a parallel architecture to spectrally divide the ultrabroadband output from a CEP-stable pump-driven HCF. Independent dispersion management, compression to few-cycle durations, CEP control, and timing adjustment are applied to each band before recombination. This enables highly customized waveform synthesis [115]. Notably, this scheme offers the sufficient flexibility that allows integration of up to four spectral channels while maintaining a relatively small footprint [293]. This compact design promotes setup stability, as demonstrated in the synthesizer's successful use in attosecond-resolved experiments [154, 255, 294].

Building upon the scheme pioneered in the visible range by Wirth et al. (2011) and Hassan et al. (2012) [115, 255] employing a kHz Ti:Sa pump, an upgrade of the system [117] demonstrated the synthesis of a 320- μ J half-cycle pulses lasting only 980 as. This is the only system capable of producing an IAP in the visible range to date. More recently, Ridente et al. (2022) [157] extended this approach to the infrared range using a kHz Yb:YAG laser system, demonstrating the synthesis of 5- μ J sub-cycle pulses with a duration of 3.8 fs (0.7 cycles) at $\lambda_0 \approx 1.7 \mu\text{m}$.

Despite their advantages and unique properties, HCF-based synthesizers face limitations such as inherent energy/power scalability restrictions (discussed in Sec. 2.4.2). Additionally, their spectral non-uniform broadening often results in significant energy differences between spectral components. For instance, in the synthesizer by Hassan et al. (2016) [117], the highest frequency component (at $\approx 0.3 \mu\text{m}$) contains nearly two orders of magnitude less energy than the component at the fundamental frequency (at $\approx 0.8 \mu\text{m}$).

- **Parallel scheme:** In a PWS, a single CEP-stable beam derived from the pump laser seeds multiple OP(CP)As. This seed beam can be manipulated in two ways: it can either be first spectrally broadened and then split into constituent spectral channels, or it can be split into channels and then undergo spectral broadening within each. Following this manipulation, cascaded OP(CP)As pumped by the main laser, amplify the CEP-stable seed within each channel's specific spectral range. Before recombination, independent dispersion management, CEP control, and delay adjustment are applied in each channel, along with a portion of the combined beam being dedicated to diagnosis and synchronization. This design allows for extensive customization of each channel.

Compared to the HCF-based waveform synthesizer, the parallel PWS

scheme is inherently more complex and spatially demanding. This complexity makes waveform synthesis, i.e., the sub-cycle locking of relative delays and CEP across independent constituent pulses, more challenging. However, this scheme offers significant advantages: energy scalability can be achieved by adding OP(CP)A stages, and the achievable bandwidth can be extended by incorporating additional spectral channels with tailored optics. Importantly, unlike the HCF-based synthesizer, a PWS can maintain a more uniform energy distribution across spectral channels, avoiding the orders-of-magnitude differences seen in HCF systems. This characteristic is evident in existing PWS setups, where constituent pulses often possess average energies within the same order of magnitude, and up to three spectral channels have been successfully integrated [290, 291]. A more homogeneous spectral distribution enables the synthesis of a wider variety of waveforms.

A number of synthesizer setups based on this scheme have been successfully implemented with various systems, based on Ti:Sa [110, 291] and Yb:YAG [286, 287, 290] pump lasers. These setups demonstrate the scheme's versatility, enabling synthesis across the near-infrared ($\approx 1 - 1.4 \mu\text{m}$) [110, 286, 290, 291] and into the mid-infrared (at $\approx 4.2 \mu\text{m}$) [287] spectral ranges, and with the capability of producing pulses with durations spanning from nearly half-cycle [110] to nearly-single-cycle [287, 290] and extending into the few-cycle regime [286, 291]. Moreover, these systems have demonstrated the scheme's adaptability to different energy levels, ranging from tens of microjoules [286, 287, 290] to the sub-mJ level [110] and even multi-mJ energies [291].

As will be discussed in detail in the next section, this particular scheme is the one implemented in the waveform synthesizer used in this thesis. It enabled the synthesis of 0.6-cycle pulses at $1.4 \mu\text{m}$ with 0.5 mJ of average energy using a kHz Ti:Sa system [109]. Other setups, mentioned in the previous paragraph, have successfully demonstrated variations of this scheme utilizing the signal, pump, and idler from an OPA as constituent pulses [287, 291, 292].

- **Serial scheme:** In a serial PWS, a CEP-stable seed undergoes spectral broadening via WLG. The resulting broadband spectrum is then directed into a pulse shaper, where its spectral phase is sculpted to achieve a desired waveform. This tailored signal is subsequently amplified through cascaded OPAs tuned for specific spectral ranges and finally compressed. Since pulses travel a common path, there is no need for complex recombination optics, simplifying synchronization (often requiring only active CEP stabilization). While potentially energy-scalable, achievable bandwidth, as with HCF-based synthesizers, is

limited by the initial seed's broadband spectrum. Additionally, the need for ultrabroadband, low-dispersion optics presents a bandwidth limitation, posing challenges for phase manipulation.

Waveform shaping in serial synthesizers can be less flexible due to the lack of individual delay and CEP control. While AOPDFs can be used, they introduce power losses and potentially narrow the achievable bandwidth even further. These constraints complicate the synthesis of sub-cycle pulses.

This synthesis scheme has been successfully implemented by Rivas et al. (2017) [288] with a 10 Hz, Nd:YAG laser system. To date, this is the near-infrared system delivering the highest output energy (100 mJ) with synthesized pulses lasting less than 2 cycles, reaching multi-TW peak power levels. Notably, Lin et al. (2020) [289] employed a hybrid approach (serial + parallel) using a 200 Hz Ti:Sa system. They achieved sub-cycle pulses (0.73 cycle duration) with 32 μ J average energy at 1.8 μ m, with amplification in a serial OPA configuration but parallel dispersion management.

4.2 Parametric waveform synthesizer

This section introduces the parallel PWS setup used in this thesis [110, 126], starting with a general system overview before providing a more elaborate description of individual components.

The system builds upon a previous version [295], and was extensively re-engineered by Dr. Giulio Rossi and Dr. Roland Mainz. Their work included a complete optomechanical redesign (including modifications to the pump laser beam path) and implementation of active stabilization for coherent temporal superposition. Dr. Rossi and Dr. Fabian Scheiba characterized the temporal profile of the constituent pulses, compressing them near their FTL duration [296]. For a detailed description of these steps, please refer to Refs. [109, 130, 297]. The author of this thesis, along with Dr. Scheiba, implemented the spatial overlap of the constituent beams and characterized their transverse beam profiles [298]. These contributions, in conjunction with the substantial foundational work established previously, enabled the successful synthesis of the sub-cycle waveforms reported in this section.

Figure 4.3 presents a schematic overview of the PWS architecture, including its key subsystems and diagnostics. The heart of the system is a commercial pump laser¹ delivering 20 mJ, 150 fs pulses at a 1 kHz repetition rate. The choice of 150 fs pulses is to assure stability in the multiple nonlinear processes it employs (OPA, WLG, SHG). While shorter pulses can introduce

¹*Coherent, Inc.*

4. SUB-CYCLE OPTICAL FIELD SYNTHESIS

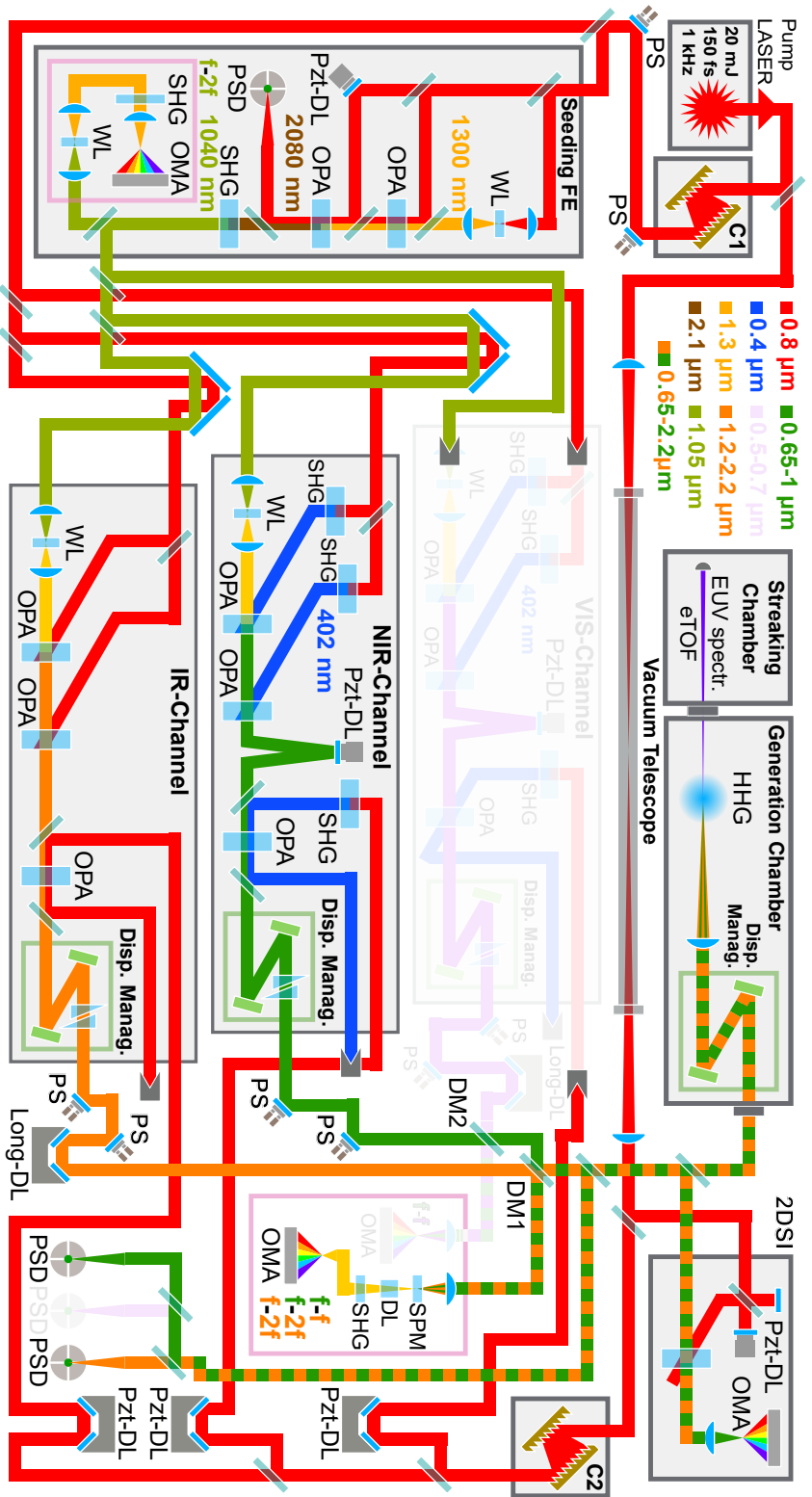


Figure 4.3: Parametric waveform synthesizer. The setup comprises a pump laser with two compressors (C1, C2), a CEP-stable seeder (gray box) with an f -2 f interferometer (pink box) generating a 1040 nm signal, NIR, IR, and VIS (not yet implemented) spectral channels (gray boxes), each with dispersion management (green boxes), a dual-phase meter (pink box) for measuring f - f and f -2 f signals to stabilize CEP and relative delays, a 2DSI characterization station (gray box) for temporal envelope characterization of constituent pulses, and an attosecond beamline (with final dispersion management, green box) including an attosecond streaking setup for direct measurement of the synthesized waveform. The setup utilizes white-light (WL) sources, optical parametric amplifiers (OPAs), dichroic beam combiners (DM1, DM2), piezo-controlled delay lines (PzT-DL) for fine CEP and relative delay adjustments, long-range delay lines (Long-DL) for additional timing control, and actuators (PS) and position-sensitive detectors (PSD) for active beam stabilization. Adapted from [110].

chirp-related instabilities, longer pulses increase the risk of crystal damage. Moreover, the relatively narrow bandwidth of 150 fs pulses reduces dispersion during propagation through air and crystals, ensuring consistent temporal characteristics throughout the system.

The pump laser drives a CEP-stable seeder, generating a CEP-stable $\approx 1 \mu\text{m}$ beam that seeds three spectral channels, that in total cover more than two octaves in bandwidth: infrared (IR; $\approx 1.2\text{-}2.2 \mu\text{m}$), near-infrared (NIR; $\approx 0.65\text{-}1.0 \mu\text{m}$), and visible (VIS; $\approx 0.5\text{-}0.7 \mu\text{m}$). Currently, only the IR and NIR channels are fully operational. Cascaded OPAs, pumped by either the pump laser's fundamental wavelength or its second harmonic, amplify the individual signals to sub-mJ energy levels, resulting in a combined energy at the mJ level. Diagnostics, active stabilization systems, and beam pointing actuators ensure precise control for waveform synthesis upon recombination via broadband dichroic optics.

In this PWS implementation, two primary parameters are actively controlled: First, piezos and translation stages positioned along the beam paths adjust the relative delays (τ_{1i}) among constituent pulses. Secondly, a piezo in the CEP-stable seeder controls a common CEP shift ($\Delta\varphi$) experienced by all constituent pulses. This common CEP shift, directly determined by the CEP-stable seed itself, defines the CEP of the synthesized waveform.

Accordingly, the resulting synthesized waveform of the original, envisioned three-channel system can be modeled, in a simplified manner, as:

$$E(t) = \sum_{i=1,2,3} \varepsilon_i(t - \tau_{1i}) \cos(\omega_i(t - \tau_{1i}) + \phi_i + \Delta\varphi), \quad (4.4)$$

where $i = 1, 2, 3$ indexes the IR, NIR, and VIS channels, respectively, and ϕ_i represents any constant accumulated phase offset accumulated by the i -th constituent pulse during its propagation through the setup. The relative field amplitudes among the channels are not actively controlled and depend directly on the energy ratio between the amplified signals in each channel.

After coherent synthesis, the pulses enter an attosecond beamline. This beamline incorporates the final pulse compression stage, designed for the three-channel synthesizer's full bandwidth [78]. Combined with precise dispersion management within the spectral channels, this stage compresses the constituent pulses close to their FTL durations, enabling the synthesis of sub-cycle waveforms [295]. The beamline also includes streaking capabilities for direct characterization of the synthesized electric field, thus completing the waveform synthesis process.

To ensure optimal performance and stability, the CEP-stable seeder and spectral channels utilize custom-designed, 50-mm thick aluminum breadboards.

These breadboards, along with custom aluminum optics mounts, enhance compactness and reduce mechanical vibrations. They are rigidly interconnected and affixed to the table. For further vibrational dampening, they rest on rubber sheets and are enclosed within acrylic boxes to mitigate air disturbances. Finally, resistive heating maintains the breadboards at a slightly elevated temperature, achieving thermal stability below 1 mK (rms). These comprehensive measures significantly reduce both mechanical and thermal sources of instability in the PWS system [109, 130].

4.2.1 Laser system

The femtosecond laser system begins with a *Vitesse 800*, a diode-pumped Ti:Sa oscillator. It generates linearly polarized pulses centered at ≈ 800 nm, delivering sub-100 fs pulses with 80 MHz repetition rate, with an average energy of 3 nJ per pulse.

These pulses enter the *Legend Elite Duo HE+*, where they are initially stretched to several ps to prevent damage within its amplification stages. These stages consist of a regenerative amplifier (REGEN) followed by a single-pass amplifier (SPA), both operating at 1 kHz. A frequency-doubled *Evolution HE Nd:YLF* laser (at ≈ 530 nm), driven by ≈ 20 A of current, pumps these amplifiers. This pump power totals ≈ 40 W and is divided equally between the REGEN and SPA stages. Within the REGEN cavity, pulses undergo multiple passes until saturation, reaching ≈ 5 mJ of energy. Pockels cells control pulse extraction at a 1 kHz repetition rate, directing the amplified pulses to the SPA for a final energy boost to ≈ 10 mJ per pulse. Peltier elements maintain optimal amplifier crystal temperatures at -10 degrees.

The final amplification stage employs a *Legend Elite Cryo PA*. This single-pass amplifier is pumped by two counter-propagating Evolution HE lasers, together providing a combined 80 W of power. A closed-loop helium compressor² cryogenically cools the amplifier to ≈ 85 K. To prevent condensation on the Ti:Sa crystal, its housing within a chamber is held at $10^{-(8-9)}$ Torr. Finally, this stage delivers an output exceeding 20 mJ per pulse prior to final compression.

The final amplification stage was significantly modified to meet the requirements of the PWS [109, 130]. Modifications included a beam pointing stabilization system³ for precise seed beam alignment throughout the amplifier. Additionally, a half-wave plate and thin-film polarizer were used to divide the amplified beam into two outputs: a low-energy beam (transmitted), directed to an internal compressor and resulting in ≈ 4 mJ pulses, and a high-energy, uncompressed beam (reflected) carrying ≈ 16 mJ. The high-energy

²*Cryomech, Inc.*

³TEM Messtechnik (Aligna)

beam is compressed externally after precautions are taken to ensure optimal quality: it propagates through a 6-meter vacuum tube ($\approx 10^{-3}$ mbar) to prevent air-induced nonlinearities and undergoes Rayleigh imaging with a 4-f telescope.

System stability

To maintain the long-term stability of this complex system, several measures are in place. Photodiodes were installed to track beam energy, and analysis and visualization software was developed [130]. Additionally, a network of cameras monitors spatial beam profiles on a daily basis. This vigilance is crucial for optimal performance of the PWS, as any deviation from the ideal beam profile can compromise the entire system. Cameras are strategically installed at key points [297]: after the output of the Legend Elite Duo HE+ (ensuring input beam quality to the cryogenically-cooled amplifier), after the internal compressor (monitoring the low-energy output and input for the CEP-stable seeder and first amplification stages), and at two points surrounding the high-energy beam path: one before the vacuum tube and one after the vacuum tube and external compressor. Software to automate daily beam profile analysis was also developed [297]. This comprehensive monitoring ensures that potential issues are detected early, allowing for corrective action to maintain peak PWS performance.

4.2.2 CEP-stable seeder

The CEP-stable seeder derives its seed from the low-energy, compressed (4 mJ, 150 fs) output of the laser system. This seed undergoes several nonlinear transformations: first, white-light generation (WLG) in a YAG crystal, followed by initial amplification at around 1300 nm in an OPA stage (Type-II phase-matching, BBO crystal). To optimize the CEP stability, the signal passes through a narrowband (3 nm) bandpass filter before entering a second OPA stage, also pumped by the primary laser and employing Type-II phase-matching (BBO). This second stage generates the CEP-stable 2080 nm idler, which serves as the frequency-doubled seed for the spectral channels. The system is designed to minimize dispersion, ensuring both the pump and idler pulses remain nearly FTL throughout. Crucially, the bandpass filter extends the seed pulse duration beyond that of the pump. This has two key benefits: first, it minimizes the impact of pump-seed jitter on the idler's CEP, and second, it enables the use of a piezo-driven mirror in the pump's optical path for active control and stabilization of the idler's CEP [299], directly impacting the phase shifts ($\Delta\varphi$) in the constituent channels mentioned earlier (see Eq. 4.4).

Type-II (oe) phase matching was chosen for its unique property of generating counter-propagating signal and idler pulses relative to the pump. As

discussed in Sec. 2.4.1, this configuration creates a temporal trapping mechanism, allowing for amplification beyond the typical pulse splitting length and operation closer to pump depletion. In this pump saturation regime, shot-to-shot energy fluctuations of the signal and idler are minimized, becoming primarily dependent on the more stable pump energy, enhancing overall system stability.

Finally, a Type-I (ooe) BBO crystal frequency-doubles the CEP-stable 2080 nm idler to 1040 nm. The near-FTL nature of the idler ensures its CEP stability is preserved during frequency-doubling, making it ideal for seeding the spectral channels. A portion of this 1040 nm pulse is directed to an f-2f interferometer for CEP stabilization and control within a feedback loop.

f-2f interferometer

The f-2f interferometer consists of a WLG stage, a filter, an additional SHG stage (Type-I, BBO), and a linear polarizer. Inside, the BBO crystal frequency-doubles the driving $\approx 1 \mu\text{m}$ WL. A filter before the SHG crystal suppresses dominant spectral components of the WL driver, ensuring optimal signal quality. A linear polarizer then projects both fields onto the same polarization axis, enabling their interference. A custom-built spectrometer, using a Si-based linear array CCD⁴, measures the resulting interference pattern. CEP fluctuations are extracted by means of f-2f interferometry explained in Sec. 2.5.2.

Optimal stabilization performance relies on a rapid process: calculating the phase of the CCD-collected interference pattern, determining control signals (Proportional-Integral-Derivative (PID) parameters), and physically actuating the mirror. A Field-Programmable Gate Array (FPGA)-encoded FFT algorithm calculates the phase in under 500 μs . A microcontroller analyzes this data, generating the proportional and integral feedback loop parameters. The resulting control signal drives a piezoelectric actuator integrated into the second-stage OPA pump mirror. This entire process occurs within 1 ms, enabling control of the relative delay between the first-stage OPA signal and the second-stage pump, thus achieving single-shot control over the idler's CEP [130].

The CEP control system's parameters can be remotely adjusted via a MATLAB interface. This provides flexibility for locking the CEP to arbitrary functions and fast scanning through different values.

4.2.3 Broadband parametric amplification

The CEP-stable seeder outputs pulses at $\approx 1 \mu\text{m}$ with $\approx 5 \mu\text{J}$ of energy per pulse. These pulses are split into different spectral channels with nJ-level

⁴Hamamatsu (model: S10453)

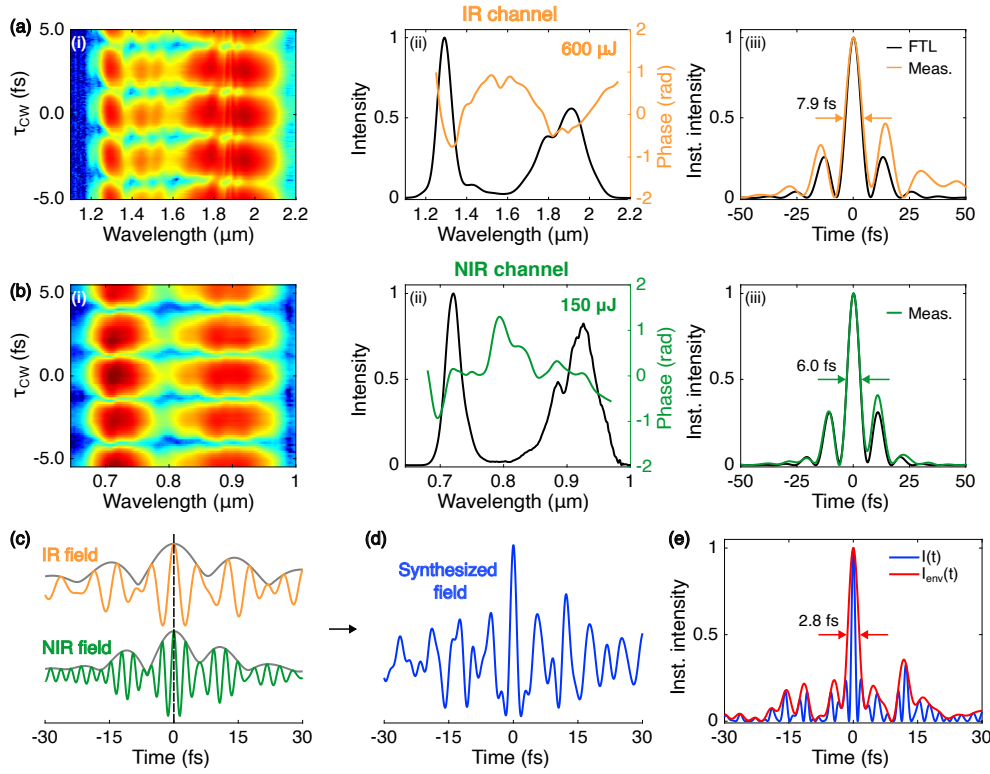


Figure 4.4: Spectral and temporal characteristics of PWS. (a) IR and (b) NIR channels. For each case: (i) 2DSI trace (τ_{CW} denoting the ancillary delay). (ii) Measured spectra (left axis) and retrieved spectral phases (right axis, colored). Average energy after amplification is indicated (top right). (iii) Temporal envelope profile (colored) with FWHM indicated, compared to the FTL case (gray). (c) Constituent electric fields (colored), with their respective temporal envelopes (gray) assuming zero phase offset and delay. (d) Corresponding synthesized waveform. (e) Instantaneous intensity (blue) and envelope (red) of the synthesized waveform, with FWHM indicated. Adapted from [110].

energies. To ensure synchronization, the beam paths are adjusted so pulses arrive simultaneously at the input of their respective channels. Each spectral channel, designed to cover the VIS ($\approx 0.5\text{-}0.7\ \mu\text{m}$), NIR ($\approx 0.65\text{-}1.0\ \mu\text{m}$), or IR ($\approx 1.2\text{-}2.2\ \mu\text{m}$) spectral regions, aims to amplify the seed energy to sub-mJ levels. Within each channel, individual WLG is performed. This approach eliminates the need for complex dispersion compensation that would be required with long broadband pulse propagation from a single WLG stage. The result is a shorter beam path, improved beam quality, increased compactness, and enhanced stability. Additionally, dedicated WLG stages enable tailoring to the specific needs of each spectral channel, optimizing performance [126].

As discussed in Sec. 2.4.1, broadband amplification strategies depend on the desired spectral region. In this setup, a NOPA (non-collinear OPA) pumped

by the 400 nm SHG of the fundamental beam is planned for the VIS channel. This configuration would enable broad amplification away from degeneracy.

Currently, the fully operational IR and NIR channels employ DOPAs (degenerate OPAs), pumped by the 800 nm fundamental and its SHG, respectively. To optimize amplification and minimize issues like superfluorescence, three cascaded stages are used. The first two stages utilize the low-energy laser output as their pump, while the final stage is powered by the high-energy output. This approach yields $\approx 1\mu\text{J}$ (both channels) in the first stage, $\approx 20\mu\text{J}$ (both channels) in the second stage, and 150 μJ (NIR) and 600 μJ (IR) in the third stage. The difference in final energy between the channels is primarily due to the difference in pump energy used in the third amplification stage: $\approx 1\text{ mJ}$ for NIR and $\approx 6\text{ mJ}$ for IR [109]. Fig. 4.4a-b (ii) shows the spectra of the amplified channels (after the third OPA), exhibiting their characteristic M-shape inherited from the BBO crystal's gain bandwidth [70], with central wavelengths typically around $\approx 0.8\ \mu\text{m}$ for the NIR pulse and $\approx 1.6\ \mu\text{m}$ for the IR pulse.

To achieve stable and efficient ultrabroadband amplification, the seed pulse duration must be substantially shorter than that of the pump pulse, ensuring complete temporal overlap and amplification across the entire seed bandwidth. This configuration, where the pump pulse fully envelops the seed, not only enhances robustness against pump-seed timing jitter but also allows for controlled delay of the amplified signal relative to a reference frame without sacrificing amplification efficiency [299]. Based on this idea, a piezo actuator in the NIR channel is employed to modulate the seed-pump timing in the third-stage OPA, enabling sub-femtosecond-scale delay adjustments of the amplified signal relative to another constituent pulse, while preserving both its amplification efficiency and spectral characteristics.

4.2.4 Pulse compression and characterization

To maintain optimal amplification and stability, where the seed pulse is shorter than the pump pulse as previously discussed, dispersion compensation is needed between OPA stages in all spectral channels.

In the PWS, a dispersion management scheme based on custom-designed chirped mirrors (with $>90\%$ reflectivity for each channel) and thin wedges allows fine-tuning the chirp and even the higher-order dispersion terms, critical in nearly-octave-spanning bandwidths [126]. In the VIS and NIR ranges, a few fused-silica wedges, offering positive dispersion, suffice. However, the IR channel (1.1-2.2 μm) has fewer material options for positive dispersion. ZnSe was chosen for its surface quality [109], cuttability into wedge shapes, and relatively low positive dispersion compared to Si, enabling better dispersion control and minimizing nonlinearities, though they remain to some degree.

As the synthesized pulses are used in the attosecond beamline held under vacuum, achieving the shortest possible durations directly within the chamber is essential. The dispersion management strategy accounts for all dispersive elements encountered by each channel to guarantee optimal compression. Before entering the vacuum, the pulses must be combined to facilitate diagnosis, stabilization, and control. Dual adiabatic chirped mirrors [78] were fabricated to handle the entire PWS bandwidth (>2 octaves, considering VIS, NIR, and IR channels). These mirrors compensate for air propagation, broadband dichroic beam combiners, the 3-mm input window to the vacuum chamber, and the 3-mm plate for splitting the beam into HHG and streaking arms. Fine-tuning with fused-silica wedges for VIS/NIR and ZnSe wedges for IR allows pulses to be compressed close to their FTL.

In the current PWS version, utilizing only the NIR and IR channels (>1.7 octave bandwidth), 2DSI measurements (see Sec. 2.6.1) confirm compressed pulse durations of 6 fs for the NIR and 8 fs for the IR pulses, as illustrated in Fig. 4.4a-b. Assuming zero phase offset and relative delay between them, the synthesized waveform last only 2.8 fs, corresponding to 0.6 cycles at 1.4 μm (see Fig. 4.4c-e).

4.2.5 Beam profiling

Beyond the spectro-temporal characteristics, the transverse beam quality is a critical determinant of optimal performance for both the NIR and IR beams, directly impacting HHG efficiency. These beam profiles and their focusing characteristics are carefully optimized during alignment of the spectral channels. Figure 4.5a-b shows their collimated (far-field) transverse profiles measured before entering the attosecond beamline. The NIR beam profile is captured using a Si-based CCD⁵, while the IR beam profile is measured with a pyroelectric detector⁶. To ensure the beams reach the same waist size after being focused, the NIR beam waist ($1/e^2$) is adjusted to be as close as possible to half of the IR beam ($w_0 \approx 5$ mm).

In the experiments presented in this thesis, beam waists at focus reach sizes up to ≈ 100 μm . While two-dimensional detectors with pixel dimensions of a few μm can readily resolve such waists, they are typically Si-based and thus primarily sensitive to the spectral range of the NIR beam (0.65 - 1.0 μm) rather than the IR beam (1.2-2.2 μm). To measure the focused IR beam profile, the two-photon absorption signal on the Si-based detector is utilized. As this process scales quadratically with intensity, the actual beam waist can be estimated by multiplying the measured value by $\sqrt{2}$. This method was compared with knife-edge measurements and found to agree within $<2\%$ [297].

⁵Spiricon SP620

⁶Pyrocam IV

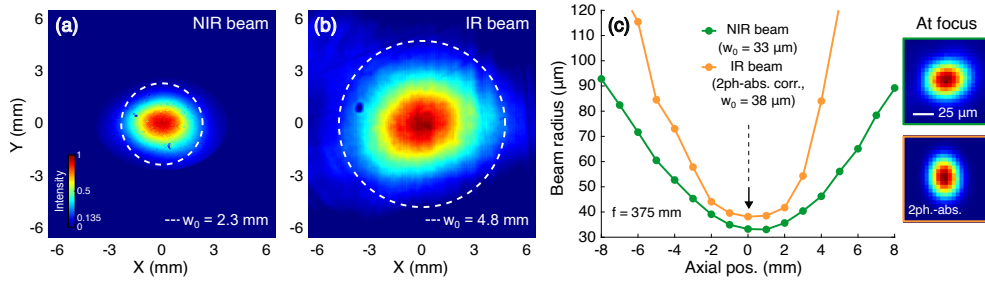


Figure 4.5: Beam profile characterization. (a) NIR and (b) IR collimated beam profiles measured before the HHG chamber. White dashed circles indicate the mean $1/e^2$ waist radius w_0 , calculated as $w_0 = (w_x + w_y)/2$, where $w_{x,y}$ represents the beam waist along the x- and y-axes. For the NIR beam $w_x = 2.7$ and $w_y = 2.0$ mm. For the IR beam, $w_x = 5.4$ and $w_y = 4.2$ mm. (c) Mean beam waist evolution for NIR (green) and IR (orange) beams across the focus using a spherical mirror ($f = 375$ mm). The IR beam caustic has been corrected for 2-photon absorption. The NIR Rayleigh length is $z_R = 2.7$ mm, and for the IR, $z_R = 1.2$ mm (fitted with Eq. 2.12). Insets: Beam profiles at focus (IR shows raw 2-photon absorption signal).

4.2.6 Waveform stabilization and control

Following amplification and coherent combination, the constituent pulses exhibit drifts in CEP and relative delay. These fluctuations, arising from spectral broadening, amplification, as well as mechanical and thermal instabilities within the synthesizer setup, necessitate active stabilization to maintain the stability of the synthesized waveform.

To counteract these drifts, a dual phase-meter system, illustrated in Fig. 4.6a, is implemented. This system extracts a weak replica of the synthesized field after coherent combination but before it enters the attosecond beamline. By incorporating both an f - $2f$ interferometer and an f - f interferometer, the system simultaneously monitors CEP drifts and tracks Relative Phase (RP) drifts, which encode relative delay drifts between the constituent pulses.

To ensure a distinct f - f interference pattern, a delay is introduced between the constituent pulses by passing the replica beam through a glass plate. Spectral broadening of the IR pulse via WLG, combined with the glass plate delay and attenuation of the NIR beam, ensures sufficient spectral overlap and generates a well-defined f - f interference pattern from which the RP between the pulses can be retrieved.

For CEP detection, a portion of the IR pulse is frequency-doubled, creating a beat signal with the low-frequency side of the NIR pulse. A second glass plate generates an additional f - $2f$ signal at a different periodicity, enabling CEP retrieval without cross-talk from the f - f signal.

Changes in CEP and RP manifest as modulations in the spectral fringes observed on the spectrometer (Fig. 4.6b). This phenomenon is evident both when these parameters are actively scanned with a sawtooth pattern and

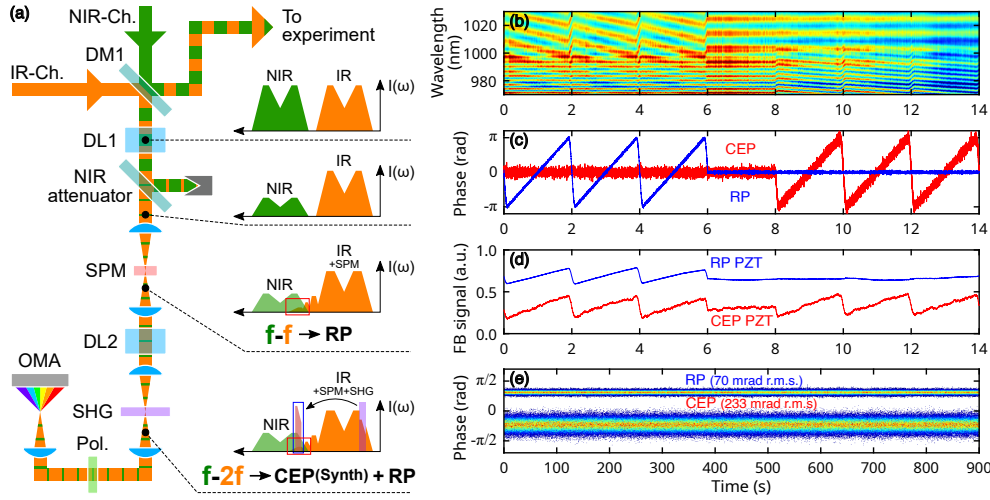


Figure 4.6: Waveform synthesis active stabilization and control. (a) Schematic of the f-f and f-2f interferometry setup for measuring relative phase (RP) and CEP fluctuations in a synthesized waveform. For the f-f signal, a glass plate (DL1) delays the spectrally broadened IR pulse (via SPM), overlapping it with the attenuated NIR pulse to generate clear interference fringes. For f-2f interferometry, the red-frequency side of the IR pulse is frequency-doubled (SHG) and interfered with the red-frequency side of the NIR pulse. Another glass plate (DL2) ensures distinct fringe periodicity from the f-f signal, and a polarizer (Pol.) balances SHG and fundamental contributions. (b) Example spectrogram from the dual-phase meter, showcasing RP sawtooth scan, simultaneous RP/CEP locking, and CEP sawtooth scan. (c) Extracted RP and CEP values during the scans. (d) Feedback signals (FB) applied to the RP and CEP piezos (PZT). (e) Histograms of extracted RP and CEP values under full locking, indicating the RP and CEP residual phase noise computed over 9×10^5 consecutive shots. Adapted from [110].

when they are maintained at a fixed (locked) value. The extracted RP-CEP values from the f-f and f-2f spectral interferometry analysis are illustrated in Figure 4.6c, while Fig. 4.6d shows how feedback signals are imprinted on the corresponding piezo-controlled actuators for the CEP and RP, located in the CEP-stable seeder and NIR channel. The relative delay (τ) between the NIR and IR pulses can be calculated from the measured RP ($\Delta\Phi_{RP}$), after subtracting the CEP contribution, using the following relation:

$$\tau = \Delta\Phi_{RP} \cdot T_{RP} / (2\pi),$$

where T_{RP} (≈ 3.25 fs) is the oscillation period corresponding to the wavelength ($\lambda_{RP} \approx 974$ nm) at which the RP is measured. With both phases actively stabilized, the residual phase noise, as depicted in the histograms in Fig. 4.6e, is 70 mrad RMS for the relative phase and 233 mrad RMS for the CEP, calculated over 9×10^5 shots.

4.2.7 Coherent spatiotemporal synthesis

Successful pulse synthesis necessitates both temporal and spatial overlap of the constituent beams. Spatial overlap must be achieved in both the far-field

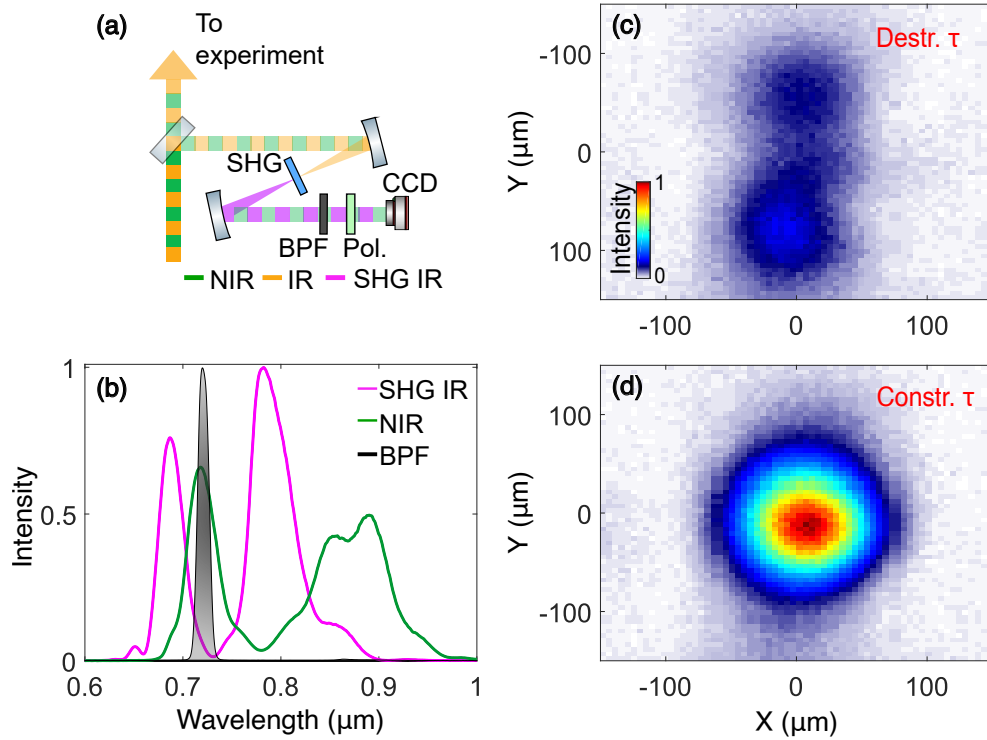


Figure 4.7: Real-time spatiotemporal overlap monitoring. (a) Schematic of the setup. A weak replica of the synthesized NIR/IR beam is used. The IR beam is frequency-doubled (SHG) to interfere with the NIR. A bandpass filter (BPF) selects the spectral region of interest, and a polarizer (Pol.) balances the NIR and SHG-IR intensities. A CCD camera records single-shot spatial interference patterns. (b) Measured spectra (NIR, SHG-IR) with BPF transmission (shaded). (c-d) Interference patterns at different relative delays (τ), demonstrating destructive (c) and constructive (d) interference. Adapted from [126].

and near-field to ensure not only co-location of the beams but also their co-propagation with the same direction. Maintaining this overlap on a single-shot basis is particularly crucial to guarantee consistent beam alignment for each individual pulse.

Upon achieving spatial, temporal, and spectral overlap of the constituent beams, spatial interference fringes emerge. These fringes serve as a sensitive indicator of relative phase fluctuations between the pulses, enabling the monitoring of both temporal and spatial stability within the synthesized beam [126].

To leverage this precise spatiotemporal overlap for continuous monitoring, a near-field characterization station was developed to assess the overlap between the constituent beams at the 1 kHz repetition rate (Fig. 4.7a). After ensuring far-field overlap (i.e., while collimated), a weak replica of the combined beam is utilized. Given the distinct spectral characteristics of the NIR and IR channels, preventing detection by a common detector, the IR beam

undergoes frequency doubling via a 100- μm -thick Type-I BBO crystal and spatially overlapped with the NIR beam. This arrangement allows for the generation of an interference pattern, which is then isolated using a band-pass filter (Fig. 4.7b). A wire grid polarizer placed before a high-speed camera⁷ ensures equal intensity contributions from the NIR and frequency-doubled IR (IR-SHG) components. The camera, operating in single-shot mode, captures the spatial interference pattern without averaging, facilitating the direct correlation of fluctuations with variations in CEP and RP. Notably, the observed interference patterns exhibited a distinct sensitivity to both CEP and RP modulation, as reported in Ref. [297]. Figures 4.7c-d exemplify this phenomenon for overlapping beams, showcasing the adjustments in relative delay (while maintaining the CEP locked) that lead to destructive and constructive interference, respectively. This characterization method, executed in parallel with ongoing experiments, enables continuous, real-time monitoring of the spatiotemporal overlap between the NIR and IR beams.

Based on this near-field characterization and monitoring methodology, an active beam stabilization system⁸ was implemented for each constituent beam to counteract long-term drift in the pointing of each constituent beam. A weak replica of the synthesized beam, generated via reflection from a thin glass plate positioned after beam combination, serves as the input for this stabilization system. Dichroic mirrors subsequently separate this replica into its NIR and IR spectral components, directing them onto position-sensitive detectors (PSDs). Given the spectral mismatch between the Si-based PSD and the IR beam, a secondary frequency doubling stage is introduced in the IR beam path prior to detection.

4.3 Attosecond beamline

The attosecond beamline discussed in this section was originally constructed by Dr. Yudong Yang [274] and is based on a Mach-Zehnder interferometer design. In this scheme, the input beam is spatially separated into two arms: one for generating the HHG beam and another for the optical beam. These arms are subsequently manipulated independently before being recombined with a defined time delay. This approach contrasts with collinear geometries, where both the HHG and optical beams co-propagate [140], offering greater flexibility in manipulating the individual beams. Within the apparatus, mirrors are coated according to their function: those designed for reflecting optical light have a protective silver coating, while those intended for HHG light utilize a gold coating, both offering broadband reflection.

⁷Basler acA640-750um

⁸TEM Messtechnik, Aligna

4. SUB-CYCLE OPTICAL FIELD SYNTHESIS

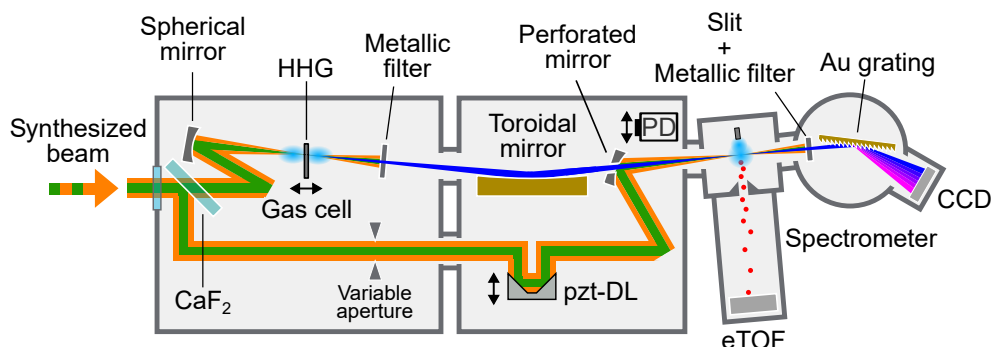


Figure 4.8: Attosecond beamline schematic. The synthesized beam enters the beamline through a CaF_2 window and is split by a second CaF_2 window by Fresnel reflection into a HHG-driving beam and an optical streaking beam. HHG is driven in a gas cell, with metallic filters blocking residual optical light in the HHG arm. A photodiode (PD) measures HHG photon flux. A toroidal mirror images the HHG beam onto a neon gas jet, with ionized electron spectra recorded by an electron time-of-flight (eTOF) spectrometer. The diverging beam's spectrum is measured by a spectrometer (slit, grating, CCD). The optical path includes a variable aperture and piezo-driven delay line (pzt-DL) for streaking, recombining with the HHG beam via a perforated mirror.

The beamline underwent subsequent modifications by the author of this thesis and Dr. Scheiba [297], and its final configuration is detailed in later chapters. For comprehensive computer-aided design (CAD) drawings of the beamline, the reader is referred to Refs. [274, 297].

Figure 4.8 provides a schematic overview of the attosecond beamline. To prevent absorption of the generated HHG radiation, the entire beamline operates under high vacuum conditions. It consists of two custom-designed vacuum chambers and a commercial EUV/soft X-ray spectrometer⁹, all connected by flexible bellows and capable of being vacuum-isolated via gate valves. The beamline achieves a base pressure of $10^{-(6-7)}$ mbar across all chambers when evacuated. This vacuum level is attained through the utilization of turbo molecular pumps¹⁰, backed by dry scroll pumps¹¹ for the pre-vacuum. Under HHG generation conditions, with gas loads of $\approx 10^2$ mbar for gases such as argon and krypton, the pressure at the spectrometer side remains largely unaffected. The pressure in the first chamber increases to $\approx 10^{-4}$ mbar, while the second chamber experiences pressures of $\approx 10^{-(5-6)}$ mbar.

The first chamber houses the final pulse compression stage for the input pulses, bringing them close to their FTL duration (see Fig. 4.4). It is within

⁹McPherson 251 MX

¹⁰First chamber: HiPace 1500 (Pfeiffer Vacuum)

Second chamber: HiPace 300 and 400 (Pfeiffer Vacuum)

eTOF: HiPace 300 M (Pfeiffer Vacuum)

Spectrometer: TV 301 Navigator (Agilent)

¹¹XDS35i (Edwards Vacuum)

this chamber, where the input beam is split into the HHG-driving arm and the optical beam arm. This beam splitting is achieved via Fresnel reflection from a 3-mm-thick CaF₂ plate oriented for a 55° AOI. Due to the nearly-flat reflectivity across the optical spectral range, the CaF₂ plate effectively splits the broadband input pulses, reflecting $\approx 12\%$ of the input energy. The transmitted beam, constituting the HHG-driving arm, retains $\approx 76\%$ of the input energy. The HHG gas target is also situated within this chamber.

The second chamber contains transport and focusing optics for both the HHG and streaking beams. These optics mainly include a toroidal mirror to focus and image the HHG beam, retroreflecting mirrors for adjusting the relative delay between both beams, and a perforated mirror for their spatial recombination. Additionally, a manipulator allows for the insertion of a calibrated soft X-ray photodiode¹² into the HHG beam path to measure the photon flux. Integrated into an attached cube-shaped chamber is an eTOF spectrometer¹³, enabling attosecond streaking measurements.

The soft X-ray photodiode has an active area of 10 mm x 10 mm. Its induced current is amplified by an operational amplifier¹⁴ and converted to a measurable voltage signal using a 10 G Ω resistor. The photon flux is then calculated from this voltage signal and the responsivity (illustrated in Fig. 4.9a) provided by the photodiode manufacturer. Calibration of the photodiode was performed at the P04 beamline in Petra-III, operated by Dr. Moritz Hoesch. Deviations in the measured photocurrent compared to the P04 beamline's reference photodiode amount to less than $\approx 30\%$ around 100 eV, less than $\approx 50\%$ around 200 eV, and less than $\approx 10\%$ from 250 eV onwards [297].

The eTOF spectrometer consists of an electrostatic lens, a 294 mm drift tube, a 107.5 mm post-acceleration stage and a MCP detector. While the electrostatic lens remains inactive for the presented experiments, the drift tube is occasionally employed with a retarding potential of a few hundred volts, and the post-acceleration stage voltage is set to 1000 V. The MCP detector output is recorded by an oscilloscope¹⁵ operating with a 4 GHz analog bandwidth and a 20 Gs/s sampling rate. A fast photodiode¹⁶ illuminated by the optical laser, triggers data acquisition. With a typical time-of-flight in the nanosecond range, a well-defined photoelectron spectrum is obtained by adjusting the oscilloscope's sweep window and accumulating data over several hundred to a few thousand sweeps, which takes up to a few milliseconds.

The third chamber encloses a grating-based spectrometer equipped with

¹²SXUV100 (Opto Diode Corp)

¹³ETF11 (Stefan Kaesdorf)

¹⁴AXUB100HYB1V, (IRD Inc.)

¹⁵WaveRunner 640Zi, Teledyne LeCroy

¹⁶ET4000 (Electro-Optics Technology, Inc.)

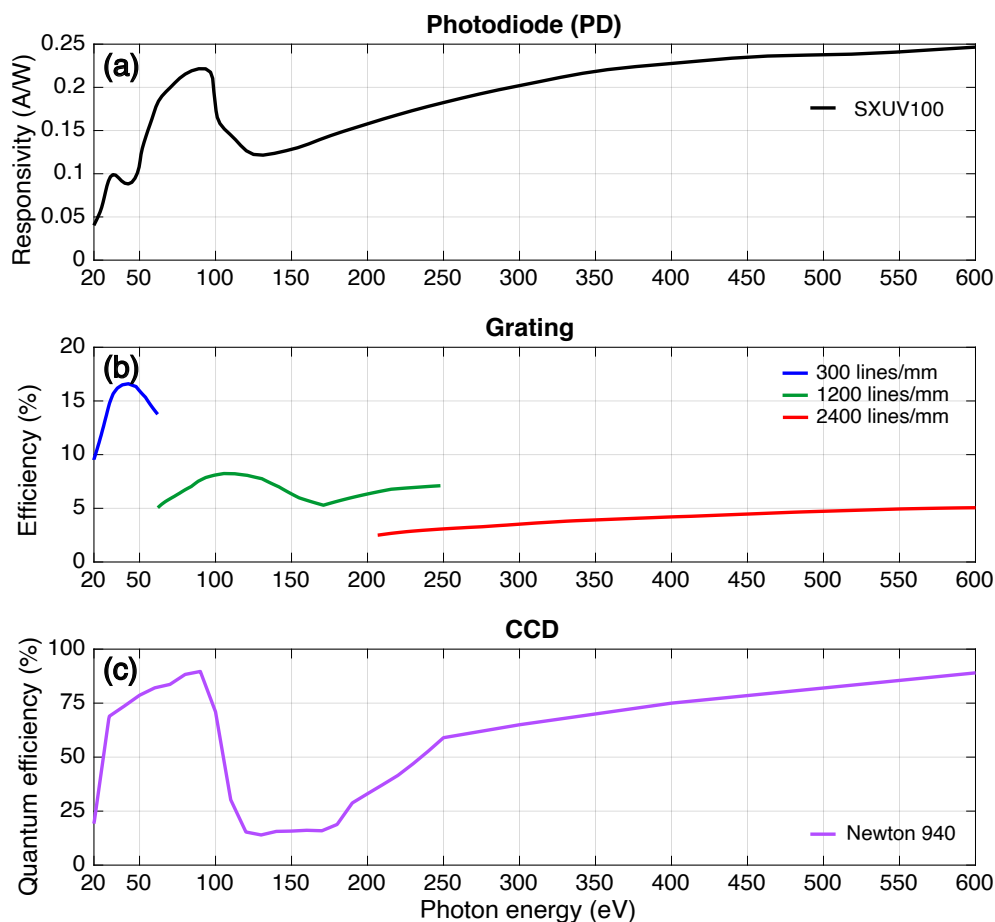


Figure 4.9: Detector and spectrometer component spectral responses. (a) Photodiode responsivity. (b) Grating efficiencies for 300, 1200, and 2400 lines/mm gratings. (c) CCD quantum efficiency (all curves from manufacturer data).

a thermoelectrically cooled, back-illuminated CCD detector¹⁷ for recording HHG spectra. The spectrometer offers flexibility in spectral range selection through two interchangeable diffraction gratings, easily switched using a handle. For the experiments presented in this thesis, three gold-coated, concave variable line spacing (VLS) gratings were utilized: 300 lines/mm and 1200 lines/mm with an 87° AOI, and 2400 lines/mm with an 88.65° AOI. These gratings cover the ranges of 15-65 eV (20-80 nm), 62-248 eV (5-20 nm), and 248-1240 eV (1-5 nm), respectively. Their corresponding efficiencies are shown in Fig. 4.9b. The CCD detector itself consists of 2048 x 512 pixels, each measuring $13.5 \mu\text{m} \times 13.5 \mu\text{m}$, and is maintained at -50° during operation. The quantum efficiency of the detector is presented in Fig. 4.9c.

To achieve attosecond stability in pump-probe experiments, sources of tim-

¹⁷Newton 940 (Andor Technology Ltd.)

ing jitter (e.g., vibrations induced by turbo molecular pumps) must be minimized. To this end, the attosecond beamline employs a passive stabilization system to mitigate mechanical instabilities. This is achieved by decoupling the optical setup from the vacuum chambers. The vacuum chambers are mounted on independent aluminum profile frames, which are securely anchored to the laboratory floor. Within each chamber, 20-mm-thick optical breadboards are supported by three posts rigidly affixed to the optical table, ensuring no direct contact with the vacuum chambers. Flexible bellows connect the vacuum chambers to these posts, maintaining the vacuum seal while allowing for mechanical isolation. This approach has been reported to achieve a passive stability of ≈ 50 as r.m.s. [274].

In the following, the HHG and optical arms are described in detail.

HHG beam arm

In the HHG arm, a spherical mirror ($f = 375$ mm) focuses the optical beam into a ≈ 2 -mm glass gas cell filled with ≈ 100 -300 mbar of argon, where HHG takes place. The gas cell is mounted on a three-axis motorized stage for optimal beam alignment and control of the HHG phase-matching position. The gas cell's backing pressure is monitored with a pressure gauge located outside the vacuum chamber and controlled via a valve.

Pulse energies, measured immediately before the gas cell, are in the range of ≈ 50 μJ for the NIR and ≈ 150 μJ for the IR. Figure 4.5c shows the beam waist focusing for the NIR and IR beams at the gas cell position, with focal waist sizes of 33 μm and 38 μm , respectively. Based on these waist sizes and pulse energies, the estimated peak intensities, calculated using the actual pulse shapes (see App. A), reach $\approx 3 \times 10^{14}$ Wcm^{-2} and $\approx 5 \times 10^{14}$ Wcm^{-2} for the NIR and IR pulses, respectively.

The gas cell is pre-drilled with another Ti:Sa laser, creating ≈ 300 -400 μm side holes. Unlike metallic gas cells, glass cells can withstand the synthesized pulse intensities, enabling indefinite cell usage. However, non-uniformities in the laser drilling process and imperfect alignment of the gas cell with the driving laser beam can reduce energy throughput, thus lowering the actual peak intensity within the interaction region.

The HHG beam emerging from the gas cell is first transmitted through an metallic filter¹⁸, which blocks the residual optical driving field. The filtered beam is then reflected at an 86° AOI by a toroidal mirror. This mirror, with sagittal and tangential radii of 39 mm and 8 m, respectively, is positioned 760 mm from the HHG source and images the beam onto a neon gas target

¹⁸Lebow Company

located 440 mm away¹⁹. This configuration minimizes coma aberrations within the constraints of the beamline setup. The mirror itself is mounted on a linear stage, a goniometer, and an actuated mirror mount, to provide precise control for beam steering, alignment, and optimal imaging.

The resulting diverging HHG beam subsequently passes through a second metallic filter. The transmitted HHG beam then goes through a slit, positioned 237 mm from the grating. The grating focuses the beam along the diffraction axis and spectrally disperses it onto the detector, located 235 mm away. A metallic baffle within the spectrometer blocks the zeroth-order diffraction, preventing it from obscuring the first-order signal, thereby enabling recording of the HHG spectrum.

Both filters located before toroidal mirror and before the spectrometer are part of a filter wheel containing various thin metallic foils. These foils serve multiple purposes: blocking the optical beam, acting as bandpass or short-pass filters, and for spectrometer calibration.

Optical beam arm

The optical beam, designated as the streaking beam in this experiment, traverses a 3 mm-thick CaF₂ plate at Brewster's angle, acquiring dispersion comparable to the HHG-driving beam, thus ensuring near-FTL duration. The intensity of the beam is controlled with a variable aperture. Retro-reflecting mirrors on a translation stage²⁰ introduce a controlled time delay relative to the HHG beam.

After this, the beam reflects from a spherical mirror ($f = 500$ mm) and a perforated mirror before being blocked by the metallic filter at the entrance of the HHG spectrometer. The spherical mirror focuses the streaking beam onto the gas target, ensuring its focal plane coincides with that of the HHG beam. The gas target is formed by a jet of neon gas ejected from a nozzle backed with a few mbar of neon. The design of the eTOF spectrometer necessitates positioning the neon target 3 mm in front of its entrance.

¹⁹The sagittal (f_{sag}) and tangential (f_{tan}) focal lengths of a toroidal mirror are given by

$$f_{\text{sag}} = \frac{r}{2 \cos \alpha}$$

$$f_{\text{tan}} = \frac{R \cos \alpha}{2},$$

where r and R are the sagittal and tangential radii, respectively, and α is the AOI. In this beamline, the toroidal mirror has $r = 39$ mm, $R = 8$ m, and $\alpha = 86^\circ$, resulting in $f_{\text{tan}} \approx f_{\text{sag}} \approx 279$ mm. This value can be represented as an effective focal length f_{eff} . With this, given the source distance $S = 760$ mm, the thin lens equation yields an image distance of $S' \approx 440$ mm.

²⁰SLC-2445 (Smaract GmbH)

The perforated mirror, mounted on an actuated mirror mount and a three-axis motorized stage, is positioned after the toroidal mirror, allowing the smaller, less divergent HHG beam to pass through its central aperture while reflecting the larger streaking beam. Through careful alignment of this mirror, the HHG beam and streaking field are spatially overlapped at the gas target and co-propagate towards the spectrometer. The size difference between the NIR and IR beams results in a greater proportion of the NIR beam being reflected by the perforated mirror, thus altering the intensity ratio between the two beams. Consequently, the streaking waveform differs from the HHG-driving waveform.

4.3.1 HHG driven by NIR and IR pulses

Figure 4.10 presents a scan of harmonic spectra as a function of the gas-cell position relative to the focus, driven in argon by either the NIR or IR pulse individually. While the CEP of these pulses was not actively stabilized during these scans, the inherent passive stability of the CEP-stable seed still minimizes CEP fluctuations. A 300-nm aluminum or a 500-nm beryllium filter was employed in each of the presented scans.

In the case of NIR-driven HHG (Fig. 4.10a-b), optimal harmonic yield is observed after the focus ($z_0 = +0.6$ mm) at 100 mbar and before the focus ($z_0 = -0.2$ mm) at 300 mbar, with the lower pressure case exhibiting a nearly six-fold increase in intensity. For IR-driven HHG, the optimal pressure for both brightest emission and most extended cutoff is found to be around 300 mbar. Under these conditions, the brightest emission and most extended cutoff coincide at approximately $z_0 = -0.5$ mm, clearly reaching the aluminum filter edge at approximately 72 eV (Fig. 4.10c). Figure 4.10d displays lineouts of spectra recorded at the optimal gas-cell positions. The near-two-cycle NIR pulse generates a spectrum with high-contrast interference fringes in the plateau region, followed by a smooth continuum beyond the cutoff at ≈ 40 eV. In contrast, the sub-two-cycle IR pulse produces a quasi-continuum spectrum, exhibiting faint, low-contrast spectral fringes below 45 eV that transition into a fringe-less region at higher energies, which may also be attributed to residual CEP fluctuations further washing out the low-contrast fringe structure.

Despite the potential influence of CEP fluctuations, these observations are consistent with HHG emission driven by two-cycle and single-cycle pulses, respectively, as illustrated in Figs. 3.14-3.15 and discussed in Sec. 3.5.1. The near-two-cycle NIR pulse generates a train of four bursts, with one dominant in intensity and photon energy, while two or three (depending on the CEP value) remain comparatively weaker. The marginal difference in strength between the strongest and adjacent half-cycles accounts for the narrowband smooth continuum observed beyond the cutoff in the resulting spectrum.

4. SUB-CYCLE OPTICAL FIELD SYNTHESIS

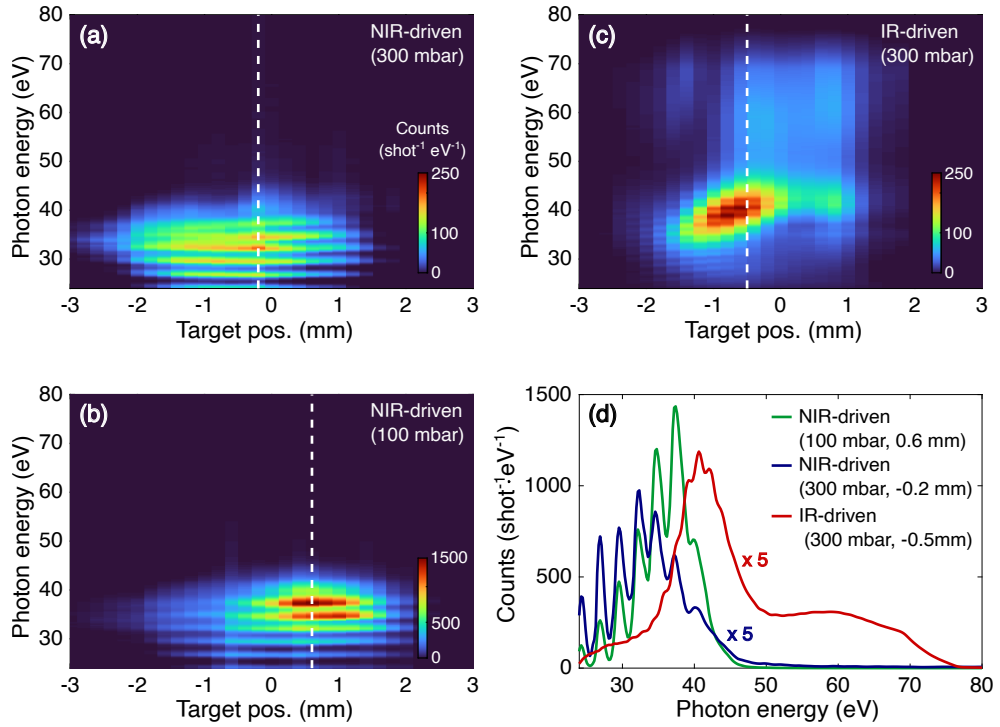


Figure 4.10: HHG gas-cell scans in argon driven by NIR and IR pulses. HHG spectra driven by the NIR pulse at 300 mbar (a) and 100 mbar (b), and by the IR pulse at 300 mbar (c), as a function of gas-cell position relative to the laser focus. (d) Lineouts of NIR- and IR-driven spectra extracted from (a-c) at optimal target positions (marked as vertical white dashed lines). The CEP of the pulses was only passively-stabilized. All spectra were acquired with the 300 lines/mm grating and a 300 nm Al filter, and are shown as recorded by the CCD.

Conversely, the sub-two-cycle IR pulse, with a more pronounced disparity between consecutive half-cycles, primarily generates one strong burst accompanied by weaker satellite pulses. This asymmetry in half-cycle strength results in a broad, smooth spectral region extending from the plateau through the cutoff, overlaid with low-contrast fringes in the lower-energy region due to the weaker bursts.

In the NIR-driven scans (Fig. 4.10a-b), the optimal phase-matching location shifts from before the focus at higher pressures to after the focus at lower pressures. This observation aligns with the qualitative phase-matching analysis given in Sec. 3.2.2. Furthermore, the phase-matching pressure estimations in Table 3.1 (200 mbar for 0.8 μm and 500 mbar for 1.6 μm), also derived in Sec. 3.2.2, not only fall within the experimental pressure range but also anticipate the trend of higher required pressure for IR compared to NIR. This agreement, even at high intensities where ionization is expected, is likely due to plasma defocusing (Sec. 3.3), which rapidly attenuates the driving pulse as it propagates through the medium, leading to a decreased

ionization fraction, thus validating the non-ionized assumption in this context.

4.4 Direct measurement of synthesized waveforms

This section provides experimental evidence of IAP generation in the EUV spectral range and demonstrates the shot-to-shot and long-term stability of the synthesized driving waveforms.

4.4.1 IAPs driven by synthesized waveforms

Figure 4.11a-c presents HHG spectra generated in argon by different synthesized waveforms, each achieved by imparting a specific CEP shift, $\Delta\phi$, and delay, τ , between the IR and NIR pulses. In other words, for each case, the synthesized waveform was locked to a particular CEP and relative delay. Spectra were acquired following optimization of the gas cell position relative to the laser focus, while maintaining a constant pressure of 300 mbar. A 300-nm thick aluminum filter, placed before the toroidal mirror, blocked the residual optical driving beam.

The presented spectra represent the HHG emission at the streaking gas target, corrected for the spectral response of the CCD and 300 lines/mm grating. In each case, the solid line results from averaging 10^4 acquisitions, each integrated over 50 ms, with shaded areas representing standard deviations. The minimum observed in the spectra at ≈ 53 eV corresponds to the well-known Cooper minimum, resulting from the recombination of the electron with the parent ion [300].

The observed generation of both narrowband and broadband, continuous, and smooth EUV spectra suggests the successful of high-contrast IAPs. The primary fluctuations observed are in intensity, rather than in the spectral shape, indicating that the smooth spectral character cannot be attributed to averaging over various CEP values [57]. The r.m.s. energy fluctuations of these spectra are 17% and 12% for the broadband cases, and 7% for the narrowband case. This stability indicates high reproducibility of the driving field waveform in individual laser shots, as even minor waveform fluctuations would be amplified in the HHG spectrum. Additionally, the spatial distribution of these spectra was found to be smooth and continuous [297], confirming that spectral smoothness is not an artifact of spatial averaging.

Figure 4.11d further supports the generation of IAPs, as evidenced by the clear π -periodicity in both intensity and energy cutoff of the HHG spectra upon scanning the CEP (i.e., half-cycle cutoffs, see Sec. 3.5.1). This scan was obtained by collecting HHG spectra across a linearly scanned CEP range 0 to $\approx 4\pi$ of the synthesized waveform, while maintaining a fixed relative delay

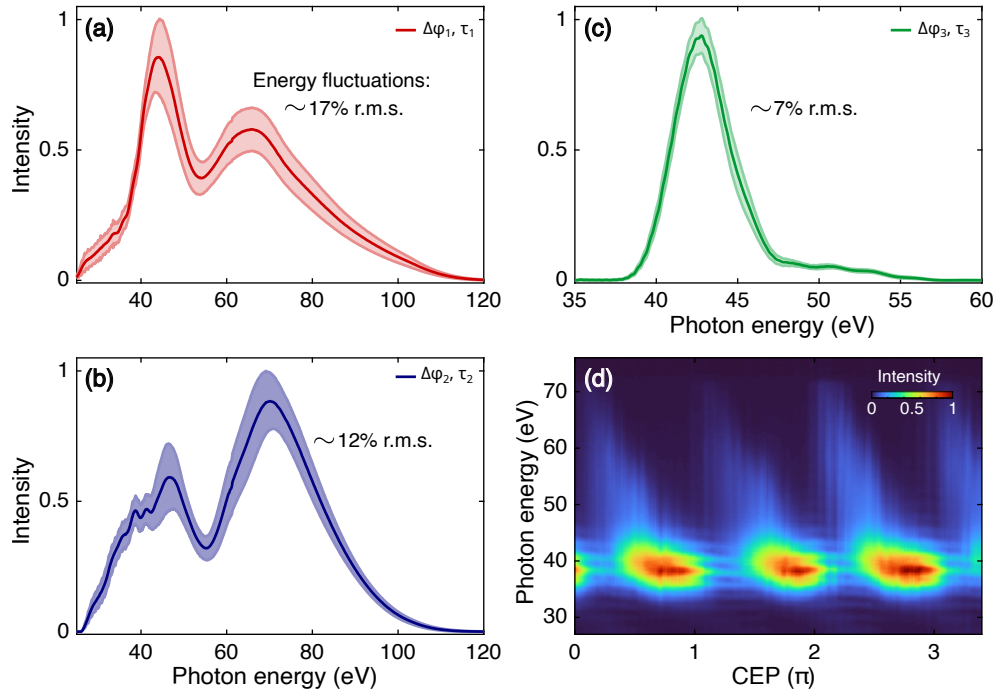


Figure 4.11: IAP spectra stability and half-cycle cutoffs in argon. (a-c) EUV continua driven by different synthesized waveforms (synthesis settings: $\Delta\varphi_i, \tau_i$) showing mean spectrum (solid line) and standard deviation over 10^4 spectra. (d) CEP-dependent HHG spectra evidencing half-cycle cutoffs. All spectra were acquired with 300 mbar backing pressure, the 300 lines/mm grating, 50 ms integration time, and a 300 nm Al filter.

between the NIR and IR pulses. The scan was performed using a driving waveform that yields a narrowband spectrum similar to that shown in Fig. 4.11c. While these half-cycle cutoffs are demonstrated here only for the narrowband case, the following chapter will show that broadband spectra also exhibit this pattern, indicating the generation of broadband IAPs.

4.4.2 Attosecond streaking and waveform reproducibility

To definitively confirm both the generation of IAPs and the reproducibility of the synthesized waveforms, the narrowband attosecond pulses centered at ≈ 42 eV (Fig. 4.11c) were used for attosecond streaking in neon ($I_p \approx 22$ eV). Ionization with the 43 eV IAP results in an electron wavepacket with a kinetic energy centered at ≈ 20 eV. The EUV-ionized electrons were then streaked by the optical field at a peak intensity of $4.6 \times 10^{11} \text{ Wcm}^{-2}$. The resulting streaking trace, shown in Fig. 4.12a, was acquired with a delay step size of 200 as and an integration time of ≈ 1 s per photoelectron spectrum. The absence of fringes in the streaking spectrogram confirms the generation of a high-contrast IAP. Although not shown in the figure, the pulse duration was reconstructed to be 280 as using the VTGPA [297].

4.4. Direct measurement of synthesized waveforms

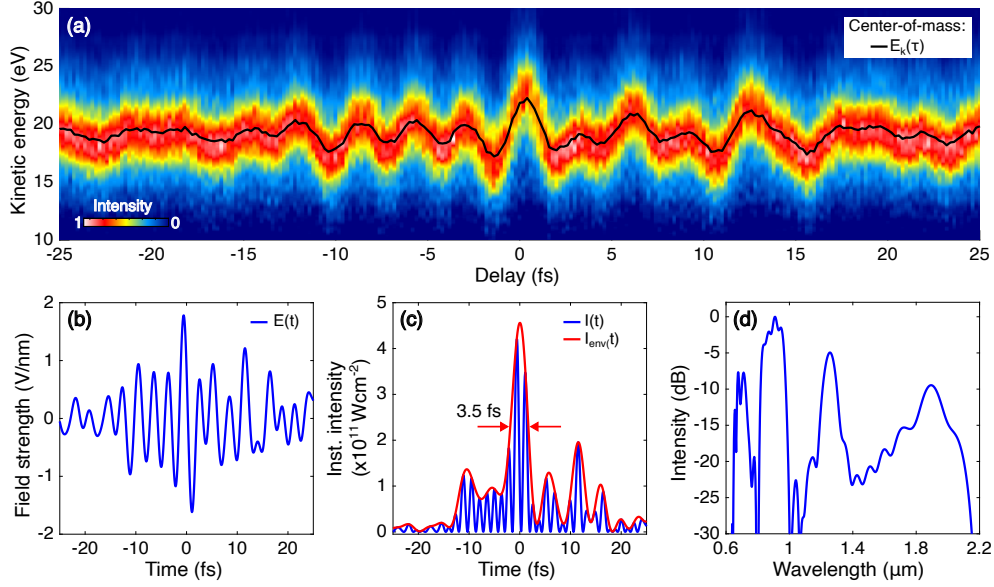


Figure 4.12: Direct electric field measurement of synthesized waveform. (a) Attosecond streaking spectrogram in Ne, with kinetic energy trace $E_k(\tau)$ (black solid line). (b) Retrieved electric field. (c) Instantaneous intensity (blue) and envelope (red). (d) Corresponding spectrum. Adapted from [110].

The resulting kinetic energy trace, obtained by extracting the center of mass of photoelectron spectra at each delay, is overlaid on the photoelectron spectrogram (Fig. 4.12a). Following the procedure outlined in Sec. 3.6.2, this trace is utilized to derive the streaking electric field waveform. The retrieved waveform, along with its instantaneous intensity and spectral intensity, are presented in Fig. 4.12b-d. The measured pulse duration (Fig. 4.12c) is only 3.5 fs. Furthermore, the spectral shape of the retrieved waveform encompasses all frequency components present in the NIR and IR pulses, preserving their spectral profiles and confirming coherent synthesis.

The central wavelength (centroid) of this retrieved spectrum is approximately 1.1 μm , corresponding to a 3.7 fs period. This implies the synthesis of a sub-cycle pulse lasting 0.9 cycles at this wavelength. Notably, the streaked waveform is not representative of the actual synthesized waveform driving HHG, as the recombination mirror adjusts the ratio between the constituent pulses. The actual synthesized waveform, designed to achieve sub-cycle duration, is characterized in the final chapter of this thesis, demonstrating the synthesis of 0.6-cycle pulses at 1.4 μm .

The long-term stability of the setup and the reproducibility of the synthesized waveforms are further demonstrated in Figure 4.13a-f, which presents six consecutive streaking spectrograms acquired over nearly three hours, each recorded over ≈ 30 min. Figures 4.13a-e utilize the same field wave-

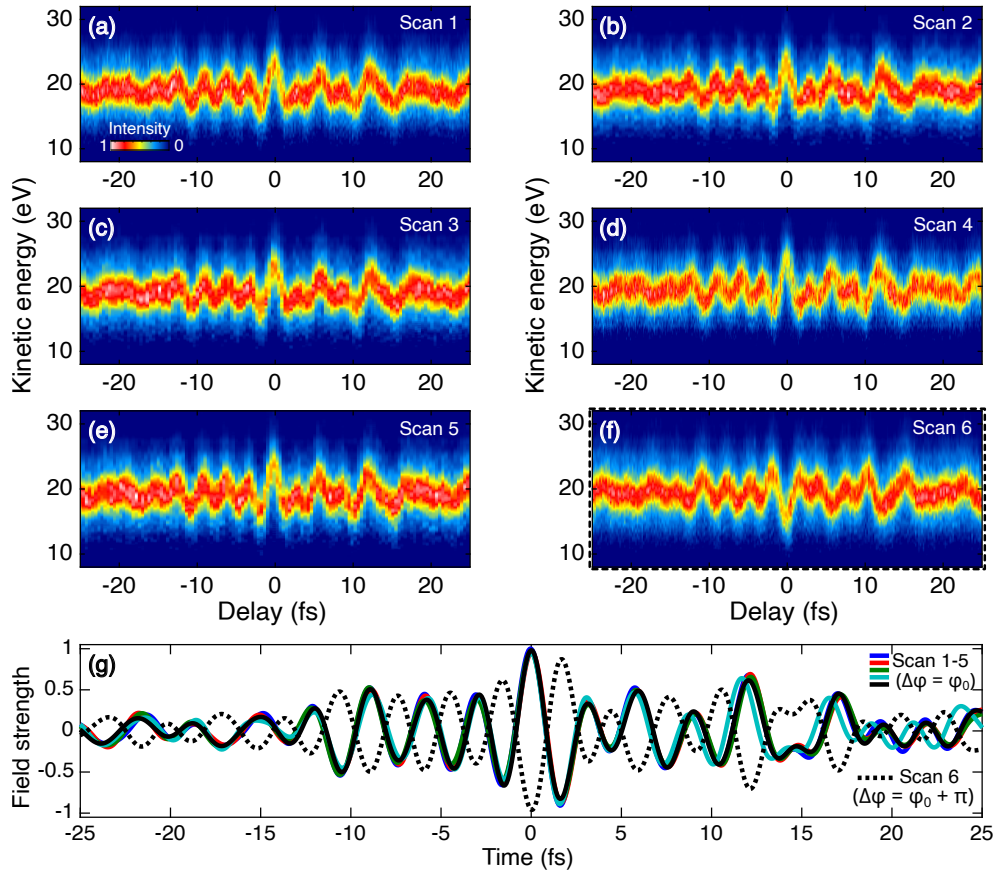


Figure 4.13: Reproducibility of synthesized waveforms. (a-e) Sequential streaking traces acquired with same electric field from Fig.4.12 and (f) with a π CEP shift. (g) Retrieved electric fields from streaking traces (a-e: solid line, f: dashed line). Adapted from [126].

form, while in Fig. 4.13f a CEP shift of π has been introduced. The corresponding retrieved electric fields are illustrated in Fig. 4.13g.

The consistent agreement between individual streaking traces and their associated retrieved fields underscores the long-term stability of the experimental apparatus. Moreover, the retrieved field from the trace in Fig. 4.13c precisely corresponds to a π -shifted field compared to the reference waveforms. Despite relying solely on passive stabilization for the attosecond beamline, minimal discrepancies are observed between retrieved fields, and these are primarily attributed to drifts within the HHG and streaking arm interferometers.

Tunable extreme ultraviolet isolated attosecond pulses

This chapter demonstrates the generation of tunable isolated attosecond pulses (IAPs) spanning the extreme ultraviolet (EUV) and soft X-ray spectral regions, with energies up to 200 eV. Attosecond streaking measurements confirm IAP emission, while single-atom simulations elucidate the underlying generation mechanism. The findings presented in this chapter are largely based on the work published in Ref. [256].

5.1 Sub-cycle control of attosecond pulses

The coherent superposition of two fields oscillating at different frequencies, such as one at twice the frequency of the other, enables sub-cycle tailoring of the synthesized waveform through controlled interference. As the three-step HHG process unfolds within a single cycle, this precise waveform control offers the potential to manipulate each step individually.

Figure 5.1 illustrates sub-cycle shaping achieved through such controlled interference. Two constituent Gaussian pulses, Field 1 centered at $1.6 \mu\text{m}$ and Field 2 centered at $0.8 \mu\text{m}$, are coherently superposed with a variable relative delay (see Fig. 5.1a). Field 2 remains fixed in time, while Field 1's delay is adjusted, with positive delays indicating its arrival before Field 2. Both pulses share a 7 fs duration, a common CEP set to zero, and a fixed intensity ratio where Field 2 possesses 30% of Field 1's intensity.

In the absence of the weaker Field 2, and for a near-single-cycle pulse like Field 1 with a 2.7 fs half-cycle duration, the dominant electron trajectories originate and recombine within a cycle defined by two consecutive half-cycles underneath the pulse's envelope. Depending on the chosen starting point (either the left or central half-cycle), this cycle encompasses either the

5. TUNABLE EXTREME ULTRAVIOLET ISOLATED ATTOSECOND PULSES

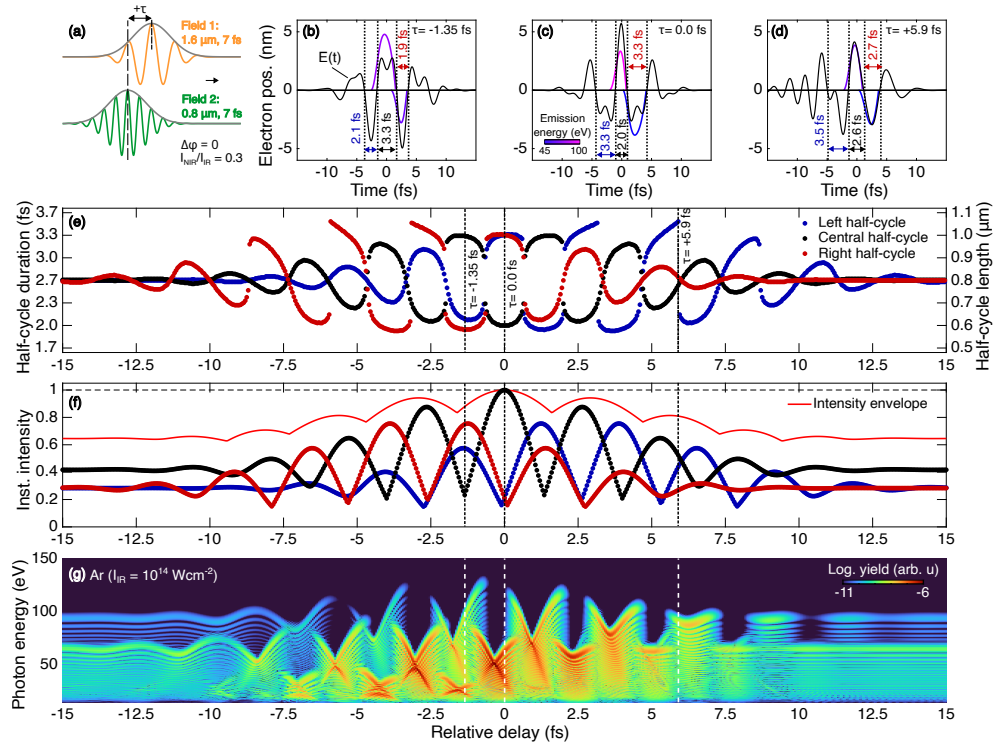


Figure 5.1: HHG sub-cycle control with tailored waveforms. (a) Gaussian constituent pulses Field 1 ($1.6 \mu\text{m}$) and Field 2 ($0.8 \mu\text{m}$) with 7 fs FWHM duration and CEP = 0. The intensity ratio of Field 2 to Field 1 is 0.3, with Field 1 delayed relative to Field 2 (positive delays indicate Field 1 arriving after Field 2). (b-d) Resulting synthesized waveforms at delays of -1.35 fs, 0 fs, and 5.9 fs, showing cutoff electron trajectories (color-coded by emitted photon energy) and half-cycle durations for dominant half-cycles. (e) Half-cycle duration (left axis) and corresponding half-cycle length (right axis) versus delay. (f) Peak intensity of dominant half-cycles versus delay, normalized to peak intensity under perfect overlap ($\tau = 0$ fs). Red solid line indicates the maximum intensity of the synthesized waveform's temporal envelope. (g) Simulated single-atom HHG spectra in argon versus delay, assuming a peak intensity of $1 \times 10^{14} \text{ Wcm}^{-2}$ for Field 1.

left and central or the central and right half-cycles. Within each cycle, electrons ionized in the earlier half-cycle recombine in the later one, with the ionizing half-cycle's amplitude primarily determining the brightness of the emitted harmonic burst, and the recombining half-cycle's amplitude and duration governing its cutoff energy. Thus, each consecutive pair of half-cycles effectively produces a unique harmonic cutoff with its corresponding yield. However, the coherent superposition of Field 1 and Field 2, complicates this picture. The resulting interference modifies each half-cycle, leading to variations not only in their amplitude and shape, but also in their duration. Consequently, consecutive half-cycles no longer form neat pairs, and the concept of a cycle becomes less straightforward. HHG then depends on the specific shape of the consecutive half-cycles, necessitating their individual consideration.

Figures 5.1b-d depict three distinct synthesized waveforms, each resulting from different relative delays between Field 1 and Field 2. Here, half-cycles are identified as waveform segments between consecutive nodes. In each of these cases, the three dominant half-cycles exhibit different shapes and duration, with the latter ranging from 1.9 fs to 3.5 fs. Additionally, the relative amplitudes of consecutive half-cycles vary, enabling configurations such as a dominant central half-cycle, equally intense left and right half-cycles surpassing the central one, or a less intense right half-cycle. These unique half-cycle configurations directly impact HHG, producing distinct cutoff trajectories and resulting in photon emission with energies ranging from 45 eV to 100 eV.

Figure 5.1e-f illustrates the detailed dependence of half-cycle reshaping on the relative delay between the two constituent fields. Figure 5.1e reveals the modulation of half-cycle duration and length, while Fig. 5.1f shows the modulation of the half-cycle maximum intensity (normalized to the peak intensity at zero relative delay). As expected, the half-cycle duration approaches that of the stronger Field 1 (2.7 fs) at large relative delays. Furthermore, the right (left) half-cycle experiences sinusoidal-like modulation in both duration and intensity when Field 2 trails (leads) Field 1, oscillating with a period approximately matching that of Field 2. Given the relationship between the HHG energy cutoff, with the intensity and wavelength, the cutoff of the emitted bursts is expected to be modulated when adjusting the relative delay. Furthermore, as left half-cycles reach maximum intensity at positive relative delays and encounter a less-depleted atomic medium, the harmonic yield is expected to be enhanced at positive delays compared to negative delays.

Figure 5.1f further reveals that the highest half-cycle intensities are achieved within the temporal overlap region of the two fields, approximately between -10 fs and 10 fs. These peak intensities, exceeding twice those observed at large relative delays, result in both an extension of the cutoff energy and an enhancement of the harmonic emission yield compared to those produced by Field 1 alone. Within this overlap region, the dominance of half-cycle intensity variations over half-cycle duration variations indicates that the cutoff modulation and extension is primarily driven by the increased intensity.

Figure 5.1e shows the corresponding single-atom HHG relative delay scan, illustrating the impact of half-cycle duration and intensity modulation on the HHG spectra as the relative delay is varied. Several features are observed: spectral fringes arising not only from spectrally-overlapping emissions (predominantly in the low-energy region) but also from interference between long and short trajectories, two distinct energy cutoffs ("low-energy" at ~ 60 eV and "high-energy" at ~ 100 eV) that exhibit a sinusoidal-like modulation with relative delay, increased harmonic yield and cutoff extension within the

overlap region, and asymmetry in yield favoring positive delays. Notably, the modulation of the low-energy cutoff closely mirrors the intensity pattern of the right half-cycle, while the high-energy cutoff follows the intensity pattern of the central half-cycle (Fig. 5.1f). This correspondence discloses that the high-energy cutoff is driven by the half-cycle pair comprising the left and central half-cycles, whereas the low-energy cutoff is driven by the pair involving the central and right half-cycles.

A number of previous experiments [301–306] have investigated HHG by varying the relative delay between two few- or multi-cycle NIR and IR pulses, typically centered around $\sim 0.8 \mu\text{m}$ and $\sim 1.4 \mu\text{m}$ and derived from a Ti:Sa pump laser and OPA. These studies consistently observed both cutoff extension (even reaching up to 160 eV and 200 eV in argon and neon, respectively [301]), and yield enhancement exceeding an order of magnitude within the temporal overlap region [303, 305]. However, it is likely that due to the use of phase-unstabilized pulses, clear modulations in the energy cutoff and yield, as shown in Figure 5.1e, were not readily apparent in the HHG spectra [306], nor was the generation of phase-stable attosecond pulses possible. In contrast, the experiments reported in this thesis employ nearly single-cycle pulses centered at $\sim 1.6 \mu\text{m}$ and nearly two-cycle pulses centered at $\sim 0.8 \mu\text{m}$, both derived from a waveform synthesizer. These characteristics—short pulse duration and phase stabilization—enable the study of not only HHG but also IAP generation upon scanning the relative delay [256].

While the preceding discussion focused on controlling the energy cutoff (and thus central energy) and yield of the emitted HHG radiation, it's important to note that the attochirp, scaling as $\beta \propto 1/I_0\lambda$ would also be modulated upon scanning the relative delay between the constituent pulses. Moreover, as the relative delay finely modifies the half-cycle shape, the ionization time of electron trajectories can also be controlled. This enables, for instance, placing the half-cycle peak close to the birth times of short trajectories, thereby enhancing their contribution in the emitted burst relative to long trajectories [48].

5.2 Waveform-controlled EUV continua

To investigate the extent to which the spectral amplitude and phase of EUV IAPs can be controlled, a systematic scan of HHG spectra is conducted, wherein each spectrum is associated with a distinct driving waveform. The PWS, as detailed previously (see Sec. 4.2.6), tailors these waveforms via two parameters: the relative delay (τ), encoded in the relative phase (RP) between the constituent pulses, and a common CEP shift ($\Delta\phi$), effectively controlling the resultant waveform's CEP. This waveform scan, represented

by an $M \times N$ matrix with each $(\tau_i, \Delta\phi_j)$ pair containing an HHG spectrum, is called an HHG RP-CEP or delay-CEP scan. This scanning approach extends previous work primarily in two ways: first, by employing constituent pulses capable of synthesizing sub-cycle pulses, and second, by achieving sub-cycle resolution through active stabilization of the RP and CEP, in contrast to unstabilized cross-correlation measurements, which are mainly sensitive to the overall envelope of the driving waveform. Furthermore, scanning over the CEP for each delay allows for the observation of CEP dependencies in the generated HHG spectra, allowing the identification of half-cycle cutoffs (see Sec. 3.5.1), a signature of IAP generation.

This measurement procedure is implemented using the experimental setup described in Sec. 4.3. In brief, the synthesized beam enters the attosecond beamline, where it is split into two components: one drives HHG within a gas target, and the other serves as the streaking field. A spherical mirror ($f = 375$ mm) focuses the HHG-driving beam into a gas target filled with either argon or neon, backed with 300 mbar of pressure. The gas target is positioned for optimal HHG cutoff and yield when driven by the IR pulse alone. Spectral filtering is achieved using either a 500 nm-thick beryllium filter, transmitting energies below ~ 110 eV, or a 300 nm-thick zirconium filter, transmitting energies below ~ 220 eV. The 300 lines/mm grating is employed to spectrally resolve the emission in the energy range from 15 eV to 65 eV, while the 1200 lines/mm grating enables the detection of higher-energy spectral components.

Prior to the HHG delay-CEP scan, a preliminary “unlocked” cross-correlation measurement is performed between the NIR and IR pulses, without actively stabilizing the RP or CEP. This measurement, completed within a few minutes and relying solely on the inherent CEP stability of the constituent pulses inherited from the CEP-stable seed, serves to rapidly identify the region of spectral overlap and establish a zero-delay reference point for the subsequent locked (actively-stabilized) scan. Figure 5.2 illustrates an example of such an HHG cross-correlation measurement using argon as the generation medium, with negative delays indicating the IR pulse preceding the NIR pulse. Figure 5.2a presents the scan obtained with a 300 lines/mm grating, while Figure 5.2b corresponds to the 1200 lines/mm grating. Features include: sinusoidal-like modulation of harmonics at large delays, increased HHG yield approximately within the -5 to 5 fs overlap region, apparent cutoff extension within this region approaching zero delay, asymmetry in HHG yield favoring positive delays, and the appearance of an harmonic continuum reaching the beryllium edge near the overlap region.

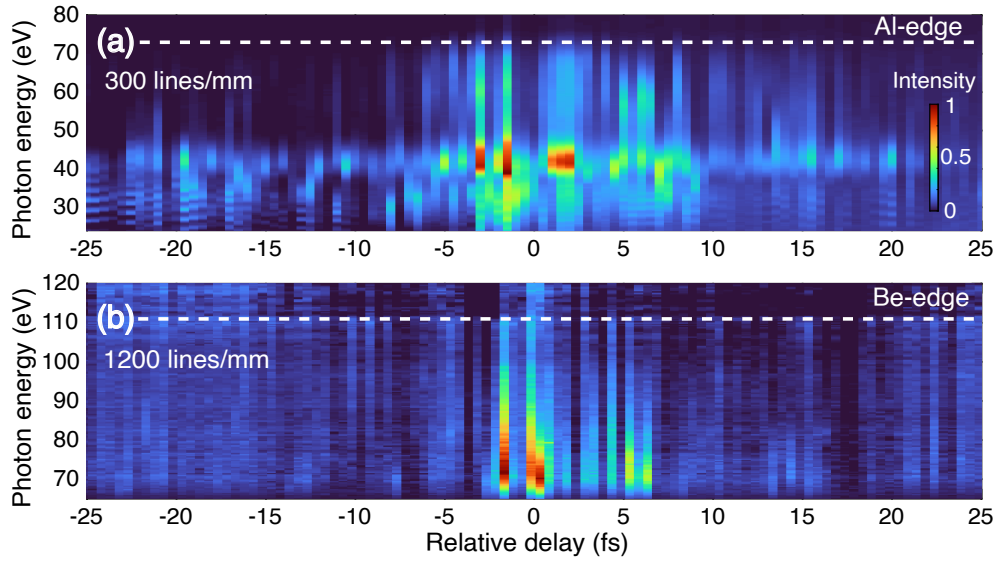


Figure 5.2: Unlocked HHG cross-correlation in argon. (a) Cross-correlation measured with the 300 lines/mm grating, 300 nm Al filter, 0.5 s integration time, and 0.5 fs delay steps. (b) Same as (a) but with the 1200 lines/mm grating and 500 nm Be filter, and 2 s integration time. The RP and CEP were not actively-stabilized in these measurements.

Waveform scanning procedure

Following the cross-correlation measurement and identification of a suitable scanning range, a locked HHG delay-CEP scan is performed. This scan commences with the relative delay shifted to a negative value. HHG spectra are continuously recorded while the CEP is swept over a range of approximately 3π radians using a sawtooth pattern with a 4-second period. This range and period allow for the grouping of HHG spectra driven by similar waveforms, considering the 2π periodicity of the CEP. Subsequently, the RP is incremented in 0.8 radian (delay step = 0.4 fs) steps over a total range of -40 to +40 radians (-20 to +20 fs), with two complete CEP scans performed at each RP step.

To correlate HHG spectra with specific $(\tau_i, \Delta\phi_j)$ pairs, an LED controlled by the active-stabilization system flashed the spectrometer at the beginning of each CEP ramp. This established an absolute time grid on the CCD data, ensuring synchronization with the control system. The resulting data matrix contained 4-8 highly reproducible spectra per bin. Finally, the average spectrum for each bin was calculated and stored in its corresponding $(\tau_i, \Delta\phi_j)$ bin, yielding a complete 100×16 RP-CEP matrix.

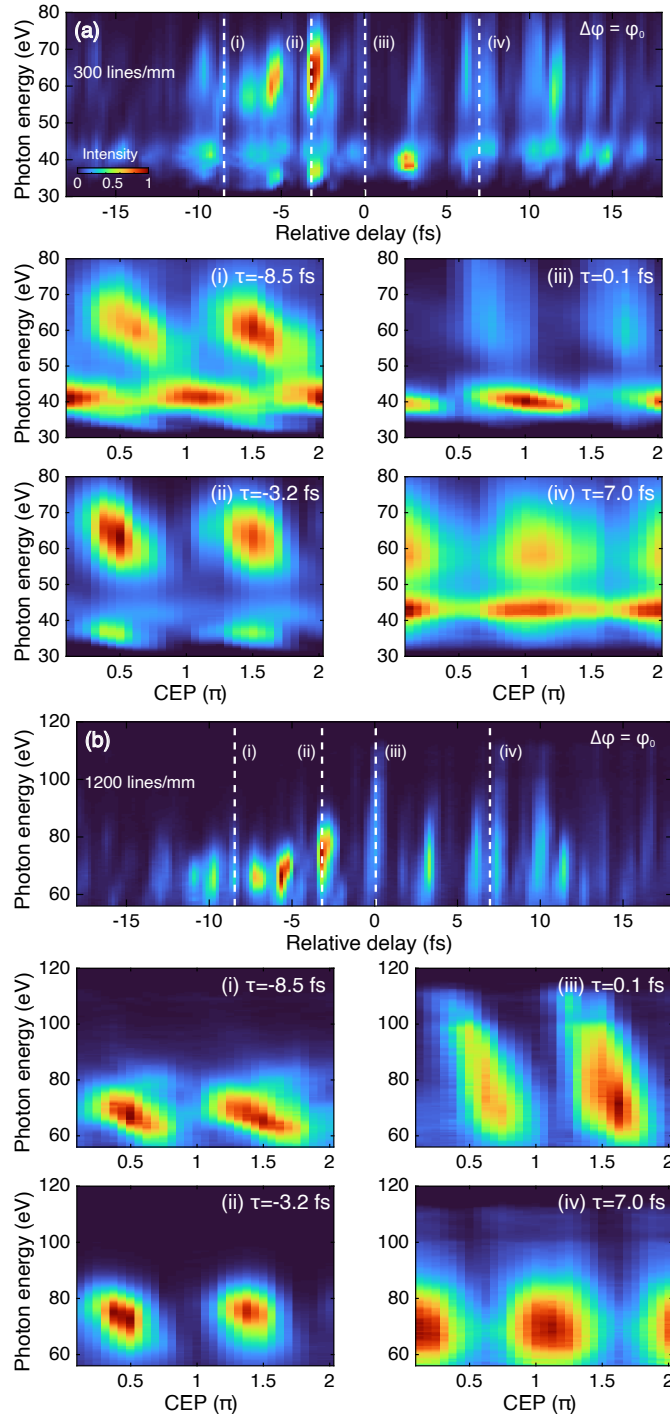


Figure 5.3: HHG delay-cep scan in argon. HHG spectra emitted from argon and recorded with two different gratings, (a, i-iv) 300 lines/mm and (b, i-iv) 1200 lines/mm, after passing through a 500-nm-thick Be filter. Each spectrum was integrated for 200 ms. (a, b) Delay scans at a fixed CEP ($\Delta\varphi = \varphi_0$), with negative values indicating the IR pulse arrives before the NIR pulse. (i-iv) CEP scans at various selected delay values. Adapted from [256].

5.2.1 HHG delay-cep scan

Figure 5.3a-b presents HHG delay-CEP scans recorded with 300 lines/mm and 1200 lines/mm gratings, respectively. Each panel displays cross-sections of the data set, showcasing relative delay scans at a fixed CEP of $\Delta\varphi = \varphi_0$ and CEP scans at selected relative delays. For the CEP scans, the CEP axis represents a shift relative to φ_0 rather than an absolute value.

The delay scans at fixed CEP exhibit the expected characteristic features, namely, an apparent cutoff extension and increased yield when the pulses approach temporal overlap. While sinusoidal-like modulations of the spectra have been observed in previous locked delay-CEP scans [109], they are absent in the present measurements (Fig. 5.3) due to the narrow scanning range focused on the high-yield region. Notably, within this overlap region, a vast majority of the EUV spectra exhibit a remarkably continuous, smooth profile with a broad plateau (35-100 eV), extending in some cases to the beryllium edge (~ 110 eV).

The diversity in EUV continua shapes and yields observed in the delay scan at a fixed CEP is further explored through CEP scans at specific delay values (-8.5 fs, -3.2 fs, 0.1 fs, and 7.0 fs). These scans reveal the generation of broadband IAPs, evidenced by the appearance of half-cycle cutoffs (see Sec. 3.5.1), i.e., a π -periodic modulation of the cutoff yield with CEP variation across the entire EUV bandwidth. Moreover, they demonstrate the potential for tailoring IAP spectral properties. For instance, at $\tau = -8.5$ fs, spectra peak around 40 eV at CEP $\sim m\pi$ and around 60 eV at $\sim (m + 1/2)\pi$. At $\tau = 0.1$ fs, the CEP scan demonstrates selective generation of either narrowband IAPs (at CEP values round $\sim m\pi$) or broadband IAPs extending to the beryllium edge (at $\sim (m + 1/2)\pi$). At $\tau = -3.2$ fs and 7.0 fs, only broadband IAPs are produced, but the spectral shape is skewed either towards higher (-3.2 fs) or lower (7.0 fs) energies depending on the relative delay.

In pursuit of extending the accessible photon energy range beyond the beryllium edge, a similar delay-CEP scan was conducted in neon. The backing pressure of the gas cell was maintained at 300 mbar, and the target position was adjusted closer to the beam focus to optimize the HHG yield. A 300-nm thick Zr filter was used to transmit photon energies above 80 eV, and the 1200 lines/mm was employed to spectrally-resolve the harmonic emission. Figure 5.4a presents a delay scan at a fixed CEP, revealing diverse soft X-ray continua shapes and yields, with the latter increasing as the pulses approach zero delay —replicating the trend observed in the EUV case, with energies reaching up to ~ 200 eV.

A cross-section at a fixed relative delay of 0.4 fs from this HHG delay-CEP scan (Fig. 5.4b) shows clear half-cycle cutoffs across a spectral range of 60 eV to 200 eV, further supporting the generation of IAPs in this regime. Extracted

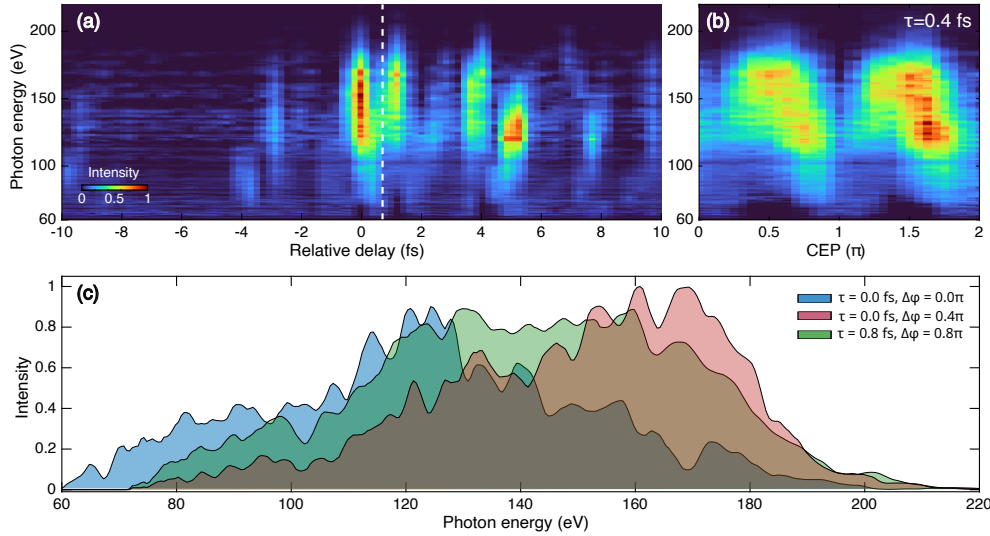


Figure 5.4: HHG delay-cep scan in neon. HHG spectra emitted from neon recorded with the 1200 lines/mm grating, after passing through a 300-nm-thick Zr filter. Each spectrum was integrated for 200 ms. (a) Delay scan at a fixed CEP, with negative values indicating the IR pulse arrives before the NIR pulse. (b) CEP scan at a selected delay value ($\tau = 0.4$ fs, white dashed line in (a)). (c) Representative single HHG spectra extracted from the full HHG delay-cep scan. Adapted from [256].

lineouts (Fig. 5.4c) demonstrate that tailoring the driving waveform pulses enables tunable spectra peaking at 120 eV, 145 eV, and 170 eV.

Taken together, these measurements demonstrate the generation of EUV and soft X-ray continua with argon and neon, respectively, spanning a combined tunable range from 30 to 200 eV. Notably, this broad tunability is achieved solely by adjusting the gas type and target position, while maintaining a constant gas pressure. Furthermore, the spectral shape of these continua can be tailored exclusively through sub-cycle manipulation of the driving waveform. CEP scans indicate that these spectrally tailored continua correspond to IAPs.

5.2.2 Attosecond pulse characterization

To verify the generation of IAPs and characterize their temporal profile, attosecond streaking measurements were performed with narrowband and broadband HHG emission generated in both argon and neon. The streaking apparatus, identical to the one described in Sec. 4.3, involved a spherical mirror ($f = 500$ mm) that focused the streaking field onto a neon gas target at a backing pressure of a few mbars. A 100-nm thick aluminum filter was employed to block the residual optical beam in the HHG arm, and the intensity of the streaking field was adjusted using a variable aperture.

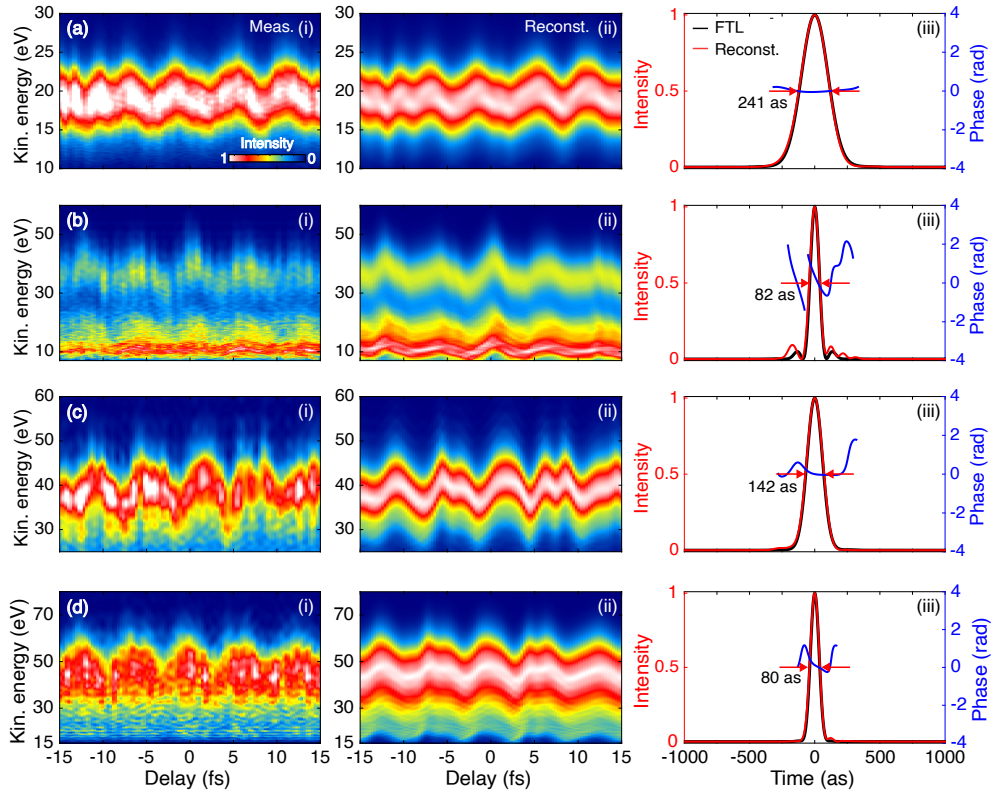


Figure 5.5: Isolated attosecond pulse reconstruction. Attosecond streaking in Ne with (a-b) Ar-driven and (c-d) Ne-driven HHG. Shown are: (i) measured trace, (ii) reconstructed trace, and (iii) reconstructed IAP temporal profile (red, left axis), corresponding FTL pulse (black), and instantaneous phase (blue, right axis). Adapted from [256].

The results of these streaking measurements are presented in Fig. 5.5, which shows measured streaking spectrograms alongside reconstructed spectrograms and the corresponding reconstructed IAPs, obtained with VTGPA (see Sec. 3.6.4). In Figs. 5.5a-b, HHG was driven in argon, while in c-d, HHG was driven in neon. The measurement of well-defined attosecond streaking traces, coupled with the successful reconstruction of IAPs, confirms their generation in all cases. The reconstructed traces and photoelectron spectrograms exhibit strong agreement, with the IAP durations nearly matching the FTL duration of their corresponding spectra (240 as and 80 as for argon-driven HHG, and 142 as and 80 as for neon-driven HHG). The near-uniform intensity distribution of the streaking traces further validates the quasi-chirp-free nature of the reconstructed IAPs. Moreover, as expected, any residual chirp lacks a negative component, indicating that these IAPs originate predominantly from the recombination of short trajectories favored by the phase-matching conditions.

The pulse energies and photon flux values of the reconstructed IAPs, inte-

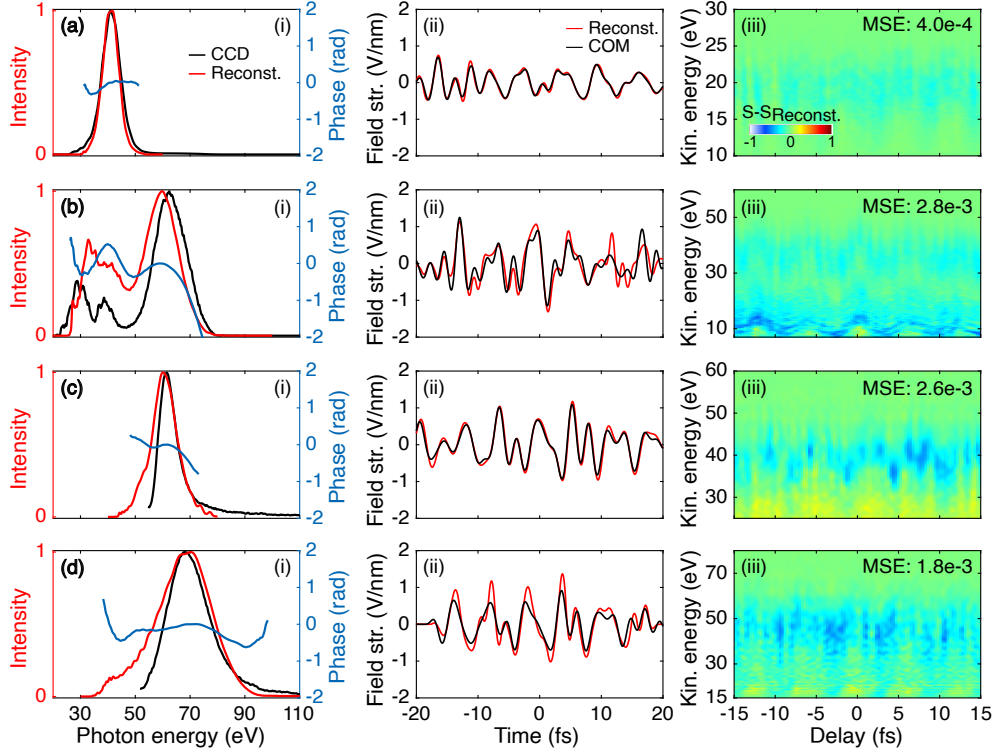


Figure 5.6: Reconstruction fidelity assessment. Validation of streaking traces from photoelectron spectrograms shown in Fig. 5.5 with (a-b) Ar-driven and (c-d) Ne-driven HHG: (i) Reconstructed spectrum (red, left axis) and spectral phase (blue, right axis) compared to independently CCD-measured spectrum (black, left axis). (ii) Retrieved streaking fields using center of mass (COM, Sec. 3.6.2) and VTGPA methods. (iii) Error spectrogram (difference between normalized experimental and reconstructed spectrograms), with residual mean squared error (MSE) after 300 iterations indicated. Adapted from [256].

grated over their full spectral range, were also measured. For the argon-driven IAPs (Fig. 5.5a-b), pulse energies are 467 pJ and 79 pJ, respectively, corresponding to photon flux values of 7.2×10^{10} and 9.2×10^9 photons/s. For the neon-driven IAPs (Fig. 5.5c-d), the corresponding pulse energies are 11 pJ and 13 pJ, with photon flux values of $1e \times 10^9$ and $1.1e \times 10^9$ photons/s. This order-of-magnitude difference in yield between the argon- and neon-driven IAPs is attributed to the lower ionization rate of neon compared to argon, which also manifests as a reduced signal-to-noise ratio in the corresponding streaking traces (Fig. 5.5c-d). These values were measured at the streaking target location, with corresponding values at the HHG source (upstream in the beamline) estimated to be approximately 20% higher.

While the streaking measurements presented thus far focused on spectra within the operational range of the TOF spectrometer, attempts were also made to characterize broader spectra, such as those reaching the beryllium edge shown in Fig. 5.3(iii). Despite successfully generating measurable pho-

toelectron signals, the TOF's limited energy range introduced significant distortions in the intensity distribution of these broadband signals, preventing reliable measurements. However, the streaking traces presented in Fig. 5.5, which fell within the TOF's operational range, exhibited minimal distortion. The photoelectron spectra closely matched the expected single-photon transition profile, calculated as the product of the squared neon dipole moment and the photon spectrum measured with the CCD, after accounting for the instrument's transfer function (metal filter, grating, and CCD).

To ensure the fidelity of the reconstruction process, several independent verification measures were employed, as illustrated in Fig. 5.6. The reconstructed EUV spectra (derived from the streaking traces) closely match those measured independently with the CCD spectrometer (Fig. 5.6a). Similarly, the reconstructed streaking fields from the VTGPA are in close agreement to those obtained independently using the center-of-mass (COM) method (see Sec. 3.6.2 and Fig. 5.6b). The minimal difference between measured and reconstructed streaking traces, and the mean square error (after 300 iterations) of 10^{-3} or less (Fig. 5.6c), further supports the high fidelity of the reconstruction. This was additionally corroborated by consistent results obtained from independent reconstructions of different segments of each streaking trace shown in Fig. 5.5 (e.g., encompassing two consecutive half-cycles of the streaking field), which exhibited a maximum discrepancy of $\sim \pm 1\%$.

5.3 Single-atom HHG modeling with synthesized waveforms

To gain insights into the mechanisms governing IAP generation and the spectral tunability observed experimentally, single-atom HHG simulations are performed using realistic waveforms achievable with the PWS. These simulations begin by constructing the synthesized electric field in the frequency domain, leveraging the complex spectral representations (amplitude and phase) of the constituent NIR and IR pulses obtained from 2DSI measurements (Secs. 2.6.1 and 4.2.4). To tailor the synthesized waveform, the relative delay (τ) between the pulses is introduced via a linear phase term applied to the IR field, and a common CEP shift ($\Delta\varphi$) is added to both fields.

The time-domain representation of the synthesized field, $E(t)$, is then obtained by an inverse Fourier transform on their coherent sum:

$$E(t) = \mathcal{F}^{-1} \left\{ \left[E_{\text{NIR}}(\omega) + E_{\text{IR}}(\omega)e^{-i\omega\tau} \right] e^{i\Delta\varphi} \right\} \quad (5.1)$$

In this equation, $E_{\text{NIR}}(\omega)$ and $E_{\text{IR}}(\omega)$ represent the complex spectral representations of the NIR and IR pulses. The simulation framework allows

5.3. Single-atom HHG modeling with synthesized waveforms

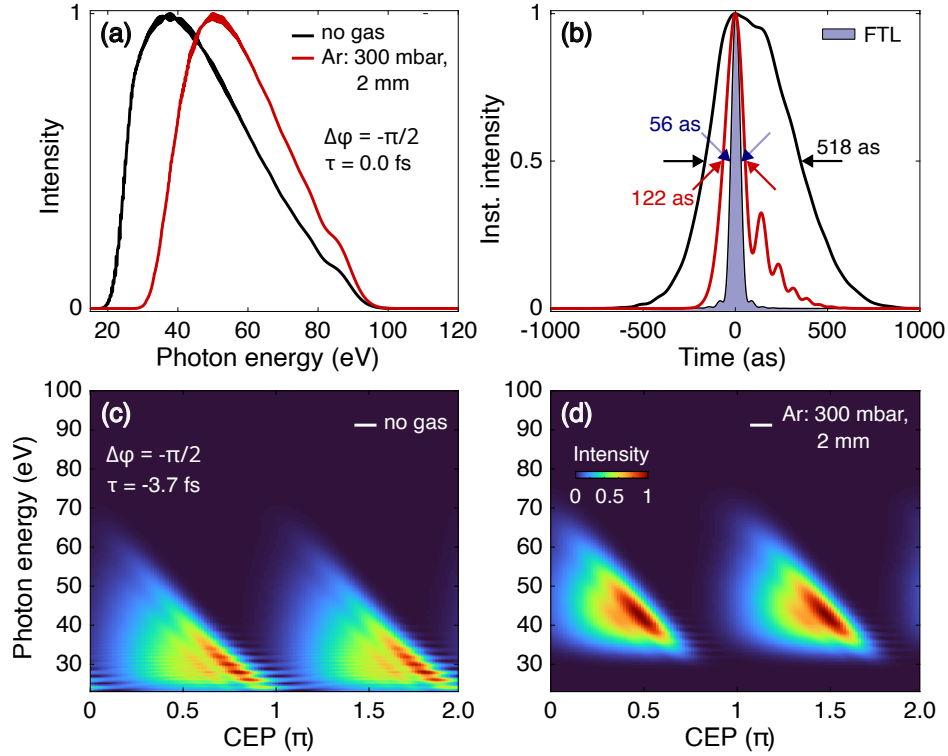


Figure 5.7: Attosecond pulse propagation in argon. (a-b) Spectral and instantaneous intensities of an IAP without (black) and with (red) propagation through 2 mm of Ar at 300 mbar. (c-d) HHG spectra vs. CEP under (c) no propagation and (d) with propagation. The driving waveform uses synthesized NIR and IR pulses (measured via 2DSI), with a peak intensity of $2.5 \times 10^{14} \text{ Wcm}^{-2}$ under perfect overlap and an NIR to IR intensity ratio of 0.25. The synthesis parameters ($\tau, \Delta\phi$) are indicated. The single-atom response simulation considers only short trajectories.

for adjusting the intensity of each pulse, which is encoded in its spectral amplitude. For the presented simulations, the peak intensity of the synthesized waveform is set to $2.5 \times 10^{14} \text{ W}\cdot\text{cm}^{-2}$ at perfect overlap between the constituent pulses ($\tau = 0, \Delta\phi = 0$). The intensity of the NIR pulse is set to one-quarter of the IR pulse intensity.

The simulations exclusively consider the contribution of short trajectories, motivated by their favorable phase-matching conditions and higher fluence at the detector due to reduced divergence compared to long trajectories [202]. This choice is further supported by the observation that the reconstructed IAPs predominantly originate from short trajectories (Fig. 5.5). Additionally, the simulations incorporate the spectral response (i.e., the complex refractive index) of the 2 mm thick argon generation medium at 300 mbar pressure into the computed complex harmonic field, $E_h(\omega)$ (c.f. Eq. 3.14), as specified by Eqs. 2.4-2.5.

The impact of incorporating argon's spectral response is illustrated in Fig. 5.7. For a broadband IAP (Fig. 5.7a-b), the strong absorption below ~ 40 eV (Fig. 3.8b) effectively removes the strongly chirped, low-energy components, reshaping the IAP spectrum. This spectral filtering significantly affects the temporal profile of the IAP. Without considering the argon response, the pulse duration is 518 as. However, incorporating the argon response, which includes both the negative chirp in the strong absorption region and the absorption itself, reduces the pulse duration to 122 as, which is more than twice its FTL duration of 56 as. Similarly, for the CEP scan with a narrow-band EUV spectrum (Fig. 5.7c-d), which reveals half-cycle cutoffs, incorporating the argon response eliminates low-energy spectral fringes. This elimination of fringes facilitates the removal of low-energy satellite pulses, thereby enabling the generation of an IAP.

Figure 5.8a shows a simulated delay scan at a fixed CEP of $-\pi/2$, where positive delays indicate the IR pulse arrives after the NIR pulse. The simulations qualitatively reproduce the experimental delay scan (Fig. 5.3), demonstrating periodic bright HHG continua alternating with low-yield regions. This pattern arises from the constructive and destructive interference of half-cycles at different delays, as illustrated in Fig. 5.1. The resulting half-cycles with weaker amplitudes lead to the emission of lower-energy photons that are more susceptible to absorption by the gas medium. Conversely, at delays where the half-cycles have higher amplitudes, the electrons are accelerated to greater energies, leading to the emission of photons with energies falling within the more transparent region of the gas medium.

Expanding upon the simulated delay scan, extracted continua at specific delays (-3.6 fs, -0.2 fs, and 3.0 fs) shown in Fig. 5.8b illustrate a variety of smooth, continuous spectra with diverse bandwidths, specifically a narrow-band centered around 40 eV, a broadband extending beyond 100 eV, and an intermediate bandwidth reaching up to 80 eV. These spectra correspond to FTL durations of 273 as, 57 as, and 90 as, respectively. Figures 5.8c-e elucidate the specific waveforms driving these spectra, the responsible short electron trajectories, and the corresponding emitted attosecond pulses. In all cases, the simulations predict the generation of IAPs, consistent with the experimental observations and analysis that both narrowband and broadband continua are emitted as IAPs. Of special note is the close agreement between the narrowband IAP duration and the FTL duration, aligning with the VT-GPA reconstruction in Fig. 3.17a. However, for broader bandwidth IAPs, the simulated durations are up to nearly twice their FTL durations. This discrepancy between simulated and reconstructed durations is attributed to the simulations' neglect of phase-matching effects, which can significantly impact the temporal characteristics of broader bandwidth emissions.

The computed electron trajectories, weighted by their emission probability

5.3. Single-atom HHG modeling with synthesized waveforms

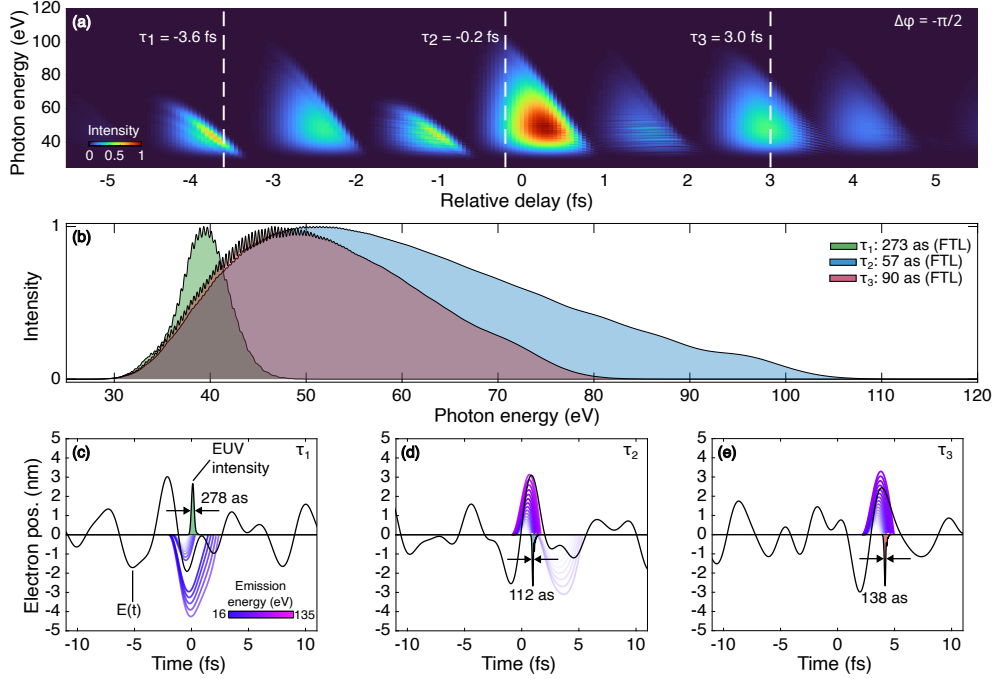


Figure 5.8: Single-atom HHG delay scan for argon.(a) Simulated EUV spectra as a function of IR-NIR delay (positive delays indicate IR arriving after NIR) at fixed CEP = $-\pi/2$, including linear propagation through 2 mm of argon at 300 mbar. Only short trajectories are considered. (b) EUV spectra lineouts at selected delays (dashed lines in (a)), with corresponding FTL pulse durations indicated. (c-d) Classical electron trajectories (purple) and emitted EUV attosecond bursts (shaded areas) for the synthesized waveforms at the selected delays. Trajectories are color-coded by emitted photon energy, and transparency reflects their emission probability (see Sec. 3.1.5). Synthesized waveform parameters are as in Fig. 5.7. Adapted from [256].

(see Sec. 3.1.5), predominantly reveal a single dominant ionization and recombination event occurring near the strongest half-cycle of the driving waveform. This observation supports the notion that IAP generation is largely driven by the confinement of electron ionization within a single optical cycle (see Fig. 3.2). Analyzing these trajectories further elucidates the distinct mechanisms underlying the generation of narrowband and broadband IAPs, as detailed below.

For the waveform driving the narrowband continuum (Fig. 5.8c), electron ionization occurs primarily within the dominant half-cycle peaked at $t = -2$ fs. The subsequent weaker half-cycle accelerates and recombines these electrons, resulting in photon emission centered around 40 eV. Analysis of the electron trajectories reveals two distinct recombination times contributing to this emission: $t = 0$ fs, corresponding to the main IAP, and $t = 2.7$ fs. Trajectories recombining around 2.7 fs originate closer to the peak of the half-cycle, suggesting a high probability of contributing to HHG emission. In contrast, trajectories recombining near 0 fs originate from ionization at

a weaker segment of the half-cycle, making them less probable. However, their shorter travel time minimizes wavepacket spreading in the continuum, compensating for the reduced ionization probability and resulting in comparable emission strength to the 2.7 fs trajectories. The presence of faint spectral fringes across the entire bandwidth of the narrowband spectrum (see Fig. 5.8b) is attributed to the emission of photons with similar energies at these distinct recombination times ($t = 0$ fs and $t = 2.7$ fs). This is further supported by the temporal profile of the emission, which, upon closer inspection, reveals a second, weaker burst at 2.7 fs (not clearly visible in Fig. 5.8b due to its small scale) in addition to the main IAP at 0 fs. Despite comparable theoretical emission probabilities, the observed dominance of one emission is likely due to the model's neglect of the overlap integral between continuum and bound states (Sec. 3.1.5).

In contrast to the narrowband case, the waveform generating the broadband continuum involves the participation of three half-cycles in harmonic emission, with the central cycle (formed by two consecutive half-cycles peaking at $t = -1$ fs and $t = 1$ fs) being the dominant contributor. The half-cycle peaking at $t = -1$ fs primarily ionizes the electrons, while the subsequent half-cycle, being 20% stronger, accelerates them to energies sufficient for recombination and emission of photons exceeding 100 eV. The analysis further reveals that this stronger half-cycle can itself ionize a second set of trajectories, which recombine in the following, much weaker half-cycle with a duration of approximately 3.6 fs. This second recombination results in photon energies roughly 50% lower (≈ 50 eV) than those emitted in the first recombination. While ionization alone would suggest comparable emission strengths for both sets of trajectories, the shorter travel time of the first set (recombining at $t = 1$ fs) minimizes wavepacket spreading, leading to a higher emission probability compared to the trajectories recombining in the subsequent, longer half-cycle.

Finally, the waveform producing the intermediate bandwidth primarily ionizes electrons within the half-cycle peaked at $t = 2$ fs, with subsequent recombination occurring within the half-cycle peaking around $t = 4$ fs. Notably, the ionizing half-cycle is only about 20% stronger than the recombining half-cycle, ensuring that the recombining trajectories lead to the emission of relatively high-energy photons, up to approximately 80 eV. In this case, the confined ionization within the strongest half-cycle predominantly determines the IAP emission.

Thus, this analysis demonstrates that sub-cycle tailoring of the driving waveforms, facilitated by the PWS, enables the generation of tunable IAPs. The broad bandwidth of the synthesized waveforms provides the necessary flexibility to precisely shape individual half-cycles, thereby controlling the ionization, acceleration, and recombination steps of the HHG process. This

5.3. Single-atom HHG modeling with synthesized waveforms

precise control, coupled with the achievable sub-cycle duration of the waveforms, ensures that the resulting HHG emission occurs in the form of an IAP.

Water-window, soft X-ray isolated attosecond pulses

This chapter presents the generation of attosecond pulses within the soft X-ray spectral range, specifically the water window (284-543 eV), using helium and neon. Through a combination of experimental data and simulations, underlying mechanisms of IAP generation in this regime are elucidated. Absolute photon flux values are provided for various intensity and phase-matching conditions. Additionally, it is demonstrated that HHG driven by tailored synthesized waveforms can achieve higher efficiency compared to HHG driven only by the IR field. The direct characterization of driving fields at the HHG source enables the identification of the waveforms responsible for this enhancement.

6.1 Soft X-ray HHG beamline

Designing an apparatus for generating and detecting high-order harmonics in the water window spectral region using infrared lasers presents two key challenges. The first is the low photon flux of the harmonics at the HHG source, due to the efficiency scaling of $\propto \lambda^{-(5-6)}$ [41]. This flux is further reduced at the target and detector, resulting in weak signal levels. The second challenge involves managing the multi-atmospheric pressures of neon or helium, which are required for efficient phase-matching of the generated harmonics (Sec. 3.2.2).

Several strategies can be employed to address the challenge of low photon flux, beyond optimizing the HHG process itself for maximum efficiency. These include reducing absorptive elements in the beam path, selecting optical coatings with maximal reflectivity, using spectrometers with high detection efficiency for the relevant energy range, and employing noise reduction techniques to improve the signal-to-noise ratio. The challenge of operating

at multi-atmospheric pressures can be addressed with powerful pumping systems and differential pumping schemes.

In this work, the apparatus described in Sec. 4.3 was modified to incorporate some of these strategies. The main modifications are illustrated in Fig. 6.1. To maximize HHG photon flux, the beam splitting for the streaking arm was removed, directing all laser energy to the HHG arm. Additionally, a CCD camera¹ can temporarily replace the gas target when needed to characterize and optimize the beam profile and focusing quality, thereby improving both HHG efficiency and harmonic beam quality [212].

To manage the multi-atmospheric pressures at the HHG gas target, the following measures were implemented:

- **Differential pumping housing:** This custom-made aluminum housing, designed and built by Dr. Scheiba [297], is directly connected to a vacuum pump and isolates the high-pressure gas target and the xyz-motorized stage that positions it. Two brass screws with conical holes further limit gas flow into the main chamber, reducing the overall gas load. The *HiPace 1500* turbo molecular pump then extracts any remaining gas, maintaining vacuum levels of $\approx 10^{-2}$ to 10^{-1} mbar, even when operating the gas target at pressures of up to 10 bars.
- **Metallic gas cell:** A metallic gas cell with variable thickness (0.5–1.5 mm) is used as the gas target. The cell is laser-drilled by the same focused beam that drives HHG, minimizing gas outflow as the hole diameter is about the size of the beam's spot. The input hole is larger than the output hole: the larger input allows more energy into the gas cell, while the smaller output reduces the amount of gas escaping. Although the output hole may clip the fundamental beam, this is not an issue since the HHG mode is smaller. This design makes it easier for the pump to maintain the required vacuum levels. The optimal hole size, which balances maximum beam throughput with manageable gas load, is achieved by laser-drilling the cell while scanning it along the focused beam axis and rastering it transversally in concentric circles. This method typically produces holes as small as ≈ 200 μm .
- **Pumping system:** A robust pumping system is implemented to handle high gas loads, particularly from light noble gases like neon and helium, while preserving the necessary vacuum levels in the remaining sections of the beamline. Initially, two scroll pumps² sufficed for limited durations, enabling short-term measurements before the gas pressure caused the turbo pumps to spin down. Subsequently, a roots

¹daA3840-45uc, Basler AG

²XDS35i (Edwards Vacuum)

pump³ backed by a multistage roots pump⁴ was installed, reducing the gas pressure by two orders of magnitude [297] and enabling sustained high-pressure operation.

- **Controlled valve:** A calibrated, actively-stabilized valve⁵, capable of handling pressures from ≈ 100 mbar to 10 bar, maintains a consistent preset backing pressure for the gas target and ensures its precise measurement and control.

After generation, the resulting soft X-ray HHG beam exits the high-pressure management system and passes through either a 100 nm or 150 nm aluminum filter⁶ held within a gate valve⁷ installed between the first and second chambers. This filter setup blocks the residual optical driving beam, minimizes scattered light along the propagation axis, and reduces gas flow into the beamline. The *Luxel* filters were selected for their high manufacturing quality, particularly their lack of pinholes, which helps prevent unwanted light from reaching the detector.

While the aluminum filter effectively blocks most optical light, it still transmits harmonics within the EUV range (≈ 10 – 120 eV). To further attenuate these harmonics, which can be orders of magnitude brighter than those in the soft X-ray range (>120 eV), a 100 nm Luxel copper filter, mounted on a filter wheel, is employed. Although less effective at blocking optical light, the copper filter efficiently absorbs these stronger EUV harmonics. Together, the 100 nm aluminum and copper foils form a short-pass filter, achieving transmissions on the order of 10^{-3} in the EUV range and below 10^{-4} at lower photon energies, while isolating soft X-ray harmonics. However, this leads to transmission values between 0.1 and 0.5 in the water window range. A single 200-nm thick titanium filter can provide higher transmission levels (e.g., >0.5 above 300 eV), but it also allows greater transmission of VUV and EUV photon energies (5–30 eV), which can become particularly intense when using the synthesized beam.

The filtered HHG beam is then imaged as close as possible to the entrance slit of the spectrometer by a gold-coated toroidal mirror configured in a 2f-2f geometry ($f = 373$ mm, 86-degree AOI). When the upstream aluminum and copper filters are not in use, a titanium or aluminum filter placed directly in front of the spectrometer blocks the residual optical light. The spectrometer employs the 2400 lines/mm grating to resolve the generated harmonics in the spectral range beyond 200 eV. Compared to the EUV range (the focus of Ch.4-5), the reflective optics used in this spectral range result in lower

³Ruvac WH700, (Leybold)

⁴Ecodry 65 plus, (Leybold)

⁵EL-PRESS-960036, (Bronkhorst)

⁶VF111, Luxel

⁷01.0 Mini UHV Gate Valve, VAT Group AG

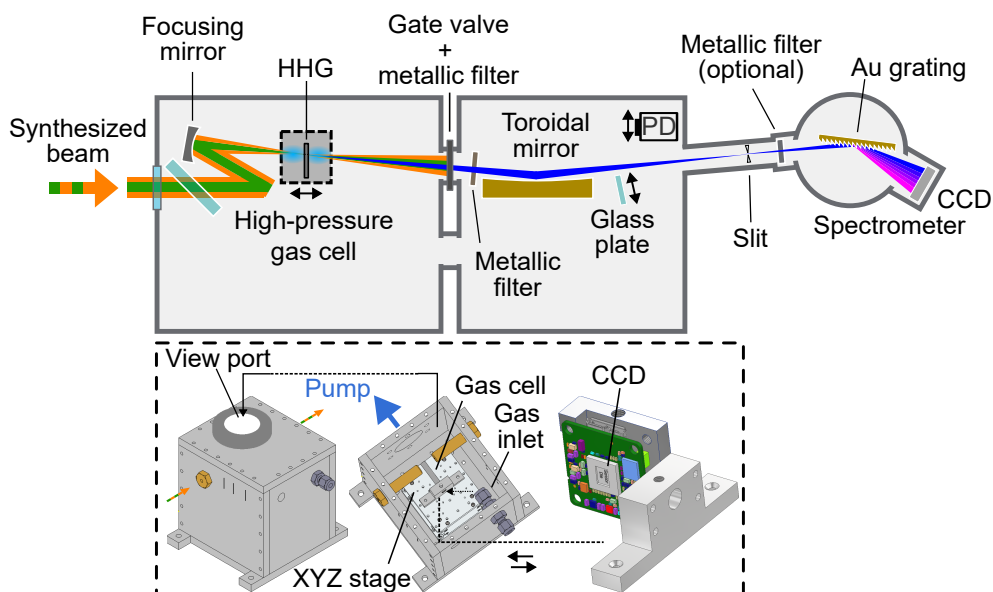


Figure 6.1: Water window HHG beamline. Based on the beamline in Fig.4.8, this modified version keeps the CaF_2 plate (previously used also for beam splitting) for pulse compression before the focusing mirror ($f = 500, 400, \text{ or } 200 \text{ mm}$). The beam is focused into a metallic gas-cell (replaceable with a CCD camera for beam profiling) enclosed in an aluminum housing with an xyz-motorized stage (inset) [297]. The gas load exiting the gas-cell is directly extracted by the roots and multistage roots pumps. Brass screws with drilled conical holes limit the gas flow into the main chamber, where the turbo molecular pump maintains vacuum. A gate valve with integrated metallic filter and additional filters block residual light. A movable glass plate can be inserted into the beam path to absorb soft X-rays for background subtraction. The toroidal mirror images the beam near the entrance slit of the CCD spectrometer operating with the 2400 lines/mm grating.

detected signals due to reduced efficiency. Specifically, the gold coating's reflectivity drops from about 80% in the EUV range to 40% beyond 200 eV, while the grating efficiency is limited to around 5% (Fig. 4.9b). To prevent further signal loss near the carbon absorption edge, the optics are periodically cleaned with UV light⁸ to remove carbon contamination from airborne organic particles [307].

A glass plate, mounted on a translation stage and positioned after the toroidal mirror, enables background subtraction from the soft X-ray signal. When inserted into the beam path, the plate absorbs soft X-rays while transmitting most of the optical light, allowing for the recording of a background signal comprising solely optical noise. By subtracting this background from the total signal, a clean, background-free measurement of the soft X-ray signal is obtained. To further minimize optical noise during measurements, all light sources within the apparatus, including hot filaments in pressure gauges and close-loop actuator indicators, are deactivated.

⁸HNS 6 W G5, (Osram GmbH)

6.2 Phase-matching water window HHG

The generation of water window HHG emission was investigated under varying focusing conditions ($f = 200, 400, 500$ mm), corresponding to different intensity levels. The study began by generating HHG with the IR pulse alone, followed by the utilization of synthesized waveforms. As detailed in Sec. 4.2.5, for all focusing scenarios, the spot sizes at focus and focal planes of the NIR and IR beams are matched as closely as possible, ensuring that the Rayleigh length of the NIR beam is approximately twice that of the IR beam ($z_R^{\text{NIR}} \approx 2 \cdot z_R^{\text{IR}}$). The NIR to IR intensity ratio for all cases is estimated to be $\approx 30\%$. Additionally, unless otherwise specified, all spectra presented in this section were binned into 128 pixels along the diffraction axis. After calibration [297], this resulted in an energy axis with an average energy bin size of 4.5 eV within the 200–500 eV range.

6.2.1 HHG driven by IR pulses

Figure 6.2 shows gas-cell position scans in neon at various backing pressures. A spherical mirror with a focal length of 500 mm was used, resulting in an estimated peak intensity (at focus) of $\approx 2.7 \times 10^{14}$ Wcm $^{-2}$. To average out CEP effects, the CEP was linearly scanned from 0 to 2π multiple times for each recorded spectrum.

The gas-cell scans reveal that for each pressure, there exists a gas-cell position around which the signal maximizes. This position can shift from +0.5 mm to -0.75 mm as the backing pressure increases from 1 bar to 4 bar, with the overall signal yield maximizing at 3 bar. This shift is accompanied by a decrease in the energy cutoff from ≈ 280 eV to 260 eV. Such pressure-dependent behavior, as detailed in Sec. 3.2.2, arises from the interplay between gas dispersion (neutral atoms and plasma) and dipole phase, which must balance the Gouy phase for optimal phase-matching.

Increasing the intensity to $\approx 4.3 \times 10^{14}$ Wcm $^{-2}$ using a 400 mm focal length enabled the generation of water window harmonics, as demonstrated in Fig. 6.3 for neon (2 bar) and helium (8 bar). A series of gas-cell pressure scans (not shown, but similar to Fig. 6.2) revealed that the phase-matching pressure for neon is 2 bar, as indicated in Fig. 6.3. In helium, higher yields were observed at 10 bar, but due to turbo pump performance limitations, measurements at this focal length were restricted to 8 bar.

Figure 6.3 also shows that the maximum observed photon energy in neon is approximately 310 eV, while helium reaches up to 450 eV, despite both gases being driven at the same peak intensity. Such highest observed photon energy in neon corresponds to the phase-matching cutoff, a concept introduced in Sec. 3.2.1. As discussed in that section, when the intensity exceeds a certain threshold—referred to as the critical intensity—it leads to a plasma fraction

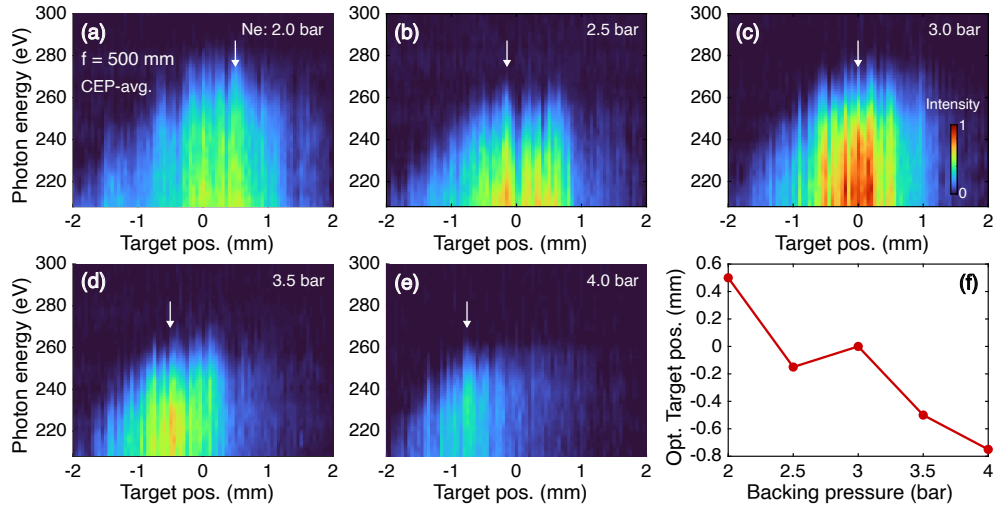


Figure 6.2: HHG gas-cell scans in Ne driven by IR pulse ($f = 500$ mm). HHG spectra as a function of gas target position, measured at backing pressures of (a) 2 bar, (b) 2.5 bar, (c) 3 bar, (d) 3.5 bar, (e) and 4 bar. (f) Optimal target positions (highest integrated signal; white arrows in a-e) versus backing pressure. In (a-e), each spectrum was filtered with a 200 nm Ti filter, and integrated for 2 s. Spectra are averaged over the CEP and are shown as recorded by the CCD. The optimal target position at 3 bar was defined as the zero position. Positive position values indicate the gas target is further from the focusing optic and negative values closer.

that surpasses a critical value, η_{cr} , beyond which phase-matching becomes increasingly difficult. This critical intensity defines the maximum photon energy that can be phase-matched, and it is known as the phase-matching cutoff (Eq. 3.39). For a 7-fs Gaussian pulse centered at $1.6 \mu\text{m}$, this cutoff is 345 eV and is reached at a critical intensity of $4.3 \times 10^{14} \text{ Wcm}^{-2}$ (see Fig. 3.10). In helium, the critical intensity is $\approx 40\%$ higher, meaning plasma effects are not yet dominant in scans shown in Fig. 6.3c-d, and the highest observed photon energy remains close to the value predicted by the single-atom cutoff formula (Eq. 3.11).

The CEP scans in Fig. 6.3b-d, taken at the +1.2 mm gas-cell position for both neon and helium, show a strong dependence of the half-cycle cutoffs on the CEP. This behavior is consistent with the near-single-cycle duration of the IR pulse (as discussed in Sec. 3.5.1) and further supports the potential for generating IAPs via amplitude gating (see Sec. 3.5). To implement this gating technique, spectral filtering would need to select energies above ≈ 280 eV for neon and above 380 eV for helium.

Finally, Fig. 6.4a-b shows gas-cell scans in neon (8 bar) and helium (10 bar) with tighter focusing ($f = 200$ mm), using an off-axis parabolic mirror to achieve a peak intensity of $\approx 4.5 \times 10^{14} \text{ Wcm}^{-2}$. This intensity is lower than the four-fold increase expected compared to $f = 400$ mm due to lower available pulse energies and potential astigmatism introduced by the parabolic

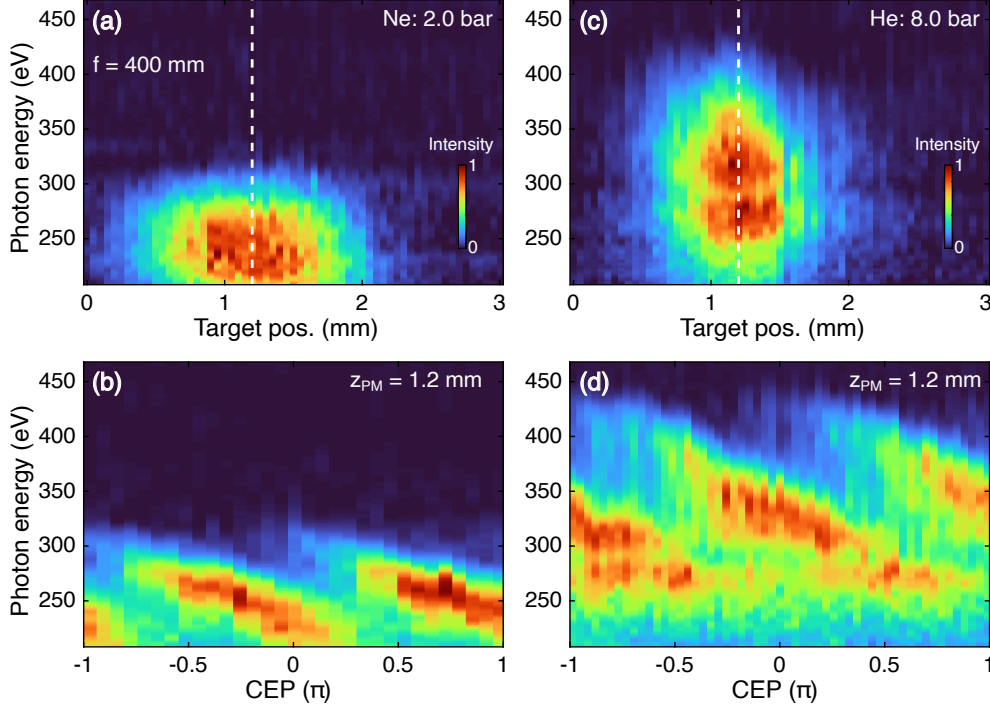


Figure 6.3: HHG gas-cell and CEP scans in Ne and He driven by IR pulse ($f = 400$ mm). (a-b) Ne at 2 bar: HHG spectra vs. gas target position (a), and vs. CEP at 1.2 mm (b, white dashed line in (a)). (c-d) Same as (a-b) but for He at 8 bar. Spectra were filtered with a 100 - nm Al and Cu filters, and integrated for 2 s ((d) for 1 s). Spectra in (a, c) are averaged over IR pulse's CEP.

mirror. Unlike previous measurements, the IR pulse CEP was locked for these scans. In neon (Fig. 6.4a), this results in a clear decrease of the photon energy as the gas target moves across the focus (from before to after). This reduction is attributed to the decreasing intensity of the driving field as the target moves further from the focus. Fig. 6.4c shows lineouts extracted from the gas-cell scans of neon (-0.15 mm) and helium (+0.10 mm), revealing broad spectra with neon reaching the critical phase-matching cutoff around 345 eV and helium extending up to 450 eV. The noticeable absorption dip around 284 eV in the helium spectrum is caused by carbon contamination on the optics.

Based on the measured Rayleigh lengths ($z_R^{\text{IR}} \approx 3, 2, 0.5$ mm for $f = 500, 400,$ and 200 mm, respectively) the estimated phase-matching pressures (see Sec. 3.2.2) for neon are $\approx 1, 2,$ and 8 bar, respectively, and $\approx 3, 4,$ and 15 bar for helium. These values are within approximately a factor of two of the reported backing pressures. For the 200 mm focal length, the estimated phase-

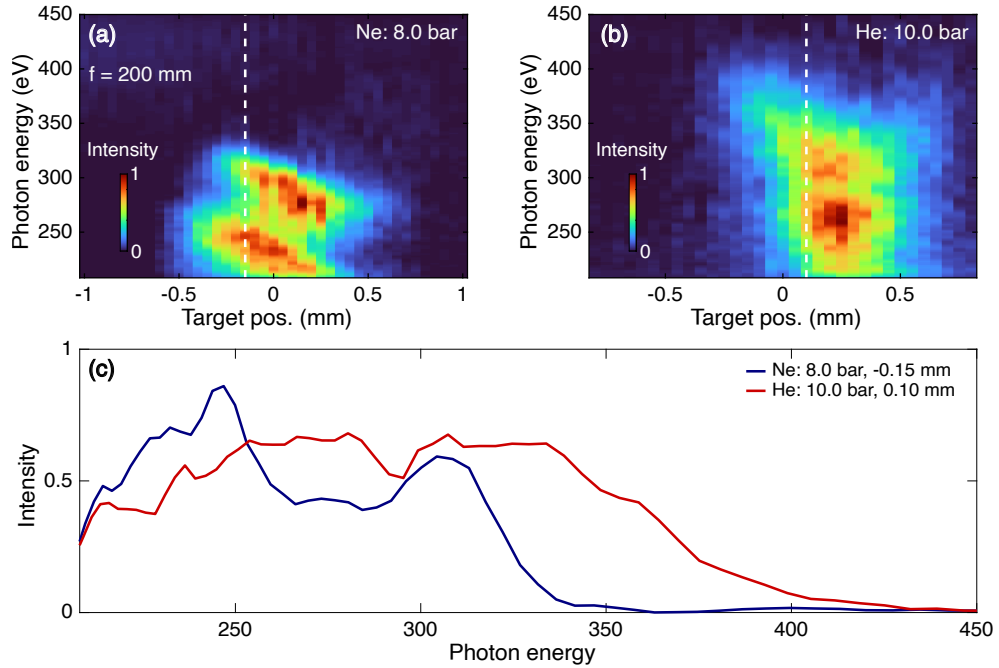


Figure 6.4: HHG gas-cell scan in Ne and He driven by IR pulse ($f = 200$ mm) with locked CEP. HHG spectra as a function of gas target position for Ne at 8 bar (a) and He at 10 bar (b). (c) Lineouts of single HHG spectra extracted from (a) and (b) at the selected positions (white dashed lines). Each spectrum was filtered with a 300-nm thick Ti filter and integrated for 2 s.

matching pressure in helium exceeded the gas valve's operational limit of 10 bar, precluding any measurement at higher pressures.

6.2.2 HHG driven by synthesized waveforms

To explore water-window HHG driven by synthesized waveforms, the NIR pulse was superimposed onto the IR field. Unlike the delay scans in Ch. 5, where the IR pulse was delayed relative to the NIR pulse, the roles are reversed in this section due to changes in beam path within the PWS. Negative delays now indicate the NIR pulse arriving before the IR pulse, and positive delays indicate the opposite. Here, the zero delay position was defined as in Ch. 5. Although the optimal phase-matching conditions for HHG driven by the IR pulse alone were known, minimal adjustments were made to maximize the signal yield in the temporal overlap region where both fields start to strongly interfere.

Figure 6.5 presents relative delay scans at a fixed CEP in neon for each focal length. For $f = 500$ mm (Fig. 6.5a), at large delays, the cutoff photon energies closely match those observed with the IR pulse alone (≈ 250 eV). Scanning the NIR pulse reveals a sinusoidal modulation in the photon energies, with a period closely matching that of the NIR pulse (≈ 2.8 fs). As

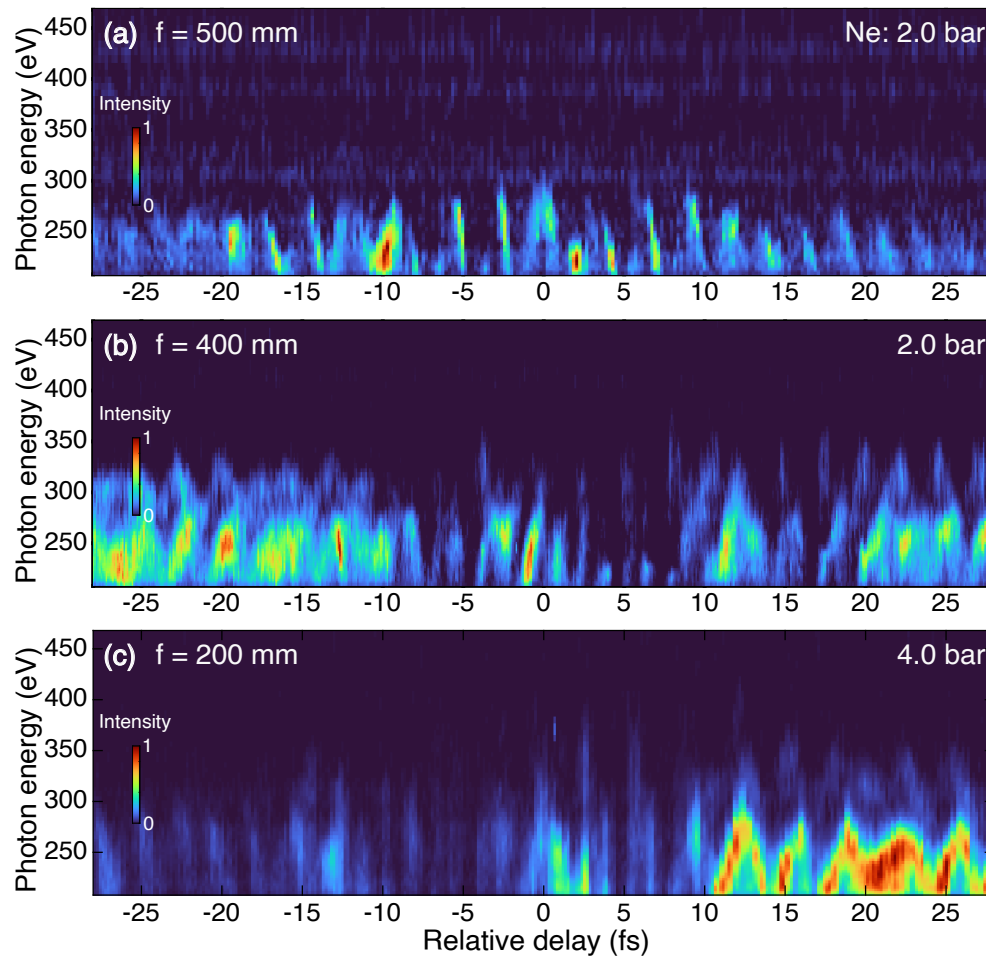


Figure 6.5: HHG delay scans in Ne with varying focal lengths. (a-c) HHG spectra vs. NIR-IR delay (negative delays indicate NIR pulse arriving first) at fixed CEP, using focusing mirrors of (a) 500 mm, (b) 400 mm, and (c) 200 mm focal lengths. The backing pressures are indicated. Spectra were filtered with 100 nm Al and Cu filters (a-b) or a 300 nm Ti filter (c), and integrated for 1 s (a-b) or 2 s (c). Delay steps: 0.2 fs (a), 0.1 fs (b), and 0.17 fs (c). Zero delay may not indicate actual temporal overlap of the NIR and IR pulses.

the pulses approach overlap, the increased intensity from the synthesized waveforms results in both an increase in yield and a rise in the energy cutoff from ≈ 250 eV (at large delays) to ≈ 300 eV (near overlap). These results align with the qualitative behavior predicted by the single-atom response delay scan shown in Fig. 5.1.

In contrast, the behavior observed with $f = 400$ mm (Fig. 6.5b) is more complex. Two distinct cutoffs, at approximately 250 eV and 300 eV, emerge, each associated with different half-cycles of the driving field—the stronger half-cycle producing the higher cutoff and a weaker, neighbouring half-cycle generating the lower one. As the relative delay increases -and the intensity of

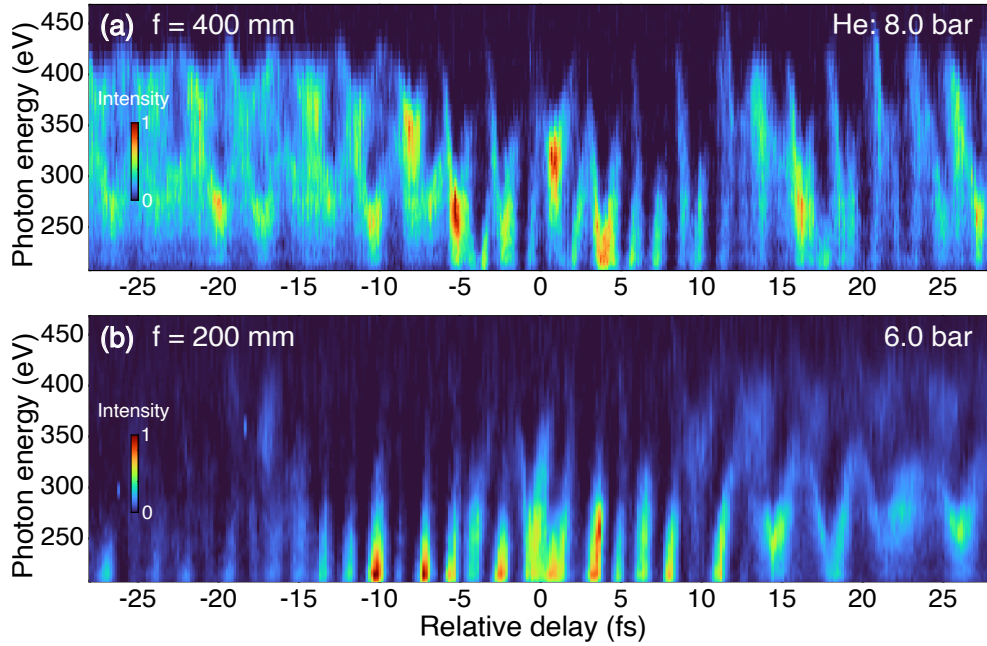


Figure 6.6: HHG delay scans in He with varying focal lengths. (a-b) HHG spectra vs. NIR-IR delay (negative delays indicate NIR pulse arriving first) at fixed CEP, using focusing mirrors of (a) 400 mm, and (b) 200 mm focal lengths. The backing pressures are indicated. Spectra were filtered with 100 nm Al and Cu filters (a) or a 300 nm Ti filter (b), and integrated for 1 s (a) or 2 s (b). Delay steps: 0.10 fs (a) or 0.16 fs (b). Zero delay may not indicate actual temporal overlap of the NIR and IR pulses.

the synthesized field decreases- these cutoffs become more distinguishable. Both cutoffs continue to exhibit sinusoidal modulation as the relative delay is scanned. However, in contrast to the results with the 500 mm focal length or the predictions from the single-atom response, the yield of the higher cutoff diminishes significantly as the pulses approach temporal overlap ($\tau \approx -10$ to 20 fs), leaving only the lower energy cutoff visible. In some cases (e.g., $\tau = 0-10$ fs), even the remaining cutoff yield decreases sharply.

At the highest intensity achieved with $f = 200$ mm (Fig. 6.5c), a substantial reduction in the overall signal yield is observed over a wide range of relative delays. This contrasts with the behavior at 400 mm, where the low-energy cutoff persists across most delays. Additionally, for both the 200 mm and 400 mm focal lengths, emission beyond the phase-matching cutoff (≈ 345 eV) remains negligible, further indicating that intensity alone does not lead to higher-energy emission under these conditions.

Figure 6.6 shows relative delay scans in helium for $f = 400$ and 200 mm (HHG was not observed at the lower intensities achievable with $f = 500$ mm). Due to helium's higher ionization potential, higher intensities are required to achieve similar plasma levels as those observed in neon. Similar

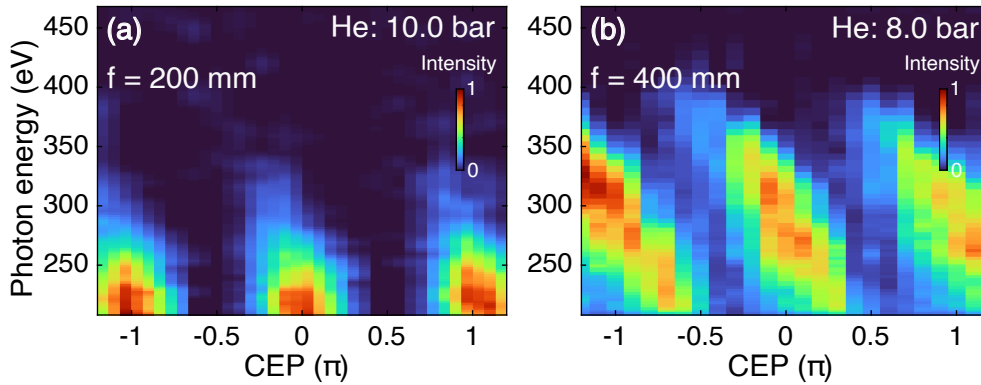


Figure 6.7: HHG CEP scans with synthesized pulses in He. HHG spectra vs. synthesized pulse CEP (at fixed near-zero NIR-IR delay) for (a) $f = 200$ mm focusing (filtered with two 100 nm Al filters) and (b) $f = 400$ mm focusing (filtered with 100 nm Al and Cu filters). In (a) each spectrum was integrated for 2 s and in (b) for 1 s.

to the results in neon, the $f = 400$ mm case (Fig. 6.6a) reveals two distinct half-cycle cutoffs, now reaching 300 eV and 400 eV, with sinusoidal modulation as the NIR pulse delay is scanned. As the pulses approach overlap, the yield at the highest photon energies (near the 400-eV cutoff) decreases, leaving predominantly photon energies around the 300-eV cutoff.

At even higher intensities with $f = 200$ mm (Fig. 6.6b), unlike in neon, the signal in the overlap region is not fully suppressed. Instead, bright emissions with photon energies below 300 eV remain, suggesting that both the half-cycle responsible for this emission and the emission itself can still be phase-matched, even at these higher intensities.

Overall, the collection of data from delay scans at different focal lengths in both neon and helium, along with the gas-cell scans presented in the previous section, consistently shows that increasing intensity does not always lead to a higher cutoff energy. As will be shown in the next section, plasma levels must be carefully controlled to maintain proper phase matching, as excessive plasma generation can disrupt the conditions required to produce higher-energy photons.

Building on the analysis of intensity effects and phase matching, the next step is to assess whether the synthesized field under different focusing conditions can still generate IAPs. Examining the spectral modulation as a function of the CEP of the synthesized fields reveals a clear π -periodicity. Figure 6.7 illustrates this behavior in helium for the $f = 200$ mm and $f = 400$ mm focal lengths. The CEP scans were acquired at relative delays near perfect overlap between the pulses. Unlike the IR-only CEP scans (Fig. 6.3), which showed IAP generation was limited to the cutoff region, the current CEP scans with the synthesized fields demonstrate that the bandwidth

of the IAPs can extend into the plateau region, as evidenced by minimal overlap between consecutive broadband π -periodic patterns.

While measuring photon flux is essential for determining the optimal conditions—whether neon or helium, and under which focusing (intensity) scenario—several factors made it difficult to identify the best configuration in this experimental campaign. For instance, switching focal lengths altered the focal spots, and despite careful alignment, residual astigmatism varied between setups. Looser focusing also required larger gas-cell apertures to ensure sufficient beam throughput, which increased gas flow and raised beam-line pressures to the mbar range, reducing the turbo pump’s ability to maintain sub-mbar vacuum levels. Consequently, each change in focal length involved balancing beam throughput with maintaining acceptable vacuum conditions. Additionally, periodic optimization of the OPAs between focusing conditions introduced subtle variations in pulse and beam properties, further complicating the evaluation. Nevertheless, representative and highest observed photon flux values for both IR pulses and synthesized pulses under different focusing scenarios are reported in Ref. [297].

In addition to a systematic study comparing photon flux at different intensities and with various driving fields, understanding the mechanisms behind the experimental observations necessitates modeling the generation process under multi-atmospheric pressures with multi-octave spanning, sub-cycle driving fields, similar to those used in the experiment. Furthermore, analyzing the time-frequency profile of the emitted HHG radiation can help distinguish between isolated emissions and those that are not. These topics will be addressed in the following sections.

6.3 On-axis macroscopic modeling of HHG

Macroscopic modeling of the HHG process under high-intensity and high-pressure conditions is essential for gaining insights into its underlying mechanisms. However, performing a full 4D (or 3D, assuming cylindrical symmetry) simulation that considers all spatial and temporal dimensions, while simultaneously scanning pressure, gas target position, and driving waveform, is computationally impractical.

Building on the success of the on-axis phase-matching analysis presented in Sec. 3.2, which effectively captured key experimental observations such as pressure dependencies in gas-cell scans and the phase-matching cutoff in neon, a simplified on-axis macroscopic model is employed here. This model, closely following Refs. [170, 216, 219], integrates the electric field wave equation along the propagation axis, neglecting transverse variations. Although simplified, this approach provides a computationally feasible way to explore and optimize HHG under realistic experimental conditions. Many

of the variables and parameters used in this model are defined in Chs. 2 and 3.

6.3.1 Optical driving field propagation

The initial step in macroscopically describing HHG involves computing the propagation of the optical driving field through the medium. This allows for the computation of single-atom dipole moments at each axial position, which are then coherently summed to simulate the macroscopic buildup of the HHG beam. This decoupled computational approach is justified by the negligible back action of the harmonic beam on the driving field, as the harmonic intensity is orders of magnitude weaker than the optical field [219].

To describe this propagation, the influence of the neutral atomic gas and generated plasma must be considered. Using the Slowly-Evolving Wave Approximation (SEWA), which is valid for pulses with durations near a single optical cycle [308], the resulting equation for a plane wave optical field, expressed in the reference frame of the speed of light as $\tilde{E}(t)$, is given by:

$$\begin{aligned} \frac{\partial \tilde{E}}{\partial z}(\omega, z) = & i \left[k(\omega) - k_n(\omega, z) \right] \tilde{E}(\omega, z) \\ & + \frac{i}{2\omega c} \mathcal{F} \left\{ \frac{\partial J_{\text{abs}}}{\partial t}(t, z) + \omega_p^2(t, z) \tilde{E}(t, z) \right\}, \end{aligned} \quad (6.1)$$

where $k_n(\omega, z)$ accounts for the linear dispersion and is scaled according to the medium's density, $\rho(z)$. The medium density is defined as $\rho(z) = P(z)n_0$, with $P(z)$ being the pressure distribution (see Sec.3.2). The term involving the plasma frequency ω_p^2 , defined as

$$\omega_p^2(t, z) = \frac{e^2 \rho(z) \eta_e(t, z)}{\epsilon_0 m_e}, \quad (6.2)$$

describes plasma dispersion and leads to blue-shift (see Sec. 3.3). This frequency becomes both time- and spatially-dependent due to the medium's density distribution and the continuous deformation of the optical field along the propagation axis. If transverse coordinates were considered, this term would also encompass plasma defocusing. Finally, the term J_{abs} in Eq. 6.1 accounts for the energy loss from the laser field due to strong-field ionization of the medium, and is given by [170]:

$$J_{\text{abs}}(t, z) = \rho(z) [1 - \eta_e(t, z)] \frac{I_p w(|\tilde{E}(t, z)|)}{\epsilon_0 |\tilde{E}(t, z)|^2} \tilde{E}(t, z), \quad (6.3)$$

Focused propagation

The previously discussed equation is valid for a plane wave. To account for beam focusing, the synthesized beam is modeled as the coherent sum of N constituent beams, \tilde{E}_j :

$$\tilde{E}(\omega, z) = \tilde{E}_1(\omega, z) + \tilde{E}_2(\omega, z) + \dots + \tilde{E}_N(\omega, z). \quad (6.4)$$

Each constituent beam is assumed to follow the longitudinal axial profile of a focused Gaussian beam (see Sec. 2.1.4). According to these equations, the on-axis ($r = 0$) field of the j -th constituent beam can be expressed as:

$$\tilde{E}_j(\omega, z) = \frac{E_j(\omega)}{(1 + \hat{z}_j^2)^{\frac{1}{2}}} e^{i\zeta(\hat{z}_j)}, \quad (6.5)$$

where $E_j(\omega)$ is the spectral representation of the j -th constituent pulse, and $\hat{z}_j = (z - z_0^j)/z_R^j$ is a normalized axial coordinate. Here, z_0^j is the focal position of the j -th beam, and z_R^j is its Rayleigh length evaluated at the beam's central wavelength. This implies an assumption of no spatiotemporal coupling, meaning that all frequencies within the spectrum of the j -th constituent pulse share the same Rayleigh length z_R^j .

With this representation of the constituent beams, the spatial evolution (in vacuum) of the focused synthesized beam (Eq. 6.4) satisfies the following equation:

$$\frac{\partial \tilde{E}}{\partial z}(\omega, z) = \sum_{j=1}^N g(\hat{z}_j) E_j(\omega, z) \equiv G_{\text{foc}}(\omega, z), \quad (6.6)$$

where the focusing coefficient $g(\hat{z})$ is defined as:

$$g(\hat{z}) \equiv \frac{i - \hat{z}}{z_R(1 + \hat{z}^2)} \quad (6.7)$$

By incorporating the term $G_{\text{foc}}(\omega, z)$, which encodes the focusing of the beam during propagation, into Eq. 6.1 an approximation of the full non-linear propagation equation is obtained:

$$\begin{aligned} \frac{\partial \tilde{E}}{\partial z}(\omega, z) + i \left[k_n(\omega, z) - k(\omega) \right] \tilde{E}(\omega, z) = G_{\text{foc}}(\omega, z) \\ + \frac{i}{2\omega c} \mathcal{F} \left\{ \frac{\partial J_{\text{abs}}}{\partial t}(t, z) + \omega_p^2(t, z) \tilde{E}(t, z) \right\}, \end{aligned} \quad (6.8)$$

6.3.2 Harmonic field propagation

To describe the macroscopic buildup of HHG, the SEWA is also invoked for the harmonic field, and its evolution is likewise expressed in the reference frame of the speed of light. For the harmonic field, focusing effects are neglected, implying that the difference in divergence between short and long trajectories is not considered [202], which leads to contributions from both in the resulting spectra. Under this assumption, the harmonic field \tilde{E}_h is governed by:

$$\frac{\partial \tilde{E}_h}{\partial z}(\omega, z) + i \left[k_n(\omega, z) - k(\omega) - i \frac{\alpha(\omega, z)}{2} \right] \tilde{E}_h(\omega, z) = -\frac{i\omega}{2c\epsilon_0} \tilde{P}_{\text{NL}}(\omega, z) \quad (6.9)$$

This equation incorporates the linear dispersion and absorption experienced by the high-harmonic emission across its entire bandwidth. The absorption is captured by a z -dependent coefficient, also scaled by the medium's density, $\rho(z)$. The term on the right-hand side, $\tilde{P}_{\text{NL}}(\omega, z) = \rho(z) \mathcal{F}\{[1 - \eta_e(t, z)] \cdot d_h(t, z)\}$, represents the nonlinear polarization and encapsulates the single-atom dipole moment, $d_h(t, z)$. This dipole moment is calculated at each spatiotemporal coordinate using the propagated driving field $\tilde{E}(t, z)$, and is then weighted by the density of the remaining neutral atoms at that coordinate.

Due to the linearity of Eq. 6.9 with respect to \tilde{E}_h , an analytical form of its solution exist, and is given by:

$$\tilde{E}_h(\omega, z = L_{\text{med}}) = -\frac{i\omega}{2c\epsilon_0} \int_0^{L_{\text{med}}} \tilde{P}_{\text{NL}}(\omega, z) e^{-i \left[k_n(\omega, z) - k(\omega) - i \frac{\alpha(\omega, z)}{2} \right] (L_{\text{med}} - z)} dz, \quad (6.10)$$

where L_{med} is the length of the medium.

6.3.3 Numerical solution

The evolution of the optical driving field, $\tilde{E}(t, z)$, as described by Eq. 6.8, is computed using the fourth-order Runge-Kutta (RK4) method. The harmonic field, $\tilde{E}_h(\omega, z)$, is obtained via direct cumulative evaluation of Eq. 6.10.

For 2D scans, such as those involving relative delay vs. CEP or focus position vs. CEP, parallel computation is utilized to expedite the process. For each parallel worker, a temporary file is initially created for each initial electric field $\tilde{E}^k(t)$ in the scan. Each file is then propagated using the RK4 method, yielding solutions $\tilde{E}^k(t, z)$, which are saved in new temporary

files. The original input files are subsequently deleted to maximize storage space during computation.

The propagated waveforms are subsequently fed into *HHGmax* [196]. For each waveform, the dipole response $d_h^k(t, z)$ is computed, and Eq. 6.10 is evaluated to obtain $\tilde{E}_h^k(t, z)$. These results are also stored in temporary files. Finally, a function merges all resulting temporary files into a single matrix, with optional down-sampling for memory optimization.

6.3.4 Simulations with Gaussian pulses

Preliminary simulations assess the model's capacity to qualitatively reproduce trends of the previous experimental observations. These simulations employ 7-fs Gaussian pulses centered at 0.8 μm and 1.6 μm , with Rayleigh lengths of 4 mm and 2 mm, respectively, and with spatially overlapping foci. The target gas medium has a length of $L_{\text{med}} = 0.5$ mm with a rectangular pressure distribution centered at $z = 0$. Specific features to reproduce include: pressure-dependent behavior of gas-cell scans; the observed phase-matching cutoff in neon when utilizing the IR pulse; and the disappearance of the high-energy half-cycle cutoff when both the NIR and IR pulses approach overlap in a delay scan.

Figure 6.8 shows gas-cell scans at different pressures in helium using a 1.6 μm pulse with a peak intensity of 4×10^{14} W/cm². In these scans, the focus position was varied along the propagation axis, while the gas target remained fixed at the origin. To express the results relative to the focus (with negative values indicating the target is positioned before the focus), the focus position grid was multiplied by -1. The fringe-like features observed in the spectra arise from the interference of short and long trajectories, as well as from multiple emissions occurring within the driving field.

The presented scans are CEP-averaged, with a CEP scan over the range $[0, \pi)$ performed at each simulated target position. With 31 target positions and 21 CEP points, a total of 651 simulations were run at each pressure. The simulations used a 40-fs time window (-20 to 20 fs), sampled with a temporal resolution of approximately ≈ 5 as, ensuring the Nyquist frequency exceeds the frequency corresponding to the HHG cutoff energy. The propagation axis was discretized with a step size of 2 μm to ensure full convergence of the driving field. With these parameters, a single simulation producing one macroscopic spectrum takes less than 3 minutes on a standard desktop PC. Running the entire gas-cell CEP scan sequentially would take about 1.5 days, but with parallel computation using 100 workers, the total runtime is reduced to less than 2 hours.

The gas-cell scans in Fig. 6.8a-e demonstrate the trends consistent with the theoretical analysis in Sec. 3.2.2 and the experimental scans in Fig. 6.2.

6.3. On-axis macroscopic modeling of HHG

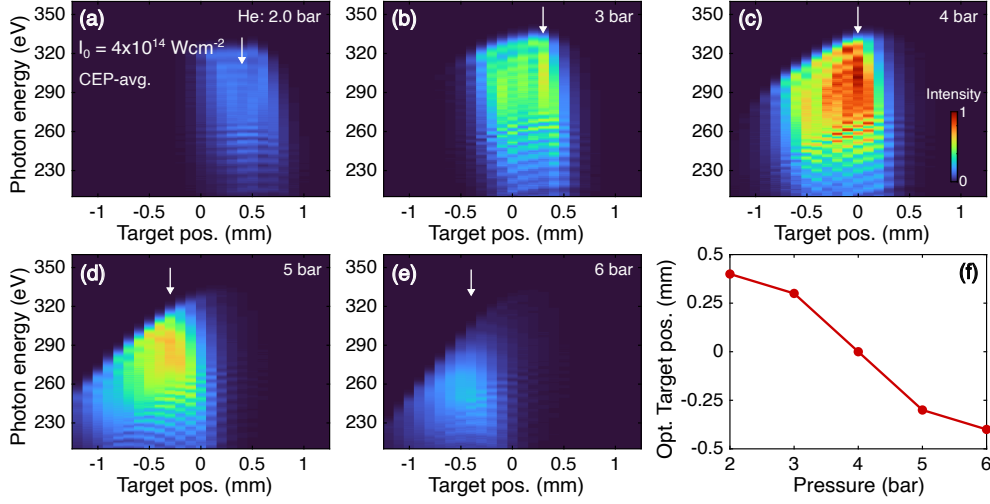


Figure 6.8: HHG gas-cell scans in He driven by a $1.6 \mu\text{m}$, 7-fs Gaussian pulse. HHG spectra as a function of target position at different pressures (a) 2 bar, (b) 3 bar, (c) 4 bar, (d) 5 bar, and (e) 6 bar. (f) Optimal target position (highest integrated signal; white arrows in a-e) versus pressure. The peak intensity at focus is $4 \times 10^{14} \text{ Wcm}^{-2}$, the Rayleigh length is $z_R = 2 \text{ mm}$, and the medium length is $L_{\text{med}} = 0.5 \text{ mm}$, with a rectangular pressure profile. Spectra are averaged over the driving field's CEP and are multiplied by the beamline's transfer function (Al 150 nm + Cu 100 nm, Au toroidal mirror, 2400 lines/mm grating, and CCD).

First, the maximum yield is achieved at a pressure of 4 bar, closely aligning with the estimated pressure of 3.7 bar from the analytical model (see Table 3.1). Second, Fig. 6.8f exhibits the shift of the optimal gas-cell position that transitions from +0.4 mm after the focus at 2 bar to -0.4 mm before the focus at 6 bar. This shift goes together with a decrease in the energy cutoff from $\approx 320 \text{ eV}$ to $\approx 300 \text{ eV}$.

Next, the ability to simulate the phase-matching cutoff observed in neon is evaluated. Figure 6.9 presents gas-cell scans in neon at 2 bar and helium at 4 bar, both with a peak intensity (at focus) of $5 \times 10^{14} \text{ W/cm}^2$ at focus. At this intensity, the cutoff energy, E_{cutoff} , is $\approx 400 \text{ eV}$ for both gases, according to the well-known cutoff formula (Eq. 3.11). The direct comparison between the neon and helium scans highlights a clear difference in the maximum photon energies achieved in each of them when driven at the same peak intensity. As was shown in Fig. 3.10, for a $1.6 \mu\text{m}$, 7 fs pulse, the critical intensity in neon is approximately $4.3 \times 10^{14} \text{ W/cm}^2$, resulting in a phase-matching cutoff ($E_{\text{cutoff}}^{\text{PM}}$) of 345 eV. This photon energy is around the upper limit of the brightest spectral region in the neon scan (Fig. 6.9a). In contrast, in the helium scan, where the critical intensity has not yet been reached ($\approx 6.2 \times 10^{14} \text{ W/cm}^2$), the spectra extend up to 400 eV, closely matching the cutoff predicted by the cutoff formula.

Finally, the influence of a relative delay between the $0.8 \mu\text{m}$ (Field 1) and

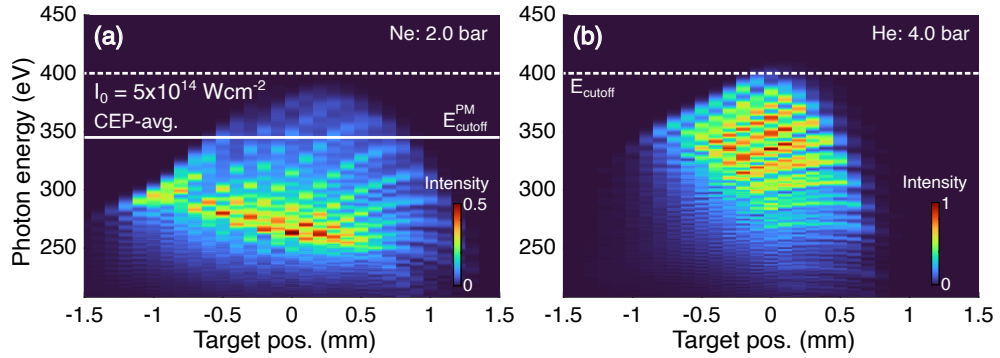


Figure 6.9: HHG gas-cell scans in He and Ne driven by a 1.6 μm , 7-fs Gaussian pulse. HHG spectra as a function of gas target position for Ne at 2 bar (a) and He at 4 bar (b). The peak intensity at focus is $I_0 = 5 \times 10^{14} \text{ Wcm}^{-2}$. The beam and medium geometries are as in Fig. 6.8. Scans are CEP-averaged. White solid lines show the phase-matching cutoff $E_{\text{cutoff}}^{\text{PM}}$ calculated using the critical intensity ($I_{\text{cr}} = 4.27 \times 10^{14} \text{ W/cm}^2$), and dashed lines represent the single-atom cutoff E_{cutoff} computed with I_0 . The beamline's transfer function has been applied to the simulated spectra.

1.6 μm (Field 2) pulses on the macroscopic harmonic emission is examined. Figure 6.10a presents a delay scan in neon, maintaining a constant CEP of zero for both pulses. The peak intensity of Field 2 at focus is fixed at $3.5 \times 10^{14} \text{ Wcm}^{-2}$, while the intensity of Field 1 is set to one-third of this value. Positive relative delays indicate Field 1 arriving after Field 2. The resulting electric field waveforms at the medium's entrance and after propagation are illustrated for three selected relative delays (-9, -1.85, and +0.9 fs) in Figs. 6.10b-d. The critical ionization in neon ($\eta_{\text{cr}} = 0.22\%$) at 1.6 μm is shown for reference. Figure 6.10e shows the single-atom response delay scan, while Fig. 6.10f shows the on-axis propagation simulation, assuming 2 bar of neon with the gas target centered at the focus position.

Concentrating on Fig. 6.10e-f, a qualitative similarity is observed between the single-atom and on-axis propagation simulations outside the overlap region, roughly between -8 fs and 8 fs. In this range, the ionization fraction remains below η_{cr} , and the propagating driving waveform experiences minimal distortion. This is illustrated by the waveform at $\tau_1 = -9$ fs (Fig. 6.10b), where the plasma fraction is only 0.15%.

Within the overlap region, significant differences between the single-atom and macroscopic simulations become apparent. While the single-atom simulation extends up to ≈ 400 eV, the macroscopic simulation shows a cutoff limited to below 300 eV. This reduction arises from the attenuation of the field as it propagates through the medium, primarily due to energy loss from strong-field ionization (described by the J_{abs} term in Eq. 6.1). The reduction in amplitude of the strongest half-cycle within the field leads to lower electron acceleration, resulting in a decreased energy cutoff.

6.3. On-axis macroscopic modeling of HHG

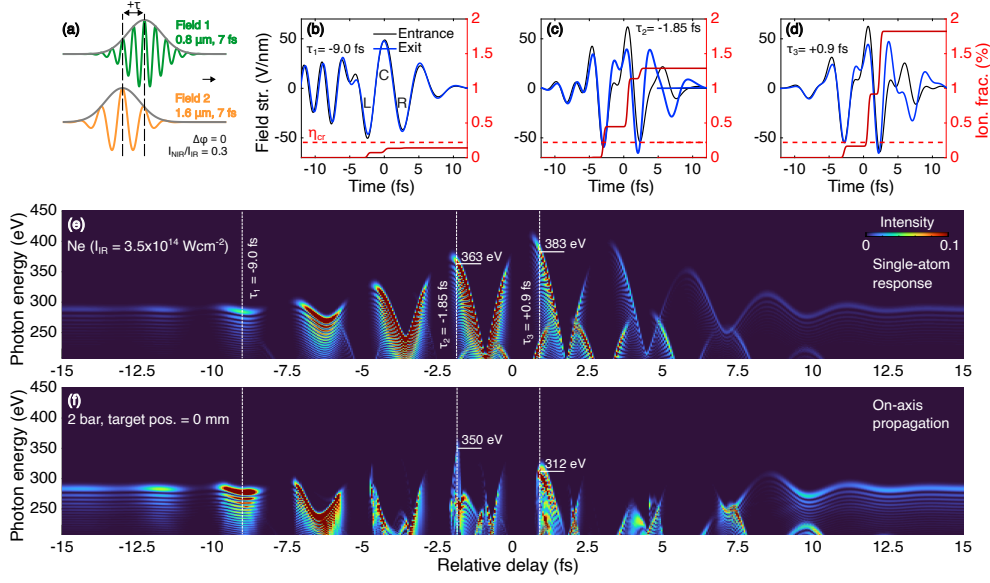


Figure 6.10: HHG delay scan in Ne with 0.8 μm and 1.6 μm , 7-fs Gaussian pulses. (a) Gaussian constituent pulses Field 1 (0.8 μm) and Field 2 (1.6 μm) with 7 fs FWHM duration and CEP = 0. The peak intensity at focus for Field 2 is $3.5 \times 10^{14} \text{ Wcm}^{-2}$. The intensity ratio of Field 2 to Field 1 is 0.3, with Field 1 delayed relative to Field 2 (positive delays indicate Field 1 arriving after Field 2). (b-d) Resulting synthesized waveforms at delays of $\tau_1 = -9$ fs, $\tau_2 = -1.85$ fs, and $\tau_3 = 0.9$ fs: electric field at medium entrance/exit (left axis), ionization fraction at entrance (right axis). The 0.5 mm-long gas medium, pressurized to 2 bar, is centered at the beam's focus (target position = 0 mm). The critical ionization fraction (red dashed line) $\eta_{cr} = 0.22\%$ is marked as reference. (e) Single-atom HHG delay scan. (f) Macroscopic, on-axis HHG delay scan. White dashed lines indicate delays corresponding to the waveforms in (b-d). The labels "L", "C", and "R" in (b) indicate the left, central and right half-cycles, respectively.

This effect is visible in the input and propagated waveforms at relative delays $\tau_2 = -1.85$ fs and $\tau_3 = 0.9$ fs (Fig. 6.10c-d), where the central half-cycle ("C" in the figure) experiences a reduction of about 30% after propagation. Interestingly, despite the waveform similarity at these two delays, they lead to markedly different phase-matching conditions and thus distinct spectral outcomes. For instance, at the single-atom level, τ_3 exhibits a cutoff at ≈ 383 eV, which is higher than the cutoff at τ_2 (≈ 363 eV). After propagation, τ_2 undergoes a 10 eV reduction, resulting in a cutoff of ≈ 350 eV. In contrast, the cutoff for τ_3 is reduced by nearly 70 eV. Additionally, an analysis of the yields at the single-atom level and after propagation reveals that, while τ_2 initially has a higher yield than τ_3 at the single-atom level, this relationship reverses after propagation.

The observed spectral features can be attributed to the differing ionization dynamics at the medium's entrance. Specifically, τ_3 induces a higher initial ionization fraction (1.8%) compared to τ_2 (1.3%). Due to the exponential nature of ionization, the higher-ionizing field associated with τ_3 undergoes

more rapid attenuation as it propagates through the medium, limiting the buildup of the harmonic signal. Only after propagating $\approx 150 \mu\text{m}$ does the field's deformation become more gradual, allowing for signal buildup. At this distance, the ionization fraction at the moment of HHG emission approaches the critical value, enabling phase-matching and a high yield. However, by this point, the intensity of the half-cycle responsible for the highest energy emission is insufficient to generate photons beyond 312 eV.

In contrast, for the τ_2 delay, the closer match of the cutoff energy after propagation to the single-atom response indicates that signal buildup occurs already from the very beginning of the medium. The slightly lower intensity of the input waveform results in a more gradual reduction in field intensity during propagation, allowing for coherent buildup within the first $\approx 20 \mu\text{m}$, where the field strength is still sufficient to generate photons up to $\approx 350 \text{eV}$. However, in this case, the ionization fraction at the moment of emission never reaches the critical value required for optimal phase-matching, leading to a lower yield compared to the τ_3 delay.

These initial simulations with Gaussian pulses successfully capture the general qualitative features observed in the experimental scans in Sec. 6.2. However, to gain a more detailed understanding of the mechanisms involved and to obtain the time-frequency profile of the HHG emission under different macroscopic conditions, precise knowledge of the driving waveforms at the HHG target is required. The following sections present the experiments and numerical modeling conducted to achieve this goal.

6.4 Tailored waveforms for high-flux IAPs

This section explores the dependence of HHG yield, spectral shape, and time-frequency profile on the synthesized driving waveform under various controlled intensity and phase-matching regimes.

6.4.1 Methods

The experimental setup, illustrated in Fig. 6.11, closely resembles that presented in Sec. 6.1, with two main modifications: (1) the driving field intensity is adjusted using reflective neutral density (ND) filters⁹ (2-mm UV fused silica substrates), and (2) driving waveforms are characterized *in-situ* via the TREX technique (see Sec. 2.6.2) [159]. The dispersion within the NIR and IR channels was adjusted to ensure pulse compression at the interaction point, while the focal length was fixed to $f = 400 \text{mm}$. This focusing resulted in measured Rayleigh lengths for the IR and NIR pulses of $z_R^{\text{IR}} \approx 2 \text{mm}$ and $z_R^{\text{NIR}} \approx 4 \text{mm}$, respectively. The gas-cell had an inner thickness of $\approx 1 \text{mm}$.

⁹NDUV2R(01A-03A), (Thorlabs, Inc)

Table 6.1: Measured NIR and IR pulse energies at the gas target for the different ND filters. The ND 0.0 filter corresponds to the 2-mm UV fused silica substrate without the reflective coating.

ND	NIR (μJ)	IR (μJ)	Total (μJ)
0.0	20	170	190
0.1	19	163	182
0.2	16	126	142
0.3	11	77	88

This ND filter approach to attenuating the driving beam energy offers several advantages over the previous method of adjusting the focal spot. Maintaining consistent focusing properties and medium characteristics (e.g., gas-cell hole sizes) across varying intensities allows for a reliable comparison of photon flux. Additionally, the ability to simply switch ND filters, without requiring time-consuming beamline realignment, preserves system stability and ensures consistent beam and pulse properties across measurements. Table 6.1 lists the individual (NIR, IR) and combined pulse energies measured at the gas target for various attenuation levels (ND0.0 - ND0.3), where ND0.0 represents the uncoated 2-mm UV fused silica plate. The combined beam energy decreases in transmission relative to the ND0.0 filter, with transmissions of approximately 96% for ND0.1, 75% for ND0.2, and 46% for ND0.3.

Measuring the driving waveform directly at the HHG target position also offers advantages. *Ex-situ* measurement of the driving waveforms would necessitate knowledge of the complex-valued transfer function from the measurement point to the HHG generation point. Typically, only an estimate of this transfer function is available, and can lead to significant uncertainties in the actual driving waveform. The *in-situ* approach circumvents this issue entirely. Furthermore, the Gouy phase shift due to tight focusing and the intensity ratio between the constituent pulses, both critical factors in HHG, vary along the beam path. By measuring the waveform at the HHG generation point, these spatial variations are inherently captured, providing a more precise characterization of the HHG driving field.

Measurement and simulation procedure

On the experimental side, the measurement procedure, performed in both helium and neon, each with ND filter values of 0.0, 0.1, and 0.2, consists of the following steps:

1. **IR-only phase-matching:** CEP-averaged, gas-cell scans at various backing pressures are performed to identify the combination of backing pressure (P_b) and gas target position (z_{PM}) that maximizes the HHG yield when driven only by the IR pulse.

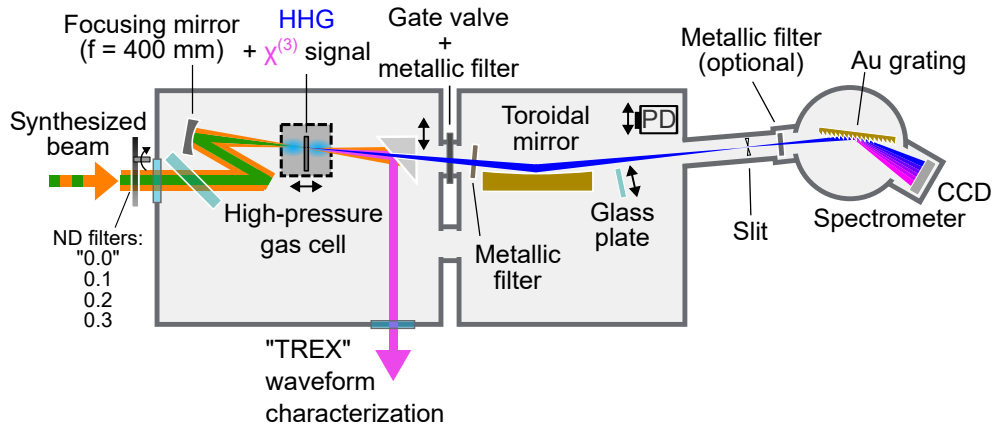


Figure 6.11: Experimental setup. The water window HHG beamline (Fig. 6.1) incorporates a "TREX" in-situ waveform characterization setup (see main text) and a series of 2-mm reflective neutral density (ND) filters (optical densities [OD]: 0.1-0.3, and a "0.0" filter consisting of only the UV fused-silica substrate). The synthesized beam, after passing through a selected ND filter (attenuating $\approx 96\%$ (ND0.1), 75% (ND0.2), 46% (ND0.3), with respect to the ND0.0 filter across the full synthesizer bandwidth), is focused ($f = 400$ mm) into the 1-mm gas target (Ne or He), generating HHG and a non-linear χ^3 signal. A movable prism mirror can direct the χ^3 signal to an external optical spectrometer via UV-enhanced Al mirrors. All TREX scans are performed with the ND0.3 and 1 bar of He.

2. **IR-only CEP scan:** A CEP scan is conducted under the phase-matching (P_b, z_{PM}) conditions identified in step 1. This serves to verify the IAP gating capability of the IR pulse and to spot CEP values that maximize the photon flux within a specific energy range.
3. **In-situ waveform characterization:** A TREX measurement is performed using helium at 1 bar and at the optimized target position (z_{PM}) determined in step 1. This establishes the time-zero reference for subsequent relative delay scans and characterizes the driving waveforms precisely where the IR-only HHG yield was maximized.
4. **Relative delay scans:** Four relative delay scans are performed around the established time-zero, under the optimized (P_b, z_{PM}) conditions identified in step 1. Each scan is conducted at a different CEP value: the reference CEP (the initial lock point) φ_0 , $\varphi_0 - \pi/4$, $\varphi_0 - \pi/2$, and $\varphi_0 - \pi$. This last step verifies the consistency of the delay scan over a full CEP cycle.

Thus, this procedure enables the assignment of a driving waveform to each recorded spectrum from the delay scan. Additionally, since the spectrometer is calibrated with the photodiode, the photon flux can also be determined for each spectrum.

On the simulation side, the procedure replicates the experimental steps. Starting with step 1, the simulation uses the experimentally characterized

Table 6.2: Phase-matching conditions for IR-only HHG. Combinations of backing pressure and gas target position for phase-matching the IR-only HHG in neon and helium, under various ND filters (see Fig.6.12).

ND	Helium		Neon	
	Backing pressure (bar)	Target pos. (mm)	Backing pressure (bar)	Target pos. (mm)
0.0	8.0	0.8	4.0	1.0
0.1	6.0	1.0	4.0	1.0
0.2	6.0	1.5	4.0	1.0

IR waveforms from the TREX measurement (step 3) to identify the pressure and gas target position (P, z_{PM}) combinations that phase-match the simulated IR-only HHG. Once these optimal (P, z_{PM}) conditions are identified, CEP and delay scans are simulated, incorporating the characterized NIR and IR waveforms and their experimentally determined intensity ratio.

A complete set of measurements and simulations used for the analysis in this section is available in App. D.

IR-only phase-matching

Figure 6.12 shows HHG gas cell scans acquired using the IR pulse only, at various backing pressures in neon (2, 4, and 6 bar) and helium (6, 8, and 10 bar), each with corresponding attenuation levels. The combinations of backing pressure and target position that produced the highest yield and cutoff for each attenuation level, as identified from these scans, are listed in Table 6.2.

A closer look at Fig. 6.12 highlights the distinct effect of ND filters on both the cutoff energy and yield of the HHG spectra in helium and neon. With no attenuation (ND0.0), the photon energy reaches approximately 360 eV in helium and 345 eV in neon. When the attenuation is increased to ND0.1, the cutoff in helium decreases moderately to around 345 eV, while in neon, it remains nearly unchanged, dropping by only about 5 eV. However, with ND0.2, the maximum photon energy in both gases is reduced significantly to ≈ 280 eV, falling below the water window region. The fact that this energy limit is reached in both gases suggests minimal plasma influence on the driving field propagation at the intensity corresponding to the ND0.2 filter.

The ND filters also have a notable impact on the HHG yield. As expected, the highest yield for both gases is achieved with ND0.0, with the maximum yield in helium (at 8 bar) being approximately 10% of that in neon (at 4 bar). In neon, increasing the attenuation from ND0.0 to ND0.1 results in a minor 10% reduction in yield, while in helium, this same increase leads to a more

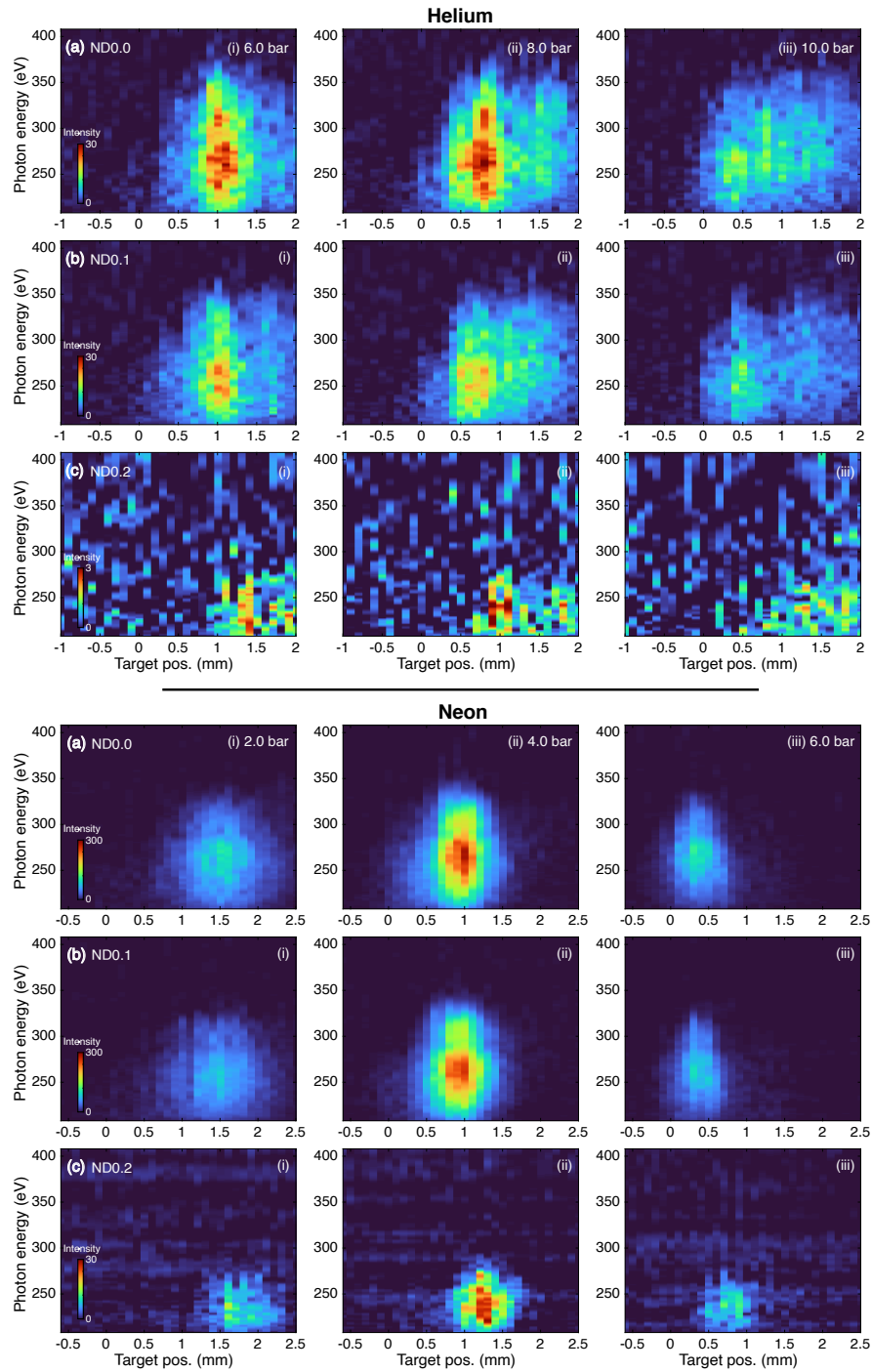


Figure 6.12: HHG gas-cell scans in He and Ne driven by the IR pulse with varying ND filters. HHG spectra as a function of gas target position for ND filters: (a) 0.0, (b) 0.1, and (c) 0.2. Each panel shows scans in He (i: 6 bar, ii: 8 bar, iii: 10 bar) and Ne (i: 2 bar, ii: 4 bar, iii: 6 bar), averaged over the CEP. The residual optical beam was blocked by a 150 nm Al filter, and each spectrum was integrated for 2 s.

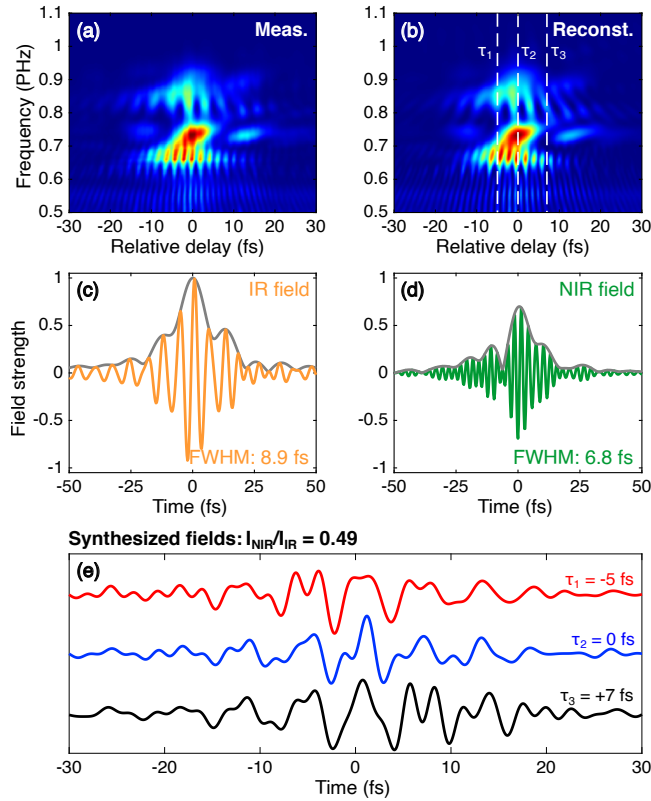


Figure 6.13: TRES measurement for in-situ waveform characterization. (a) Measured and (b) reconstructed TRES scans at the optimal gas target position for He ($z_{PM} = 1.5$ mm, 1 bar, ND0.3 filter). (c, d) Reconstructed IR and NIR fields (colored) and their respective temporal envelopes (gray), with FWHM durations indicated. (e) Synthesized waveforms resulting from the combination of the NIR and IR pulses at the indicated relative delays (white dashed lines in panel b).

significant 25% drop. For both gases, further attenuation to ND0.2 causes an order of magnitude decrease in yield.

In-situ waveform characterization

A TRES scan [159] is performed at each of the optimal gas target positions listed in Table 6.2 for both gases and attenuation levels. To minimize distortion of the driving field by plasma generation, the measurements are taken using the ND0.3 filter (which attenuates the synthesized beam by $\approx 46\%$) with helium at 1 bar backing pressure as the target gas. This setup ensures minimal plasma generation, allowing the measured waveforms to closely resemble the vacuum conditions at the generation point.

The TRES signal, extending down to 230 nm, is directed out of the HHG beamline using UV-enhanced aluminum mirrors. A pair of UV fused silica prisms then spatially disperse the beam, separating the third-order (χ^3) fre-

Table 6.3: Reconstructed intensity ratios for different ND filters. NIR-to-IR intensity obtained from TREX waveform reconstructions at the optimal gas target positions (Table 6.2), and corrected for the transmission difference with respect to the ND0.3 filter (used in TREX measurements)

ND	He	Ne
0.0	0.35	0.33
0.1	0.37	0.33
0.2	0.42	0.46

quencies from the much stronger fundamental optical beam. The filtered χ^3 component is subsequently focused into a commercial grating spectrometer¹⁰.

Figure 6.13a shows an example TREX scan measured at the optimal position for helium with the ND0.2 filter ($z_{\text{PM}} = 1.5$ mm). The corresponding reconstructed scan is presented in Fig. 6.13b, demonstrating high-fidelity reconstruction where even subtle features are faithfully reproduced. The reconstructed NIR and IR pulses are shown in Fig. 6.13c-d, revealing an IR pulse duration of ≈ 9 fs and an NIR pulse duration of ≈ 7 fs, with a NIR-to-IR intensity ratio of 0.49. The central wavelengths of the NIR and IR fields are ≈ 0.84 μm and 1.80 μm , respectively. Since the TREX technique provides the full temporal map for various relative delays between the NIR and IR pulses, all possible synthesized waveforms within the scanned delay range are known. Figure 6.13e illustrates three such synthesized fields, each corresponding to a distinct relative delay ($\tau_1 = -5$ fs, $\tau_2 = 0$ fs, and $\tau_3 = 7$ fs), where zero delay ($\tau_2 = 0$ fs) is defined as the point where the centers of mass of the constituent pulse envelopes coincide.

Importantly, the waveforms were measured with the ND0.3 filter. However, to determine the precise waveforms driving HHG with the less attenuating ND filters (ND0.0, ND0.1, and ND0.2), two factors must be considered. First, the different transmission levels for each constituent pulse (NIR and IR) affect the intensity ratio between them. Second, the slight differences in thickness—on the order of tens of microns—between the ND filters introduce a phase shift that must be accounted for.

The transmission ratios between the ND filters are adjusted using the known transmission values for the NIR and IR pulses listed in Table 6.1. The thickness differences between the ND filters were measured with a Michelson interferometer. Using these measurements, along with the known refractive index of UV-fused silica [309], the corresponding phase shifts were calculated (see Eq. 2.5) and numerically applied to the ND0.3 waveforms to obtain the corrected waveforms for the less attenuating filters.

¹⁰USB2000+, (OceanOptics.)

Simulated IR-only phase-matching

For the gas-cell scan simulations, the peak intensity of the IR pulse at focus is a crucial input. For the ND0.0 case, this peak intensity is estimated to be approximately $4 \times 10^{14} \text{ W/cm}^2$, based on the measured pulse energy (170 μJ), beam waist ($w_0 \approx 45 \text{ }\mu\text{m}$), and the "temporal area" (see App.A) of the intensity envelope ($\approx 13 \text{ fs}$) for the reconstructed IR pulse. However, a comparison between simulated and experimental spectra, using the energy cutoffs achieved in helium, suggests that this estimate overshoots the actual experimental value by about 5%. This discrepancy is likely due to astigmatism observed in the beam focusing or by the actual amount of energy that enters the gas-cell. Both situations can reduce the intensity at the interaction region. Therefore, for the simulations, the peak intensity for the ND0.0 case is adjusted to $3.80 \times 10^{14} \text{ Wcm}^{-2}$. The corresponding peak intensities for the other ND filter levels (ND0.1 and ND0.2) are derived from their transmission values listed in Table 6.1, resulting in $3.65 \times 10^{14} \text{ Wcm}^{-2}$ for ND0.1 and $2.81 \times 10^{14} \text{ Wcm}^{-2}$ for ND0.2.

In addition to peak intensity, two other critical parameters for the simulation are the longitudinal distribution of the gas within the target medium and the Rayleigh length. For these simulations, the experimentally determined Rayleigh length of $z_R^{\text{IR}} = 2 \text{ mm}$ was used. The longitudinal distribution of the gas, however, deviates from a perfect rectangular profile due to gas emerging from the gas cell's side holes, extending beyond the main cell. This extended gas still contributes to HHG, as shown by the gas cell scans in helium (Fig. 6.12), where emission occurs over a range approximately twice the length of the gas target itself.

To account for the extended gas and model the pressure distribution, a constant pressure P is maintained within the main cell, defined by the interval $[-\frac{L_{\text{cell}}}{2}, \frac{L_{\text{cell}}}{2}]$. Outside this region, the pressure gradually decreases following a smooth \cos^2 window function over the intervals $[-\frac{L_{\text{med}}}{2}, -\frac{L_{\text{cell}}}{2}]$ and $[\frac{L_{\text{cell}}}{2}, \frac{L_{\text{med}}}{2}]$. For helium simulations, $L_{\text{med}} = 2 \text{ mm}$ and $L_{\text{cell}} = 0.4 \text{ mm}$ were used, while for neon, $L_{\text{med}} = 1.2 \text{ mm}$ and $L_{\text{cell}} = 0.2 \text{ mm}$ were chosen. This difference in gas-cell dimensions is due to the fact that neon, being heavier than helium, escapes more slowly from the high-pressure region, resulting in a different pressure profile. The pressure profiles were chosen to more closely match the experimental scans. For field propagation within these media, a step size of $dz = 4 \text{ }\mu\text{m}$ was used.

Finally, the relationship between the simulated pressure P and the experimental backing pressure P_b is defined by a scaling factor r , which accounts for the difference between the backing pressure and the actual pressure inside the gas cell. The value of r is chosen by adjusting the simulated pressure so that the yield ratios between experimental scans at different pressures are

6. WATER-WINDOW, SOFT X-RAY ISOLATED ATTOSECOND PULSES

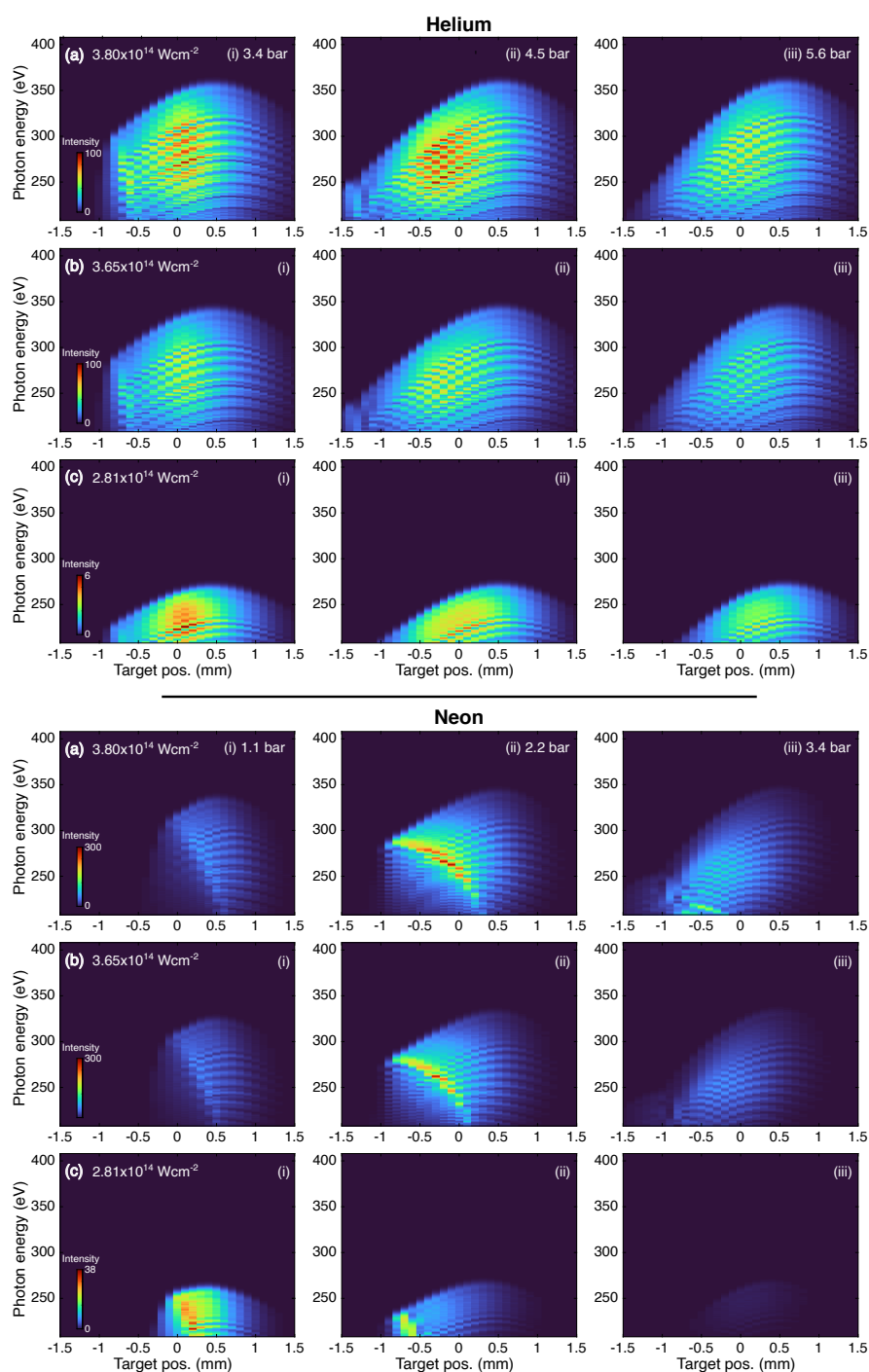


Figure 6.14: Simulated HHG gas-cell scans in He and Ne driven by the IR pulse with varying ND filters. HHG spectra as a function of gas target position for ND filters: (a) 0.0, (b) 0.1, and (c) 0.2. Each panel shows scans in He (i: 6 bar, ii: 8 bar, iii: 10 bar) and Ne (i: 2 bar, ii: 4 bar, iii: 6 bar), averaged over the CEP. The spectra are multiplied by the beamline's transfer function.

Table 6.4: Simulated phase-matching conditions for IR-only HHG. Combinations of backing pressure and gas target position for phase-matching the simulated IR-only HHG in neon and helium, under various ND filters (see Fig.6.14).

ND	Helium		Neon	
	Pressure (bar)	Target pos. (mm)	Pressure (bar)	Target pos. (mm)
0.0	4.5	-0.1	2.2	0.1
0.1	3.4	0.1	2.2	0.1
0.2	3.4	0.6	2.2	0.1

reproduced. This ensures the pressure-dependent changes in yield observed experimentally are reflected in the simulations. In this study, the scaling factor was determined to be 0.56.

Figure 6.14 presents the simulated HHG gas cell scans, driven only by the IR pulse, for various combinations of backing pressures in neon (1.1, 2.2, and 3.4 bar) and helium (3.4, 4.5, and 5.6 bar), along with different ND filter attenuation levels (ND0.0, ND0.1, and ND0.2). Each combination corresponds to a unique peak intensity at focus, as described earlier. For neon, the peak intensities result in maximum ionization fractions of approximately 0.26%, 0.20%, and 0.03%, with the ND0.0 case approaching the critical ionization fraction for neon at 1.6 μm . In contrast, plasma effects are unlikely to play a significant role in the ND0.2 case due to the much lower ionization fraction. Meanwhile, the maximum ionization fraction for helium remains negligible ($\leq 0.1\%$) across all ND levels. This justifies adjusting the simulated peak intensity for helium (ND0.0 case) to match the experimentally observed cutoff, as the absence of significant plasma effects allows the cutoff to be predicted by the cutoff formula (Eq. 3.11), as shown in Fig. 6.9.

Based on the simulated gas-cell scans shown in Figure 6.14, combinations of phase-matching position and pressure were selected for further simulations. These selections, listed in Table 6.4, were chosen to replicate the experimental trends. In the case of neon, as in the experiment, the pressure and gas-cell position were kept constant across all attenuation levels. A detailed analysis of the simulated scans reveals several notable agreements with the experimental observations.

First, with the exception of the ND0.2 neon scan, the simulations accurately reproduce the pressure-dependent yield behavior observed in the experiments. Second, the simulated energy cutoffs closely match the experimental values across all attenuation levels. Third, the model captures the relative yield reductions between different attenuation levels effectively. For example, the transition from ND0.0 to ND0.1 results in a simulated yield reduction of 8% in neon and 28% in helium, which aligns well with the experimental reductions of 5% and 25%, respectively. Furthermore, both

the simulations and experiments show an approximately tenfold decrease in yield between the ND0.0 and ND0.2 filter levels for both gases.

While the model successfully predicts yield ratios within a single gas type across different attenuation levels, it underestimates the yield ratio between different gas types. For instance, in the ND0.0 cases, the simulations predict the maximum helium yield to be about one-third of the maximum neon yield, whereas experimental results indicate it is an order of magnitude lower. This discrepancy may stem from the gas cell profile used in the simulations, as both the medium and cell lengths significantly influence the resulting HHG yield. Further investigation is needed to pinpoint the exact cause.

Additionally, the simulated neon gas-cell scans do not align well with experimental observations, likely due to the absence of intensity fluctuations in the simulations. With the ND0.0 and ND0.1 filters, the IR field is close to the critical ionization fraction for phase matching, so even slight deviations can alter the spectral shape. Incorporating these fluctuations in the simulations could average the conditions around optimal phase matching, potentially improving the match with experimental data.

6.4.2 IR-only CEP scans

Figure D.1 in App. D presents the complete set of measured and simulated IR-only HHG CEP scans for both neon and helium. These scans were acquired with a 150-nm thick aluminum filter under the phase-matching conditions specified in Tables 6.2-6.4. The simulated scans account for the 300 mrad r.m.s CEP noise of the driving laser pulses by averaging each spectrum over the CEP axis using a Gaussian weighting function centered around the nominal CEP value.

Focusing on the ND0.0 case in neon, Fig. 6.15 provides a detailed analysis of one of the HHG CEP scans. Panel (a) displays the scan itself, while panel (b) shows the corresponding photon flux integrated within a 10% bandwidth (BW) around 300 eV. This flux, presented at the HHG source before any beamline attenuation, reaches a maximum of $(6.8 \pm 1.4) \times 10^5$ photons/s/10% BW at a CEP value of 0.53π . In comparison, the maximum flux achieved in helium under its phase-matching conditions is about 10% of that value, at $(7.2 \pm 1.5) \times 10^4$ photons/s.

The corresponding simulated scan is shown in Fig. 6.15c, with panel (d) comparing the simulated spectrum at the optimal CEP to the experimentally obtained spectrum, both maximizing flux around 300 eV. Unlike the experimental spectrum, where the fringes are smeared out due to detector resolution, the simulated spectrum exhibits clear spectral fringes around 250 eV. These faint fringes are primarily attributed to two consecutive emissions oc-

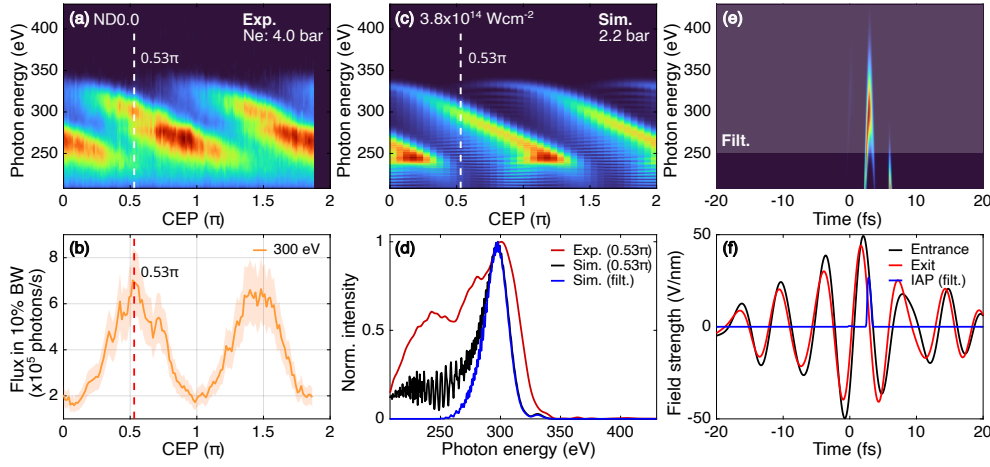


Figure 6.15: IR-only CEP scan in Ne driven with ND0.0 filter. (a) Measured CEP scan at 4 bar driven by an IR pulse, with the gas target positioned at 1.0 mm. (b) Integrated photon flux around 300 eV in a 10% bandwidth. The shaded area represents the measurement uncertainty. (c) Simulated CEP scan at 2.2 bar and with the gas target positioned at 0.1 mm. The reconstructed IR pulse ($I_0 = 3.8 \times 10^{14} \text{ Wcm}^{-2}$) obtained via the TREX technique is used as driving field. White dashed lines in (a-c) indicate the CEP maximizing 300 eV flux. (d) Experimental and simulated spectra at optimal CEP. (e) Corresponding time-frequency analysis of (d), with shaded area representing a spectral filter for IAP gating. (f) Optimal driving field at medium entrance/exit, and resulting IAP after applying the spectral filter.

curing around $t = 3$ fs and $t = 6$ fs, as revealed by the time-frequency analysis of the emission in panel (e). Figure 6.15f illustrates the driving IR field at both the entrance and exit of the medium. By applying a spectral filter to select energies beyond 250 eV, a 600-as IAP can be gated. If only short trajectories contributed to this IAP—given that the larger divergence of long trajectories likely leads to their suppression in reality—its duration would be reduced to 300 as.

6.4.3 Relative delay scans

This section presents the experimental and simulated HHG delay scans, encompassing CEP shifts of $(0, \pi/4, \pi/2, \pi)$ for both helium and neon gases across all attenuation levels (ND0.0 - ND0.2). A comprehensive set of these scans is presented in App. D. The phase-matching conditions employed for these scans are detailed in Tables 6.2 and 6.4.

Experimentally, these scans were acquired using a 150 nm thick aluminum filter and a 100 nm thick copper filter, with a 2 s integration time. All spectra—both experimental and simulated—are presented at the CCD point, incorporating the beamline’s transfer function to facilitate direct comparison. However, the reported photon flux values have been corrected for this transfer function, corresponding to those at the HHG generation point.

For the simulations, each individual spectrum employed a 100 fs time window to ensure full temporal coverage of the synthesized pulse. A time step size of 3 as was selected to achieve the spectral resolution necessary for capturing the highest cutoff energies generated by the most intense driving fields. The delay grid spanned from -20 fs to +20 fs with a 100 as step size, and was coupled with a CEP grid sampled from -0.75π to $+0.25\pi$ in 0.05π increments. This detailed CEP sampling was designed to account for the CEP r.m.s. noise in the simulated delay scan. Consequently, over 8000 on-axis propagation simulations were performed for each attenuation level and gas type.

Figure 6.16 presents a delay scan in helium, acquired with the ND0.2 filter at a CEP shift of $\pi/4$ and a combined field energy of 142 μJ . The simulated scan (a) closely matches the experimental scan (b), which was recorded over a narrower delay range (-9 fs to +3 fs). The strong agreement in the position, relative intensity, and energy cutoff of the bright features validates the accuracy of the TREX technique in characterizing the waveforms at the HHG target and linking them to specific harmonic spectra. Both the simulated and experimental scans demonstrate an increase in yield and an extension of the cutoff within the temporal overlap region (-6 fs to +3 fs). Notably, at this attenuation level (ND0.2), macroscopic effects do not significantly influence the shape of the harmonic spectra, despite ionization fractions reaching up to 0.3%. This argument is supported by single-atom response simulations (not shown), which exhibit a similar qualitative agreement with the experimental scan. Therefore, as discussed in Sec. 5.1, the observed increase in yield and cutoff extension in the experiment is primarily driven by the constructive interference between the NIR and IR pulses, resulting in a more intense synthesized field.

The absolute photon flux, integrated within the water window range (284-543 eV) and shown in Fig. 6.16c, quantifies the yield increase as a function of the relative delay. At a delay of $\tau = -2.8$ fs, the synthesized field produces a photon flux of $(1.4 \pm 0.3) \times 10^5$ photons/s. This represents a 40% increase compared to the optimized flux from the IR pulse (ND0.0) alone ($(1.0 \pm 0.2) \times 10^5$ photons/s), despite the synthesized field having 16% less energy than the 170 μJ IR pulse and using phase-matching conditions optimized for the IR field rather than the synthesized field.

Figures 6.16d-f provide insights on the observed emission by displaying the driving waveform at the entrance and exit of the medium, along with the time-frequency analysis of the HHG emission at selected delays ($\tau = -2.5$ fs, 0.3 fs, and 1.6 fs). Unlike the spectra in panels (a-b), which account for the full beamline's transfer function, the time-frequency analysis considers only the effects of the metal filters and toroidal mirror, offering a closer representation of how the emission would interact with a potential target.

6.4. Tailored waveforms for high-flux IAPs

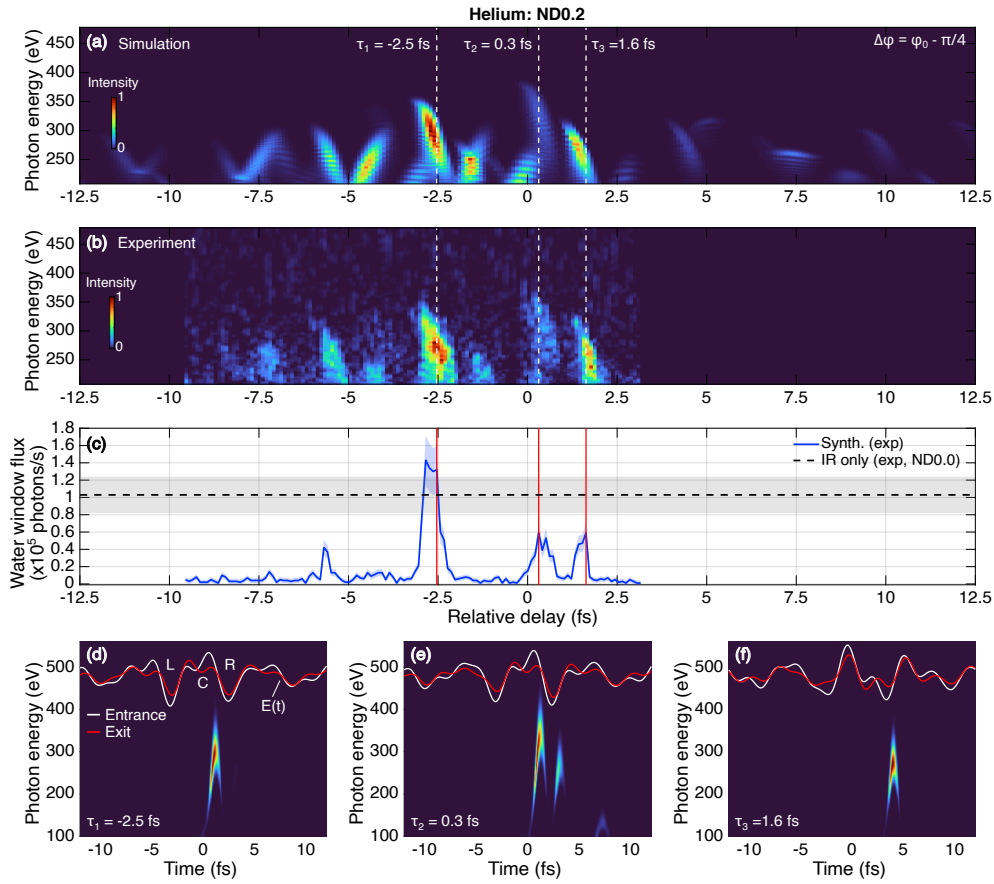


Figure 6.16: Relative delay scan in He with ND0.2 filter. (a) Simulated and (b) measured HHG spectra as a function of the relative delay between the NIR and IR pulses (combined beam energy: 142 μJ). A CEP shift of $-\pi/4$ is applied. Negative delays indicate the NIR pulse precedes the IR pulse. (c) Water window photon flux (at the source) as a function of the relative NIR-IR delay. Dashed horizontal line indicates the flux from the IR pulse with the ND0.0 filter (170 μJ), optimized for phase-matching and CEP. The shaded areas represent the measurement uncertainty. (d-f) Driving waveforms at the entrance/exit of the medium and time-frequency analysis of simulated spectra extracted from the scan at relative delays of $\tau = -2.5$ fs, 0.3 fs, and 1.6 fs. The time-frequency analysis represents the on-target emission (excluding grating/CCD effects). The labels "L", "C", and "R" indicate the left, central and right half-cycles, respectively. For the experiment, the pressure was set to 6 bar and the target position to 1.5 mm. For the simulation, a pressure of 3.4 bar and a target position of 0.6 mm were used. For the simulation, the IR peak intensity was $2.81 \times 10^{14} \text{ Wcm}^{-2}$, and the NIR/IR intensity ratio was 0.42 (from TRES).

As with the analysis presented in Figs. 5.1 and 6.10, the influence of the driving waveforms on the observed spectra can be understood by focusing on the three strongest half-cycles (labeled L, C, and R for left, central, and right, respectively). At $\tau = -2.5$ fs (panel d), the time-frequency analysis reveals a broadband, isolated emission spanning from ≈ 200 to 350 eV, originating within the central half-cycle. Although short trajectories domi-

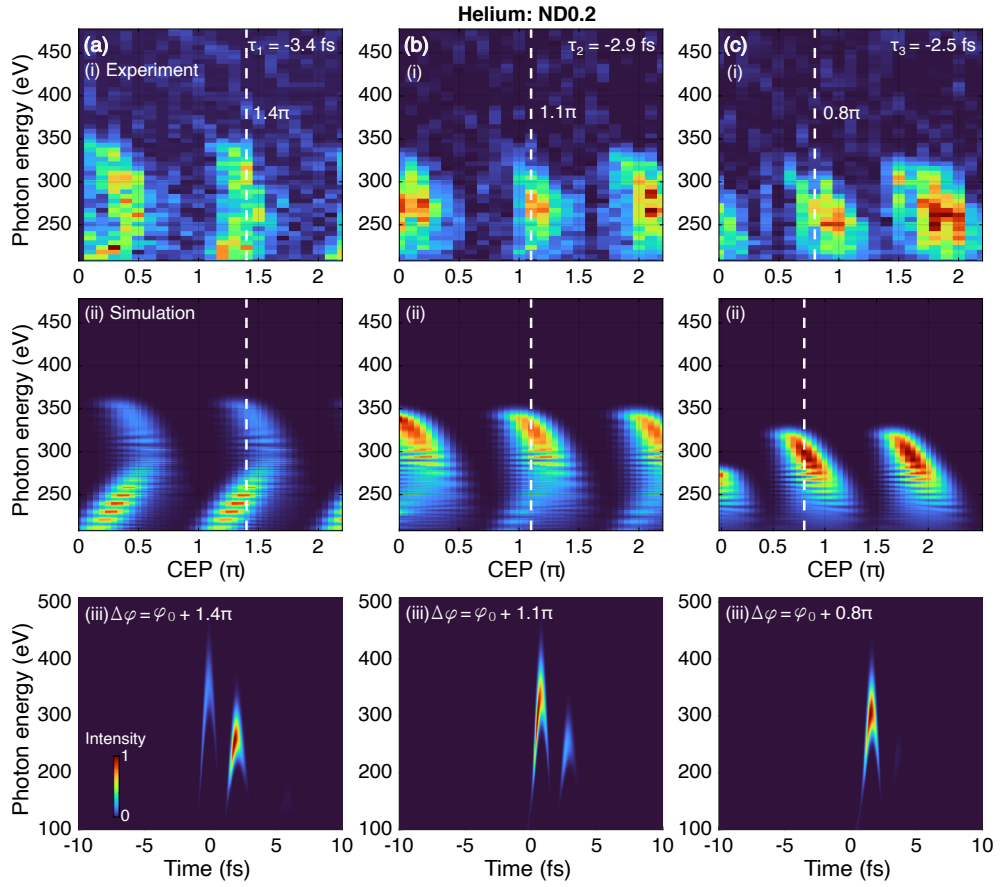


Figure 6.17: CEP scans at different relative delays in He with ND0.2 filter. CEP-dependent HHG spectra at three different delays: (a) $\tau = -3.4$ fs, (b) -2.9 fs, and (c) -1.6 fs. Each column presents (i) the measured spectra, (ii) the simulated spectra, and (iii) the time-frequency analysis at specific CEP shifts (indicated by white dashed lines in (a) and (b)). The CEP scans were extracted from a delay-CEP scan using the same waveforms and experimental conditions as in Fig. 6.16.

nate this emission, the presence of remaining long trajectories results in an IAP with a FWHM of 640 as. In contrast, at $\tau = 0.3$ fs (panel e), emission arises from recombination in both the central and right half-cycles. The central half-cycle contributes to the spectral range up to ≈ 400 eV, while the right half-cycle generates emission centered around 250 eV. In this scenario, achieving an IAP would necessitate a spectral filter to remove energies below ≈ 300 eV. Finally, at $\tau = 1.6$ fs (panel f), another isolated broadband emission centered around 250 eV is observed, arising solely from recombination in the right half-cycle. As in the case at $\tau = -2.5$ fs, the IAP remains primarily composed of short trajectories; however, the presence of residual long trajectories causes the pulse to have a FWHM duration of 620 as.

To further substantiate the idea that the observed emission results from re-

combination within either two consecutive half-cycles (leading to two attosecond bursts) or within a single half-cycle (leading to an IAP), additional evidence is presented in Fig. 6.17. This figure shows a series of measured (i) and simulated (ii) CEP scans, along with corresponding time-frequency analyses (iii), recorded using the same driving waveforms and phase-matching conditions as in Fig. 6.16, at three different delays: -3.4 fs, -2.9 fs, and -2.5 fs. Consequently, the CEP scan at -2.5 fs (Fig. 6.17c) corresponds to the same driving waveform as in Fig. 6.16d. The strong agreement between simulations and experiments is observed once again. Since the absolute CEP value (φ_0) is accurately retrieved from the TREX characterization, no additional adjustments to the CEP axis are necessary to align the simulations with the experiments, as further evidenced in Figs. D.2-D.3 in App. D.

This selected delay window from -3.4 fs to -2.5 fs effectively captures the transition from double to single emission as the delay changes. At $\tau = -3.4$ fs and -2.9 fs, where two emissions are generated, the less energetic emission (centered around 250 eV) produced by the right half-cycle increases its cutoff as the CEP shift is incremented, while the more energetic emission (extending up to about 350 eV) decreases. This simultaneous increase in one half-cycle cutoff and decrease in the other creates a “boomerang” shape in the π -periodic pattern. This occurs because, as the CEP shifts in the shown direction, the amplitude of the right half-cycle increases while the amplitude of the central, stronger half-cycle decreases. At $\tau = -2.5$ fs, the CEP scan indicates that the spectrum primarily results from the central half-cycle, as depicted in Fig. 6.16d. The observed HHG spectra show a single cutoff that decreases with the CEP shift, without any visible contribution from another half-cycle. This type of CEP scan, observed at $\tau = -2.5$ fs, aligns with findings from other setups where the presence of IAPs has been confirmed [32, 249], including through attosecond streaking [143, 260].

As noted earlier, although the ND0.2 case simulations included an on-axis macroscopic model, the results remained qualitatively similar to those from single-atom response simulations, suggesting that plasma-induced effects are not yet significant at this intensity. However, when switching from the ND0.2 to the ND0.1 filter, the energy increases to 182 μ J, allowing the synthesized waveforms to reach intensities up to 10^{15} W/cm². This results in ionization fractions of up to 1.2%, leading to more pronounced plasma contributions and making the signal more sensitive to waveform distortions.

Figure 6.18 presents a delay scan in helium using the ND0.1 filter with a CEP shift of $-\pi/2$. The simulated and experimental scans (panels a-b) show good agreement outside the temporal overlap region ($|\tau| > 4$ fs), but discrepancies become evident within it. To illustrate these similarities and differences, three representative cases at relative delays of $\tau = -2.6$ fs, 0.5 fs, and 4.6 fs are highlighted in Fig. 6.18d-f.

6. WATER-WINDOW, SOFT X-RAY ISOLATED ATTOSECOND PULSES

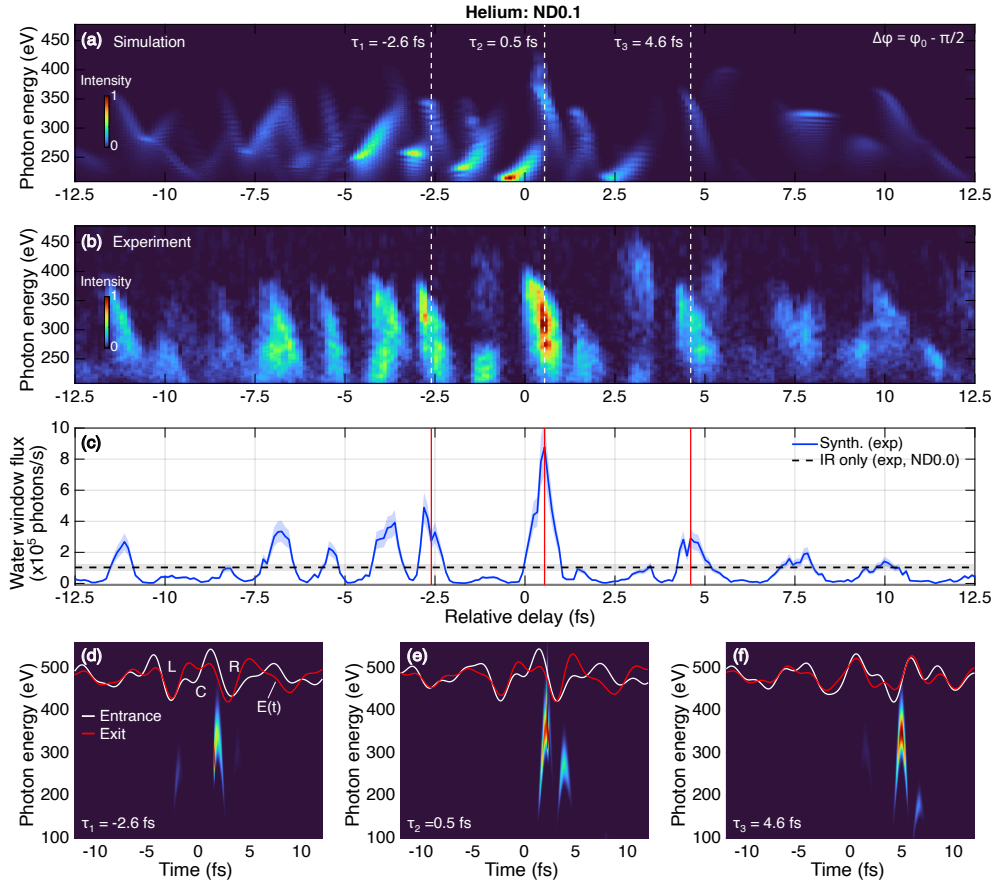


Figure 6.18: Relative delay scan in He with ND0.1 filter. Similar to Fig.6.16, but with the following differences: Combined beam energy: 182 μJ , CEP shift: $-\pi/2$. Experimental target position: 1 mm. Simulation parameters: 0.1 mm target position. For the simulation, the IR peak intensity was $3.65 \times 10^{14} \text{ Wcm}^{-2}$, and the NIR/IR intensity ratio was 0.37. (d-f) Synthesized waveform and time-frequency analysis at delays of $\tau = -2.6$ fs, 0.5 fs, and 4.6 fs.

Focusing first on the similarities, at $\tau = 4.6$ fs, there is a strong match between the simulation and the experimental trace. At this delay, the ionization fraction reaches up to 0.1%, a level where plasma effects have minimal influence on the resulting signal. As shown in Fig. 6.18f, the emission corresponds to an IAP, originating solely from a single half-cycle—in this case, the right half-cycle.

Conversely, significant discrepancies arise within the overlap region. A key difference is the absence of emissions centered around 250 eV in the experimental data, which the simulations predict to originate from non-central half-cycles (primarily the right half-cycle). Instead, the emissions observed in the experimental scan are dominated by contributions from the central half-cycle, which reach higher photon energies. For instance, at $\tau = -2.6$ fs (Fig. 6.18d), the simulation predicts two dominant emissions: one centered

around 250 eV from recombination mainly in the left half-cycle, and another higher-energy emission from the central half-cycle. A similar pattern is predicted at $\tau = 0.5$ fs (Fig. 6.18e), with two emissions expected—this time with the 250 eV emission originating from the right half-cycle. However, in the experimental data, these lower-energy emissions around 250 eV are entirely absent, leaving the central half-cycle emission as the most prominent feature, particularly at $\tau = 0.5$ fs (Fig. 6.18b).

The absence of these expected lower-energy emissions suggests a significant underlying mechanism not accounted for in the on-axis simulations, most likely plasma defocusing. At $\tau = 0.5$ fs, the ionization fraction reaches 0.4%, which is sufficient to trigger this effect (see Fig. 3.13). The right half-cycle, encountering a higher plasma density, would be more susceptible to defocusing and attenuation, leading to an emission with a lower central photon energy, potentially falling below the detectable range or being blocked by the metallic filter. This suggests that the experimentally observed spectra, which display a single half-cycle cutoff, may indeed come in the form of IAPs.

Shifting focus to photon flux, the synthesized waveforms in Fig. 6.10c demonstrate a nearly nine-fold increase within the water window, with a photon flux reaching $(8.8 \pm 1.8) \times 10^5$ photons/s at a relative delay of $\tau = +0.5$ fs, compared to $(1.0 \pm 0.2) \times 10^5$ photons/s for the IR-only case (ND0.0). These flux values correspond to emission energies of 44 ± 9 fJ and 5 ± 1 fJ for the synthesized and IR pulses, respectively. Given that the synthesized field has an energy of 182 μ J and the IR pulse has 170 μ J, this translates to efficiencies of 2.4×10^{-10} and 2.9×10^{-11} , respectively. Thus, the efficiency in the water window energy range is increased by a factor of eight.

Turning to the behavior in neon with a CEP shift of $\pi/4$ and still using the ND0.1 attenuation level, the plasma fractions can now reach up to 7.6%, significantly amplifying the impact of plasma-induced propagation effects, as shown in Fig. 6.19. The simulated and experimental scans generally align well, particularly outside the temporal overlap region, which spans from approximately -15 fs to +7 fs. Both scans capture the signal's disappearance—corresponding to the emission from the two strongest half-cycles—and the asymmetry caused by the higher ionization fraction when the NIR pulse precedes the IR pulse (negative delays). However, a closer examination reveals notable differences: the region where the signal vanishes is smaller in the simulations compared to the experimental results. Additionally, the normalized yield predicted in the simulations within this region is about ten times higher than what is observed experimentally. These discrepancies likely stem from the model's neglect of plasma defocusing, which would exacerbate the deterioration of the driving waveform.

6. WATER-WINDOW, SOFT X-RAY ISOLATED ATTOSECOND PULSES

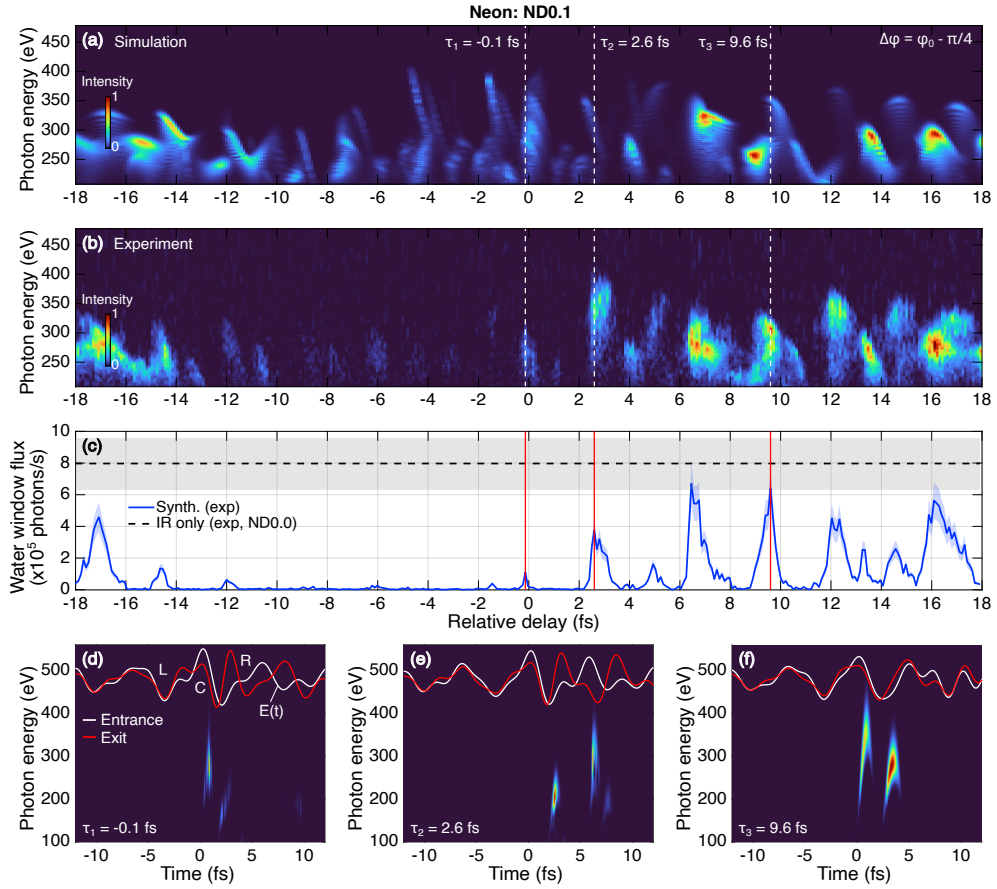


Figure 6.19: Relative delay scan in Ne with ND0.1 filter. Similar to Fig.6.16, but with the following differences: Combined beam energy: 182 μ J, CEP shift: $-\pi/4$. Experimental gas backing pressure and target position: (4 bar, 1 mm). Simulation parameters: (2.2 bar, 0.1 mm). For the simulation, the IR peak intensity was 3.65×10^{14} Wcm $^{-2}$, and the NIR/IR intensity ratio was 0.33. (d-f) Synthesized waveform and time-frequency analysis at delays of $\tau = -0.1$ fs, 2.6 fs, and 9.6 fs.

The time-frequency analysis and waveforms at selected relative delays ($\tau = -0.13$ fs, 2.6 fs, 9.6 fs) are presented in Fig. 6.19d-f. At $\tau = 9.6$ fs, which lies outside the temporal overlap region, the simulated and experimental scans exhibit strong agreement, despite the ionization fraction reaching 0.3%—about 1.5 times the critical ionization of neon at 1.6 μ m. At this delay, emissions from two half-cycles (the central and the right) are clearly visible in both the spectra (Fig. 6.19a-b) and the time-frequency analysis (Fig. 6.19f).

Within the temporal overlap region, as previously discussed, the influence of the generated plasma becomes increasingly pronounced, further highlighting the discrepancies between the experimental data and simulations. For instance, at $\tau = -0.13$ fs, both the simulation and experiment show a weak signal, but the simulated spectrum extends up to 350 eV, whereas the exper-

imental cutoff reaches only ≈ 300 eV.

A more significant discrepancy emerges at $\tau = 2.6$ fs, where the experimental spectrum shows an emission that resembles a single half-cycle emission and extends nearly to 390 eV, surpassing the phase-matching cutoff from the IR field alone (≈ 350 eV). This feature is not reproduced in the simulations, which instead predict two emissions (Fig. 6.19e): one around 200 eV and the other extending up to about 350 eV.

Single-atom response simulations using the same driving waveforms do predict an emission reaching 390 eV, along with another, less-energetic one extending only up to 300 eV. As discussed in Fig. 6.10, the highest photon energies, even those exceeding the phase-matching cutoff, can still be phase-matched at the very beginning of the medium, where the responsible half-cycle has not yet been significantly attenuated. The failure to capture this scenario in the simulations may stem from the implementation of the focusing term, G_{foc} (Eq. 6.6), in the model (Eq. 6.8), which does not account for the transversal diffraction of the during propagation. This omission could cause the simulated field to attenuate more rapidly than in reality, leading to abrupt waveform changes early in the medium. Consequently, phase-matching is hindered, likely resulting in the absence of the high-energy emission reaching up to 390 eV in the simulations.

Limitations in the simulation model not only affect the high-energy emission but also have implications for the lower-energy emission, as already observed in the helium case with ND0.1 attenuation (see Fig. 6.18). The lower-energy emission, originating from trajectories recombining within the right half-cycle, is more susceptible to plasma defocusing, likely explaining its absence in the experimental signal. Thus, in this scenario as well, plasma defocusing may contribute to producing the observed isolated burst that, according to simulations, would otherwise appear as two distinct bursts.

Moving on to the measured photon flux, the behavior in neon contrasts sharply with the helium case, where the water window photon flux increased by nearly a factor of nine. In neon, as shown in Fig. 6.19c, the photon flux remains below the level achieved with the IR pulse alone ($(8.0 \pm 1.6) \times 10^5$ photons/s). However, with other CEP shifts, such as the one without any shift ($\Delta\varphi = \varphi_0$) shown in Fig. D.11 in App. D, there is a modest flux increase by a factor of approximately 1.4, reaching $(1.1 \pm 0.2) \times 10^6$ photons/s. This increase occurs outside the overlap region, at a relative delay of $\tau \approx 16$ fs, where the constituent pulses are already distinguishable, and the synthesized waveform closely resembles the IR field alone. At this point, the effects of waveform synthesis, particularly interference, are less pronounced.

This section has elucidated the time-frequency profiles of observed emissions under varying intensity and phase-matching conditions. It has identified scenarios where IAPs are generated with minimal influence from plasma-

induced macroscopic effects, as demonstrated with ND0.2 in helium. Conversely, it has also highlighted cases—whether through higher intensities or the use of neon—where plasma-induced effects, like plasma defocusing, may contribute to IAP generation by suppressing one of the emissions from double bursts. While these findings are compelling, confirmation requires simulations that account for the transverse evolution of the propagated field—a task that is currently underway.

Additionally, the yield of emissions from synthesized waveforms has been shown to surpass that of the optimized IR-only field under certain conditions. A more systematic analysis of HHG efficiency across different intensity and phase-matching conditions will be discussed in the next section.

6.4.4 Water window yield efficiency

This section analyzes HHG yield and efficiency under varying conditions, including attenuation levels, gas types, and driving fields (synthesized or IR-only). Plasma effects are discussed, and driving waveforms leading to observed yields and efficiency enhancements are reported.

Figure 6.20 presents the measured photon flux, energy, and efficiencies within a 10% bandwidth centered at 225, 250, 275, . . . , 425 eV for both helium (a) and neon (b), driven by IR-only and synthesized fields across all attenuation levels (ND0.0-ND0.2). These values correspond to those at the HHG source, as the beamline's transfer function has been accounted for in the reported measurements. The generation conditions are detailed in Table 6.2. For each attenuation level, the IR-only values reflect the peak yield from the corresponding measured CEP scan, while the synthesized field values represent the highest yield obtained across the four measured delay scans with different CEP shifts (0 , $\pi/4$, $\pi/2$, and π). All measurements are contained in App. D. The specific delay and CEP shift settings leading to these yields are shown in Fig. 6.21.

In the IR-only scenario, Fig. 6.20 shows that higher yields and efficiencies in both helium and neon correlate with increased peak intensities, enabled by higher energies, with maximum values at the lowest attenuation level (ND0.0). In helium, the transition from ND0.2 to ND0.1 can yield nearly a sevenfold efficiency increase at 275 eV or a twofold increase at 225 eV. Moving from ND0.1 to ND0.0 results in a consistent doubling of efficiencies across the entire energy range. A similar pattern is observed in neon, where ND0.2 to ND0.1 leads to about an order of magnitude increase, and ND0.1 to ND0.0 produces a uniform twofold increase. These variations align with ionization fraction trends: in helium, ionization drops from 0.01% at ND0.0 to about 70% of this at ND0.1, and to 10% at ND0.2. Similarly, neon's ionization fraction decreases from 0.26% at ND0.0 to 80% of this at ND0.1, and to

6.4. Tailored waveforms for high-flux IAPs

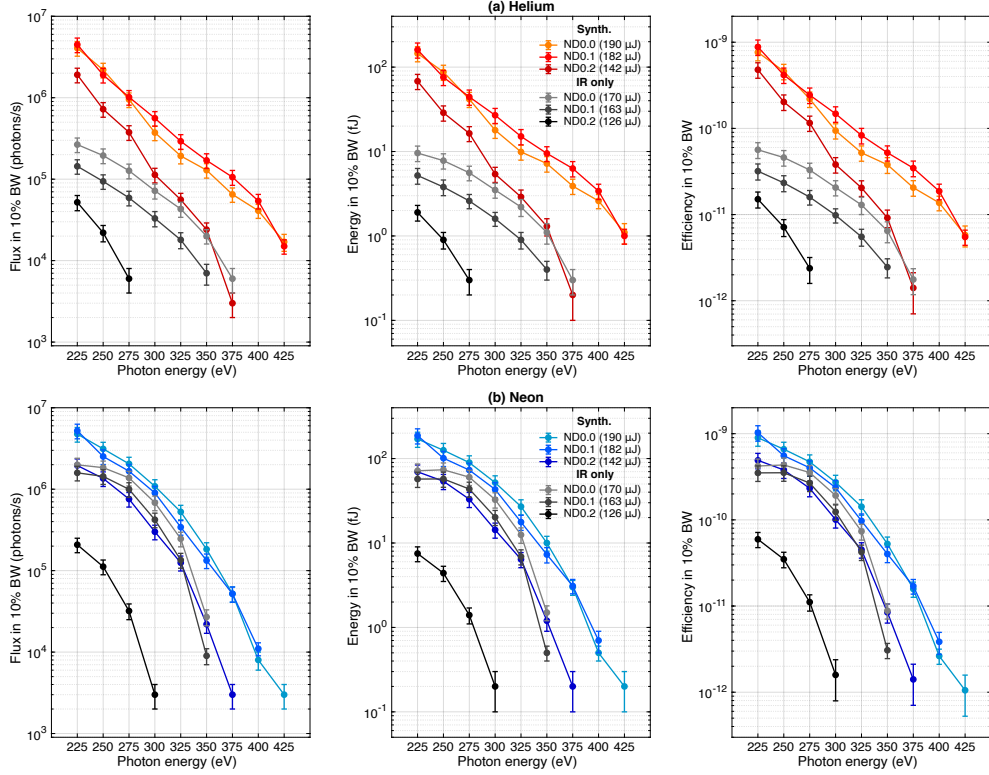


Figure 6.20: Measured absolute HHG yield and efficiency in He and Ne with IR-only and synthesized fields. Photon flux, energy, and efficiency ($E_{\text{out}}/E_{\text{in}}$) within a 10% bandwidth for (a) helium and (b) neon. Values represent the HHG source, produced by either the IR-only field (gray) or synthesized fields (colored) at all attenuation levels (ND0.0-0.2), with corresponding beam energies shown. The IR-only values represent the maximum flux from CEP scans, while the synthesized field values represent the maximum flux achieved across four delay scans at different CEP shifts (0 , $\pi/4$, $\pi/2$, and π ; see Fig. 6.21). Corresponding measured CEP and delay scans are found in App. D.

10% at ND0.2. Thus, the efficiency increase with lower attenuation levels is directly linked to higher ionization probabilities due to increased intensities.

Continuing with the IR-only field, a comparison between neon and helium reveals that neon generally achieves higher efficiencies than helium, except when comparing the highest attenuation in neon (ND0.2) with the lowest in helium. At ND0.0, where efficiencies are highest for both gases, neon outperforms helium, but only up to 350 eV. For instance, at 275 eV and 300 eV, neon is about ten times more efficient than helium, producing $(1.4 \pm 0.3) \times 10^6$ photons/s/10% BW at 275 eV and $(6.8 \pm 1.4) \times 10^5$ photons/s/10% BW at 300 eV. Even at 325 eV, neon remains about six times more efficient, yielding $(2.5 \pm 0.5) \times 10^5$ photons/s/10% BW. Only at 350 eV, near neon's phase-matching cutoff at $1.6 \mu\text{m}$ (≈ 345 eV), do their efficiencies become comparable, with neon producing $(2.7 \pm 0.6) \times 10^4$ photons/s/10%

BW. Beyond this energy, neon ceases to generate photons, while helium continues, providing $(6 \pm 2) \times 10^3$ photons/s/10% BW at 375 eV.

Turning to the HHG yields driven by synthesized fields, both gases exhibit a general efficiency boost compared to the IR-only (ND0.0) scenario, where the IR-only field has 170 μJ of energy. This boost is more pronounced in helium than in neon. In helium, the efficiency increase is evident across all attenuation levels of the synthesized field, with the highest efficiencies unexpectedly occurring at the intermediate attenuation level (ND0.1), where the synthesized field's energy closely matches that of the IR-only field, differing by only $\approx 7\%$. In contrast, the efficiency enhancement in neon is generally modest, not exceeding a factor of two across most of the energy range, but becomes more pronounced at 350 eV and beyond. This enhancement begins at the ND0.1 level and reaches its peak at the ND0.0 attenuation level. Notably, this enhancement beyond 350 eV, where the IR-only field ceases to generate photons but the synthesized field continues to do so, can also be seen as a cutoff extension.

A closer examination of the trend in helium, where the significant efficiency boost is observed, reveals that the HHG yield remains higher even at the highest attenuation level (ND0.2). At this level, the synthesized field has only about 80% of the IR-only energy, yet the efficiency consistently surpasses that of the IR-only field by at least a factor of two, with similar values being achieved only at 350 eV. Under the optimal attenuation level, the intermediate (ND0.1) level, particularly in the 300-350 eV range within the water window, the efficiency increases dramatically—by about 6-8 times compared to the IR-only field—and at 375 eV, it becomes nearly twenty times greater.

The absolute photon flux values in helium are $(5.6 \pm 1.1) \times 10^5$, $(1.7 \pm 0.4) \times 10^5$, and $(1.1 \pm 0.2) \times 10^5$ photons/s/10% BW at 300, 350, and 375 eV, respectively. In neon, the corresponding flux values are $(1.1 \pm 0.2) \times 10^6$, $(1.8 \pm 0.4) \times 10^5$, and $(5.2 \pm 1.1) \times 10^4$ photons/s/10% BW at 300, 350, and 375 eV¹¹. This indicates that, even with synthesized fields, helium outperforms neon beyond 350 eV. By 400 eV, helium's flux is nearly seven times greater than neon's, reaching $(5.4 \pm 1.1) \times 10^4$ photons/s/10% BW. It is important to note that phase-matching for the synthesized field has not been optimized as it was for the IR-only field. Thus, higher values than the reported ones are expected upon adjusting the pressure and gas target position.

Figure 6.21 shows the synthesis settings that led to the observed enhancements. On one hand, in helium (Fig. 6.21a), the relative delay between the NIR and IR fields that enhances efficiency is below 3 fs for ND0.2 and ND0.1, and even below 1 fs for photon energies above 325 eV (see inset). In

¹¹For context, Teichmann et al. [32] report $(2.8 \pm 0.1) \times 10^7$ photons/s/10% BW in neon and $(1.8 \pm 0.1) \times 10^6$ photons/s/10% BW in helium at the carbon K-edge (284 eV), using 400- μJ , 1.85- μm , 12-fs driving pulses focused by a $f = 100$ mm spherical mirror.

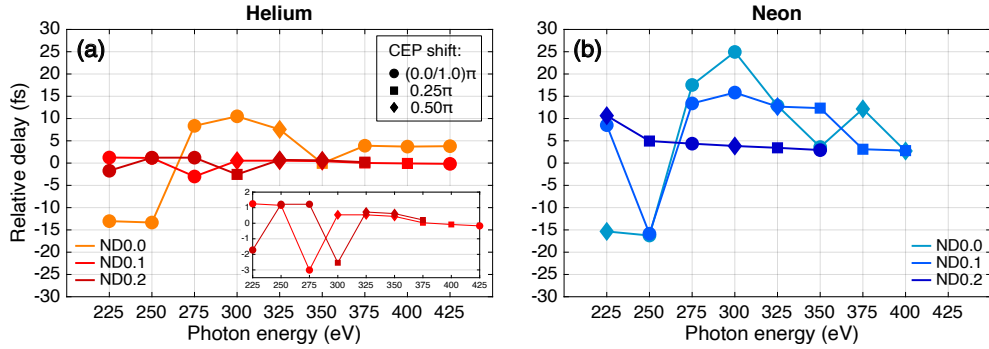


Figure 6.21: Extracted waveform synthesis settings for optimized HHG yields in He and Ne. Relative delays and CEP values (0 , $\pi/4$, $\pi/2$, π) for the synthesized waveforms that led to the highest yields (shown in Fig. 6.20) at all attenuation levels (ND0.0-0.2) in (a) helium and (b) neon. CEP markers: circles for 0 and π , squares for $\pi/4$, diamonds for $\pi/2$. The inset in (a) provides a zoomed view of the relative delay axis.

contrast, the ND0.0 case generally requires larger delays around 4 fs, 9 fs, and 13 fs. On the other hand, in neon (Fig. 6.21b), larger delays are required to achieve enhanced yields, even more so than in helium. For ND0.2, enhanced yields within the water window need relative delays around 3 fs. However, at lower attenuation levels (ND0.1 or ND0.0), delays exceeding 10 fs are generally necessary, in some cases even reaching up to 25 fs.

The need for larger relative delays between the NIR and IR fields as attenuation decreases suggests that the shortest, most intense synthesized waveforms—achieved with smaller delays—generate plasma levels that either significantly deform the driving waveform during propagation, limiting the generation of high photon energies, or exceed a threshold for effective phase-matching. At larger delays, reduced field intensity lowers plasma fractions, mitigating these issues but also decreasing ionization probabilities, which results in lower HHG yields. This effect is evident in helium when transitioning from intermediate (ND0.1) to the lowest (ND0.0) attenuation levels. At ND0.1, waveforms producing the highest yields from 225-400 eV result in ionization fractions up to 0.5%. In contrast, at ND0.0, waveforms with delays around 4 fs lead to ionization fractions below 0.3%, and at larger delays, these fractions drop further to less than 0.1%.

In neon, relative delays exceeding 10 fs cause the NIR and IR fields to start becoming distinguishable, as their separation exceeds the FWHM duration of the stronger IR field (≈ 9 fs). As a result, the three strongest half-cycles driving HHG start to resemble those of the IR field, leading to similar ionization fractions and efficiencies. Interestingly, at ND0.2, the yields from the synthesized waveforms (with relative delays around 3 fs) are lower than those driven by the IR-only field at ND0.0. This is unexpected since the ND0.2 synthesized waveforms produce ionization fractions about an order

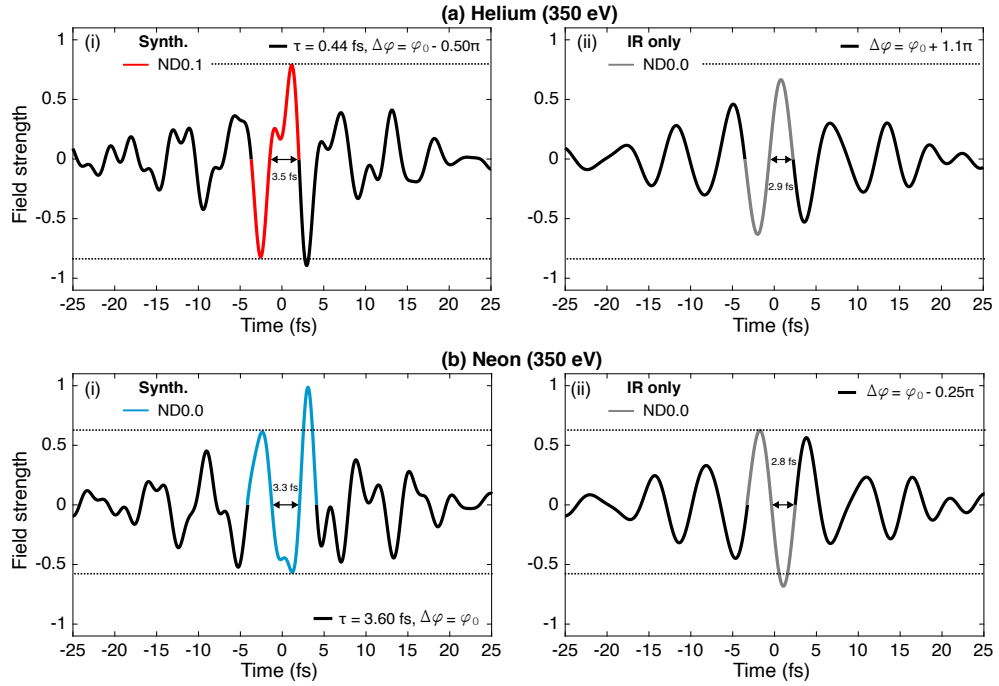


Figure 6.22: Measured waveforms for optimized HHG yields at 350 eV in He and Ne. (a) Helium: (i) Synthesized waveform (ND0.1, $\tau = 0.44$ fs, $\varphi_0 - \pi/2$) and (ii) IR-only field (ND0.0, $\varphi_0 + 1.1\pi$) yielding maximum yield at 350 eV within a 10% bandwidth. (b) Same as (a) for neon: (i) Synthesized waveform (ND0.0, $\tau = 3.60$ fs, φ_0), (ii) IR-only field (ND0.0, $\varphi_0 + 0.25\pi$). Contributing half-cycles to the emission are highlighted, with durations indicated where electron trajectories recombine. Both fields are normalized to the synthesized field's peak envelope in each gas. Dashed lines aid in comparing amplitudes between synthesized and IR-only fields.

of magnitude higher than the IR-only case at ND0.0, which would imply higher yields. The likely explanation is the large phase mismatch caused by these higher ionization fractions. The IR-only ND0.0 case was near the ideal phase-matching condition, with an ionization fraction (0.26%) close to the critical value for phase-matching ($\approx 0.2\%$). In contrast, the ND0.2 synthesized case produces ionization fractions well above this critical value, leading to phase-mismatch and, consequently, lower yields.

Figure 6.22 presents the synthesized and IR-only waveforms that produced the highest yield and efficiency at 350 eV within a 10% bandwidth in helium and neon, using ND0.1 and ND0.0 attenuation levels, respectively. In helium, the synthesized waveform improved HHG efficiency by about a factor of eight, while in neon, it achieved a sixfold increase, both relative to the IR-only (ND0.0) field (panel (ii)). The half-cycles contributing to the 350 eV emission are highlighted.

In helium (Fig. 6.22a), a single cycle of the synthesized waveform (panel (i)) produces isolated emission in this energy range. This cycle can lead to a

high yield due to two factors: a higher ionization probability, driven by the strong field at the moment of ionization (at $t = -2.7$ fs), and the long duration of the recombining half-cycle (≈ 3.5 fs). Together, these factors ensure both high ionization probabilities and increased electron acceleration. In contrast, the IR-only field (panel (ii)), even at the optimized CEP value, has a lower field strength at the moment of ionization (about 80% of the synthesized case) and a shorter half-cycle duration (≈ 2.9 fs), resulting in reduced acceleration.

In the synthesized waveform enhancing neon (Fig. 6.22b, panel (i)), three half-cycles can contribute, generating two bursts. The ionizing half-cycles, peaking at $t = -2.4$ fs and $t = 1.2$ fs, have comparable or lower amplitudes than the optimized IR-only field. However, electron acceleration is still achieved: the first ionization benefits from the longer duration (3.3 fs) of the following half-cycle, while the second ionization gains from the nearly twofold stronger field strength of its subsequent half-cycle, peaking around $t = 3$ fs. This half-cycle, peaking around 3 fs, generates an ionization fraction of about 5%, likely disrupting phase-matching and leaving only the emission from the central half-cycle. Experimental scans (Fig. D.9a in App. D) support this, suggesting that the observed emission corresponds to an isolated burst.

Building on these findings, single-atom response simulations predict even higher yields with other waveform settings. Some waveforms reduce the travel time of the ionized electron in the continuum, minimizing electron dispersion during propagation and improving overlap with the ground state upon recombination, thereby enhancing the emission yield [47, 188]. Other waveforms favor the generation of short trajectories by positioning the peak of the ionizing half-cycle just tens of attoseconds away from their moment of birth. This configuration ensures that the driving waveform concentrates energy primarily on short trajectories that will eventually achieve phase matching, thereby minimizing energy loss to long trajectories [48]. However, the increased plasma levels generated by these other waveforms ultimately led to lower HHG yields.

This study demonstrates that tailored waveforms delivered by the PWS can enhance HHG efficiencies in the water window, even without optimization of phase-matching conditions. Further improvements in yield could be achieved through finer control of plasma levels, with additional gains possible by optimizing target position and gas pressure. Additionally, it has been shown that the ability to reach sub-cycle durations with these tailored fields facilitates the emission of a single burst within a specific energy range. Introducing a third few-cycle field in the visible range [110, 295] could further boost efficiency by enabling finer shaping of the field, leading to better control of electron trajectories [48, 310]. The shorter duration would not only

further ease the generation of even broader IAPs but also allow for higher intensities with reduced plasma fractions, enabling phase-matching at higher photon energies (see Fig. 3.10).

Conclusions and Outlook

This thesis explored the generation of attosecond pulses, with a focus on isolated attosecond pulses (IAPs), via high-harmonic generation (HHG) driven by tailored optical fields capable of reaching sub-cycle durations. The objectives were to investigate the potential for generating IAPs in the extreme ultraviolet (EUV) and soft X-ray ranges, extending up to the water window (284-543 eV), using these fields. Additionally, this work examines how tailoring the waveform of the electric fields affects the spectral and temporal properties of the generated IAPs, and assesses whether such tailoring could enhance the efficiency of the generation process, particularly in the water window.

To achieve these objectives, in Ch. 4 it was first demonstrated the successful coherent synthesis of millijoule-level few-cycle pulses using a parametric waveform synthesizer (PWS). The PWS employs a parallel waveform synthesis scheme, where optical parametric amplifiers (OPAs) amplify carrier-envelope-phase (CEP)-stable pulses in different spectral ranges within dedicated channels. In the current configuration, two spectral channels are implemented: one in the near-infrared (NIR, 0.65–1 μm) and another in the infrared (IR, 1.2–2.2 μm), thus together spanning a 1.7-octave bandwidth. After amplification, the NIR and IR pulses are compressed to few-cycle durations of ≈ 6 fs and 8 fs, respectively, achieving a combined beam energy of 0.5 mJ. By coherently combining these pulses, synthesized sub-cycle pulses with a duration of 2.8 fs (0.6 optical cycles) at a central wavelength of 1.4 μm can be generated. Tailoring of the synthesized field is achieved by controlling the relative delay between the constituent pulses and the CEP of the resulting field. These tailored waveforms were then used to drive HHG in argon, producing both narrowband and broadband EUV continua.

Attosecond streaking measurements directly measured the electric field of the synthesized sub-cycle waveforms, revealing a 3.5 fs duration that preserved the spectral components of the constituent NIR and IR pulses. Addi-

tionally, the measurements confirmed the generation of an EUV IAP with a central photon energy of ≈ 40 eV and a duration of about ≈ 240 as, demonstrating both the presence of IAPs and the short-term stability of the system. Long-term stability was further validated by sequential streaking traces acquired over more than two hours, showing minimal deviations in the retrieved electric fields. These results provided a robust starting point for further exploration of IAP generation and the effects of waveform tailoring.

In Ch. 5, experimental evidence of tunable IAP generation in the EUV and soft X-ray regions, employing argon and neon with ≈ 300 mbar of pressure was presented. By performing waveform scans, where the delays between the NIR and IR pulses were systematically varied at a fixed CEP, a diverse range of smooth spectral shapes was observed. These shapes exhibited bandwidths ranging from narrowband to broadband, with photon energies spanning from ≈ 30 to 110 eV in argon and up to ≈ 200 eV in neon, depending on the delay. Furthermore, CEP scans at fixed delays revealed a strong π -periodic modulation of the spectra, indicating the emission of IAPs. Attosecond streaking measurements confirmed the IAP nature of selected emissions within these scans, revealing IAP pulse durations from ≈ 80 to 240 as. Single-atom response simulations and classical trajectory analysis highlighted the mechanisms behind IAP generation facilitated by the driving fields. The tailoring of individual half-cycles of the synthesized waveform allows precise control over the trajectory of the ionized electron, which in turn affects the energy and phase of the resulting emission. Furthermore, the sub-cycle duration of the synthesized fields permits the confinement of HHG to a single optical cycle, thereby enabling the generation of broadband IAPs and bypassing the need for conventional gating techniques.

Chapter 6 details the generation of water window HHG driven by IR-only and synthesized fields in multi-atmospheric neon and helium targets. This study was conducted in two parts.

The first part systematically explored water window generation under various focusing conditions ($f = 200, 400, 500$ mm). Optimizing the gas target position and backing pressure was crucial for achieving optimal phase-matching, which lead to water window spectra extending to ≈ 350 eV in neon and 450 eV in helium. In neon, the 350 eV cutoff is attributed to a critical intensity, determined by the critical ionization fraction, beyond which phase-matching becomes increasingly difficult. Similar to the EUV case, CEP scans revealed a clear π -periodic modulation of water window spectra, indicative of IAP generation with both the IR field and the synthesized field. IAPs driven by the synthesized field exhibited a broad spectrum, covering both plateau and cutoff energies, while those produced by the IR field were limited to cutoff energies. Delay scans under varying focusing conditions (and thus intensities) showed a shift from cutoff extension and yield

enhancement at lower intensities to significant signal suppression at higher intensities, likely due to plasma-induced waveform deformation or phase-mismatch. A macroscopic, on-axis numerical model of HHG was developed, which qualitatively captured these experimental observations, including the spectral dependence on pressure and gas target position, the 350 eV cutoff in neon, and the signal suppression at higher intensities.

The second part of the study investigated, under varying intensities, the time-frequency profile of the emissions, the mechanisms behind IAP generation in this spectral range, and the HHG yield. In contrast to the first part, the focal length was kept fixed to $f = 400$ mm, and reflective ND filters were used to attenuate the beam, enabling direct comparison of HHG yields and efficiencies at different intensities. The gas target position and backing pressure were optimized for maximum flux using only the IR field, with these conditions maintained when driving HHG with the synthesized waveforms. Thus, HHG driven by the synthesized waveforms was not optimized for phase-matching. Additionally, the driving waveforms were directly characterized at the HHG target, linking each to its corresponding HHG spectrum and providing input for simulations. This approach permit to expose the time-frequency profile of the measured emissions.

At intensities producing ionization fractions below or near the critical threshold, simulations showed strong qualitative agreement with experimental results, and indicated that IAP generation resulted from the confinement of HHG within a single cycle. However, at higher intensities, experiments and simulations diverged, likely due to the absence of plasma defocusing in the simulation model. Despite this divergence, the comparison suggests that plasma defocusing plays a crucial role in IAP generation by attenuating the half-cycle that would otherwise produce a second emission.

Comparisons of HHG yields and efficiencies revealed that tailored synthesized fields can achieve higher efficiencies than those driven by the IR field alone. However, high plasma fractions can hinder this enhancement due to waveform deformation during propagation or phase mismatch. Analysis of the measured waveforms showed that the observed improvement was due to two factors enabled by waveform synthesis: an intensity increase from constructive interference and the formation of half-cycles with extended duration. An eightfold efficiency boost was observed in helium, and a sixfold increase in neon, both around 350 eV. Across the entire water window range, helium showed also an eightfold efficiency increase. Even greater enhancements are expected with optimized intensity and phase-matching conditions. Measurements also indicated that neon has a superior efficiency for water window harmonics up to 350 eV, while helium is better for higher energies.

This seminal study paves the way for further research focused on optimizing conditions for high-flux HHG. Future studies will explore the impact of

adding a third field in the visible range to the existing synthesized field.

Incorporating this third channel offers several advantages. First, it would enable the synthesis of even shorter waveforms (< 2 fs [295]), which would facilitate the generation of broader IAPs than currently achievable. The shorter duration would also allow phase-matching at higher energies, as higher intensities are required to reach the critical ionization fraction (see Fig.3.10). Second, adding frequencies in the visible range would provide finer control over the shaping of individual half-cycles and, consequently, the ionized electron trajectories, offering greater tunability of the emitted IAPs. Moreover, it would shorten the time electron spends in the continuum by using the higher-frequency components in the half-cycle to return it to the parent ion more quickly, increasing the HHG yield [47, 188]. Finally, the ability to ionize short trajectories with much stronger field strength would significantly reduce energy wasted on long trajectories that typically do not phase-match or reach the detector [48]. Consequently, the efficiency could potentially increase by at least a factor of ten compared to current levels.

Thus, parametric waveform synthesis technology delivering sub-cycle optical fields proves to be a viable route for generating tunable, high-flux IAPs.

Outlook: A tunable attosecond beamline

To exploit the tunability of the generated attosecond pulses, a beamline was designed to work with the generated spectral range ($\sim 30 - 600$ eV). The author of this thesis was a main contributor to the optical and mechanical design of this new beamline, shown in Fig. 7.2. Main differences from previous versions include: (1) A toroidal mirror imaging in a 2f:2f geometry ($f = 500$ mm, 87° AOI) to focus the HHG source onto the target sample. (2) An experimental chamber designed by Dr. Scheiba [297]. (3) Four reflective zone plates (RZPs)¹ that replace the three gratings, capable of spectrally resolving light from 20 eV to nearly 600 eV (see Fig.7.1).

Another significant difference is the nickel coating on both the toroidal mirror and the diffracting optics (RZPs), which provides a relatively flat reflectivity for photon energies above approximately 100 eV and a reflectivity greater than 75%.

The four RZPs are printed on a single curved silicon substrate and are designed to operate around 44 eV (RZP1), 110 eV (RZP2), 230 eV (RZP3), and 340 eV (RZP4). These custom-made RZPs generally offer higher efficiencies than the existing gratings in the beamline, exceeding 20% for all RZPs and achieving about four times higher efficiency than gratings within the water

¹Nano Optics Berlin GmbH

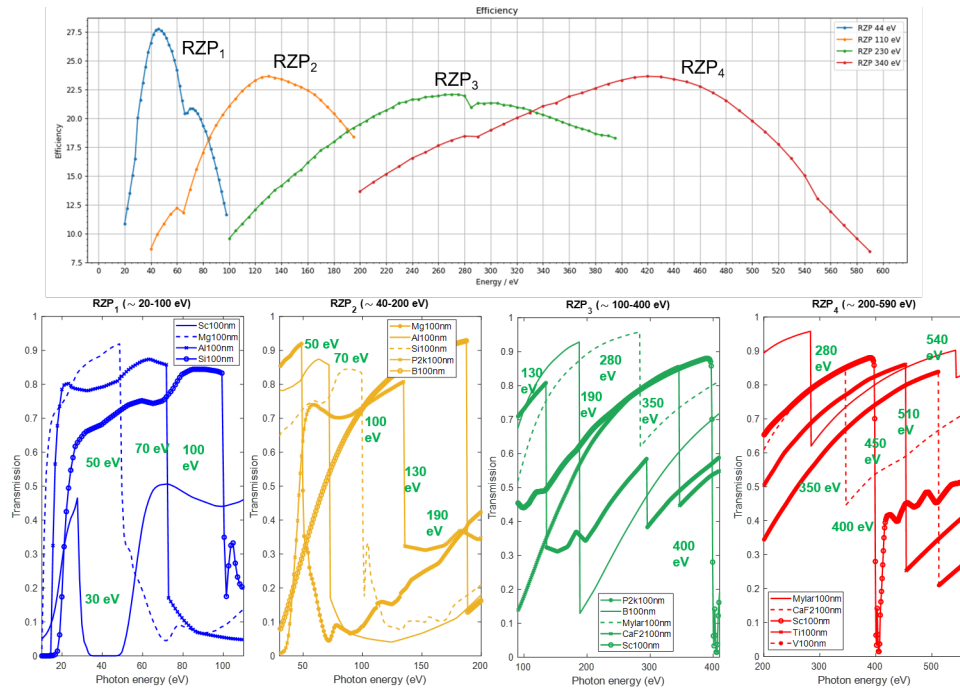


Figure 7.1: Reflective zone plates efficiency and calibration. (Top) efficiencies of custom-made reflective zone plates (RZPs). (Bottom) selection of filters for calibrating the CCD from a pixel axis to an energy axis.

window range. However, this advantage comes at the cost of lower resolution compared to gratings (not specified by the provider). The RZPs have a peak resolution ($E/\Delta E$) of approximately 750. By shifting the substrate vertically, different spectral regions can be selected without adjusting the incidence angle or CCD position. The RZP patterns account for substrate curvature, eliminating the need for realignment during vertical movement. The incidence grazing angle is 2.65° , and the reflected angles for the minimum and maximum covered wavelengths are 6.5° and 4.5° , respectively. These RZPs were designed for an HHG source with an assumed maximum transverse FWHM of $45 \mu\text{m}$ and are configured to image the source in a 1:1 geometry, with the object positioned 600 mm from the RZPs. Calibration of each RZP can be done using a set of metallic filters (see Fig. 7.1).

Several modifications have been made to the presented beamline design during the writing of this thesis. However, the optical path and components such as the toroidal mirror and RZPs remain unchanged. The HHG beam emerging from the gas cell passes through an optional set of metallic filters for RZP calibration. A palladium or aluminum filter, installed in a gate valve, isolates the first and second chambers from both vacuum and light.

The transmitted beam then passes through a second set of metallic filters for

7. CONCLUSIONS AND OUTLOOK

further spectral filtering. It reflects off a toroidal mirror, which images the beam in front of the eTOF spectrometer after passing through the hole of a perforated mirror. The toroidal mirror is precisely aligned using a linear stage, a rotation stage, and two goniometers, housed in an aluminum frame with minimal openings to reduce the risk of damage and contamination.

After the HHG beam hits the target, it can pass through a third metallic filter before reaching the set of RZPs. The RZPs are mounted on a linear stage, a rotation stage, and a vertical translation stage for alignment and selection. Additionally, a nickel-coated flat mirror is mounted on the same stage for characterizing the diverging HHG beam at the CCD. The reflecting beam from the RZPs then finally hits the CCD, with the zeroth-order beam being blocked by a baffle.

The optical beam passes through a set of CaF₂ wedges, which allow for the control of the CEP of the synthesized waveform and the relative delay between the pulses within a range of ~ -10 to $+10$ fs. This configuration allows for the independent tailoring of the pump waveform, without affecting the HHG driving waveform. The beam is then recombined using a perforated spherical mirror ($f = 400$ mm) and directed onto the target. The metallic filter integrated in a gate valve before the RZP is used to block the optical light.

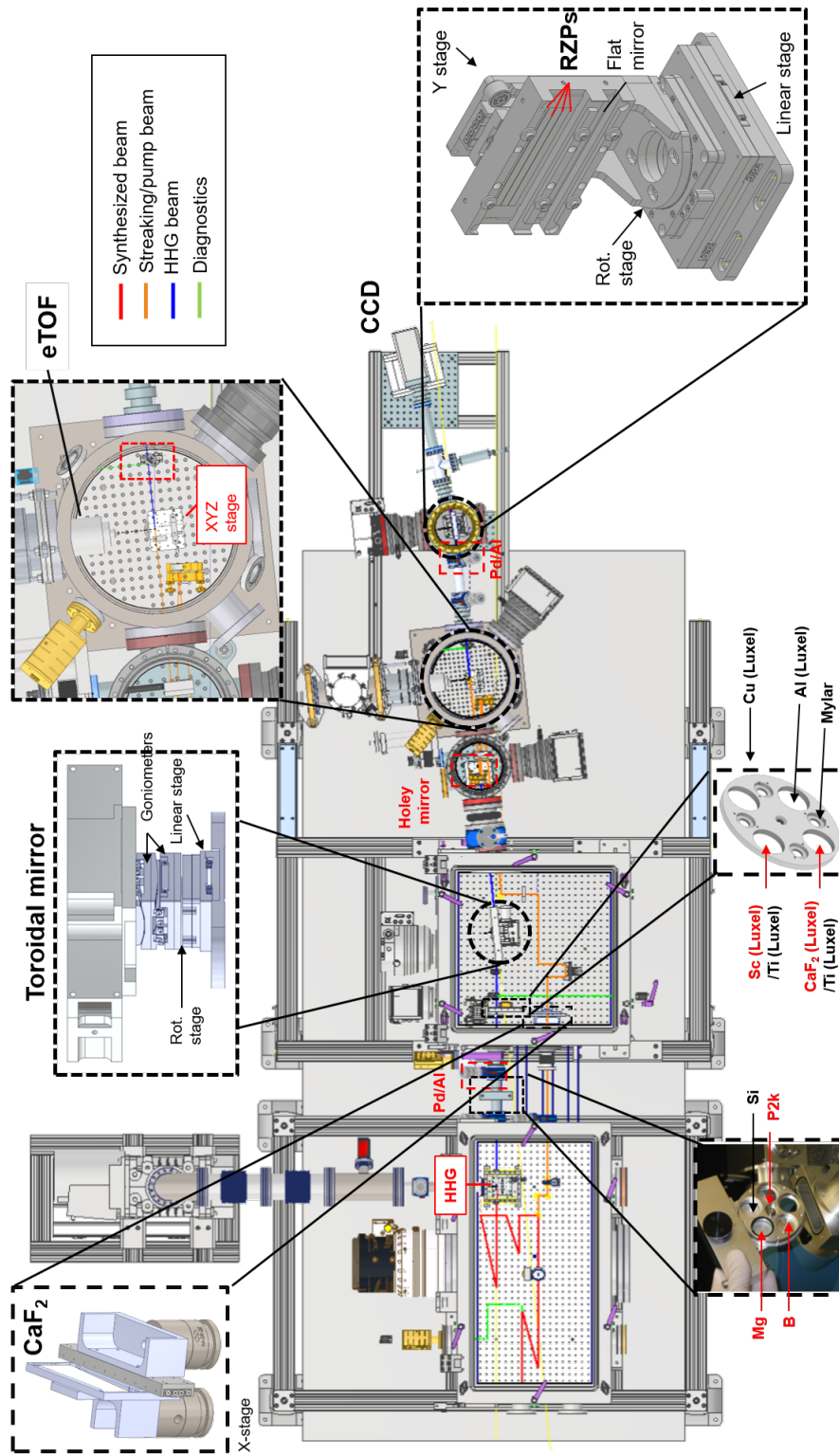


Figure 7.2: Tunable attosecond beamline

Appendix A

Peak intensity estimation

When working with high-harmonic generation (HHG), it is essential to estimate the peak intensity on the target. This can be done based on measurable quantities like the pulse energy, temporal profile, and beam waist. The following derivations, which align with expected values and expressions found in the literature [52], were used in this work.

One assumes a linearly polarized pulsed beam with an electric field that can be written as:

$$E(r, \theta, t) = E_0 \hat{\varepsilon}(t) \cos(\omega_0 t + \varphi) \cdot \hat{G}(r, \theta), \quad (\text{A.1})$$

with E_0 the peak field amplitude, $\hat{\varepsilon}(t)$ a normalized function that accounts for the envelope's temporal shape, and $G(r, \theta)$ is an axially-symmetric transverse (amplitude-normalized) distribution. The peak intensity and intensity envelope are given by

$$I_0 = \frac{1}{2} c \varepsilon_0 E_0^2 \quad (\text{A.2})$$

$$I_{\text{env}} = I_0 \cdot \hat{\varepsilon}(t)^2 \cdot \hat{G}(r, \theta)^2 \quad (\text{A.3})$$

The pulse energy, U , measured by an energy meter, relates to the peak intensity, I_0 , through an integral of the intensity envelope, I_{env} , over space and time, i.e.,

$$U = I_0 \cdot A \cdot \tau, \quad (\text{A.4})$$

where A and τ are the beam and pulse envelope's areas. These are calculated as follows:

A. PEAK INTENSITY ESTIMATION

$$A = \int_0^{2\pi} d\theta \int_0^\infty dr \cdot r \cdot \hat{G}(r, \theta)^2 \quad (\text{A.5})$$

$$\tau = \int_{-\infty}^\infty dt \cdot \hat{\varepsilon}(t)^2 \quad (\text{A.6})$$

For a Gaussian beam and temporal profiles, the distribution and envelope functions take the form

$$\hat{G}(r, \theta) = \exp(-r^2/w_0^2) \quad (\text{A.7})$$

$$\hat{\varepsilon}(t) = \exp[-2 \ln 2 (t/\tau_p)^2] \quad (\text{A.8})$$

From such expressions, the areas can be readily calculated, yielding $A = \pi w_0^2/2$, and $\tau \approx \tau_p/0.94$. This leads to the following peak intensity estimation:

$$I_0 = \frac{U}{\tau \cdot A} = 0.94 \frac{2U}{\tau_p \cdot \pi w_0^2} = \frac{2P_p}{\pi w_0^2}, \quad (\text{A.9})$$

and P_p is the pulse's peak power.

For arbitrary beam and pulse shapes, the peak intensity I_0 (Eq.A.9) must be evaluated after computing Eqs. A.5 and A.6 using measured data.

Appendix B

Photon flux measurement

Figure 6.1 illustrates the experimental setup used to measure the photon flux signal. Detailed information about the photodiode is provided in Sec.4.3 and in Fig.4.9a.

The measurement of the EUV/soft X-ray photon flux is based on the voltage recorded by the photodiode. The procedure involves calibrating the intensity axis of the CCD-based spectrometer measurements using the photodiode measurements. Once calibrated, the photon flux for a specific energy range can be computed from CCD-based signals.

Since the photodiode detector is silicon-based, measurements are performed using the IR pulse, with its spectrum ranging from 1.2 μm to 2.2 μm , instead of the NIR pulse, which spans 0.65 μm to 1.1 μm and would be absorbed by the silicon detector, complicating the distinction between EUV/SXR light and optical light. During the measurement, all other light sources on the beamline are blocked or turned off, including pressure gauges (which have a hot filament that could emit light reaching the photodiode) and infrared light from closed-loop stages. Any potential reflections inside the HHG chamber are also blocked. Additionally, to measure within the water window (see Sec.6.1), a combination of aluminum and copper filters is used. This combination ensures that neither optical light nor low-order harmonics in the vacuum UV or EUV range reach the detector.

Figure B.1 exemplifies the calibration measurements taken after these precautions have been taken. The calibration measurement begins by driving HHG and sweeping the CEP of the IR pulse over a full period multiple times. This averaging over all CEP values prevents fluctuations in photon flux that might arise from the IR field being at a specific CEP. The generated emission is recorded by both the CCD and the photodiode. The goal is to compute a voltage predicted from the CCD measurement and compare it with the voltage measured by the photodiode.

B. PHOTON FLUX MEASUREMENT

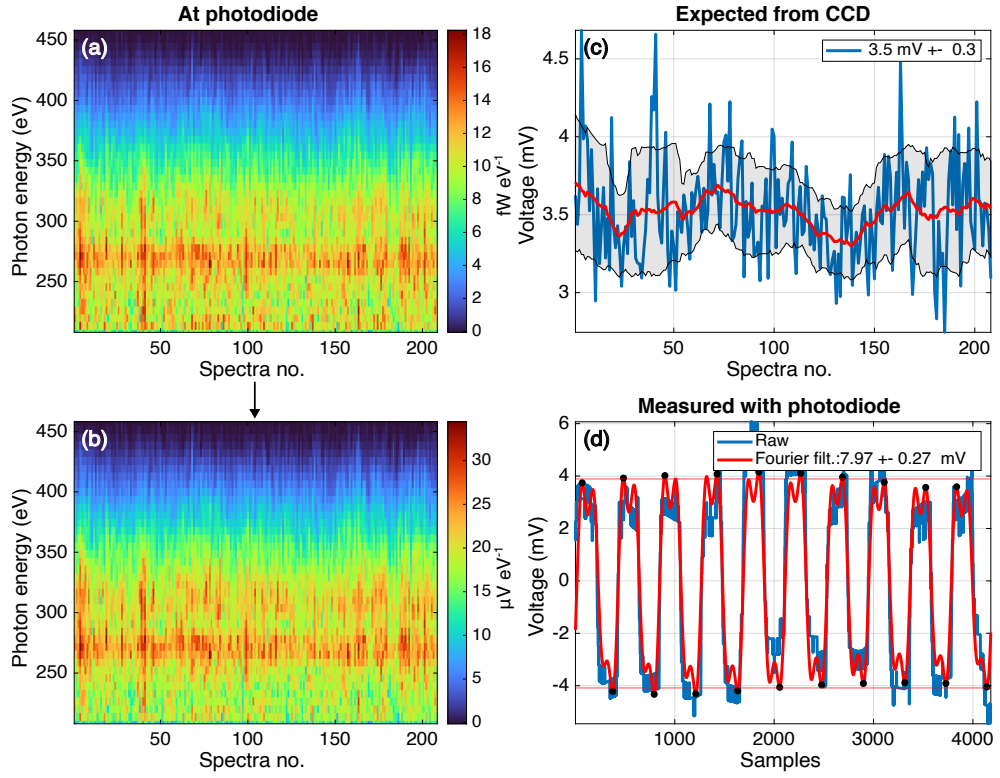


Figure B.1: CCD spectrometer calibration. (a) Power spectral density inferred from the CCD measurement at the photodiode position. (b) Converted voltage signal after accounting for photodiode responsivity (Fig.4.9a) and amplifier gain. (c) Integrated voltage signal with mean value (red line) and standard deviation (shaded area). (d) Voltage signal measured with the photodiode after background subtraction.

Focusing first on the CCD-based measurement, the number of incident photons on the CCD per eV, per second is given by [256]:

$$n_{\text{CCD}}(\omega) = \frac{S_{\text{CCD}}(\omega) \cdot \sigma}{\eta_{\text{QE}}(\omega) \cdot n_{\text{e-h}}(\omega) \cdot t_{\text{exp}}} \quad (\text{B.1})$$

where, S_{CCD} is the raw measured signal (in counts per eV), σ is the sensitivity in electrons per CCD count, η_{QE} is the CCD quantum efficiency, $n_{\text{e-h}}(\omega) = \hbar\omega/3.65$ accounts for the electron-hole pairs freed per incident photon with energy ($\hbar\omega$) in a Si-based detector [311], and t_{exp} is the exposure time.

The photon flux at the position of the photodiode (located after the gold toroidal mirror) is then given by:

$$n_{\text{PD}}(\omega) = \frac{n_{\text{CCD}}(\omega)}{\eta_{\text{g}}(\omega)} \quad (\text{B.2})$$

This calculation accounts for the grating efficiency η_g but neglects any potential transmission losses from the input slit. To determine the photon flux at the HHG source itself, the transmission through the metallic filters and reflection from the toroidal mirror would need to be taken into account. For the purposes of the calibration, the focus is solely on the photon flux reaching the photodiode.

From the photon flux, the power spectral density is calculated as:

$$P_{\text{PD}}(\omega) = n_{\text{PD}}(\omega) \cdot (\hbar\omega), \quad (\text{B.3})$$

This power spectral density is plotted in Fig.B.1a. To fully account for the photodiode's spectral response, the power spectral density is converted to a voltage signal using the photodiode's responsivity curve η_{PD} (in units of [A/W], see Fig.4.9a) and the operational amplifier's resistance R of 10 G Ω . This converted signal is shown in Fig.B.1b. Finally, integration of this signal along the energy axis yields the voltage estimated by the CCD measurement.

$$V_{\text{est.}} = \int P_{\text{PD}}(\omega) \cdot \eta_{\text{PD}} \cdot R d\omega, \quad (\text{B.4})$$

which is shown in Fig.4.9c.

The photodiode-based measurement provides a voltage signal directly. A glass plate is repeatedly inserted and removed from the beam path to distinguish the EUV/soft X-ray signal from the optical background and account for a drifting offset caused by the heating of the circuit. This creates a time-varying pattern in the photodiode voltage, as shown in Fig.4.9d. By applying a Fourier filter to remove residual noise and then analyzing the difference between the voltage levels with and without the glass plate, the true EUV/soft X-ray voltage signal, V_{PD} is extracted.

The calibration factor (α) is finally determined as the ratio between the photodiode voltage V_{PD} and the estimated voltage from the CCD measurement ($V_{\text{est.}}$). In this specific example, the calibration factor is calculated to be $\alpha = (8.0 \pm 0.3) / (3.5 \pm 0.3) = 2.3 \pm 0.2$.

Appendix C

Derivation of propagation equations

This appendix derives the propagation equations for the harmonic and optical fields used in Ch. 6. For a more comprehensive discussion of these equations, readers are referred to Refs. [170, 219]. All variable definitions employed here were previously introduced in Chs. 2 and 3.

The propagation equation for the harmonic field, E_h , is initially expressed in the time domain as:

$$\frac{\partial^2 E_h}{\partial z^2}(t, z) - \frac{1}{c^2} \frac{\partial^2 E_h}{\partial t^2}(t, z) = \mu_0 \frac{\partial^2 P}{\partial t^2}(t, z) \quad (\text{C.1})$$

Transforming this to the frequency domain, and using the relation $P(\omega) = P_L(\omega) + P_{NL}(\omega)$, where $P_L(\omega) = \epsilon_0 \chi^{(1)}(\omega) E_h(\omega)$, one obtains:

$$\frac{\partial^2 E_h}{\partial z^2}(\omega, z) + \frac{\omega^2}{c^2} \left[1 + \chi^{(1)}(\omega) \right] E_h(\omega, z) = -\frac{\omega^2}{\epsilon_0 c^2} P_{NL}(\omega, z) \quad (\text{C.2})$$

To simplify this equation, a reference frame moving at the speed of light is adopted, such that $E_h(\omega) = \tilde{E}_h(\omega) \exp(-i\omega z/c)$ and $P_{NL}(\omega) = \tilde{P}_{NL}(\omega) \exp(-i\omega z/c)$. Substituting these expressions into the previous equation and applying the SEWA yields:

$$-\frac{2i\omega}{c} \frac{\partial \tilde{E}_h}{\partial z}(\omega, z) + \frac{\omega^2}{c^2} \chi^{(1)}(\omega) \tilde{E}_h(\omega, z) = -\frac{\omega^2}{\epsilon_0 c^2} \tilde{P}_{NL}(\omega, z) \quad (\text{C.3})$$

By utilizing the relationship $n_c = n - i\beta \approx 1 + \chi^{(1)}/2$, implying $\chi^{(1)} \approx 2(n - 1 - i\beta)$, the simplified propagation equation is obtained:

$$\frac{\partial \tilde{E}_h}{\partial z}(\omega, z) + i \left[k_n(\omega) - k(\omega) - i \frac{\alpha(\omega)}{2} \right] \tilde{E}_h(\omega, z) = -\frac{i\omega}{2\epsilon_0 c} \tilde{P}_{NL}(\omega, z) \quad (\text{C.4})$$

C. DERIVATION OF PROPAGATION EQUATIONS

The previous differential equation admits an analytical solution, given by (when integrating over the medium's length L_{med}):

$$\tilde{E}_h(\omega, z = L_{\text{med}}) = -\frac{i\omega}{2c\epsilon_0} \int_0^{L_{\text{med}}} \tilde{P}_{\text{NL}}(\omega) e^{-i[k_n(\omega, z) - k(\omega) - i\frac{\alpha(\omega)}{2}](L_{\text{med}} - z)} dz, \quad (\text{C.5})$$

with $\tilde{P}_{\text{NL}}(\omega, z) = \mathcal{F}[n_0(t, z)d_h(t, z)]$.

Now, the propagation equation for the laser field, E_L , is also considered. Initially, it is also expressed in time domain as:

$$\frac{\partial^2 E_L}{\partial z^2}(t, z) - \frac{1}{c^2} \frac{\partial^2 E_L}{\partial t^2}(t, z) = \mu_0 \left(\frac{\partial^2 P_L}{\partial t^2}(t, z) + \frac{\partial J}{\partial t}(t, z) \right) \quad (\text{C.6})$$

where

$$P_L(t, z) = \epsilon_0 \int_{-\infty}^{\infty} dt' \chi^{(1)}(t - t') E_L(t') \quad (\text{C.7})$$

and

$$J(t, z) = \epsilon_0 \left[\frac{I_p}{\epsilon_0} \frac{\dot{n}_e(t, z)}{E_L(t, z)} + \int_{-\infty}^t dt' \omega_p^2(t', z) E_L(t', z) \right] \quad (\text{C.8})$$

with $\omega_p^2(t, z) = e^2 n_e(t, z) / \epsilon_0 m_e$ the plasma frequency. Transforming this equation into the frequency domain yields:

$$\frac{\partial^2 E_L}{\partial z^2}(\omega, z) + \frac{\omega^2}{c^2} E_L(\omega, z) = -\frac{\omega^2}{c^2} \chi^{(1)}(\omega) E_L(\omega, z) + \frac{i\omega}{c^2} \mathcal{F}[J(t, z)] \quad (\text{C.9})$$

Again, the assumption is made that $E_L(\omega, z) = \tilde{E}_L(\omega) \exp(-i\omega z/c)$ and $J(\omega, z) = \tilde{J}(\omega, z) \exp(-i\omega z/c)$. Invoking the SEWA once more, and using the definition of the first order response (neglecting absorption) $\chi^{(1)} \approx 2(n - 1)$, the following simplified equation is obtained:

$$\begin{aligned} \frac{\partial \tilde{E}_L}{\partial z}(\omega, z) = i \left[k(\omega) - k_n(\omega) \right] \tilde{E}_L(\omega, z) \\ + \frac{i}{2\omega c} \mathcal{F} \left\{ i\omega [J_{\text{abs}}(t, z) + J_{\text{pl}}(t, z)] \right\} \end{aligned} \quad (\text{C.10})$$

In this equation, the absorption term has been neglected due to its negligible contribution for optical and infrared frequencies. Notably, the term within the brackets introduces a time derivative to J_{abs} cancels the integral in J_{pl} , leading to the final form:

$$\begin{aligned} \frac{\partial \tilde{E}_L}{\partial z}(\omega, z) = & i \left[k(\omega) - k_n(\omega) \right] \tilde{E}_L(\omega, z) \\ & + \frac{i}{2\omega c} \mathcal{F} \left[\frac{\partial J_{\text{abs}}}{\partial t}(t, z) + \omega_p^2(t, z) \tilde{E}_L(t, z) \right] \end{aligned} \quad (\text{C.11})$$

Supplementary plots water window IAP generation

This section presents measured and simulated CEP and delay scans of water window spectra. All spectra are shown at the CCD point, without accounting for the beamline's transfer function.

Simulated delay scans in this section were computed using the cycle-averaged ADK model, unlike those in Ch. 6, which used the Tong-Lin model. The CEP scans presented here and in Ch. 6 were both computed using the Tong-Lin formula.

D. SUPPLEMENTARY PLOTS WATER WINDOW IAP GENERATION

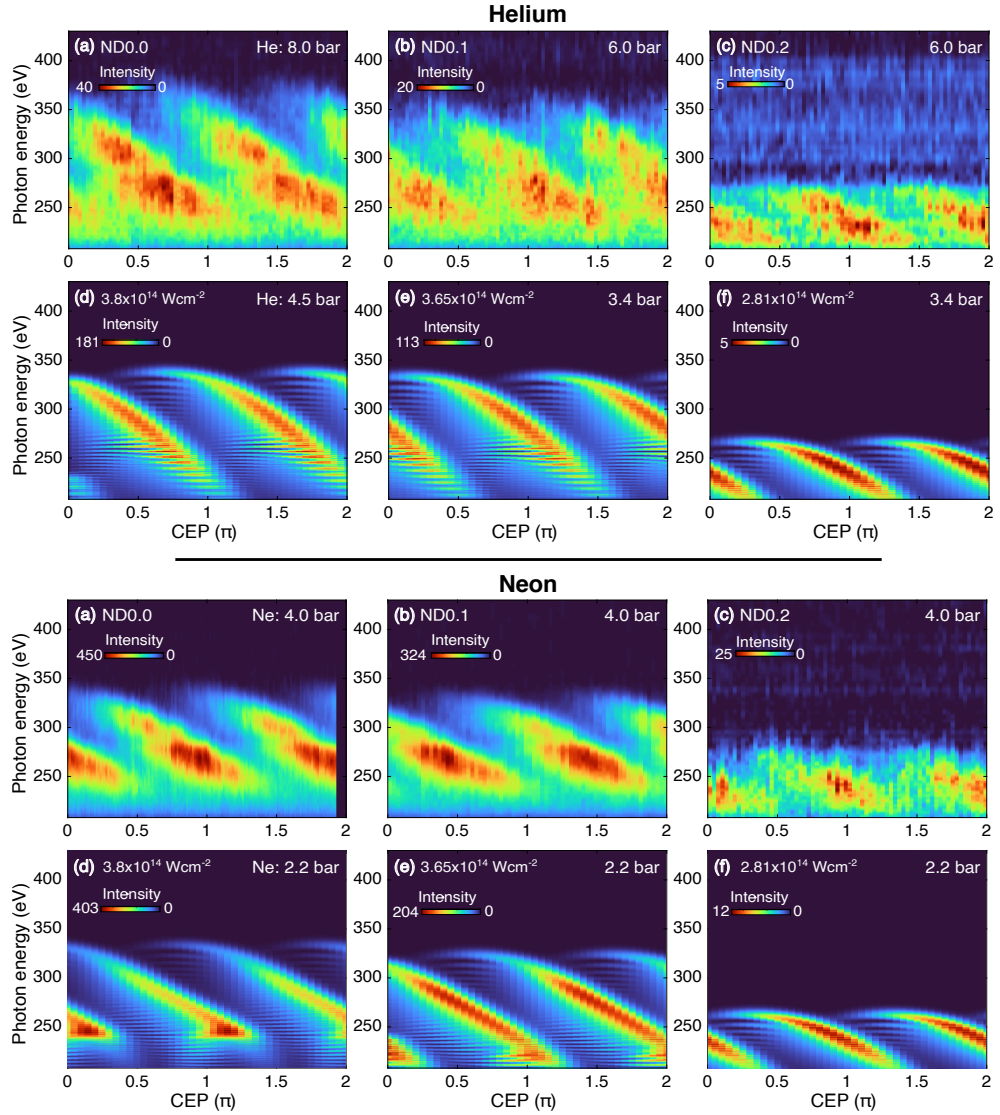


Figure D.1: Measured and simulated CEP scans in He and Ne driven by the IR pulse with varying ND filters. HHG spectra as a function of CEP for ND filters: (a) 0.0, (b) 0.1, and (c) 0.2. The phase-matching conditions (pressure and target position) are specified in Tables 6.2 and 6.4.

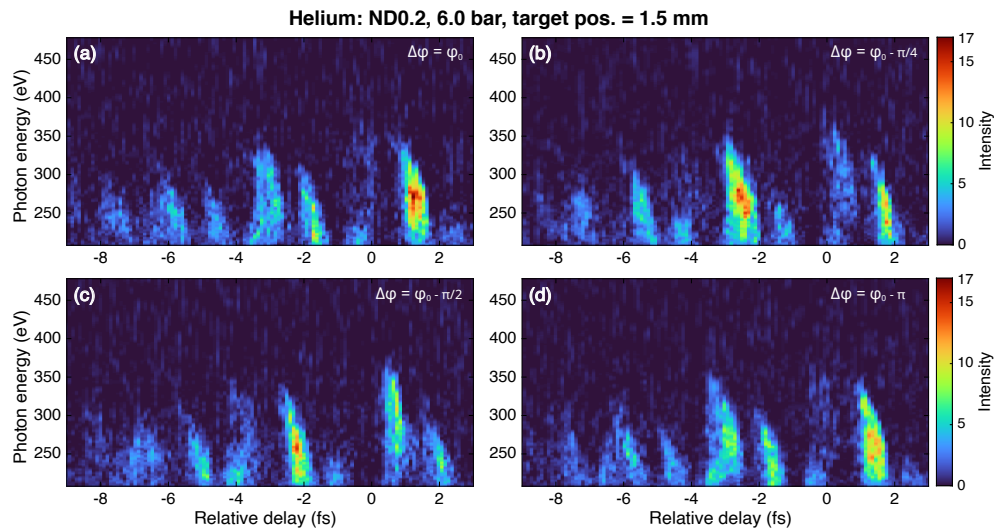


Figure D.2: Experimental relative delay scan in He with ND0.2 filter at various CEP shifts.

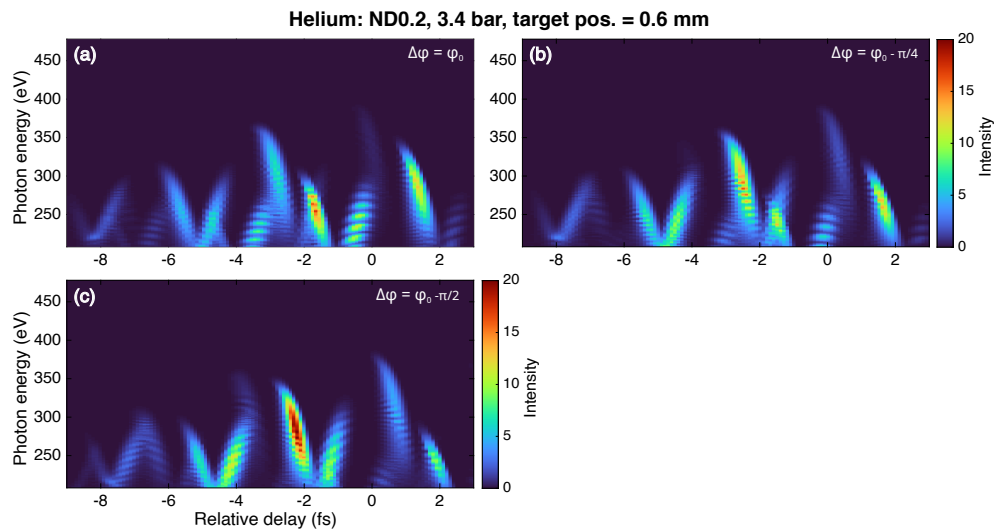


Figure D.3: Simulated relative delay scan in He with ND0.2 filter at various CEP shifts.

D. SUPPLEMENTARY PLOTS WATER WINDOW IAP GENERATION

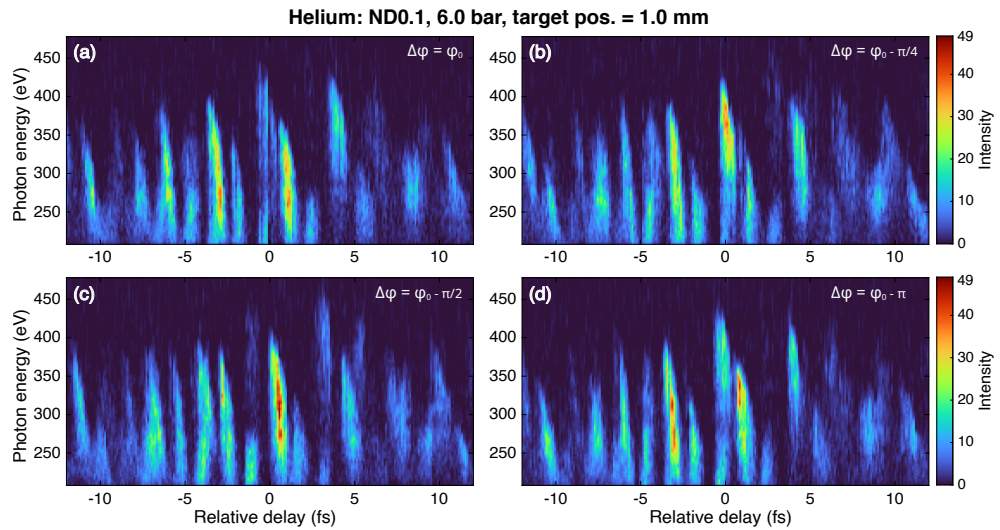


Figure D.4: Experimental relative delay scan in He with ND0.1 filter at various CEP shifts.

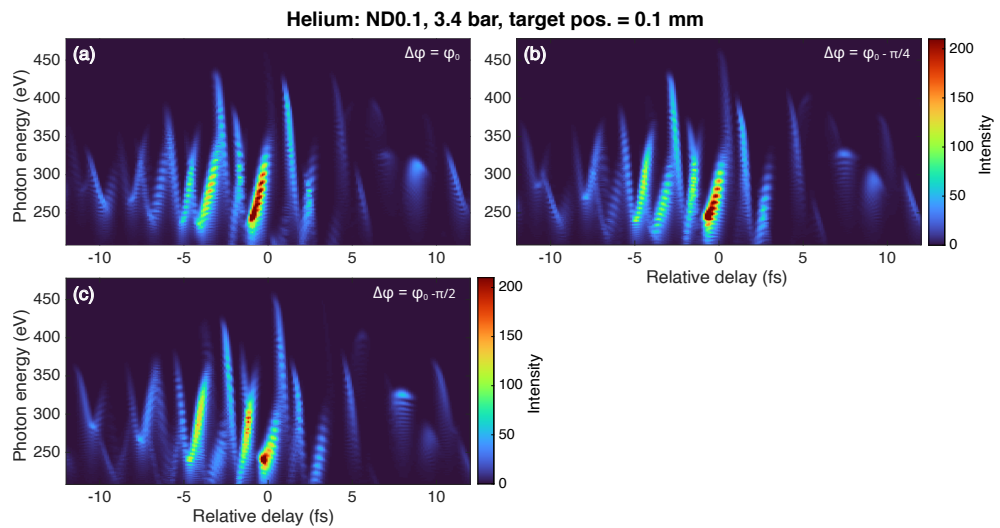


Figure D.5: Simulated relative delay scan in He with ND0.1 filter at various CEP shifts.

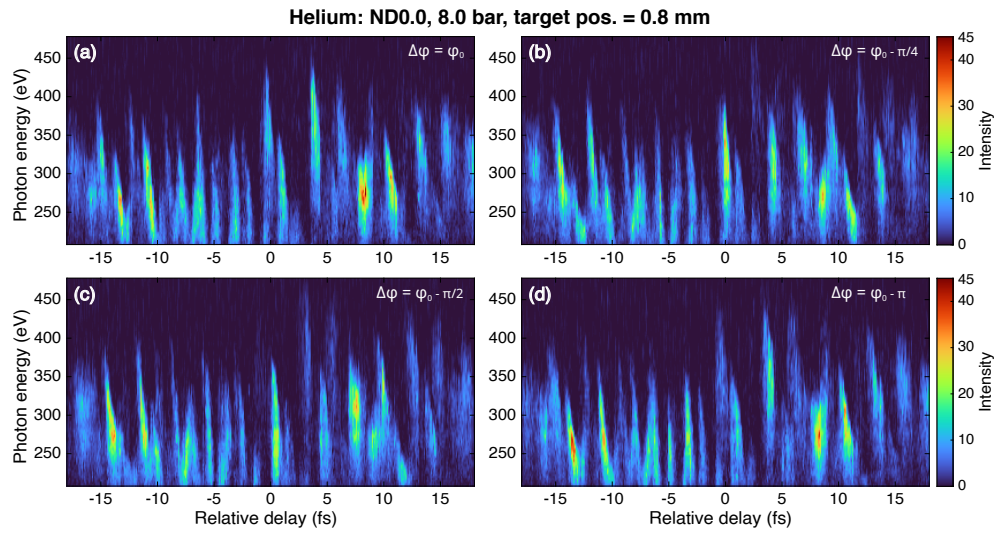


Figure D.6: Experimental relative delay scan in He with ND0.0 filter at various CEP shifts.

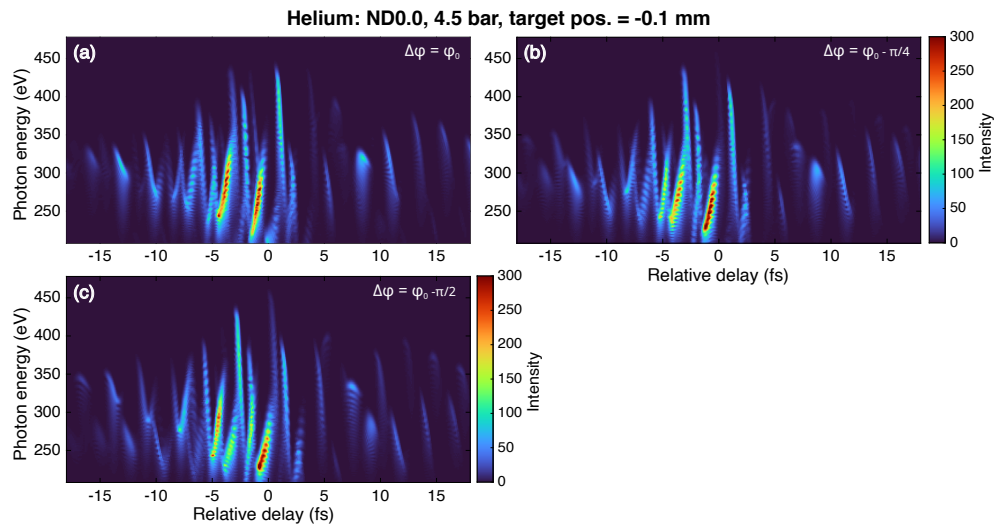


Figure D.7: Simulated relative delay scan in He with ND0.0 filter at various CEP shifts.

D. SUPPLEMENTARY PLOTS WATER WINDOW IAP GENERATION

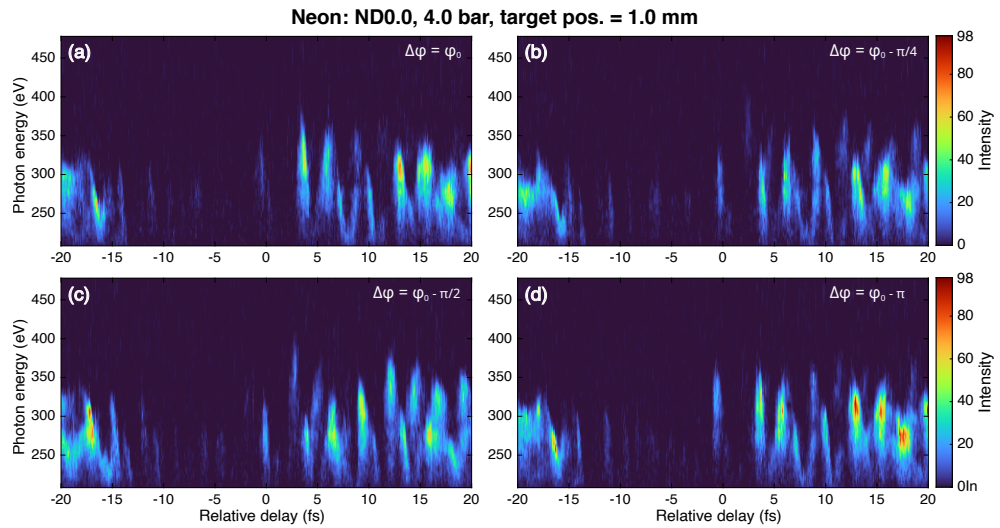


Figure D.8: Experimental relative delay scan in Ne with ND0.0 filter at various CEP shifts.

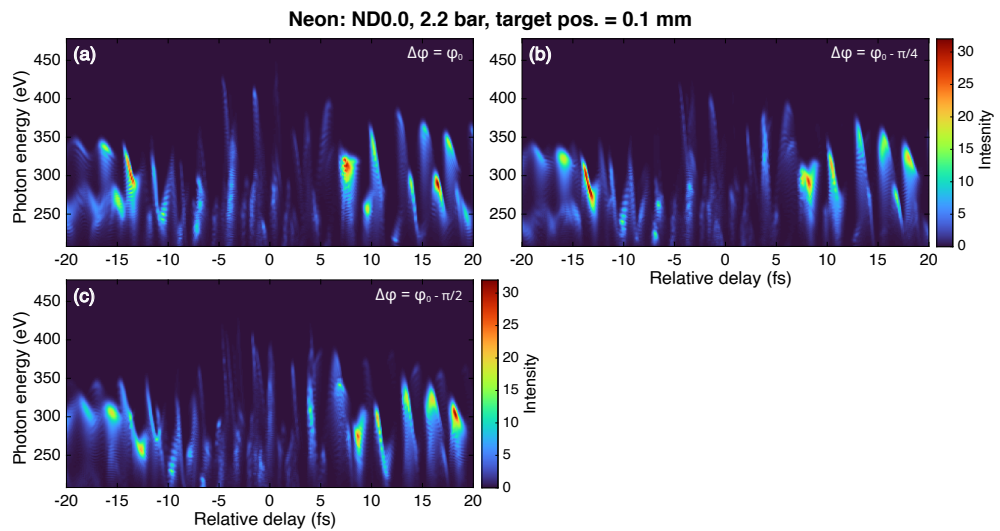


Figure D.9: Simulated relative delay scan in Ne with ND0.0 filter at various CEP shifts.

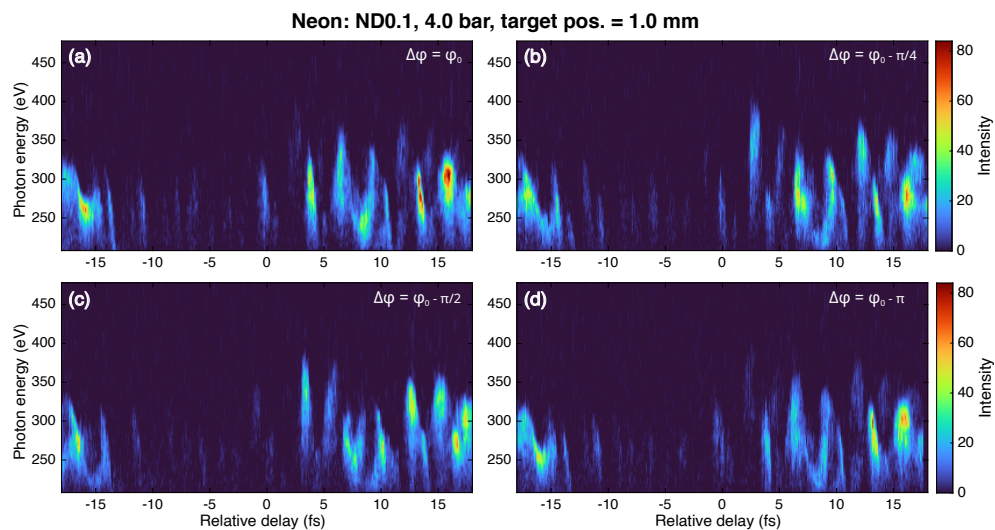


Figure D.10: Experimental relative delay scan in Ne with ND0.1 filter at various CEP shifts.

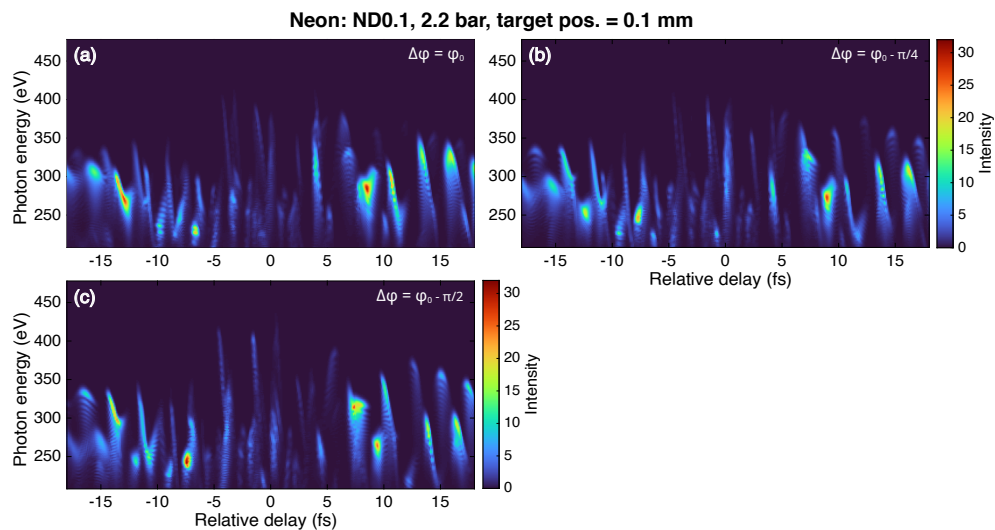


Figure D.11: Simulated relative delay scan in Ne with ND0.1 filter at various CEP shifts.

D. SUPPLEMENTARY PLOTS WATER WINDOW IAP GENERATION

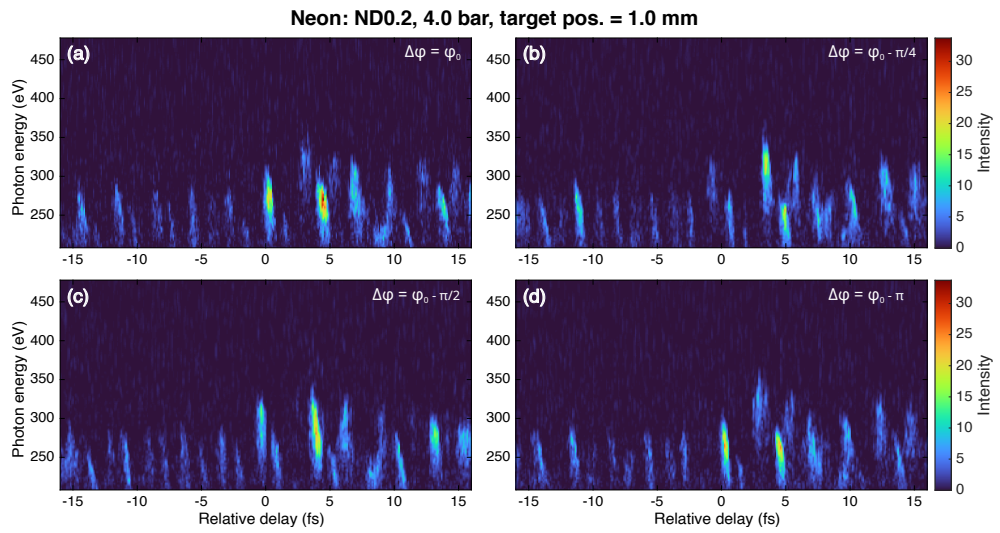


Figure D.12: Experimental relative delay scan in Ne with ND0.2 filter at various CEP shifts.

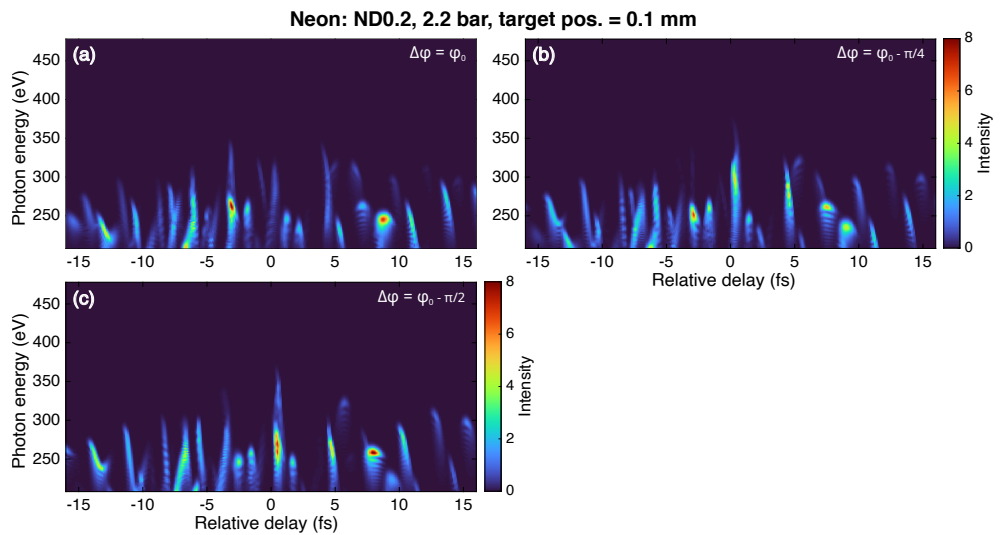


Figure D.13: Simulated relative delay scan in Ne with ND0.2 filter at various CEP shifts.

Bibliography

- [1] A. H. Zewail, "Femtochemistry: atomic-scale dynamics of the chemical bond," *The Journal of Physical Chemistry A*, vol. 104, pp. 5660–5694, Jun 2000.
- [2] F. Krausz and M. Ivanov, "Attosecond physics," *Rev. Mod. Phys.*, vol. 81, pp. 163–234, Feb 2009.
- [3] H. Abraham and J. Lemoine, "Disparition instantanée du phénomène de kerr," *CR Acad. Sci. Hebd Seances Acad. Sci. D*, vol. 129, pp. 206–208, 1899.
- [4] M. Maiuri, M. Garavelli, and G. Cerullo, "Ultrafast spectroscopy: State of the art and open challenges," *Journal of the American Chemical Society*, vol. 142, pp. 3–15, Jan 2020.
- [5] L. Young, K. Ueda, M. Gühr, P. H. Bucksbaum, M. Simon, S. Mukamel, N. Rohringer, K. C. Prince, C. Masciovecchio, M. Meyer, A. Rudenko, D. Rolles, C. Bostedt, M. Fuchs, D. A. Reis, R. Santra, H. Kapteyn, M. Murnane, H. Ibrahim, F. Légaré, M. Vrakking, M. Isinger, D. Kroon, M. Gisselbrecht, A. L'Huillier, H. J. Wörner, and S. R. Leone, "Roadmap of ultrafast x-ray atomic and molecular physics," *Journal of Physics B: Atomic, Molecular and Optical Physics*, vol. 51, p. 032003, Jan 2018.
- [6] U. Keller, "Recent developments in compact ultrafast lasers," *Nature*, vol. 424, pp. 831–838, Aug 2003.
- [7] F. Krausz, "The birth of attosecond physics and its coming of age," *Physica Scripta*, vol. 91, p. 063011, May 2016.
- [8] A. H. Zewail, *Femtochemistry: Ultrafast Dynamics of the Chemical Bond*. World Scientific Publishing Company, 1994.

- [9] D. Strickland and G. Mourou, "Compression of amplified chirped optical pulses," *Optics Communications*, vol. 56, no. 3, pp. 219–221, 1985.
- [10] M. Ferray, A. L'Huillier, X. F. Li, L. A. Lompre, G. Mainfray, and C. Manus, "Multiple-harmonic conversion of 1064 nm radiation in rare gases," *Journal of Physics B: Atomic, Molecular and Optical Physics*, vol. 21, p. L31, feb 1988.
- [11] M. Chini, K. Zhao, and Z. Chang, "The generation, characterization and applications of broadband isolated attosecond pulses," *Nature Photonics*, vol. 8, pp. 178–186, Mar 2014.
- [12] M. Hentschel, R. Kienberger, C. Spielmann, G. A. Reider, N. Milosevic, T. Brabec, P. Corkum, U. Heinzmann, M. Drescher, and F. Krausz, "Attosecond metrology," *Nature*, vol. 414, pp. 509–513, Nov 2001.
- [13] E. Goulielmakis, Z.-H. Loh, A. Wirth, R. Santra, N. Rohringer, V. S. Yakovlev, S. Zherebtsov, T. Pfeifer, A. M. Azzeer, M. F. Kling, S. R. Leone, and F. Krausz, "Real-time observation of valence electron motion," *Nature*, vol. 466, pp. 739–743, Aug 2010.
- [14] F. Calegari, D. Ayuso, A. Trabattori, L. Belshaw, S. D. Camillis, S. Anumula, F. Frassetto, L. Poletto, A. Palacios, P. Decleva, J. B. Greenwood, F. Martín, and M. Nisoli, "Ultrafast electron dynamics in phenylalanine initiated by attosecond pulses," *Science*, vol. 346, no. 6207, pp. 336–339, 2014.
- [15] M. Schultze, M. Fieß, N. Karpowicz, J. Gagnon, M. Korbman, M. Hofstetter, S. Neppl, A. L. Cavalieri, Y. Komninos, T. Mercouris, C. A. Nicolaides, R. Pazourek, S. Nagele, J. Feist, J. Burgdörfer, A. M. Azzeer, R. Ernstorfer, R. Kienberger, U. Kleineberg, E. Goulielmakis, F. Krausz, and V. S. Yakovlev, "Delay in photoemission," *Science*, vol. 328, no. 5986, pp. 1658–1662, 2010.
- [16] R. Geneaux, H. J. B. Marroux, A. Guggenmos, D. M. Neumark, and S. R. Leone, "Transient absorption spectroscopy using high harmonic generation: a review of ultrafast x-ray dynamics in molecules and solids," *Philosophical Transactions of the Royal Society A: Mathematical, Physical and Engineering Sciences*, vol. 377, no. 2145, p. 20170463, 2019.
- [17] R. Borrego-Varillas, M. Lucchini, and M. Nisoli, "Attosecond spectroscopy for the investigation of ultrafast dynamics in atomic, molecular and solid-state physics," *Reports on Progress in Physics*, vol. 85, p. 066401, may 2022.
- [18] NobelPrize.org, "Advanced information." <https://www.nobelprize.org/prizes/physics/2023/advanced-information/>, Aug. 2024.

- [19] A. Palacios and F. Martín, "The quantum chemistry of attosecond molecular science," *WIREs Computational Molecular Science*, vol. 10, no. 1, p. e1430, 2020.
- [20] R. Santra, "Concepts in x-ray physics," *Journal of Physics B: Atomic, Molecular and Optical Physics*, vol. 42, p. 023001, dec 2008.
- [21] M. Gühr, "Ultrafast Molecular Spectroscopy in the Gas Phase," in *Structural Dynamics with X-ray and Electron Scattering*, Royal Society of Chemistry, 12 2023.
- [22] Y. Pertot, C. Schmidt, M. Matthews, A. Chauvet, M. Huppert, V. Svoboda, A. von Conta, A. Tehlar, D. Baykusheva, J.-P. Wolf, and H. J. Wörner, "Time-resolved x-ray absorption spectroscopy with a water window high-harmonic source," *Science*, vol. 355, no. 6322, pp. 264–267, 2017.
- [23] A. R. Attar, A. Bhattacharjee, C. D. Pemmaraju, K. Schnorr, K. D. Closser, D. Prendergast, and S. R. Leone, "Femtosecond x-ray spectroscopy of an electrocyclic ring-opening reaction," *Science*, vol. 356, no. 6333, pp. 54–59, 2017.
- [24] C. Kleine, M. Ekimova, G. Goldsztejn, S. Raabe, C. Strüber, J. Ludwig, S. Yarlagadda, S. Eisebitt, M. J. J. Vrakking, T. Elsaesser, E. T. J. Nibbering, and A. Rouzée, "Soft x-ray absorption spectroscopy of aqueous solutions using a table-top femtosecond soft x-ray source," *The Journal of Physical Chemistry Letters*, vol. 10, no. 1, pp. 52–58, 2019.
- [25] A. D. Smith, T. Balciunas, Y.-P. Chang, C. Schmidt, K. Zinchenko, F. B. Nunes, E. Rossi, V. Svoboda, Z. Yin, J.-P. Wolf, and H. J. Wörner, "Femtosecond soft-x-ray absorption spectroscopy of liquids with a water-window high-harmonic source," *The Journal of Physical Chemistry Letters*, vol. 11, pp. 1981–1988, Mar 2020.
- [26] Z. Yin, Y.-P. Chang, T. Balčiūnas, Y. Shakya, A. Djorović, G. Gaulier, G. Fazio, R. Santra, L. Inhester, J.-P. Wolf, and H. J. Wörner, "Femtosecond proton transfer in urea solutions probed by x-ray spectroscopy," *Nature*, vol. 619, pp. 749–754, Jul 2023.
- [27] P. M. Kraus, M. Zürich, S. K. Cushing, D. M. Neumark, and S. R. Leone, "The ultrafast x-ray spectroscopic revolution in chemical dynamics," *Nature Reviews Chemistry*, vol. 2, pp. 82–94, Jun 2018.
- [28] X. Ren, J. Li, Y. Yin, K. Zhao, A. Chew, Y. Wang, S. Hu, Y. Cheng, E. Cunningham, Y. Wu, M. Chini, and Z. Chang, "Attosecond light sources in the water window," *Journal of Optics*, vol. 20, p. 023001, jan 2018.

- [29] N. Ishii, K. Kaneshima, K. Kitano, T. Kanai, S. Watanabe, and J. Itatani, "Carrier-envelope phase-dependent high harmonic generation in the water window using few-cycle infrared pulses," *Nature Communications*, vol. 5, p. 3331, Feb 2014.
- [30] S. L. Cousin, F. Silva, S. Teichmann, M. Hemmer, B. Buades, and J. Biegert, "High-flux table-top soft x-ray source driven by sub-2-cycle, cep stable, 1.85- μm 1-khz pulses for carbon k-edge spectroscopy," *Opt. Lett.*, vol. 39, pp. 5383–5386, Sep 2014.
- [31] T. Popmintchev, M.-C. Chen, A. Bahabad, M. Gerrity, P. Sidorenko, O. Cohen, I. P. Christov, M. M. Murnane, and H. C. Kapteyn, "Phase matching of high harmonic generation in the soft and hard x-ray regions of the spectrum," *Proceedings of the National Academy of Sciences*, vol. 106, no. 26, pp. 10516–10521, 2009.
- [32] S. M. Teichmann, F. Silva, S. L. Cousin, M. Hemmer, and J. Biegert, "0.5-keV soft x-ray attosecond continua," *Nature Communications*, vol. 7, p. 11493, May 2016.
- [33] N. Saito, H. Sannohe, N. Ishii, T. Kanai, N. Kosugi, Y. Wu, A. Chew, S. Han, Z. Chang, and J. Itatani, "Real-time observation of electronic, vibrational, and rotational dynamics in nitric oxide with attosecond soft x-ray pulses at 400 eV," *Optica*, vol. 6, pp. 1542–1546, Dec 2019.
- [34] K. S. Zinchenko, F. Ardana-Lamas, I. Seidu, S. P. Neville, J. van der Veen, V. U. Lanfaloni, M. S. Schuurman, and H. J. Wörner, "Sub-7-femtosecond conical-intersection dynamics probed at the carbon k-edge," *Science*, vol. 371, no. 6528, pp. 489–494, 2021.
- [35] E. Ridente, D. Hait, E. A. Haugen, A. D. Ross, D. M. Neumark, M. Head-Gordon, and S. R. Leone, "Femtosecond symmetry breaking and coherent relaxation of methane cations via x-ray spectroscopy," *Science*, vol. 380, no. 6646, pp. 713–717, 2023.
- [36] A. M. Summers, S. Severino, M. Reduzzi, T. P. H. Sidiropoulos, D. E. Rivas, N. D. Palo, H.-W. Sun, Y.-H. Chien, I. León, B. Buades, S. L. Cousin, S. M. Teichmann, T. Mey, K. Mann, B. Keitel, E. Plönjes, D. K. Efetov, H. Schwoerer, and J. Biegert, "Realizing attosecond core-level x-ray spectroscopy for the investigation of condensed matter systems," *Ultrafast Science*, vol. 3, p. 0004, 2023.
- [37] S. Severino, K. M. Ziems, M. Reduzzi, A. Summers, H.-W. Sun, Y.-H. Chien, S. Gräfe, and J. Biegert, "Attosecond core-level absorption spectroscopy reveals the electronic and nuclear dynamics of molecular ring opening," *Nature Photonics*, Apr 2024.

-
- [38] E. J. Takahashi, P. Lan, O. D. Mücke, Y. Nabekawa, and K. Midorikawa, "Attosecond nonlinear optics using gigawatt-scale isolated attosecond pulses," *Nature Communications*, vol. 4, p. 2691, Oct 2013.
- [39] J. Duris, S. Li, T. Driver, E. G. Champenois, J. P. MacArthur, A. A. Lutman, Z. Zhang, P. Rosenberger, J. W. Aldrich, R. Coffee, G. Coslovich, F.-J. Decker, J. M. Glowia, G. Hartmann, W. Helml, A. Kamalov, J. Knurr, J. Krzywinski, M.-F. Lin, J. P. Marangos, M. Nantel, A. Natan, J. T. O'Neal, N. Shivaram, P. Walter, A. L. Wang, J. J. Welch, T. J. A. Wolf, J. Z. Xu, M. F. Kling, P. H. Bucksbaum, A. Zholents, Z. Huang, J. P. Cryan, and A. Marinelli, "Tunable isolated attosecond x-ray pulses with gigawatt peak power from a free-electron laser," *Nature Photonics*, vol. 14, pp. 30–36, Jan 2020.
- [40] Y. Fu, K. Nishimura, R. Shao, A. Suda, K. Midorikawa, P. Lan, and E. J. Takahashi, "High efficiency ultrafast water-window harmonic generation for single-shot soft x-ray spectroscopy," *Communications Physics*, vol. 3, p. 92, May 2020.
- [41] J. Tate, T. Augustine, H. G. Muller, P. Salières, P. Agostini, and L. F. DiMauro, "Scaling of wave-packet dynamics in an intense midinfrared field," *Phys. Rev. Lett.*, vol. 98, p. 013901, Jan 2007.
- [42] K. Amini, J. Biegert, F. Calegari, A. Chacón, M. F. Ciappina, A. Dauphin, D. K. Efimov, C. F. de Morisson Faria, K. Giergiel, P. Gniewek, A. S. Landsman, M. Lesiuk, M. Mandrysz, A. S. Maxwell, R. Moszyński, L. Ortmann, J. A. Pérez-Hernández, A. Picón, E. Pisanty, J. Prauzner-Bechcicki, K. Sacha, N. Suárez, A. Zair, J. Zakrzewski, and M. Lewenstein, "Symphony on strong field approximation," *Reports on Progress in Physics*, vol. 82, p. 116001, oct 2019.
- [43] M. Kretschmar, E. Svirplys, M. Volkov, T. Witting, T. Nagy, M. J. J. Vrakking, and B. Schütte, "Compact realization of all-attosecond pump-probe spectroscopy," *Science Advances*, vol. 10, no. 8, p. eadk9605, 2024.
- [44] S. Li, L. Lu, S. Bhattacharyya, C. Pearce, K. Li, E. T. Nienhuis, G. Doumy, R. D. Schaller, S. Moeller, M.-F. Lin, G. Dakovski, D. J. Hoffman, D. Garratt, K. A. Larsen, J. D. Koralek, C. Y. Hampton, D. Cesar, J. Duris, Z. Zhang, N. Sudar, J. P. Cryan, A. Marinelli, X. Li, L. Inhester, R. Santra, and L. Young, "Attosecond-pump attosecond-probe x-ray spectroscopy of liquid water," *Science*, vol. 383, no. 6687, pp. 1118–1122, 2024.
- [45] Z. Guo, T. Driver, S. Beauvarlet, D. Cesar, J. Duris, P. L. Franz, O. Alexander, D. Bohler, C. Bostedt, V. Averbukh, X. Cheng, L. F.

- DiMauro, G. Doumy, R. Forbes, O. Gessner, J. M. Glowina, E. Isele, A. Kamalov, K. A. Larsen, S. Li, X. Li, M.-F. Lin, G. A. McCracken, R. Obaid, J. T. O'Neal, R. R. Robles, D. Rolles, M. Ruberti, A. Rudenko, D. S. Slaughter, N. S. Sudar, E. Thierstein, D. Tuthill, K. Ueda, E. Wang, A. L. Wang, J. Wang, T. Weber, T. J. A. Wolf, L. Young, Z. Zhang, P. H. Bucksbaum, J. P. Marangos, M. F. Kling, Z. Huang, P. Walter, L. Inhester, N. Berrah, J. P. Cryan, and A. Marinelli, "Experimental demonstration of attosecond pump-probe spectroscopy with an x-ray free-electron laser," *Nature Photonics*, vol. 18, pp. 691–697, Jul 2024.
- [46] T. Popmintchev, M.-C. Chen, D. Popmintchev, P. Arpin, S. Brown, S. Ališauskas, G. Andriukaitis, T. Balčiunas, O. D. Mücke, A. Pugzlys, A. Baltuška, B. Shim, S. E. Schrauth, A. Gaeta, C. Hernández-García, L. Plaja, A. Becker, A. Jaron-Becker, M. M. Murnane, and H. C. Kapteyn, "Bright coherent ultrahigh harmonics in the keV x-ray regime from mid-infrared femtosecond lasers," *Science*, vol. 336, no. 6086, pp. 1287–1291, 2012.
- [47] L. E. Chipperfield, J. S. Robinson, J. W. G. Tisch, and J. P. Marangos, "Ideal waveform to generate the maximum possible electron collision energy for any given oscillation period," *Phys. Rev. Lett.*, vol. 102, p. 063003, Feb 2009.
- [48] C. Jin, G. Wang, H. Wei, A.-T. Le, and C. D. Lin, "Waveforms for optimal sub-keV high-order harmonics with synthesized two- or three-colour laser fields," *Nature Communications*, vol. 5, p. 4003, May 2014.
- [49] I. P. Christov, M. M. Murnane, and H. C. Kapteyn, "High-harmonic generation of attosecond pulses in the "single-cycle" regime," *Phys. Rev. Lett.*, vol. 78, pp. 1251–1254, Feb 1997.
- [50] E. Goulielmakis, M. Schultze, M. Hofstetter, V. S. Yakovlev, J. Gagnon, M. Uiberacker, A. L. Aquila, E. M. Gullikson, D. T. Attwood, R. Kienberger, F. Krausz, and U. Kleineberg, "Single-cycle nonlinear optics," *Science*, vol. 320, no. 5883, pp. 1614–1617, 2008.
- [51] M. F. Galán, J. Serrano, E. C. Jarque, R. Borrego-Varillas, M. Lucchini, M. Reduzzi, M. Nisoli, C. Brahms, J. C. Travers, C. Hernández-García, and J. San Roman, "Robust isolated attosecond pulse generation with self-compressed subcycle drivers from hollow capillary fibers," *ACS Photonics*, vol. 11, pp. 1673–1683, Apr 2024.
- [52] Z. Chang, *Fundamentals of Attosecond Optics*. CRC Press, 2016.
- [53] A. M. Weiner, *Ultrafast Optics*. WILEY, 2009.

-
- [54] U. Keller, *Ultrafast Lasers: A Comprehensive Introduction to Fundamental Principles with Practical Applications*. Graduate Texts in Physics, Springer International Publishing, 2022.
- [55] F. Träger, *Springer Handbook of Lasers and Optics*. Springer Handbooks, Springer Berlin Heidelberg, 2012.
- [56] G. G. Paulus, F. Lindner, H. Walther, A. Baltuška, E. Goulielmakis, M. Lezius, and F. Krausz, "Measurement of the phase of few-cycle laser pulses," *Phys. Rev. Lett.*, vol. 91, p. 253004, Dec 2003.
- [57] A. Baltuška, T. Udem, M. Uiberacker, M. Hentschel, E. Goulielmakis, C. Gohle, R. Holzwarth, V. S. Yakovlev, A. Scrinzi, T. W. Hänsch, and F. Krausz, "Attosecond control of electronic processes by intense light fields," *Nature*, vol. 421, pp. 611 EP –, 02 2003.
- [58] S. Akturk, X. Gu, P. Gabolde, and R. Trebino, "The general theory of first-order spatio-temporal distortions of gaussian pulses and beams," *Opt. Express*, vol. 13, pp. 8642–8661, Oct 2005.
- [59] M. Rhodes, Z. Guang, J. Pease, and R. Trebino, "Visualizing spatiotemporal pulse propagation: first-order spatiotemporal couplings in laser pulses," *Appl. Opt.*, vol. 56, pp. 3024–3034, Apr 2017.
- [60] N. Bloembergen, "Nonlinear optics and spectroscopy," *Rev. Mod. Phys.*, vol. 54, pp. 685–695, Jul 1982.
- [61] R. Boyd, *Nonlinear Optics*. Academic Press, 2007.
- [62] W. Demtröder, *Atoms, Molecules and Photons: An Introduction to Atomic-, Molecular- and Quantum Physics*. Graduate Texts in Physics, Springer Berlin Heidelberg, 2010.
- [63] F. Shimizu, "Frequency broadening in liquids by a short light pulse," *Phys. Rev. Lett.*, vol. 19, pp. 1097–1100, Nov 1967.
- [64] R. A. Fisher, P. L. Kelley, and T. K. Gustafson, "SUBPICOSECOND PULSE GENERATION USING THE OPTICAL KERR EFFECT," *Applied Physics Letters*, vol. 14, pp. 140–143, 02 1969.
- [65] R. Alfano, *The Supercontinuum Laser Source: The Ultimate White Light*. Springer New York, 2016.
- [66] A. Couairon and A. Mysyrowicz, "Femtosecond filamentation in transparent media," *Physics Reports*, vol. 441, no. 2, pp. 47–189, 2007.
- [67] A. Braun, G. Korn, X. Liu, D. Du, J. Squier, and G. Mourou, "Self-channeling of high-peak-power femtosecond laser pulses in air," *Opt. Lett.*, vol. 20, pp. 73–75, Jan 1995.

- [68] E. T. J. Nibbering, P. F. Curley, G. Grillon, B. S. Prade, M. A. Franco, F. Salin, and A. Mysyrowicz, "Conical emission from self-guided femtosecond pulses in air," *Opt. Lett.*, vol. 21, pp. 62–64, Jan 1996.
- [69] T. Brabec and F. Krausz, "Intense few-cycle laser fields: Frontiers of nonlinear optics," *Rev. Mod. Phys.*, vol. 72, pp. 545–591, Apr 2000.
- [70] C. Manzoni, O. D. Mücke, G. Cirimi, S. Fang, J. Moses, S.-W. Huang, K.-H. Hong, G. Cerullo, and F. X. Kärtner, "Coherent pulse synthesis: towards sub-cycle optical waveforms," *Laser & Photonics Reviews*, vol. 9, no. 2, pp. 129–171, 2015.
- [71] E. Treacy, "Optical pulse compression with diffraction gratings," *IEEE Journal of Quantum Electronics*, vol. 5, no. 9, pp. 454–458, 1969.
- [72] O. E. Martinez, J. P. Gordon, and R. L. Fork, "Negative group-velocity dispersion using refraction," *J. Opt. Soc. Am. A*, vol. 1, pp. 1003–1006, Oct 1984.
- [73] R. L. Fork, C. H. B. Cruz, P. C. Becker, and C. V. Shank, "Compression of optical pulses to six femtoseconds by using cubic phase compensation," *Opt. Lett.*, vol. 12, pp. 483–485, Jul 1987.
- [74] F. Gires, "Interferometer utilisable pour la compression d'impulsions lumineuses modulees en frequence," *Compt. Rend. Acad. Sci.(Paris)*, vol. 258, p. 6112, 1964.
- [75] R. Szipöcs, K. Ferencz, C. Spielmann, and F. Krausz, "Chirped multi-layer coatings for broadband dispersion control in femtosecond lasers," *Opt. Lett.*, vol. 19, pp. 201–203, Feb 1994.
- [76] F. X. Kärtner, N. Matuschek, T. Schibli, U. Keller, H. A. Haus, C. Heine, R. Morf, V. Scheuer, M. Tilsch, and T. Tschudi, "Design and fabrication of double-chirped mirrors," *Opt. Lett.*, vol. 22, pp. 831–833, Jun 1997.
- [77] V. Pervak, "Recent development and new ideas in the field of dispersive multilayer optics," *Appl. Opt.*, vol. 50, pp. C55–C61, Mar 2011.
- [78] S.-H. Chia, G. Cirimi, S. Fang, G. M. Rossi, O. D. Mücke, and F. X. Kärtner, "Two-octave-spanning dispersion-controlled precision optics for sub-optical-cycle waveform synthesizers," *Optica*, vol. 1, pp. 315–322, Nov 2014.
- [79] F. Verluise, V. Laude, Z. Cheng, C. Spielmann, and P. Tournois, "Amplitude and phase control of ultrashort pulses by use of an acousto-optic programmable dispersive filter: pulse compression and shaping," *Opt. Lett.*, vol. 25, pp. 575–577, Apr 2000.

-
- [80] A. M. Weiner, "Femtosecond pulse shaping using spatial light modulators," *Review of Scientific Instruments*, vol. 71, pp. 1929–1960, 05 2000.
- [81] T. Kobayashi, H. Yao, K. Amano, Y. Fukushima, A. Morimoto, and T. Sueta, "Optical pulse compression using high-frequency electrooptic phase modulation," *IEEE Journal of Quantum Electronics*, vol. 24, no. 2, pp. 382–387, 1988.
- [82] M. Nisoli, S. D. Silvestri, O. Svelto, R. Szipöcs, K. Ferencz, C. Spielmann, S. Sartania, and F. Krausz, "Compression of high-energy laser pulses below 5 fs," *Opt. Lett.*, vol. 22, pp. 522–524, Apr 1997.
- [83] S. Sartania, Z. Cheng, M. Lenzner, G. Tempea, C. Spielmann, F. Krausz, and K. Ferencz, "Generation of 0.1-tw 5-fs optical pulses at a 1-khz repetition rate," *Opt. Lett.*, vol. 22, pp. 1562–1564, Oct 1997.
- [84] R. Paschotta, "Sign conventions in wave optics." https://www.rp-photonics.com/sign_conventions_in_wave_optics.html. RP Photonics Encyclopedia, Accessed: 2024-09-08.
- [85] M. A. Porras, "Ultrashort pulsed gaussian light beams," *Phys. Rev. E*, vol. 58, pp. 1086–1093, Jul 1998.
- [86] D. Hoff, M. Krüger, L. Maisenbacher, A. M. Sayler, G. G. Paulus, and P. Hommelhoff, "Tracing the phase of focused broadband laser pulses," *Nature Physics*, vol. 13, pp. 947–951, Oct 2017.
- [87] M. A. Porras, Z. L. Horváth, and B. Major, "Three-dimensional carrier-envelope-phase map of focused few-cycle pulsed gaussian beams," *Phys. Rev. A*, vol. 98, p. 063819, Dec 2018.
- [88] M. Mamaikin, E. Ridente, F. Krausz, and N. Karpowicz, "Spatiotemporal electric-field characterization of synthesized light transients," *Optica*, vol. 11, pp. 88–93, Jan 2024.
- [89] P. Moulton, "Ti-doped sapphire: tunable solid-state laser," *Optics News*, vol. 8, pp. 9–9, Nov 1982.
- [90] P. F. Moulton, "Spectroscopic and laser characteristics of ti:al₂o₃," *J. Opt. Soc. Am. B*, vol. 3, pp. 125–133, Jan 1986.
- [91] H. Fattahi, H. G. Barros, M. Gorjan, T. Nubbemeyer, B. Alsaif, C. Y. Teisset, M. Schultze, S. Prinz, M. Haefner, M. Ueffing, A. Alismail, L. Vámos, A. Schwarz, O. Pronin, J. Brons, X. T. Geng, G. Arisholm, M. Ciappina, V. S. Yakovlev, D.-E. Kim, A. M. Azzeer, N. Karpowicz, D. Sutter, Z. Major, T. Metzger, and F. Krausz, "Third-generation femtosecond technology," *Optica*, vol. 1, pp. 45–63, Jul 2014.

- [92] D. E. Spence, P. N. Kean, and W. Sibbett, "60-fsec pulse generation from a self-mode-locked ti:sapphire laser," *Opt. Lett.*, vol. 16, pp. 42–44, Jan 1991.
- [93] P. Maine, D. Strickland, P. Bado, M. Pessot, and G. Mourou, "Generation of ultrahigh peak power pulses by chirped pulse amplification," *IEEE Journal of Quantum Electronics*, vol. 24, no. 2, pp. 398–403, 1988.
- [94] J. V. Rudd, G. Korn, S. Kane, J. Squier, G. Mourou, and P. Bado, "Chirped-pulse amplification of 55-fs pulses at a 1-khz repetition rate in a ti:al₂o₃ regenerative amplifier," *Opt. Lett.*, vol. 18, pp. 2044–2046, Dec 1993.
- [95] Y. Chu, Z. Gan, X. Liang, L. Yu, X. Lu, C. Wang, X. Wang, L. Xu, H. Lu, D. Yin, Y. Leng, R. Li, and Z. Xu, "High-energy large-aperture ti:sapphire amplifier for 5 pw laser pulses," *Opt. Lett.*, vol. 40, pp. 5011–5014, Nov 2015.
- [96] P. S. Tamas Nagy and L. Veisz, "High-energy few-cycle pulses: post-compression techniques," *Advances in Physics: X*, vol. 6, no. 1, p. 1845795, 2021.
- [97] R. Baumgartner and R. Byer, "Optical parametric amplification," *IEEE Journal of Quantum Electronics*, vol. 15, no. 6, pp. 432–444, 1979.
- [98] G. Cerullo and S. De Silvestri, "Ultrafast optical parametric amplifiers," *Review of Scientific Instruments*, vol. 74, pp. 1–18, 01 2003.
- [99] C. Manzoni and G. Cerullo, "Design criteria for ultrafast optical parametric amplifiers," *Journal of Optics*, vol. 18, p. 103501, aug 2016.
- [100] A. Dubietis, G. Jonušauskas, and A. Piskarskas, "Powerful femtosecond pulse generation by chirped and stretched pulse parametric amplification in bbo crystal," *Optics Communications*, vol. 88, no. 4, pp. 437–440, 1992.
- [101] A. Dubietis, R. Butkus, and A. Piskarskas, "Trends in chirped pulse optical parametric amplification," *IEEE Journal of Selected Topics in Quantum Electronics*, vol. 12, no. 2, pp. 163–172, 2006.
- [102] A. Dubietis and A. Matijošius, "Table-top optical parametric chirped pulse amplifiers: past and present," *Opto-Electron Adv*, vol. 6, no. 3, pp. 220046–1–220046–27, 2023.
- [103] S. B. Mirov, I. S. Moskalev, S. Vasilyev, V. Smolski, V. V. Fedorov, D. Martyshkin, J. Peppers, M. Mirov, A. Dergachev, and V. Gapontsev, "Frontiers of mid-ir lasers based on transition metal doped chalcogenides," *IEEE Journal of Selected Topics in Quantum Electronics*, vol. 24, no. 5, pp. 1–29, 2018.

-
- [104] Z. Chang, L. Fang, V. Fedorov, C. Geiger, S. Ghimire, C. Heide, N. Ishii, J. Itatani, C. Joshi, Y. Kobayashi, P. Kumar, A. Marra, S. Mirov, I. Petrushina, M. Polyanskiy, D. A. Reis, S. Tochitsky, S. Vasilyev, L. Wang, Y. Wu, and F. Zhou, "Intense infrared lasers for strong-field science," *Adv. Opt. Photon.*, vol. 14, pp. 652–782, Dec 2022.
- [105] J. Rothhardt, S. Hädrich, J. Delagnes, E. Cormier, and J. Limpert, "High average power near-infrared few-cycle lasers," *Laser & Photonics Reviews*, vol. 11, no. 4, p. 1700043, 2017.
- [106] J. Schulte, T. Sartorius, J. Weitenberg, A. Vernaleken, and P. Russbueldt, "Nonlinear pulse compression in a multi-pass cell," *Opt. Lett.*, vol. 41, pp. 4511–4514, Oct 2016.
- [107] A.-L. Viotti, M. Seidel, E. Escoto, S. Rajhans, W. P. Leemans, I. Hartl, and C. M. Heyl, "Multi-pass cells for post-compression of ultrashort laser pulses," *Optica*, vol. 9, pp. 197–216, Feb 2022.
- [108] T. Nagy, M. Forster, and P. Simon, "Flexible hollow fiber for pulse compressors," *Appl. Opt.*, vol. 47, pp. 3264–3268, Jun 2008.
- [109] G. M. Rossi, *Parametric Waveform Synthesis*. Dissertation, Fachbereich Physik der Universität Hamburg, 2019.
- [110] G. M. Rossi, R. E. Mainz, Y. Yang, F. Scheiba, M. A. Silva-Toledo, S.-H. Chia, P. D. Keathley, S. Fang, O. D. Mücke, C. Manzoni, G. Cerullo, G. Cirimi, and F. X. Kärtner, "Sub-cycle millijoule-level parametric waveform synthesizer for attosecond science," *Nature Photonics*, vol. 14, pp. 629–635, Oct 2020.
- [111] D. Brida, C. Manzoni, G. Cirimi, M. Marangoni, S. Bonora, P. Villoresi, S. D. Silvestri, and G. Cerullo, "Few-optical-cycle pulses tunable from the visible to the mid-infrared by optical parametric amplifiers," *Journal of Optics*, vol. 12, p. 013001, nov 2009.
- [112] A. G. Ciriolo, M. Negro, M. Devetta, E. Cinquanta, D. Faccialà, A. Pusala, S. De Silvestri, S. Stagira, and C. Vozzi, "Optical parametric amplification techniques for the generation of high-energy few-optical-cycles ir pulses for strong field applications," *Applied Sciences*, vol. 7, no. 3, 2017.
- [113] F. J. Furch, T. Witting, M. Osolodkov, F. Schell, C. P. Schulz, and M. J. J. Vrakking, "High power, high repetition rate laser-based sources for attosecond science," *Journal of Physics: Photonics*, vol. 4, p. 032001, jun 2022.

- [114] M. Nisoli, "Hollow fiber compression technique: A historical perspective," *IEEE Journal of Selected Topics in Quantum Electronics*, vol. 30, no. 6: Advances and Applications of Hollow-Core Fibers, pp. 1–14, 2024.
- [115] M. T. Hassan, A. Wirth, I. Grguraš, A. Moulet, T. T. Luu, J. Gagnon, V. Pervak, and E. Goulielmakis, "Invited Article: Attosecond photonics: Synthesis and control of light transients," *Review of Scientific Instruments*, vol. 83, p. 111301, 11 2012.
- [116] G. Cirmi, R. E. Mainz, M. A. Silva-Toledo, F. Scheiba, H. Çankaya, M. Kubullek, G. M. Rossi, and F. X. Kärtner, "Optical waveform synthesis and its applications," *Laser & Photonics Reviews*, vol. 17, no. 4, p. 2200588, 2023.
- [117] M. T. Hassan, T. T. Luu, A. Moulet, O. Raskazovskaya, P. Zhokhov, M. Garg, N. Karpowicz, A. M. Zheltikov, V. Pervak, F. Krausz, and E. Goulielmakis, "Optical attosecond pulses and tracking the nonlinear response of bound electrons," *Nature*, vol. 530, pp. 66–70, Feb 2016.
- [118] A. Baltuska, M. Uiberacker, E. Goulielmakis, R. Kienberger, V. Yakovlev, T. Udem, T. Hansch, and F. Krausz, "Phase-controlled amplification of few-cycle laser pulses," *IEEE Journal of Selected Topics in Quantum Electronics*, vol. 9, no. 4, pp. 972–989, 2003.
- [119] H. Mashiko, C. M. Nakamura, C. Li, E. Moon, H. Wang, J. Tackett, and Z. Chang, "Carrier-envelope phase stabilized 5.6fs, 1.2mJ pulses," *Applied Physics Letters*, vol. 90, p. 161114, 04 2007.
- [120] S. T. Cundiff and J. Ye, "Colloquium: Femtosecond optical frequency combs," *Rev. Mod. Phys.*, vol. 75, pp. 325–342, Mar 2003.
- [121] J. Reichert, R. Holzwarth, T. Udem, and T. Hänsch, "Measuring the frequency of light with mode-locked lasers," *Optics Communications*, vol. 172, no. 1, pp. 59–68, 1999.
- [122] H. R. Telle, G. Steinmeyer, A. E. Dunlop, J. Stenger, D. H. Sutter, and U. Keller, "Carrier-envelope offset phase control: A novel concept for absolute optical frequency measurement and ultrashort pulse generation," *Applied Physics B*, vol. 69, pp. 327–332, Oct 1999.
- [123] J. C. Knight, T. A. Birks, P. S. J. Russell, and D. M. Atkin, "All-silica single-mode optical fiber with photonic crystal cladding," *Opt. Lett.*, vol. 21, pp. 1547–1549, Oct 1996.
- [124] A. Baltuška, T. Fuji, and T. Kobayashi, "Controlling the carrier-envelope phase of ultrashort light pulses with optical parametric amplifiers," *Phys. Rev. Lett.*, vol. 88, p. 133901, Mar 2002.

-
- [125] G. Cerullo, A. Baltuška, O. Mücke, and C. Vozzi, "Few-optical-cycle light pulses with passive carrier-envelope phase stabilization," *Laser & Photonics Reviews*, vol. 5, no. 3, pp. 323–351, 2011.
- [126] R. E. Mainz, G. M. Rossi, F. Scheiba, M. A. Silva-Toledo, Y. Yang, G. Cirimi, and F. X. Kärtner, "Parametric waveform synthesis: a scalable approach to generate sub-cycle optical transients," *Opt. Express*, vol. 31, pp. 11363–11394, Mar 2023.
- [127] M. Kakehata, H. Takada, Y. Kobayashi, K. Torizuka, Y. Fujihira, T. Homma, and H. Takahashi, "Single-shot measurement of carrier-envelope phase changes by spectral interferometry," *Opt. Lett.*, vol. 26, pp. 1436–1438, Sep 2001.
- [128] M. Takeda, H. Ina, and S. Kobayashi, "Fourier-transform method of fringe-pattern analysis for computer-based topography and interferometry," *J. Opt. Soc. Am.*, vol. 72, pp. 156–160, Jan 1982.
- [129] L. Lepetit, G. Chériaux, and M. Joffre, "Linear techniques of phase measurement by femtosecond spectral interferometry for applications in spectroscopy," *J. Opt. Soc. Am. B*, vol. 12, pp. 2467–2474, Dec 1995.
- [130] R. E. Mainz, *Sub-Cycle Light Field Synthesizer for Attosecond Science*. Dissertation, Fachbereich Physik der Universität Hamburg, 2019.
- [131] A. Herbst, K. Scheffter, M. M. Bidhendi, M. Kieker, A. Srivastava, and H. Fattahi, "Recent advances in petahertz electric field sampling," *Journal of Physics B: Atomic, Molecular and Optical Physics*, vol. 55, p. 172001, aug 2022.
- [132] D. Kane and R. Trebino, "Characterization of arbitrary femtosecond pulses using frequency-resolved optical gating," *IEEE Journal of Quantum Electronics*, vol. 29, no. 2, pp. 571–579, 1993.
- [133] C. Iaconis and I. Walmsley, "Self-referencing spectral interferometry for measuring ultrashort optical pulses," *IEEE Journal of Quantum Electronics*, vol. 35, no. 4, pp. 501–509, 1999.
- [134] J. R. Birge, R. Ell, and F. X. Kärtner, "Two-dimensional spectral shearing interferometry for few-cycle pulse characterization," *Opt. Lett.*, vol. 31, pp. 2063–2065, Jul 2006.
- [135] M. Miranda, T. Fordell, C. Arnold, A. L'Huillier, and H. Crespo, "Simultaneous compression and characterization of ultrashort laser pulses using chirped mirrors and glass wedges," *Opt. Express*, vol. 20, pp. 688–697, Jan 2012.

- [136] M. Miranda, C. L. Arnold, T. Fordell, F. Silva, B. Alonso, R. Weigand, A. L'Huillier, and H. Crespo, "Characterization of broadband few-cycle laser pulses with the d-scan technique," *Opt. Express*, vol. 20, pp. 18732–18743, Aug 2012.
- [137] T. Hammond, A. Korobenko, A. Y. Naumov, D. M. Villeneuve, P. B. Corkum, and D. H. Ko, "Near-field imaging for single-shot waveform measurements," *Journal of Physics B: Atomic, Molecular and Optical Physics*, vol. 51, p. 065603, feb 2018.
- [138] A. Gliserin, S. H. Chew, S. Kim, and D. E. Kim, "Complete characterization of ultrafast optical fields by phase-preserving nonlinear auto-correlation," *Light: Science & Applications*, vol. 11, p. 277, Sep 2022.
- [139] J. Itatani, F. Quéré, G. L. Yudin, M. Y. Ivanov, F. Krausz, and P. B. Corkum, "Attosecond streak camera," *Phys. Rev. Lett.*, vol. 88, p. 173903, Apr 2002.
- [140] E. Goulielmakis, M. Uiberacker, R. Kienberger, A. Baltuska, V. Yakovlev, A. Scrinzi, T. Westerwalbesloh, U. Kleineberg, U. Heinzmann, M. Drescher, and F. Krausz, "Direct measurement of light waves," *Science*, vol. 305, no. 5688, pp. 1267–1269, 2004.
- [141] R. Kienberger, E. Goulielmakis, M. Uiberacker, A. Baltuska, V. Yakovlev, F. Bammer, A. Scrinzi, T. Westerwalbesloh, U. Kleineberg, U. Heinzmann, M. Drescher, and F. Krausz, "Atomic transient recorder," *Nature*, vol. 427, pp. 817–821, Feb 2004.
- [142] N. Saito, N. Ishii, T. Kanai, S. Watanabe, and J. Itatani, "Attosecond streaking measurement of extreme ultraviolet pulses using a long-wavelength electric field," *Scientific Reports*, vol. 6, p. 35594, Oct 2016.
- [143] S. L. Cousin, N. Di Palo, B. Buades, S. M. Teichmann, M. Reduzzi, M. Devetta, A. Kheifets, G. Sansone, and J. Biegert, "Attosecond streaking in the water window: A new regime of attosecond pulse characterization," *Phys. Rev. X*, vol. 7, p. 041030, Nov 2017.
- [144] A. S. Wyatt, T. Witting, A. Schiavi, D. Fabris, P. Matia-Hernando, I. A. Walmsley, J. P. Marangos, and J. W. G. Tisch, "Attosecond sampling of arbitrary optical waveforms," *Optica*, vol. 3, pp. 303–310, Mar 2016.
- [145] K. T. Kim, C. Zhang, A. D. Shiner, B. E. Schmidt, F. Légaré, D. M. Villeneuve, and P. B. Corkum, "Petahertz optical oscilloscope," *Nature Photonics*, vol. 7, pp. 958–962, Dec 2013.

-
- [146] M. R. Bionta, F. Ritzkowsky, M. Turchetti, Y. Yang, D. Cattozzo Mor, W. P. Putnam, F. X. Kärtner, K. K. Berggren, and P. D. Keathley, "On-chip sampling of optical fields with attosecond resolution," *Nature Photonics*, vol. 15, pp. 456–460, Jun 2021.
- [147] Y. Liu, J. E. Beetar, J. Nesper, S. Gholam-Mirzaei, and M. Chini, "Single-shot measurement of few-cycle optical waveforms on a chip," *Nature Photonics*, vol. 16, pp. 109–112, Feb 2022.
- [148] S. B. Park, K. Kim, W. Cho, S. I. Hwang, I. Ivanov, C. H. Nam, and K. T. Kim, "Direct sampling of a light wave in air," *Optica*, vol. 5, pp. 402–408, Apr 2018.
- [149] W. Cho, S. I. Hwang, C. H. Nam, M. R. Bionta, P. Lassonde, B. E. Schmidt, H. Ibrahim, F. Légaré, and K. T. Kim, "Temporal characterization of femtosecond laser pulses using tunneling ionization in the uv, visible, and mid-ir ranges," *Scientific Reports*, vol. 9, p. 16067, Nov 2019.
- [150] A. Korobenko, K. Johnston, M. Kubullek, L. Arissian, Z. Dube, T. Wang, M. Kübel, A. Y. Naumov, D. M. Villeneuve, M. F. Kling, P. B. Corkum, A. Staudte, and B. Bergues, "Femtosecond streaking in ambient air," *Optica*, vol. 7, pp. 1372–1376, Oct 2020.
- [151] S. Sederberg, D. Zimin, S. Keiber, F. Siegrist, M. S. Wismer, V. S. Yakovlev, I. Floss, C. Lemell, J. Burgdörfer, M. Schultze, F. Krausz, and N. Karpowicz, "Attosecond optoelectronic field measurement in solids," *Nature Communications*, vol. 11, p. 430, Jan 2020.
- [152] Y. Liu, S. Gholam-Mirzaei, J. E. Beetar, J. Nesper, A. Yousif, M. Nrisimhamurty, and M. Chini, "All-optical sampling of few-cycle infrared pulses using tunneling in a solid," *Photon. Res.*, vol. 9, pp. 929–936, Jun 2021.
- [153] D. Zimin, M. Weidman, J. Schötz, M. F. Kling, V. S. Yakovlev, F. Krausz, and N. Karpowicz, "Petahertz-scale nonlinear photoconductive sampling in air," *Optica*, vol. 8, pp. 586–590, May 2021.
- [154] D. Hui, H. Alqattan, S. Yamada, V. Pervak, K. Yabana, and M. T. Hassan, "Attosecond electron motion control in dielectric," *Nature Photonics*, vol. 16, pp. 33–37, Jan 2022.
- [155] N. Altwaijry, M. Qasim, M. Mamaikin, J. Schötz, K. Golyari, M. Heynck, E. Ridente, V. S. Yakovlev, N. Karpowicz, and M. F. Kling, "Broadband photoconductive sampling in gallium phosphide," *Advanced Optical Materials*, vol. 11, no. 9, p. 2202994, 2023.

- [156] S. Keiber, S. Sederberg, A. Schwarz, M. Trubetskov, V. Pervak, F. Krausz, and N. Karpowicz, "Electro-optic sampling of near-infrared waveforms," *Nature Photonics*, vol. 10, pp. 159–162, Mar 2016.
- [157] E. Ridente, M. Mamaikin, N. Altwaijry, D. Zimin, M. F. Kling, V. Pervak, M. Weidman, F. Krausz, and N. Karpowicz, "Electro-optic characterization of synthesized infrared-visible light fields," *Nature Communications*, vol. 13, p. 1111, Mar 2022.
- [158] D. A. Zimin, V. S. Yakovlev, and N. Karpowicz, "Ultra-broadband all-optical sampling of optical waveforms," *Science Advances*, vol. 8, no. 51, p. eade1029, 2022.
- [159] M. Kubullek, M. A. Silva-Toledo, R. E. Mainz, F. Scheiba, R. de Q. Garcia, F. Ritzkowksy, G. M. Rossi, and F. X. Kärtner, "Complete electric field characterization of multi-color light fields." In review (2024), 2024.
- [160] R. Borrego-Varillas, A. Oriana, F. Branchi, S. D. Silvestri, G. Cerullo, and C. Manzoni, "Optimized ancillae generation for ultra-broadband two-dimensional spectral-shearing interferometry," *J. Opt. Soc. Am. B*, vol. 32, pp. 1851–1855, Sep 2015.
- [161] A. McPherson, G. Gibson, H. Jara, U. Johann, T. S. Luk, I. A. McIntyre, K. Boyer, and C. K. Rhodes, "Studies of multiphoton production of vacuum-ultraviolet radiation in the rare gases," *J. Opt. Soc. Am. B*, vol. 4, pp. 595–601, Apr 1987.
- [162] T. Gaumnitz, A. Jain, Y. Pertot, M. Huppert, I. Jordan, F. Ardana-Lamas, and H. J. Wörner, "Streaking of 43-attosecond soft-x-ray pulses generated by a passively cep-stable mid-infrared driver," *Opt. Express*, vol. 25, pp. 27506–27518, Oct 2017.
- [163] A. L'Huillier and P. Balcou, "High-order harmonic generation in rare gases with a 1-ps 1053-nm laser," *Phys. Rev. Lett.*, vol. 70, pp. 774–777, Feb 1993.
- [164] G. Farkas and C. Tóth, "Proposal for attosecond light pulse generation using laser induced multiple-harmonic conversion processes in rare gases," *Physics Letters A*, vol. 168, no. 5, pp. 447–450, 1992.
- [165] S. Harris, J. Macklin, and T. Hänsch, "Atomic scale temporal structure inherent to high-order harmonic generation," *Optics Communications*, vol. 100, no. 5, pp. 487–490, 1993.
- [166] K. C. Kulander and B. W. Shore, "Calculations of multiple-harmonic conversion of 1064-nm radiation in xe," *Phys. Rev. Lett.*, vol. 62, pp. 524–526, Jan 1989.

-
- [167] A. L'Huillier, K. J. Schafer, and K. C. Kulander, "Theoretical aspects of intense field harmonic generation," *Journal of Physics B: Atomic, Molecular and Optical Physics*, vol. 24, p. 3315, aug 1991.
- [168] K. C. Kulander, K. J. Schafer, and J. L. Krause, *Dynamics of Short-Pulse Excitation, Ionization and Harmonic Conversion*, pp. 95–110. Boston, MA: Springer US, 1993.
- [169] P. B. Corkum and F. Krausz, "Attosecond science," *Nature Physics*, vol. 3, pp. 381–387, Jun 2007.
- [170] C. Lin, A. Le, C. Jin, and H. Wei, *Attosecond and Strong-Field Physics: Principles and Applications*. Cambridge University Press, 2018.
- [171] L. V. Keldysh, "Ionization in the field of a strong electromagnetic wave," *Zh. Eksperim. i Teor. Fiz.*, vol. 47, pp. 1945–1307, 11 1964.
- [172] J. Jarnestad, "Laser light interacts with atoms in a gas." Accessed: 2024-05-01.
- [173] F. A. Ilkov, J. E. Decker, and S. L. Chin, "Ionization of atoms in the tunnelling regime with experimental evidence using hg atoms," *Journal of Physics B: Atomic, Molecular and Optical Physics*, vol. 25, p. 4005, oct 1992.
- [174] A. S. Landsman and U. Keller, "Attosecond science and the tunnelling time problem," *Physics Reports*, vol. 547, pp. 1–24, 2015. Attosecond science and the tunneling time problem.
- [175] G. L. Yudin and M. Y. Ivanov, "Nonadiabatic tunnel ionization: Looking inside a laser cycle," *Phys. Rev. A*, vol. 64, p. 013409, Jun 2001.
- [176] R. Boge, C. Cirelli, A. S. Landsman, S. Heuser, A. Ludwig, J. Maurer, M. Weger, L. Gallmann, and U. Keller, "Probing nonadiabatic effects in strong-field tunnel ionization," *Phys. Rev. Lett.*, vol. 111, p. 103003, Sep 2013.
- [177] P. Agostini, F. Fabre, G. Mainfray, G. Petite, and N. K. Rahman, "Free-free transitions following six-photon ionization of xenon atoms," *Phys. Rev. Lett.*, vol. 42, pp. 1127–1130, Apr 1979.
- [178] M. V. Ammosov, N. B. Delone, and V. P. Krainov, "Tunnel Ionization Of Complex Atoms And Atomic Ions In Electromagnetic Field," in *High Intensity Laser Processes* (J. A. Alcock, ed.), vol. 0664, pp. 138 – 141, International Society for Optics and Photonics, SPIE, 1986.

- [179] X. M. Tong and C. D. Lin, "Empirical formula for static field ionization rates of atoms and molecules by lasers in the barrier-suppression regime," *Journal of Physics B: Atomic, Molecular and Optical Physics*, vol. 38, p. 2593, jul 2005.
- [180] A. M. Perelomov, V. S. Popov, and M. V. Terentev, "Ionization of atoms in an alternating electric field," *Journal of Experimental and Theoretical Physics*, vol. 23, p. 207, 1966.
- [181] P. B. Corkum, "Plasma perspective on strong field multiphoton ionization," *Phys. Rev. Lett.*, vol. 71, pp. 1994–1997, Sep 1993.
- [182] D. H. Ko, K. T. Kim, and C. H. Nam, "Attosecond-chirp compensation with material dispersion to produce near transform-limited attosecond pulses," *Journal of Physics B: Atomic, Molecular and Optical Physics*, vol. 45, p. 074015, mar 2012.
- [183] J. L. Krause, K. J. Schafer, and K. C. Kulander, "High-order harmonic generation from atoms and ions in the high intensity regime," *Phys. Rev. Lett.*, vol. 68, pp. 3535–3538, Jun 1992.
- [184] M. Lewenstein, P. Balcou, M. Y. Ivanov, A. L'Huillier, and P. B. Corkum, "Theory of high-harmonic generation by low-frequency laser fields," *Phys. Rev. A*, vol. 49, pp. 2117–2132, Mar 1994.
- [185] L. Plaja and J. A. Pérez-Hernández, "A quantitative s-matrix approach to high-order harmonic generation from multiphoton to tunneling regimes," *Opt. Express*, vol. 15, pp. 3629–3634, Apr 2007.
- [186] J. A. Pérez-Hernández, L. Roso, and L. Plaja, "Harmonic generation beyond the strong-field approximation: the physics behind the short-wave-infrared scaling laws," *Opt. Express*, vol. 17, pp. 9891–9903, Jun 2009.
- [187] K. Schiessl, K. L. Ishikawa, E. Persson, and J. Burgdörfer, "Quantum path interference in the wavelength dependence of high-harmonic generation," *Phys. Rev. Lett.*, vol. 99, p. 253903, Dec 2007.
- [188] S. Haessler, T. Balčiunas, G. Fan, G. Andriukaitis, A. Pugžlys, A. Baltuška, T. Witting, R. Squibb, A. Zaïr, J. W. G. Tisch, J. P. Marangos, and L. E. Chipperfield, "Optimization of quantum trajectories driven by strong-field waveforms," *Phys. Rev. X*, vol. 4, p. 021028, May 2014.
- [189] T. Kroh, C. Jin, P. Krogen, P. D. Keathley, A.-L. Calendron, J. P. Siqueira, H. Liang, E. L. F. ao Filho, C. D. Lin, F. X. Kärtner, and K.-H. Hong, "Enhanced high-harmonic generation up to the soft x-ray region driven

- by mid-infrared pulses mixed with their third harmonic," *Opt. Express*, vol. 26, pp. 16955–16969, Jun 2018.
- [190] T. Severt, J. Troß, G. Kolliopoulos, I. Ben-Itzhak, and C. A. Trallero-Herrero, "Enhancing high-order harmonic generation by controlling the diffusion of the electron wave packet," *Optica*, vol. 8, pp. 1113–1121, Aug 2021.
- [191] T. Popmintchev, M.-C. Chen, P. Arpin, M. M. Murnane, and H. C. Kapteyn, "The attosecond nonlinear optics of bright coherent x-ray generation," *Nature Photonics*, vol. 4, pp. 822–832, Dec 2010.
- [192] A. G. Ciriolo, R. M. Vázquez, A. Roversi, A. Frezzotti, C. Vozzi, R. Osellame, and S. Stagira, "Femtosecond laser-micromachining of glass micro-chip for high order harmonic generation in gases," *Micromachines*, vol. 11, no. 2, 2020.
- [193] A. G. Ciriolo, R. Martínez Vázquez, G. Crippa, M. Devetta, D. Faccialà, P. Barbato, F. Frassetto, M. Negro, F. Bariselli, L. Poletto, V. Tosa, A. Frezzotti, C. Vozzi, R. Osellame, and S. Stagira, "Microfluidic devices for quasi-phase-matching in high-order harmonic generation," *APL Photonics*, vol. 7, p. 110801, 11 2022.
- [194] J. Pupeikis, P.-A. Chevreuril, N. Bigler, L. Gallmann, C. R. Phillips, and U. Keller, "Water window soft x-ray source enabled by a 25 w few-cycle 2.2 μm OPCPA at 100 khz," *Optica*, vol. 7, pp. 168–171, Feb 2020.
- [195] M. Gebhardt, T. Heuermann, R. Klas, C. Liu, A. Kirsche, M. Lenski, Z. Wang, C. Gaida, J. E. Antonio-Lopez, A. Schülzgen, R. Amezcua-Correa, J. Rothhardt, and J. Limpert, "Bright, high-repetition-rate water window soft x-ray source enabled by nonlinear pulse self-compression in an antiresonant hollow-core fibre," *Light: Science & Applications*, vol. 10, p. 36, Feb 2021.
- [196] M. Hoegner, "HHGmax." <https://github.com/Leberwurscht/HHGmax>. Accessed: 2023-12-14.
- [197] M. Högner, V. Tosa, and I. Pupeza, "Generation of isolated attosecond pulses with enhancement cavities—a theoretical study," *New Journal of Physics*, vol. 19, p. 033040, mar 2017.
- [198] M. Högner, *Optical High-Order Harmonic Generation in Gas Targets with Spatially Tailored Driving Fields*. Master thesis, Fachbereich Physik der Ludwig-Maximilians-Universität München, 2013.
- [199] A. Gordon and F. X. Kärtner, "Quantitative modeling of single atom high harmonic generation," *Phys. Rev. Lett.*, vol. 95, p. 223901, Nov 2005.

- [200] V.-M. Gkortsas, S. Bhardwaj, C.-J. Lai, K.-H. Hong, E. L. Falcão Filho, and F. X. Kärtner, "Interplay of multiphoton and tunneling ionization in short-wavelength-driven high-order harmonic generation," *Phys. Rev. A*, vol. 84, p. 013427, Jul 2011.
- [201] M. Lewenstein, P. Salières, and A. L'Huillier, "Phase of the atomic polarization in high-order harmonic generation," *Phys. Rev. A*, vol. 52, pp. 4747–4754, Dec 1995.
- [202] M. Bellini, C. Lyngå, A. Tozzi, M. B. Gaarde, T. W. Hänsch, A. L'Huillier, and C.-G. Wahlström, "Temporal coherence of ultrashort high-order harmonic pulses," *Phys. Rev. Lett.*, vol. 81, pp. 297–300, Jul 1998.
- [203] R. Weissenbilder, S. Carlström, L. Rego, C. Guo, C. M. Heyl, P. Smorenburg, E. Constant, C. L. Arnold, and A. L'Huillier, "How to optimize high-order harmonic generation in gases," *Nature Reviews Physics*, vol. 4, pp. 713–722, Nov 2022.
- [204] P. Salières, B. Carré, L. L. Déroff, F. Grasbon, G. G. Paulus, H. Walther, R. Kopold, W. Becker, D. B. Milošević, A. Sanpera, and M. Lewenstein, "Feynman's path-integral approach for intense-laser-atom interactions," *Science*, vol. 292, no. 5518, pp. 902–905, 2001.
- [205] A. Zaïr, M. Holler, A. Guandalini, F. Schapper, J. Biegert, L. Gallmann, U. Keller, A. S. Wyatt, A. Monmayrant, I. A. Walmsley, E. Cormier, T. Auguste, J. P. Caumes, and P. Salières, "Quantum path interferences in high-order harmonic generation," *Phys. Rev. Lett.*, vol. 100, p. 143902, Apr 2008.
- [206] P. Antoine, A. L'Huillier, and M. Lewenstein, "Attosecond pulse trains using high-order harmonics," *Phys. Rev. Lett.*, vol. 77, pp. 1234–1237, Aug 1996.
- [207] E. Constant, D. Garzella, P. Breger, E. Mével, C. Dorrer, C. Le Blanc, F. Salin, and P. Agostini, "Optimizing high harmonic generation in absorbing gases: Model and experiment," *Phys. Rev. Lett.*, vol. 82, pp. 1668–1671, Feb 1999.
- [208] "X-ray form factor, atten. & scatt. tables." <https://physics.nist.gov/PhysRefData/FFast/html/form.html>. Accessed: 2024-04-18.
- [209] C.-J. Lai and F. X. Kärtner, "The influence of plasma defocusing in high harmonic generation," *Opt. Express*, vol. 19, pp. 22377–22387, Nov 2011.
- [210] "Refractiveindex.info." <https://refractiveindex.info>. Accessed: 2024-04-18.

- [211] P. M. Paul, E. S. Toma, P. Breger, G. Mullot, F. Augé, P. Balcou, H. G. Muller, and P. Agostini, "Observation of a train of attosecond pulses from high harmonic generation," *Science*, vol. 292, no. 5522, pp. 1689–1692, 2001.
- [212] A. S. Johnson, D. R. Austin, D. A. Wood, C. Brahms, A. Gregory, K. B. Holzner, S. Jarosch, E. W. Larsen, S. Parker, C. S. Strüber, P. Ye, J. W. G. Tisch, and J. P. Marangos, "High-flux soft x-ray harmonic generation from ionization-shaped few-cycle laser pulses," *Science Advances*, vol. 4, no. 5, p. eaar3761, 2018.
- [213] J. Schötz, B. Förg, W. Schweinberger, I. Liontos, H. A. Masood, A. M. Kamal, C. Jakubeit, N. G. Kling, T. Paasch-Colberg, S. Biswas, M. Högnér, I. Pupeza, M. Alharbi, A. M. Azzeer, and M. F. Kling, "Phase-matching for generation of isolated attosecond xuv and soft-x-ray pulses with few-cycle drivers," *Phys. Rev. X*, vol. 10, p. 041011, Oct 2020.
- [214] S. C. Rae and K. Burnett, "Detailed simulations of plasma-induced spectral blueshifting," *Phys. Rev. A*, vol. 46, pp. 1084–1090, Jul 1992.
- [215] I. Tyulnev, *Sub-Cycle Nonlinear Pulse Propagation*. Master thesis, Fachbereich Physik der Universität Hamburg, 2019.
- [216] M. Geissler, G. Tempea, A. Scrinzi, M. Schnürer, F. Krausz, and T. Brabec, "Light propagation in field-ionizing media: Extreme nonlinear optics," *Phys. Rev. Lett.*, vol. 83, pp. 2930–2933, Oct 1999.
- [217] X. Tang, K. Wang, B. Li, Y. Chen, C. D. Lin, and C. Jin, "Optimal generation and isolation of attosecond pulses in an overdriven ionized medium," *Opt. Lett.*, vol. 46, pp. 5137–5140, Oct 2021.
- [218] M. Geissler, G. Tempea, and T. Brabec, "Phase-matched high-order harmonic generation in the nonadiabatic limit," *Phys. Rev. A*, vol. 62, p. 033817, Aug 2000.
- [219] M. B. Gaarde, J. L. Tate, and K. J. Schafer, "Macroscopic aspects of attosecond pulse generation," *Journal of Physics B: Atomic, Molecular and Optical Physics*, vol. 41, p. 132001, jun 2008.
- [220] F. Silva, S. M. Teichmann, S. L. Cousin, M. Hemmer, and J. Biegert, "Spatiotemporal isolation of attosecond soft x-ray pulses in the water window," *Nature Communications*, vol. 6, p. 6611, Mar 2015.
- [221] H.-W. Sun, P.-C. Huang, Y.-H. Tzeng, J.-T. Huang, C. D. Lin, C. Jin, and M.-C. Chen, "Extended phase matching of high harmonic generation by plasma-induced defocusing," *Optica*, vol. 4, pp. 976–981, Aug 2017.

- [222] B. Li, K. Wang, X. Tang, Y. Chen, C. D. Lin, and C. Jin, "Generation of isolated soft x-ray attosecond pulses with mid-infrared driving lasers via transient phase-matching gating," *New Journal of Physics*, vol. 23, p. 073051, jul 2021.
- [223] C. Spielmann, N. H. Burnett, S. Sartania, R. Koppitsch, M. Schnürer, C. Kan, M. Lenzner, P. Wobrauschek, and F. Krausz, "Generation of coherent x-rays in the water window using 5-femtosecond laser pulses," *Science*, vol. 278, no. 5338, pp. 661–664, 1997.
- [224] Z. Chang, A. Rundquist, H. Wang, M. M. Murnane, and H. C. Kapteyn, "Generation of coherent soft x rays at 2.7 nm using high harmonics," *Phys. Rev. Lett.*, vol. 79, pp. 2967–2970, Oct 1997.
- [225] M. Schnürer, C. Spielmann, P. Wobrauschek, C. Strelt, N. H. Burnett, C. Kan, K. Ferencz, R. Koppitsch, Z. Cheng, T. Brabec, and F. Krausz, "Coherent 0.5-keV x-ray emission from helium driven by a sub-10-fs laser," *Phys. Rev. Lett.*, vol. 80, pp. 3236–3239, Apr 1998.
- [226] E. A. Gibson, A. Paul, N. Wagner, R. Tobey, D. Gaudiosi, S. Backus, I. P. Christov, A. Aquila, E. M. Gullikson, D. T. Attwood, M. M. Murnane, and H. C. Kapteyn, "Coherent soft x-ray generation in the water window with quasi-phase matching," *Science*, vol. 302, no. 5642, pp. 95–98, 2003.
- [227] E. Seres, J. Seres, F. Krausz, and C. Spielmann, "Generation of coherent soft-x-ray radiation extending far beyond the titanium *L* edge," *Phys. Rev. Lett.*, vol. 92, p. 163002, Apr 2004.
- [228] J. Seres, P. Wobrauschek, C. Strelt, V. S. Yakovlev, E. Seres, F. Krausz, and C. Spielmann, "Generation of coherent keV x-rays with intense femtosecond laser pulses," *New Journal of Physics*, vol. 8, p. 251, oct 2006.
- [229] E. Seres, J. Seres, and C. Spielmann, "X-ray absorption spectroscopy in the keV range with laser generated high harmonic radiation," *Applied Physics Letters*, vol. 89, p. 181919, 11 2006.
- [230] M. Zepf, B. Dromey, M. Landreman, P. Foster, and S. M. Hooker, "Bright quasi-phase-matched soft-x-ray harmonic radiation from argon ions," *Phys. Rev. Lett.*, vol. 99, p. 143901, Oct 2007.
- [231] J. Seres, V. S. Yakovlev, E. Seres, C. Strelt, P. Wobrauschek, C. Spielmann, and F. Krausz, "Coherent superposition of laser-driven soft-x-ray harmonics from successive sources," *Nature Physics*, vol. 3, pp. 878–883, Dec 2007.

- [232] P.-A. Chevreauil, F. Brunner, U. Thumm, U. Keller, and L. Gallmann, "Breakdown of the single-collision condition for soft x-ray high harmonic generation in noble gases," *Optica*, vol. 9, pp. 1448–1457, Dec 2022.
- [233] G. Tempea, M. Geissler, M. Schnürer, and T. Brabec, "Self-phase-matched high harmonic generation," *Phys. Rev. Lett.*, vol. 84, pp. 4329–4332, May 2000.
- [234] C. Altucci, R. Bruzzese, C. de Lisio, M. Nisoli, S. Stagira, S. De Silvestri, O. Svelto, A. Boscolo, P. Ceccherini, L. Poletto, G. Tondello, and P. Villoresi, "Tunable soft-x-ray radiation by high-order harmonic generation," *Phys. Rev. A*, vol. 61, p. 021801, Dec 1999.
- [235] H. J. Shin, D. G. Lee, Y. H. Cha, K. H. Hong, and C. H. Nam, "Generation of nonadiabatic blueshift of high harmonics in an intense femtosecond laser field," *Phys. Rev. Lett.*, vol. 83, pp. 2544–2547, Sep 1999.
- [236] V. S. Yakovlev, M. Ivanov, and F. Krausz, "Enhanced phase-matching for generation of soft x-ray harmonics and attosecond pulses in atomic gases," *Opt. Express*, vol. 15, pp. 15351–15364, Nov 2007.
- [237] B. Shan and Z. Chang, "Dramatic extension of the high-order harmonic cutoff by using a long-wavelength driving field," *Phys. Rev. A*, vol. 65, p. 011804, Dec 2001.
- [238] E. J. Takahashi, T. Kanai, K. L. Ishikawa, Y. Nabekawa, and K. Midorikawa, "Coherent water window x ray by phase-matched high-order harmonic generation in neutral media," *Phys. Rev. Lett.*, vol. 101, p. 253901, Dec 2008.
- [239] H. Xiong, H. Xu, Y. Fu, J. Yao, B. Zeng, W. Chu, Y. Cheng, Z. Xu, E. J. Takahashi, K. Midorikawa, X. Liu, and J. Chen, "Generation of a coherent x ray in the water window region at 1 khz repetition rate using a mid-infrared pump source," *Opt. Lett.*, vol. 34, pp. 1747–1749, Jun 2009.
- [240] J. Rothhardt, S. Hädrich, A. Klenke, S. Demmler, A. Hoffmann, T. Gotschall, T. Eidam, M. Krebs, J. Limpert, and A. Tünnermann, "53 w average power few-cycle fiber laser system generating soft x rays up to the water window," *Opt. Lett.*, vol. 39, pp. 5224–5227, Sep 2014.
- [241] G. J. Stein, P. D. Keathley, P. Krogen, H. Liang, J. P. Siqueira, C.-L. Chang, C.-J. Lai, K.-H. Hong, G. M. Laurent, and F. X. Kärtner, "Water-window soft x-ray high-harmonic generation up to the nitrogen k-edge driven by a khz, 2.1 μm OPCPA source," *Journal of Physics B: Atomic, Molecular and Optical Physics*, vol. 49, p. 155601, jul 2016.

- [242] V. Cardin, B. E. Schmidt, N. Thiré, S. Beaulieu, V. Wanie, M. Negro, C. Vozzi, V. Tosa, and F. Légaré, "Self-channelled high harmonic generation of water window soft x-rays," *Journal of Physics B: Atomic, Molecular and Optical Physics*, vol. 51, p. 174004, aug 2018.
- [243] V. E. Leshchenko, B. K. Talbert, Y. H. Lai, S. Li, Y. Tang, S. J. Hageman, G. Smith, P. Agostini, L. F. DiMauro, and C. I. Blaga, "High-power few-cycle cr:zns mid-infrared source for attosecond soft x-ray physics," *Optica*, vol. 7, pp. 981–988, Aug 2020.
- [244] P.-A. Chevreau, F. Brunner, S. Hrisafov, J. Pupeikis, C. R. Phillips, U. Keller, and L. Gallmann, "Water-window high harmonic generation with 0.8- μm and 2.2- μm OPCPAs at 100 khz," *Opt. Express*, vol. 29, pp. 32996–33008, Oct 2021.
- [245] M. Dorner-Kirchner, V. Shumakova, G. Coccia, E. Kaksis, B. E. Schmidt, V. Pervak, A. Pugzlys, A. Baltuška, M. Kitzler-Zeiler, and P. A. Carpeggiani, "Hhg at the carbon k-edge directly driven by srs red-shifted pulses from an ytterbium amplifier," *ACS Photonics*, vol. 10, pp. 84–91, Jan 2023.
- [246] M.-C. Chen, P. Arpin, T. Popmintchev, M. Gerrity, B. Zhang, M. Seaberg, D. Popmintchev, M. M. Murnane, and H. C. Kapteyn, "Bright, coherent, ultrafast soft x-ray harmonics spanning the water window from a tabletop light source," *Phys. Rev. Lett.*, vol. 105, p. 173901, Oct 2010.
- [247] C. Ding, W. Xiong, T. Fan, D. D. Hickstein, T. Popmintchev, X. Zhang, M. Walls, M. M. Murnane, and H. C. Kapteyn, "High flux coherent super-continuum soft x-ray source driven by a single-stage, 10mj, ti:sapphire amplifier-pumped opa," *Opt. Express*, vol. 22, pp. 6194–6202, Mar 2014.
- [248] D. Popmintchev, B. R. Galloway, M.-C. Chen, F. Dollar, C. A. Mancuso, A. Hankla, L. Miaja-Avila, G. O'Neil, J. M. Shaw, G. Fan, S. Ališauskas, G. Andriukaitis, T. Balčiunas, O. D. Mücke, A. Pugzlys, A. Baltuška, H. C. Kapteyn, T. Popmintchev, and M. M. Murnane, "Near- and extended-edge x-ray-absorption fine-structure spectroscopy using ultrafast coherent high-order harmonic supercontinua," *Phys. Rev. Lett.*, vol. 120, p. 093002, Mar 2018.
- [249] J. Li, X. Ren, Y. Yin, Y. Cheng, E. Cunningham, Y. Wu, and Z. Chang, "Polarization gating of high harmonic generation in the water window," *Applied Physics Letters*, vol. 108, p. 231102, 06 2016.

- [250] M. A. Silva-Toledo, F. Scheiba, M. Kubullek, R. E. Mainz, G. M. Rossi, and F. X. Kärtner, "Water window attosecond pulses driven by sub-cycle tailored waveforms," in *CLEO 2023*, p. FW4M.5, Optica Publishing Group, 2023.
- [251] M. Nisoli and G. Sansone, "New frontiers in attosecond science," *Progress in Quantum Electronics*, vol. 33, no. 1, pp. 17–59, 2009.
- [252] G. Sansone, L. Poletto, and M. Nisoli, "High-energy attosecond light sources," *Nature Photonics*, vol. 5, pp. 655–663, Nov 2011.
- [253] J. Li, J. Lu, A. Chew, S. Han, J. Li, Y. Wu, H. Wang, S. Ghimire, and Z. Chang, "Attosecond science based on high harmonic generation from gases and solids," *Nature Communications*, vol. 11, p. 2748, Jun 2020.
- [254] K. Midorikawa, "Progress on table-top isolated attosecond light sources," *Nature Photonics*, vol. 16, pp. 267–278, Apr 2022.
- [255] A. Wirth, M. T. Hassan, I. Grguraš, J. Gagnon, A. Moulet, T. T. Luu, S. Pabst, R. Santra, Z. A. Alahmed, A. M. Azzeer, V. S. Yakovlev, V. Pervak, F. Krausz, and E. Goulielmakis, "Synthesized light transients," *Science*, vol. 334, no. 6053, pp. 195–200, 2011.
- [256] Y. Yang, R. E. Mainz, G. M. Rossi, F. Scheiba, M. A. Silva-Toledo, P. D. Keathley, G. Cirmi, and F. X. Kärtner, "Strong-field coherent control of isolated attosecond pulse generation," *Nature Communications*, vol. 12, p. 6641, Nov 2021.
- [257] P. B. Corkum, N. H. Burnett, and M. Y. Ivanov, "Subfemtosecond pulses," *Opt. Lett.*, vol. 19, pp. 1870–1872, Nov 1994.
- [258] I. J. Sola, E. Mével, L. Elouga, E. Constant, V. Strelkov, L. Poletto, P. Villoresi, E. Benedetti, J.-P. Caumes, S. Stagira, C. Vozzi, G. Sansone, and M. Nisoli, "Controlling attosecond electron dynamics by phase-stabilized polarization gating," *Nature Physics*, vol. 2, pp. 319–322, May 2006.
- [259] G. Sansone, E. Benedetti, F. Calegari, C. Vozzi, L. Avaldi, R. Flammini, L. Poletto, P. Villoresi, C. Altucci, R. Velotta, S. Stagira, S. D. Silvestri, and M. Nisoli, "Isolated single-cycle attosecond pulses," *Science*, vol. 314, no. 5798, pp. 443–446, 2006.
- [260] J. Li, X. Ren, Y. Yin, K. Zhao, A. Chew, Y. Cheng, E. Cunningham, Y. Wang, S. Hu, Y. Wu, M. Chini, and Z. Chang, "53-attosecond x-ray pulses reach the carbon k-edge," *Nature Communications*, vol. 8, p. 186, Aug 2017.

- [261] Z. Chang, "Controlling attosecond pulse generation with a double optical gating," *Phys. Rev. A*, vol. 76, p. 051403, Nov 2007.
- [262] H. Mashiko, S. Gilbertson, C. Li, S. D. Khan, M. M. Shakya, E. Moon, and Z. Chang, "Double optical gating of high-order harmonic generation with carrier-envelope phase stabilized lasers," *Phys. Rev. Lett.*, vol. 100, p. 103906, Mar 2008.
- [263] H. Mashiko, S. Gilbertson, M. Chini, X. Feng, C. Yun, H. Wang, S. D. Khan, S. Chen, and Z. Chang, "Extreme ultraviolet supercontinua supporting pulse durations of less than one atomic unit of time," *Opt. Lett.*, vol. 34, pp. 3337–3339, Nov 2009.
- [264] K. Zhao, Q. Zhang, M. Chini, Y. Wu, X. Wang, and Z. Chang, "Tailoring a 67 attosecond pulse through advantageous phase-mismatch," *Opt. Lett.*, vol. 37, pp. 3891–3893, Sep 2012.
- [265] X. Feng, S. Gilbertson, H. Mashiko, H. Wang, S. D. Khan, M. Chini, Y. Wu, K. Zhao, and Z. Chang, "Generation of isolated attosecond pulses with 20 to 28 femtosecond lasers," *Phys. Rev. Lett.*, vol. 103, p. 183901, Oct 2009.
- [266] S. Gilbertson, Y. Wu, S. D. Khan, M. Chini, K. Zhao, X. Feng, and Z. Chang, "Isolated attosecond pulse generation using multicycle pulses directly from a laser amplifier," *Phys. Rev. A*, vol. 81, p. 043810, Apr 2010.
- [267] J. Li, A. Chew, S. Hu, J. White, X. Ren, S. Han, Y. Yin, Y. Wang, Y. Wu, and Z. Chang, "Double optical gating for generating high flux isolated attosecond pulses in the soft x-ray regime," *Opt. Express*, vol. 27, pp. 30280–30286, Oct 2019.
- [268] H. Mashiko, K. Oguri, and T. Sogawa, "Attosecond pulse generation in carbon K-edge region (284eV) with sub-250 μ J driving laser using generalized double optical gating method," *Applied Physics Letters*, vol. 102, p. 171111, 05 2013.
- [269] P. Tzallas, E. Skantzakis, C. Kalpouzos, E. P. Benis, G. D. Tsakiris, and D. Charalambidis, "Generation of intense continuum extreme-ultraviolet radiation by many-cycle laser fields," *Nature Physics*, vol. 3, pp. 846–850, Dec 2007.
- [270] H. Timmers, M. Sabbar, J. Hellwagner, Y. Kobayashi, D. M. Neumark, and S. R. Leone, "Polarization-assisted amplitude gating as a route to tunable, high-contrast attosecond pulses," *Optica*, vol. 3, pp. 707–710, Jul 2016.

-
- [271] C. A. Haworth, L. E. Chipperfield, J. S. Robinson, P. L. Knight, J. P. Marangos, and J. W. G. Tisch, "Half-cycle cutoffs in harmonic spectra and robust carrier-envelope phase retrieval," *Nature Physics*, vol. 3, pp. 52–57, Jan 2007.
- [272] R. Kienberger, E. Goulielmakis, M. Uiberacker, A. Baltuska, V. Yakovlev, F. Bammer, A. Scrinzi, T. Westerwalbesloh, U. Kleineberg, U. Heinzmann, M. Drescher, and F. Krausz, "Atomic transient recorder," *Nature*, vol. 427, pp. 817–821, Feb 2004.
- [273] H. G. Muller, "Reconstruction of attosecond harmonic beating by interference of two-photon transitions," *Applied Physics B*, vol. 74, pp. s17–s21, Jun 2002.
- [274] Y. Yang, *A novel optical tool for controlling and probing ultrafast surface dynamics*. Dissertation, Fachbereich Physik der Universität Hamburg, 2017.
- [275] M. Kitzler, N. Milosevic, A. Scrinzi, F. Krausz, and T. Brabec, "Quantum theory of attosecond xuv pulse measurement by laser dressed photoionization," *Phys. Rev. Lett.*, vol. 88, p. 173904, Apr 2002.
- [276] Y. Mairesse and F. Quéré, "Frequency-resolved optical gating for complete reconstruction of attosecond bursts," *Phys. Rev. A*, vol. 71, p. 011401, Jan 2005.
- [277] J. Gagnon, E. Goulielmakis, and V. S. Yakovlev, "The accurate frog characterization of attosecond pulses from streaking measurements," *Applied Physics B*, vol. 92, pp. 25–32, Jul 2008.
- [278] M. Lucchini, M. Brüggemann, A. Ludwig, L. Gallmann, U. Keller, and T. Feurer, "Ptychographic reconstruction of attosecond pulses," *Opt. Express*, vol. 23, pp. 29502–29513, Nov 2015.
- [279] M. Chini, S. Gilbertson, S. D. Khan, and Z. Chang, "Characterizing ultrabroadband attosecond lasers," *Opt. Express*, vol. 18, pp. 13006–13016, Jun 2010.
- [280] G. Laurent, W. Cao, I. Ben-Itzhak, and C. L. Cocke, "Attosecond pulse characterization," *Opt. Express*, vol. 21, pp. 16914–16927, Jul 2013.
- [281] P. D. Keathley, S. Bhardwaj, J. Moses, G. Laurent, and F. X. Kärtner, "Volkov transform generalized projection algorithm for attosecond pulse characterization," *New Journal of Physics*, vol. 18, p. 073009, Jul 2016.

- [282] S. Bhardwaj, S.-K. Son, K.-H. Hong, C.-J. Lai, F. X. Kärtner, and R. Santra, "Recombination-amplitude calculations of noble gases, in both length and acceleration forms, beyond the strong-field approximation," *Phys. Rev. A*, vol. 88, p. 053405, Nov 2013.
- [283] T. Witting, M. Osolodkov, F. Schell, F. Morales, S. Patchkovskii, P. Šušnjar, F. H. M. Cavalcante, C. S. Menoni, C. P. Schulz, F. J. Furch, and M. J. J. Vrakking, "Generation and characterization of isolated attosecond pulses at 100 khz repetition rate," *Optica*, vol. 9, pp. 145–151, Feb 2022.
- [284] T. Gaumnitz, A. Jain, and H. J. Wörner, "Complete reconstruction of ultra-broadband isolated attosecond pulses including partial averaging over the angular distribution," *Opt. Express*, vol. 26, pp. 14719–14740, May 2018.
- [285] M. Lucchini and M. Nisoli, "Refined ptychographic reconstruction of attosecond pulses," *Applied Sciences*, vol. 8, no. 12, 2018.
- [286] H. Cankaya, A.-L. Calendron, C. Zhou, S.-H. Chia, O. D. Muecke, G. Cirimi, , and F. X. Kaertner, "40- μ J passively CEP-stable seed source for ytterbium-based high-energy optical waveform synthesizers," *Optics Express*, vol. 24, no. 22, pp. 25169–25180, 2016.
- [287] H. Liang, P. Krogen, Z. Wang, H. Park, T. Kroh, K. Zawilski, P. Schunemann, J. Moses, L. F. DiMauro, F. X. Kaertner, and K.-H. Hong, "High-energy mid-infrared sub-cycle pulse synthesis from a parametric amplifier," *Nature Communications*, vol. 8, p. 141, 2017.
- [288] D. E. Rivas, A. Borot, D. E. Cardenas, G. Marcus, X. Gu, D. Herrmann, J. Xu, J. Tan, D. Korman, G. Ma, W. Dallari, G. D. Tsakiris, I. B. Foeldes, S. w. Chou, M. Weidman¹, B. Bergues, T. Wittmann, H. Schröder, P. Tzallas, D. Charalambidis, O. Razskazovskaya, V. Pervak, F. Krausz, and L. Veisz, "Next Generation Driver for Attosecond and Laser-plasma Physics," *Scientific Reports*, vol. 7, p. 5224, 2017.
- [289] Y.-C. Lin, Y. Nabekawa, and K. Midorikawa, "Optical parametric amplification of sub-cycle shortwave infrared pulses," *Nature Communications*, vol. 11, p. 3413, 2020.
- [290] A. Alismail, H. Wang, G. Barbiero, N. Altwaijry, S. A. Hussain, V. Pervak, W. Schweinberger, A. M. Azzeer, F. Krausz, and H. Fattahi, "Multi-octave, CEP-stable source for high-energy field synthesis," *Science Advances*, vol. 6, no. 7, p. eaax3408, 2020.
- [291] B. Xue, Y. Tamaru, Y. Fu, H. Yuan, P. Lan, O. D. Mücke, A. Suda, K. Midorikawa, and E. J. Takahashi, "Fully stabilized multi-tw optical

- waveform synthesizer: Toward gigawatt isolated attosecond pulses," *Science advances*, vol. 6, no. 16, p. eaay2802, 2020.
- [292] B. Xue, Y. Tamaru, Y. Fu, H. Yuan, P. Lan, O. D. Mücke, A. Suda, K. Midorikawa, and E. J. Takahashi, "A custom-tailored multi-tw optical electric field for gigawatt soft-x-ray isolated attosecond pulses," *Ultrafast Science*, vol. 2021, p. 9828026, Aug 2021.
- [293] H. Alqattan, D. Hui, V. Pervak, and M. T. Hassan, "Attosecond light field synthesis," *APL Photonics*, vol. 7, p. 041301, 04 2022.
- [294] A. Moulet, J. B. Bertrand, T. Klostermann, A. Guggenmos, N. Karpowicz, and E. Goulielmakis, "Soft x-ray excitonics," *Science*, vol. 357, no. 6356, pp. 1134–1138, 2017.
- [295] O. D. Mücke, S. Fang, G. Cirmi, G. M. Rossi, S.-H. Chia, H. Ye, Y. Yang, R. Mainz, C. Manzoni, P. Farinello, G. Cerullo, and F. X. Kärtner, "Toward waveform nonlinear optics using multimillijoule sub-cycle waveform synthesizers," *IEEE Journal of Selected Topics in Quantum Electronics*, vol. 21, no. 5, pp. 1–12, 2015.
- [296] Scheiba, Fabian, Rossi, Giulio Maria, Mainz, Roland E., Yang, Yudong, Cirmi, Giovanni, and Kärtner, Franz X., "Millijoule-level sub-cycle pulses from two channels of a parallel parametric waveform synthesizer," *EPJ Web Conf.*, vol. 205, p. 01011, 2019.
- [297] F. Scheiba, *Strong-Field Physics with a High Energy Waveform Synthesizer*. Dissertation, Fachbereich Physik der Universität Hamburg, 2023.
- [298] M. A. Silva-Toledo, F. Scheiba, G. M. Rossi, R. E. Mainz, Y. Yang, G. Cirmi, and F. X. Kärtner, "Spatial characterization of synthesized infrared sub-cycle pulses," in *2019 Conference on Lasers and Electro-Optics Europe and European Quantum Electronics Conference*, p. cf6.6, Optica Publishing Group, 2019.
- [299] G. M. Rossi, L. Wang, R. E. Mainz, H. Çankaya, F. X. Kärtner, and G. Cirmi, "Cep dependence of signal and idler upon pump-seed synchronization in optical parametric amplifiers," *Opt. Lett.*, vol. 43, pp. 178–181, Jan 2018.
- [300] H. J. Wörner, H. Niikura, J. B. Bertrand, P. B. Corkum, and D. M. Villeneuve, "Observation of electronic structure minima in high-harmonic generation," *Phys. Rev. Lett.*, vol. 102, p. 103901, Mar 2009.
- [301] F. Calegari, C. Vozzi, M. Negro, G. Sansone, F. Frassetto, L. Poletto, P. Villoresi, M. Nisoli, S. D. Silvestri, and S. Stagira, "Efficient continuum generation exceeding 200 eV by intense ultrashort two-color driver," *Opt. Lett.*, vol. 34, pp. 3125–3127, Oct 2009.

- [302] T. Siegel, R. Torres, D. J. Hoffmann, L. Brugnera, I. Procino, A. Zair, J. G. Underwood, E. Springate, I. C. E. Turcu, L. E. Chipperfield, and J. P. Marangos, "High harmonic emission from a superposition of multiple unrelated frequency fields," *Opt. Express*, vol. 18, pp. 6853–6862, Mar 2010.
- [303] L. V. Dao, K. B. Dinh, and P. Hannaford, "Perturbative optical parametric amplification in the extreme ultraviolet," *Nature Communications*, vol. 6, p. 7175, May 2015.
- [304] B. Schütte, P. Weber, K. Kovács, E. Balogh, B. Major, V. Tosa, S. Han, M. J. J. Vrakking, K. Varjú, and A. Rouzée, "Bright attosecond soft x-ray pulse trains by transient phase-matching in two-color high-order harmonic generation," *Opt. Express*, vol. 23, pp. 33947–33955, Dec 2015.
- [305] B. D. Bruner, M. Krüger, O. Pedatzur, G. Orenstein, D. Azoury, and N. Dudovich, "Robust enhancement of high harmonic generation via attosecond control of ionization," *Opt. Express*, vol. 26, pp. 9310–9322, Apr 2018.
- [306] B. Major, E. Balogh, K. Kovács, S. Han, B. Schütte, P. Weber, M. J. J. Vrakking, V. Tosa, A. Rouzée, and K. Varjú, "Spectral shifts and asymmetries in mid-infrared assisted high-order harmonic generation," *J. Opt. Soc. Am. B*, vol. 35, pp. A32–A38, Apr 2018.
- [307] K. Zinchenko, *Attosecond time-resolved absorption spectroscopy in the water window*. Dissertation, ETH Zurich, 2020.
- [308] T. Brabec and F. Krausz, "Nonlinear optical pulse propagation in the single-cycle regime," *Phys. Rev. Lett.*, vol. 78, pp. 3282–3285, Apr 1997.
- [309] I. H. Malitson, "Interspecimen comparison of the refractive index of fused silica," *Journal of the Optical Society of America*, vol. 55, no. 10, pp. 1205–1208, 1965.
- [310] C. Jin, G. Wang, A.-T. Le, and C. D. Lin, "Route to optimal generation of soft x-ray high harmonics with synthesized two-color laser pulses," *Scientific Reports*, vol. 4, p. 7067, Nov 2014.
- [311] G. Fraser, A. Abbey, A. Holland, K. McCarthy, A. Owens, and A. Wells, "The x-ray energy response of silicon part a. theory," *Nuclear Instruments and Methods in Physics Research Section A: Accelerators, Spectrometers, Detectors and Associated Equipment*, vol. 350, no. 1, pp. 368–378, 1994.

Publication list

In Peer-reviewed journals

1. Miguel A. Silva-Toledo*, Fabian Scheiba*, Maximilian Kubullek, Rafael de Q. Garcia, Roland E. Mainz, Giulio Maria Rossi, and Franz X. Kärtner. *Water window attosecond pulse generation with sub-cycle waveforms*. In preparation (2024). *These authors contributed equally.
2. Maximilian Kubullek, Miguel A. Silva-Toledo, Roland E. Mainz, Fabian Scheiba, Rafael de Q. Garcia, Felix Ritzkowksy, Giulio Maria Rossi, and Franz X. Kärtner. *Complete electric field characterization of multi-colour light fields*. In preparation (2024).
3. Roland E. Mainz, Giulio Maria Rossi, Fabian Scheiba, Miguel A. Silva-Toledo, Giovanni Cirmi, and Franz X. Kärtner. *Parametric Waveform Synthesis: a scalable approach to generate sub-cycle optical transients*. *Opt. Express* 31, 11363-11394 (2023).
4. Giovanni Cirmi, Roland E. Mainz, Miguel A. Silva-Toledo, Fabian Scheiba, Hüseyin Çankaya, Maximilian Kubullek, Giulio Maria Rossi, and Franz X. Kärtner. *Optical waveform synthesis and its applications*. *Laser Photonics Rev.*, 2200588 (2023).
5. Yudong Yang, Roland E. Mainz, Giulio Maria Rossi, Fabian Scheiba, Miguel A. Silva-Toledo, Phillip D. Keathley, Giovanni Cirmi, and Franz X. Kärtner. *Strong-field Coherent Control of Isolated Attosecond Pulse Generation*. *Nature Communications* 12, 6641 (2021).
6. Giulio Maria Rossi, Roland E. Mainz, Yudong Yang, Fabian Scheiba, Miguel A. Silva-Toledo, Shih-Hsuan Chia, Phillip D. Keathley, Shaobo Fang, Oliver D. Mücke, Cristian Manzoni, Giulio Cerullo, Giovanni Cirmi, and Franz X. Kärtner. *Sub-cycle millijoule-level parametric waveform synthesizer for attosecond science*. *Nature Photonics* 14, 629–635 (2020).

In conference proceedings

1. Miguel A. Silva-Toledo, Fabian Scheiba, Maximilian Kubullek, Roland E. Mainz, Giulio Maria Rossi, and Franz X. Kärtner. *Phase-Matching Water Window Attosecond Pulses with Sub-cycle Waveforms*. 9th International Conference on Attosecond Science and Technology (ATTO 9) 2023, paper Fr1-2.
2. Miguel A. Silva-Toledo, Fabian Scheiba, Maximilian Kubullek, Roland E. Mainz, Giulio Maria Rossi, and Franz X. Kärtner. *Water Window Attosecond Pulses driven by Sub-cycle Tailored Waveforms*. In Conference on Lasers and Electro-Optics (CLEO) 2023, Technical Digest Series (Optica Publishing Group, 2023), paper FW4M.5.
3. Miguel A. Silva-Toledo, Fabian Scheiba, Roland E. Mainz, Yudong Yang, Giovanni Cirimi, Giulio Maria Rossi, and Franz X. Kärtner. *Soft X-ray Attosecond Control via Parametric Waveform Synthesis*. In Conference on Lasers and Electro-Optics (CLEO), OSA Technical Digest (Optical Society of America, 2021), paper FF2K.5.
4. Miguel A. Silva-Toledo, Giulio Maria Rossi, Roland E. Mainz, Yudong Yang, Fabian Scheiba, Phillip D. Keathley, Giovanni Cirimi, and Franz X. Kärtner. *Waveform reproducibility from an OPA-based parallel synthesizer*. In OSA High-brightness Sources and Light-driven Interactions Congress 2020 (EUVXRAY, HILAS, MICS), OSA Technical Digest (Optical Society of America, 2020), paper HF1B.5
5. Miguel A. Silva-Toledo, Fabian Scheiba, Giulio Maria Rossi, Roland E. Mainz, Yudong Yang, Giovanni Cirimi, and Franz X. Kärtner. *Spatial Characterization of Synthesized Infrared Sub-Cycle Pulses*. In 2019 Conference on Lasers and Electro-Optics (CLEO) Europe and European Quantum Electronics Conference, OSA Technical Digest (Optical Society of America, 2019), paper cf.6.6.

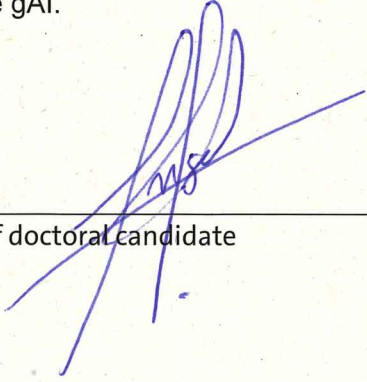
Declaration on oath

I hereby declare and affirm that this doctoral dissertation is my own work and that I have not used any aids and sources other than those indicated.

If electronic resources based on generative artificial intelligence (gAI) were used in the course of writing this dissertation, I confirm that my own work was the main and value-adding contribution and that complete documentation of all resources used is available in accordance with good scientific practice. I am responsible for any erroneous or distorted content, incorrect references, violations of data protection and copyright law or plagiarism that may have been generated by the gAI.

01.10.2024

Date


Signature of doctoral candidate

Acknowledgements

I am grateful to the many people who have accompanied me throughout this journey, which has been filled with moments of joy, hard work, and reward.

First, I sincerely thank my PhD supervisor, Prof. Dr. Franz X. Kärtner, for giving me the opportunity to work on technology at the forefront of attosecond science. The systems I worked with, which I believe are ultra-bleeding-edge, provided an incredible experience, and I appreciate the trust you placed in me to join your group and work with such advanced technology. You gave me the freedom to explore ideas while keeping me focused on the main topic. Your support throughout the long and complex water window project, which began in February 2021, was crucial. I also appreciate the occasional discussions in your office and during conferences and business trips, which provided insights to guide the work presented here. Your encouragement to attend conferences allowed me to engage with the broader academic community.

A key reason I felt confident moving from Zurich to Hamburg was meeting my PhD brother and friend, Dr. Fabian Scheiba. I also agree—this work wouldn't have happened without such a great partner. The realization of the experiments presented here was very much a shared effort throughout our PhD journeys. I admire how you always built solutions when something in the lab didn't work, making life easier for everyone. For example, your custom pieces to move the CCD spectrometer in the XYZ directions and the collection of scroll pumps in the main chamber were critical, especially for our first water window spectra. Thank you for your patience, your ability to make people feel comfortable asking questions, and your sense of humor. I'll always remember the good times: measuring beam profiles, compressing pulses, aligning the toroidal mirror, dancing during gas-cell scans, staying late in the lab just to change a damaged mirror and seeing whether the signal improves, moving the wedges of the OPAs, aligning the Cryo, the

OPERA and OPAs, and many other moments too long to include here!

Next, I'd like to thank Dr. Giulio Maria Rossi, who taught me how to correctly pronounce words like "bread" or "stuff" by adding an extra vowel at the end...ahah. Your mastery of the English language is impressive, and since then, I've continued improving to the point where people sometimes think I'm an English writer... But seriously, I'm truly grateful to have met you. I admire how you simplify complex tasks and problems, making them seem more manageable. I also appreciate the lengthy discussions, through which I learned to approach challenges from a more practical perspective. Your expertise in optics is remarkable, and I'm fortunate to have worked with an OPA master. Thank you for providing beautiful NIR beam profiles and those avocado-shaped IR beam profiles, as well as the smooth, fleshy, and wide spectra over the years. Next time you buy a beam-pointing system, you already know which company would increase your nerves and make you destroy many keyboards due to anger... Your contributions helped guide our team in the right direction and supported our collective progress, even during times when motivation fluctuated.

Dr. Roland Mainz was essential to this work—without him, nothing would have been stable. The lab would have been too warm, humidity levels too high, and there would have been no sub-cycle pulses, no tailored waveforms, and none of the results we achieved. I also admire your technical expertise in electronics, and I often suspect you had excellent chemistry teachers or were a top student, as your knowledge in that area is equally impressive. Thank you for being part of the team for so many years, for bringing humor and music to the lab, pushing the sorting of scans when needed, keeping the lock stable for hours, and creating the four unforgettable GUIs, each requiring its own MATLAB instance and countless buttons to shape the electric field. Those early and continuing efforts gave us "hairless" EUV spectra, led to the first attosecond streaking measurement, and have now resulted in the beautiful water window spectra we see today. I also learned from you how to create GUIs that operate in a "single-shot-every-shot" fashion, which led to our shared project: "THE POLICE." So thank you for that.

Next on the list is Dr. Yudong Yang, who built the first attosecond beamline and was incredibly patient with me during the early years of my PhD, teaching me how to operate it. I have fond memories of working with you on aligning the beamline, acquiring unlocked delay scans and gas-cell scans late into the night. During those times, I also became more interested in politics and history through our many discussions on these topics. I'll never forget the night we, along with others mentioned earlier, saw the first attosecond streaking trace together. Or the times we were on the verge of measuring streaking, only to face critical misalignments and have to start over. Thank you for your perseverance and motivation.

Maximilian Kubullek was a key contributor to the water window results. Early in his PhD, he updated and improved the acquisition codes, enabling systematic scans and minimizing confusion by automatically recording experimental parameters. This largely allowed the realization of the last water window experiment, and ensured clear as well as organized records of our data. Thank you for introducing me to tools like Git and Visual Studio Code. Our discussions on numerically modeling ultrashort pulse propagation helped me develop the on-axis HHG model. Additionally, the TREX technique, which originated from Giulio and was further developed by you, made the water window experiment incredibly sophisticated—arguably, in my opinion, the most advanced in HHG science to date! I'll also remember with a big smile the small gathering in our office where you were happily enjoying guacamole and listening to Latin music with the office members (Fabian, Tobi) and a few extra guests (Christian).

Almost a year ago, Rafael Garcia joined the team and has been an incredibly helpful and dedicated team player. He quickly grasped the problem, took over the HHG macroscopic code, and further developed it, implementing important mechanisms to bring it closer to the experimental data. Thanks to you, I avoided that silly mistake in my thesis! I also appreciate your hard work, curiosity and motivation.

I'd also like to express my gratitude to several others, more briefly: Dr. Oliver Mücke, Dr. Giovanni Cirimi, Dr. Guangjin Ma and Dr. Andrea Trabattoni for the early HHG discussions; Dr. Phillip "Donnie" Keathley for building the attosecond streaking reconstruction code and always being supportive in teaching us how to use it; Igor Tyulnev for the 2D few-cycle propagation code which provided valuable insights on the deformation of our sub-cycle pulses; Dr. Moritz Hoesch for allowing us to calibrate our photodiode at PETRA IV and providing feedback on the toroidal mirrors; Dr. Frank Siewert and Dr. Andrey Sokolov for characterizing our reflective zone plates and giving us such a nice time in Berlin. Thank you Thomas Tilp and Andrej Berg for your patience, and the timely designing and making of the chambers and frames of the new attosecond beamline.

I would also like to thank my former colleagues from ETH, Kristina Zincheko, and Fernando Ardana Lamas for their willingness to share their expertise on working with a water window HHG apparatus. Their valuable suggestions, including the use of Luxel filters to remove the driving pulse, and UV lamps for cleaning carbon-contaminated optics, among other recommendations, were extremely useful for the work presented here.

A special thanks to the IT department, Tim Gerhardt, and Adrian Pagel for always being helpful and solving problems quickly. To Uta Freydank for keeping the administrative work under control, and for your patience and support with extending my contracts.

ACKNOWLEDGEMENTS

Also to office and team members that contributed to the nice atmosphere in the team and with whom I eventually enjoyed a drink (or maybe two), here these are: Dr. Tobias Kroh, Dr. Xavier Gutiérrez, Dr. Neetesh Singh, Dr. Halil Olgun, Dr. Nicolai Klemke, Dr. Huseyin Cankaya, Dr. Elias Kueny, Christian Rentschler, and Markus Ludwig.

I would also like to thank to my previous advisors that supported my application for me to do my PhD in this group. Prof. Dr. Nina Rohringer, Prof. Dr. Hans Jakob Wörner, and Dr. Tran Trung Luu. And I also thank my mentor in Mexico, Prof. Dr. José Jiménez Mier y Terán, for sparking my interest in optics, atoms and molecules and that thanks to him I made it my passion.

I'd like to thank my friends Fernanda Vázquez, Adriana Sánchez, Jair Hernández, Ricardo Varela, Jacopo Mancabelli, Lisa Heinzer, and Griffin Rodgers, for staying in touch and keeping me in their life. A special thanks to Jessica Dominguez, Luis Pérez, and César García for being with me throughout this journey and providing constant emotional support and fun over the years. I'm incredibly lucky to have you in my life.

Finally, I want to thank my family. To my father, Miguel Angel Silva Méndez, and my mother, María Guadalupe Toledo Espinosa—thank you for always believing in me. I owe much of where I am today to your unwavering support, and I will always be deeply grateful to you. To my siblings, Aldo and Aline, and finally, to my life partner, Daniela, who has been an incredible support throughout these years, always bringing joy and helping me appreciate the wonderful moments in life.